A study of the elastic and electronic properties of III-nitride semiconductors

Daniel Stephen Patrick Tanner

Thesis submitted in partial fulfilment of the requirements
of the degree of Doctor of Philosophy

at the
Department of Physics,
University College Cork,
National University of Ireland

Supervisor: Prof. Eoin P. O'Reilly
Co-supervisor: Dr. Stefan Schulz
Head of Department: Prof. John G. McInerney

December 2017

Contents

Declaration

I, Daniel Stephen Patrick Tanner, declare that this thesis entitled 'A study of the elastic and electronic properties of III-nitride semiconductors' and the work presented in it are my own. I confirm that:

- This work was done wholly or mainly while in candidature for a research degree at this University.
- Where any part of this thesis has previously been submitted for a degree or any other qualification at this University or any other institution, this has been clearly stated.
- Where I have consulted the published work of others, this is always clearly attributed.
- Where I have quoted from the work of others, the source is always given. With the exception of such quotations, this thesis is entirely my own work.
- I have acknowledged all main sources of help.
- Where the thesis is based on work done by myself jointly with others, I have made clear exactly what was done by others and what I have contributed myself.

Signed: _____

Date: _____

Publications

The following is a list of published work in which aspects of the research presented in this thesis have featured.

1. Refereed journal articles

- "Random alloy fluctuations and structural inhomogeneities in c-plane $\mathrm{In}_x\mathrm{Ga1}-x\mathrm{N}$ quantum wells: theory of ground and excited electron and hole states", **Daniel S. P. Tanner**, Miguel A. Caro, Eoin P. O'Reilly, and Stefan Schulz, *RSC Adv.* **6**, 64513 (2016).
- "Atomistic analysis of the electronic structure of m-plane InGaN/GaN quantum wells: Carrier localization effects in ground and excited states due to random alloy fluctuations", **Daniel S. P. Tanner**, Miguel A. Caro, Eoin P. O'Reilly, and Stefan Schulz, *Phys. Stat. Sol. B* **253**, 853 (2015).
- "Structural, electronic and optical properties of m-plane InGaN/GaN quantum wells: Insights from experiment and atomistic theory", Stefan Schulz, **Daniel P. Tanner**, Eoin P. O'Reilly, M. A. Caro, D. Sutherland, M. J. Davies, P. Dawson, F. Tang, J. T. Griffiths, F. Oehler, M. J. Kappers, R. A. Oliver, and C. J. Humphreys *Phys. Rev. B* **92**, 235419 (2015).
- "Theoretical and experimental analysis of the photoluminescence and photoluminescence excitation spectroscopy spectra of m-plane InGaN/GaN quantum wells ", Stefan Schulz, **Daniel S. P. Tanner**, Eoin P. O'Reilly, M. A. Caro, , F. Tang, J. T. Griffiths, F. Oehler, M. J. Kappers, R. A. Oliver, C. J. Humphreys, D. Sutherland, M. J. Davies, and P. Dawson *Appl. Phys. Lett* **109**, 223102 (2016).

2. Conference talks

During the course of my doctoral research I have personally presented the following conference talks:

- "Impact of random alloy fluctuations on the electronic properties of polar InGaN wells", **Daniel P. Tanner**, Stefan Schulz, C. Coughlan, M. A. Caro, and E. P. O'Reilly *2nd UK Semiconductors & UK Nitrides Consortium Summer Meeting*, Sheffield, England (2015).
- "Elastic properties of semiconductors beyond the limit of infinitesimal strain", **Daniel S. P. Tanner**, Miguel Caro, Eoin P. O'Reilly, and Stefan Schulz *3rd Euro TMCS II*, Cork, Ireland (2016).

In addition to these talks I have also contributed to, and have had aspects of my work presented in, the following conference talks, which were presented by my colleagues and collaborators:

- "Influence of atomistic effects on device behavior in nitride-based nanostructures", Eoin O'Reilly, **Daniel S. P. Tanner**, Miguel Caro, and Stefan Schulz, *2^{nd} Ψ_K conference*, San Sebastian, Spain, (2015).
- "Impact of random alloy fluctuations on the excited electron and hole states in InGaN/GaN quantum wells", Stefan Schulz, Conor Coughlan, Miguel A. Caro, **Daniel S. P. Tanner**, and Eoin P. O'Reilly, *11th International Conference on Nitride Semiconductors*, Beijing, China, (2015).
- "Electronic and Optical Properties of m-Plane InGaN Quantum Wells: A Combined Experimental and Theoretical Analysis", S. Schulz, **D. Tanner**, M.A. Caro, E.P. O'Reilly, D. Sutherland, M.J. Davies, P. Dawson, F. Oehler, J.T. Griffiths, F. Tang, C. J. Humphreys, and R. A. Oliver, *11th International Conference on Nitride Semiconductors*, Beijing, China, (2015).
- "Impact of random composition fluctuations on electron and hole states in AlInN and InGaN alloys (Invited Talk)", E.P. O'Reilly, S. Schulz, **Daniel S. P. Tanner**,C. Coughlan, M.A. Caro, *Numerical Simulation of Optoelectronic Devices (NUSOD)* (E-MRS), Taipei, Taiwan (2015).

3. Conference posters

During the course of my doctoral research I have personally presented the following conference posters:

- "Impact of random alloy fluctuations on the properties of nitrde quantum wells", **Daniel P. Tanner**, Stefan Schulz, Conor Coughlan, Miguel A. Caro and Eoin P. O'Reilly, *Photonics Ireland*, Cork, Ireland (2015).
- "Multiscale modelling of c-plane InGaN/GaN quantum wells: effect of random alloy fluctuations and structural inhomogeneities on the electronic properties", **Daniel P. Tanner**, S. Schulz, M. A. Caro, and E. P. O'Reilly, *CeCam*, Dublin, Ireland (2016).

In addition to these posters I have also contributed to, and have had aspects of my work presented in, the following conference posters, which were presented by my colleagues and collaborators:

- "Partial Poster 1", Eoin P. O'Reilly, *3rd Workshop on Epitaxial Growth and Fundamental Properties of Semiconductor Nanostructures*, Traunkirchen, Austria (2011).

Chapter 1

Introduction and overview

In this chapter the experimental and technological motivation for the studies performed in each subsequent chapter is given, along with an overview of the contents of each chapter. Section 1.1 provides a general introduction to the III-nitrides, as well as a motivation for the study of InGaN quantum wells. The experimental properties of these systems are presented, and the possible technological advantages which an improved understanding of these properties would yield serves as a justification for the study of each of the InGaN systems found in later chapters. Section 1.2 summarises the contents of each section.

1.1 Background and motivation

The solid state lighting revolution is now well underway, with solid state lighting sources finding mass application and providing considerable energy savings in, amongst other things, traffic lights, street lamps, and coloured lighting for building exteriors. An important technological step forward will be the replacment of current inefficient fluorescent and incandescent white light sources now predominantly used for household lighting. This would lead to huge economic and ecological benefits such as cheaper lighting (which can account for up to 40% of electricity use in developing countries) [1] and greatly reduced greenhouse gas emissions [2]. Nitride-based semiconductor devices are the most promising candidates for this eventual replacement [3], making the understanding of their properties a pressing scientific issue.

The III-nitrides comprise the compounds of nitrogen (N) with aluminium (Al), galium (Ga), and indium (In). The primary attraction of this material system lies in the nature and span of the band-gaps of its constituent semiconductors. They are all direct-gap semiconductors, with band gaps of 6.14 eV for AlN, 3.43 eV for GaN, and 0.64 eV for InN [4]. No other material system can boast emission over such a wide spectral range, whilst maintaing a direct gap.

However, it was not until the breakthroughs by I. Akasaki, H. Amano and S. Nakamura [3, 5–7], culminating in the fabrication of *efficient* bright blue light emitting diodes (LEDs), that the rare properties of the III nitrides could be utilised for novel device applications. The importance of this pioneering research was recognised when the Nobel Prize was conferred on I. Akasaki, H. Amano and S. Nakamura in 2014.

Shortly after these breakthroughs, the large band-gaps and efficient low wavelength emission afforded by the nitrides, found application in greatly increasing the capacity for optical storage on Blu-Ray discs [8]. More importantly, with the possibility of producing all three primary colours in LEDs, nitride devices offer the potential to emit white light, replacing incandescent and fluorescent sources. Complementarily to emission, the band gap range also affords in nitride materials the ability to absorb light at all visible wavelengths. This allows for the production of higly efficient solar cells, with early InGaN solar cells achieving already $\approx 40\%$ external efficiencies [9]. These visible spectrum applications lie within the remit of InGaN alloys, and these are the primary subject of this work.

One of the main challenges faced today in the developement of nitride devices is the lack of suitable substrates for film growth. The strong chemical bonds in nitride materials (which have many advantages such as stability and resistence to degradation under conditions of high current and intense light illumination) mean that high growth temperatures are needed during device fabrication [3]. These high temperatures limit the substrate choice and so materials such as sapphire and silicon carbide, whose lattice parameters differ greatly from those of nitride compounds, must be used. Because of this, poor quality epitaxial films with high extended defect densities, of the order 10^9 cm^{-2}, are produced [10, 11]. In semiconductor devices made from other materials, this normally leads to low radiative recombination rates and thus low device efficiency. For example, dislocation densities as low as 10^3 cm^{-2} are known to quench emission in GaAs [12]. However, the particularities of the microstructure of InGaN devices appear to overcome these obstacles. Determining the mechanisms by which the microstructure of these devices leads to the situation of high efficiency in spite of a high defect density, is one of the aims of this work.

Carrier localisation is the widely accepted explanation for the defect insensitivity of nitride-based devices. Under this description, the carriers are localised to small regions of the InGaN devices such that they cannot diffuse to defects and recombine non-radiatively. Experimental evidence for localisation was discovered very soon after Nakamura's breakthrough in 1993 [13, 14]. Support for carrier localisation has since continued to mount. In particular photoluminesence (PL) measurements in InGaN quantum wells (QWs) have revealed large linewidths and large Stokes shifts between the PL peak and a broadened absorption edge, all of which are indicative of localised carriers [15]. Furthermore, the PL peak energy in these QW systems has shown an anomalous "S-shaped" dependence on temperature, whilst the peak

energy in electroluminesence experiments shows a similar dependence on current density [16–18]. These phenomena are imputed to the redistribution of carriers amongst localised states. Another experimental peculiarity is that in time resolved PL measurements the decay times are non-exponential and vary across the spectrum, consistent with a model of individually localised electrons and holes [19]. And, importanly to this study, the decrease in device efficiency with increasing current, known as "efficiency droop", has been attributed by some authors to the saturation of localised states [18, 20, 21].

While these experiments corroborate the explanation for the defect insensitivity in InGaN devices in terms of carrier localisation, they do not reveal the exact nature and cause of this localisation. For example, localisation in InGaN QWs was formerly considered to be primarily excitonic localisation at gross indium clusters [13] (In this context "gross" indium clusters are nanometer-scale indium rich regions, resulting, for example, from the immiscibility of the In in InGaN). However, increasingly careful structural studies have shown that in many cases this gross clustering can be attributed to artefacts of the measurement process [22]. In particular, Smeeton *et. al.* [23] concluded from transmission electron microscope (TEM) studies that the gross indium clusters found in standard *c*-plane InGaN wells were in fact caused by electron beam damage. Subsequent measurements using atom probe tomography (APT) and high resolution transmission electron microscopy (HRTEM) with low exposure times on other *c*-plane systems, revealed indium distributions that matched what would be expected in the case of a random alloy [23, 24]. While these results make a strong argument against gross indium clustering, there are still cases where it is argued to occur [25]. Other widely reported sources of carrier localisation are well width fluctuations (WWFs) [26, 27] and random alloy fluctuations [24, 28, 29]. In this work we focus our attention on the localising effects of WWFs and random alloy fluctuations.

Relevant to these localisation mechanisms, and the means by which WWFs are able to localise carriers at all, is another challenge faced in nitride systems: due to the large ionicity of nitride compounds, large spontaneous and strain dependent piezoelectric polarisation fields in the direction of the *c*-axis are present. These polarisation fields result in electric fields of up to $\approx 10^6$ V cm^{-1} across *c*-plane InGaN/GaN QWs [30]. These fields serve to separate charge carriers in devices and reduce their efficiencies. Because the built-in electric fields increase with the increasing strain that results at increasing indium contents, there is an increasing reduction in device efficiency as one increases the emission wavelength of InGaN devices. This contributes, along with decreasing material quality and increasing lateral localisation, to what is known as the 'green-gap' problem. The green-gap stands as a significant barrier to the realisation of all LED white light sources, given the lack of any other suitable material systems to emit in this range [3, 31, 32].

One way to circumvent the problems associated with these large built-in fields is to grow InGaN/GaN QWs on planes parallel to the spontaneous and piezoelectric polarisation vectors. There are two such stable growth planes in the nitrides, the a-plane and the m-plane. However, recent studies have suggested that InGaN/GaN QWs grown on the a-plane are susceptible to indium clustering [25]. Since this work is focussed on the impact of random alloy fluctuations, we focus our attention on only the non-polar m-plane in wurtzite (WZ) QWs. In m-plane InGaN QWs, the lack of a built in field across the heterostructure separating the charge carriers is manifest in PL studies as much shorter radiative recombination timescales, as well as single-exponential decay times [33, 34]. This is indicative of exciton localisation, as the Coulomb interaction is no longer negated by the built in field, and the carriers localise in the same spatial position [34]. Furthermore, differences in the hole effective masses along the growth direction and in the growth plane, combined with additional anisotropic strain-induced differences in the growth plane, results in a breaking of valence band degeneracies, and the emission of light with a high degree of optical linear polarisation [35, 36]. This has useful applications such as energy efficient backlit liquid crystal displays [2, 36].

However, problems associated with growth on m-plane subtrates, such as cost and poor indium incorporation [37, 38], have led people to look for other ways around the green gap problem in the nitrides. A promising route is through use of nitride crystals grown in the metastable cubic/zincblende crystal phase. Like WZ nitride crystals grown on the m- and a-plane, the crystal symmetry in the cubic nitrides produces no built-in field in the [001] growth direction. In addition, cubic GaN has a band gap narrower by 0.2 eV [39] than that of WZ GaN. With the small bandgap of cubic InN reduced also with respect to its WZ variant, this 30 nm headstart towards the longer wavelengths means less indium need be incorporated in order to shift the wavelength to the green and yellow spectral region. Furthermore, the bandstructure of the cubic phase of GaN is such that the carriers have smaller effective masses, higher carrier mobilities, higher doping efficiency, and smaller Auger losses [37, 40]. This is an attractive prospect, given the crucial role often attributed to Auger recombination in the efficiecy droop of nitride-based devices [41, 42]. Similarly to WZ nitride systems, cubic nitride systems also exhibit pronounced evidence of localisation [40] .

The experimental results discussed above, when taken together, emphasise an important interplay between the microscopic alloy fluctuations, and the macroscopic effects of the built-in field. Furthermore, results such as the "S-shaped" temperature dependence of the PL peak energy, the broadened PL full width at half maximum (FWHM), large Stokes shifts, and the eventual efficiency droop at high current densities, reveal that a large distribution of localised states determine the properties of InGaN QWs. However, previous theoretical approaches have generally not described simulatenously these three properties: atomistic level alloy fluctuations, macroscopic built in field in combination with larger scale structural inhomogeneities, and a large density of localised states.

Nevertheless, previous atomistic empirical pseudopotential [29, 43] and density functional theory (DFT) [44, 45] calculations on bulk alloys, have confirmed the importance of random alloy fluctuations as a fundamental mechanism for the localisation of valence band edge states in both cubic and WZ InGaN. In particular, these studies have shown the importance of In-N-In chains [29, 43–45], occuring naturally due to random alloy fluctuations, as localisation sites. When it comes to modelling InGaN wells however, the most common approach is continuum-based [33, 46–48]. These studies have confirmed the deleterious effects of the built in fields on device efficiencies, and demonstrated localisation of conduction band states within WWFs. Amongst these, the work of Watson-Parris [48] included approximately the effects of alloy fluctuations using a single-band effective mass approximation (EMA), through use of material parameters which varied spatially in accordance with a random indium composition distribution. While this work achieved the simultaneous description of the aforementioned microscopic and macroscopic localisation mechanisms, whilst also treating a large number of states, the approximation cannot treat atomistic effects fully. Thus, this approach does not have sufficent resolution to treat effects such as In-N-In chains, or more generally the impact underlying anion-cation structure, which has shown to be important in nitride systems [49].

Based on the studied experimental properties, and the theoretical corroboration of the fundamental mechanisms at play, we conclude that first principles theoretical approaches will provide an incomplete description of these systems due to their incapacity to model the large numbers of atoms needed to describe realistic QW structures. Neither will the small number of states which it is computationally tractable to calculate using first principles methods be sufficient to account for the phenomena attributed explicitly to the multiplicity of localised states, such as the changing decay times across PL curves, and those attributed to the saturation of localised states, such as efficiency droop. Conversely the description of empirical continuum models will be incomplete due to their neglect of the atomistic source of localisation, without which nitride devices would not emit any light. Particularly well suited then, to the description of this materials system, are atomistic empirical models, which describe fully the atomistic structure, and offer the computational efficacy necessary to treat realistically sized QWs.

In this work the tight-binding method is employed, whose localised basis set is ideal for the efficient treatment of atomistic phenomena. This model also accounts accurately for local strain and polarisation fluctuations arising from random alloy effects. It is used to study the electronic and optical properties of c- and m-plane InGaN QWs. For the case of cubic InGaN, a semi-empirical theoretical framework with which to analyse the system, with the completeness and utility of the currently available tight-binding framework for WZ materials, is not yet available. We thus turn after the description of the c- and m-plane systems, to the developement of such a framework, begining with the description of the elastic and structural properties of the cubic nitrides, and other III-V semiconductor matierials.

1.2 Thesis outline and overview

Chapter 2, *Theory and Methods*, introduces the background for the different components of the theoretical framework used. Particular attention is given to the theory of finite strain, the use of which requires some justification, given its extra complexity when compared with small strain theory.

Chapter 3, *Electronic properties of c-plane InGaN/GaN Quantum Wells*, examines the electronic properties of WZ c-plane InGaN QWs. The calculations reveal that in c-plane structures, the localisation of both electrons and holes is enhanced by the built-in field. In particular, we find that the built-in field, in combination with structural inhomogeneities such as alloy fluctuations as well as WWFs, can lead to significant electron localisation. Furthermore, the built-in field acts against the Coulomb interaction to separate the electrons and holes along the growth axis, leading to the situation of individually localised electrons and holes. This is consistent with the non-exponential decay transients measured in time-dependent PL experiments on c-plane structures and early simple models used to interpret them. Our study of the excited states confirms that localisation effects persist into the valence band, for at least 100 meV, and therefore will play a role in determining device properties at ambient temperature. By studying the localisation over many states and over different indium conents, we find that increasing the indium content in the QW increases the energy range over which localised carriers are found, and that strong localisation effects are found for as little as 10% indium.

Chapter 4, *Electronic properties of m-plane InGaN/GaN Quantum Wells*, examines the electronic properties of InGaN QWs grown on the non-polar m-plane. For the m-plane system, where the macroscopic built in field is absent, we find that the Coulombic interaction becomes significant, and electrons and holes are localised together as excitons at indium-rich regions of the QW. This is consistent with the experimentally measured single exponential decay transients found in time resolved PL measurements performed on m-plane structures. Similarly to the case of c-plane systems, we find that localisation effects in m-plane quantum wells persist into the valence band over an energy range of at least 100 meV, and that these localisation effects are such that they will significantly affect the overlap between hole states, and thus the transport properties of m-plane InGaN devices.

Chapter 5, *Elastic Properties of zincblende III-V semiconductors*, seeks to establish the theoretical methods needed to model the promising cubic nitrides, starting with the elastic properties. In a first step, the harmonic elastic properties are extracted from density functional theory data. Relations amongst the determined elastic constants and Kleinman parameter are used to illustrate shortcomings in the currently available valence force field models used to calculate local strain and relaxed atomic positions in III-V semiconductor alloys. A new valence force

field implementation is introduced which makes explicit use of elastic properties formerly neglectd by ubiquitous valence force field models. The new method provides simple expressions to derive a valence force field model, which is straightforward to apply to most III-V materials, but which is not immediately applicable in its current form to III-N zincblende alloys. In a second step, recognising the large strains that may occur in the semiconductor devices made using higly lattice-mismatched materials such as InN and GaN, third order elastic properties are extracted from density functional theory data. The DFT data are fitted to third order elastic formulae, using finite-strain theory. Finally, the utilisation of these properties in a valence force field model is discussed, and an appropriate functional form is suggested.

In chapter 6, we present the conclusions drawn from the work presented in this thesis, as well as an outlook and suggestions for further steps.

Chapter 2

Theory and Methods

In this chapter we present the theory behind the methods used in this work. In section. 2.1, we discuss phenomena related to the elasticity of semiconductor materials, and in section. 2.2, we present the tight binding method which we use to calculate the electronic properties of InGaN/GaN quantum wells.

2.1 Elasticity in semiconductor materials

In this section we discuss the deformation of materials. The mathematical description of deformation is discussed in section 2.1.1. The forces that arise in a material as a result of this deformation and their relation to the material properties are discussed in section 2.1.2. The microscopic phenomenon of internal strain, which lies outside the purview of the classical macroscopic theory, is discussed in section 2.1.3.

2.1.1 The specification of strain

When some part of a material is deformed, the atoms in all other parts in general also undergo displacement. When a part of a material is displaced it may be displaced as a rigid body, undergoing simultaneously rotation and translation, or it may be deformed, where the lengths between atoms in that section of the material change. It is the fractional changes in the lengths which occur with deformation that are physically significant, and this is what the term strain describes.

To arrive at a definition of strain, we will examine the means by which the positions of the atoms in a material may be transformed during a deformation, starting with the simple one dimensional case, and then extending the analysis to the two and three dimensional cases.

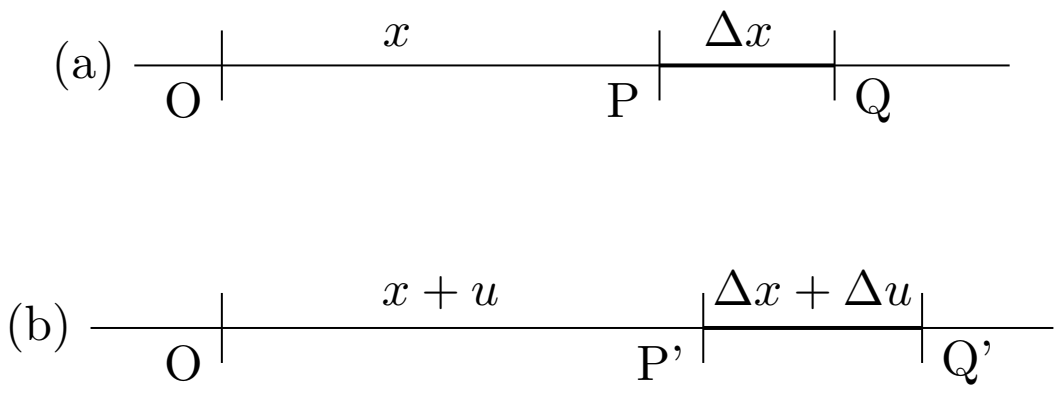

FIGURE 2.1: (a) Unstrained and (b) strained state of an extensible 1D object

2.1.1.1 One-dimensional strain

Consider the extensible string in Fig. 2.1. The unstretched string is shown in Fig. 2.1(a). We mark the origin O and two points on the string as P and Q. The point P is a distance x from the origin, and Q is a distance Δx from P. Treating the case of homogeneous stretching, the coordinate, x, on the string is transformed to x':

$$x' = x + u. \tag{2.1}$$

We note that, if u were a constant, then eq. (2.1) would represent simply a translation. The whole string would be moved to the right by an amount u, but not stretched. For stretching or squeezing to occur the displacement, u, must change with material coodinate x. This is shown in Fig. 2.1(b), where the length P'Q' is increased by amount Δu. Thus, we may simply define the strain of the section PQ in this situation as:

$$\frac{\text{increase in length}}{\text{original length}} = \frac{\text{P'Q'} - \text{PQ}}{PQ} = \frac{\Delta u}{\Delta x}. \tag{2.2}$$

While the strain at the point P is defined as:

$$\varepsilon = \lim_{\Delta x \to 0} \frac{\Delta u}{\Delta x} = \frac{du}{dx} = \frac{\Delta L}{L_0}, \tag{2.3}$$

where L_0 refers to the unstretched length of the whole string, and ΔL refers to the change in length of the whole string. This strain measure, of length change relative to original length, is referred to as the "engineering strain"; we note that ε, the derivative of the displacement, is equal to the engineering strain for the case of a homogeneous 1D deformation, and gives the strain at any point in the material. This definition of strain as a derivative of the displacement has the advantage that it does not depend on the origin and excludes translations from the description of strain.

It will be useful to express transformation from the unstrained coordinates to the strained coordinates, and the strain itself, in terms of the deformation gradient, normally denoted by F:

$$\begin{aligned} x' &= Fx, \\ F &= \frac{dx'}{dx} = 1 + \frac{du}{dx}, \\ \varepsilon &= F - 1. \end{aligned} \tag{2.4}$$

So in the 1D case, the strain is exactly and uniquely specified by the deformation gradient, or the strain measure ε. Furthermore, the observation that the difference between the transformation between the strained and unstrained coordinates (the deformation gradient, F), and the identity matrix I ($\equiv$1 in the 1D case here), is a good specification of strain, will be useful in later developments.

2.1.1.2 Two and three-dimensional strain

When moving to higher dimensions, the deformation gradient alone ceases to be a complete specification of the state of strain. The primary reason for this is that, while the deformation gradient excludes rigid body displacements, it is affected by rigid body rotations. In two dimensions, the deformation gradient is a tensor with the form:

$$\mathbf{F} = \begin{pmatrix} \frac{dx_1'}{dx_1} & \frac{dx_1'}{dx_2} \\ \frac{dx_2'}{dx_1} & \frac{dx_2'}{dx_2} \end{pmatrix} = \begin{pmatrix} 1 + \frac{du_1}{dx_1} & \frac{du_1}{dx_2} \\ \frac{du_2}{dx_1} & 1 + \frac{du_2}{dx_2} \end{pmatrix}. \tag{2.5}$$

While this no longer fully specifies the strain of a given deformation, it still provides the change in the position vector of a given point under uniform deformation:

$$\mathbf{r}' = \mathbf{F}\ \mathbf{r}. \tag{2.6}$$

Here $\mathbf{r}'$ is the position vector of a point after the deformation, and $\mathbf{r}$ is the undeformed position. Following the procedure for the one dimensional case, we may seek a measurement for the strain in terms of the difference between the deformation gradient, $\mathbf{F}$, and the identity, $\mathbf{I}$:

$$\epsilon = \mathbf{F} - \mathbf{I} = \begin{pmatrix} \frac{du_1}{dx_1} & \frac{du_1}{dx_2} \\ \frac{du_2}{dx_1} & \frac{du_2}{dx_2} \end{pmatrix}. \tag{2.7}$$

To examine the properties of this strain measure, in Fig. 2.2, the general displacement of an extensible 2D body is shown. The changes in the displacement Δu, shown in the figure, are,

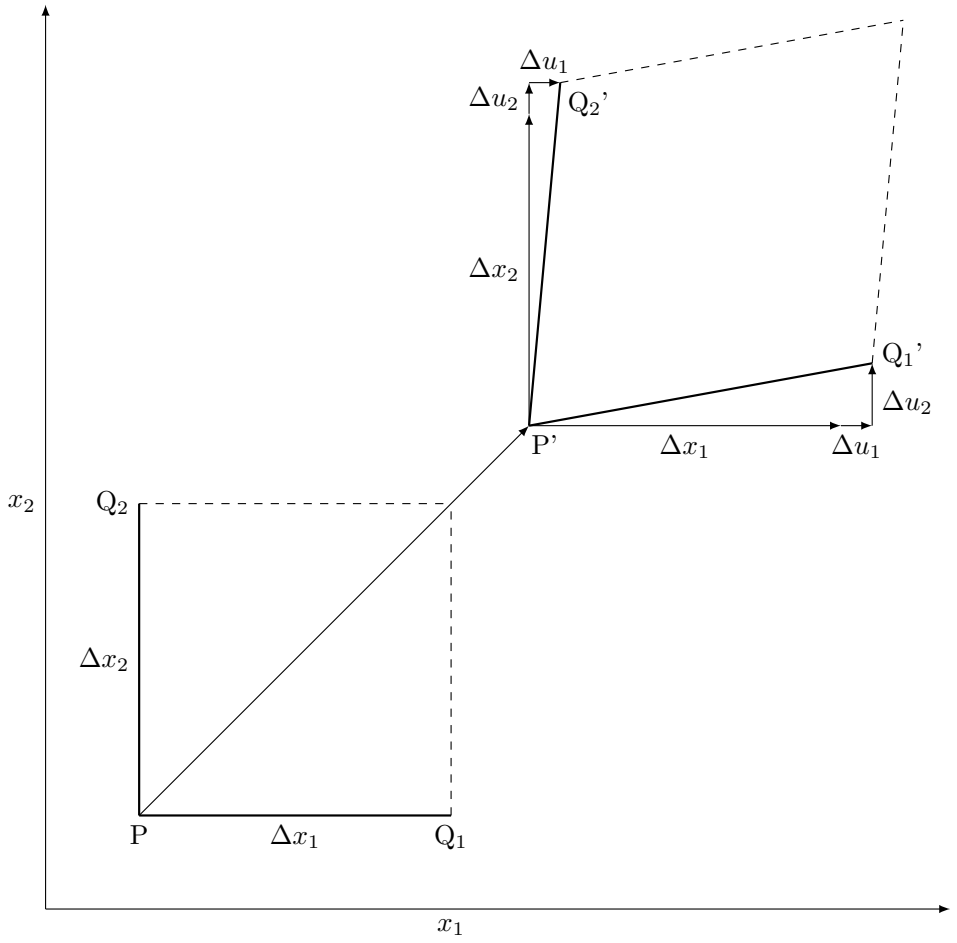

FIGURE 2.2: General displacement of an extensible 2D object.

at a particular position, related to the tensor, ϵ, by:

$$\Delta u_1 = \frac{du_1}{dx_1}\Delta x_1 + \frac{du_1}{dx_2}\Delta x_2, \tag{2.8}$$

$$\Delta u_2 = \frac{du_2}{dx_1}\Delta x_1 + \frac{du_2}{dx_2}\Delta x_2, \tag{2.9}$$

or, more concisely:

$$\Delta u_i = \epsilon_{ij}\Delta x_j. \tag{2.10}$$

Considering the line P'Q' in the figure, we see that in two dimensions the tensor has the useful property that it describes relative length changes in the material along a given axis:

$$\frac{\Delta u_1}{\Delta x_1} = \frac{\partial u_1}{\partial x_1} = \epsilon_{11}. \tag{2.11}$$

Likewise, ϵ_{22} describes the fractional length change of the material in the x_2 direction.

To interpret the off-diagonal terms, we look at a simplified shear case shown in Fig.2.3. In this

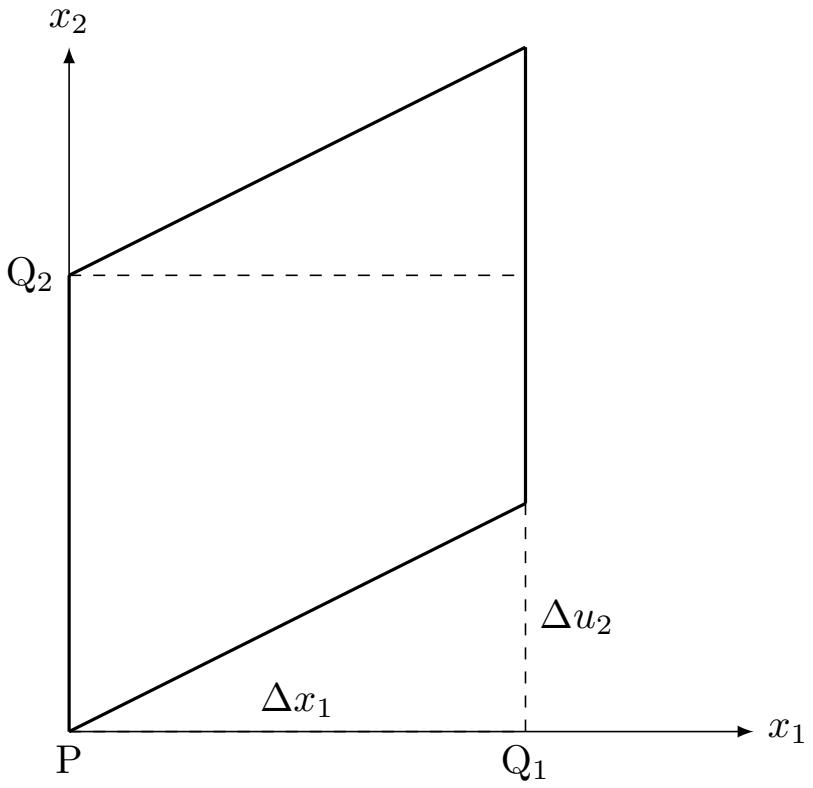

FIGURE 2.3: Simple shear of a 2D body.

scenario it is clear that, referring to P'Q':

$$\frac{\Delta u_2}{\Delta x_1} = \frac{\partial u_2}{\partial x_1} = \epsilon_{12} = \tan\theta. \tag{2.12}$$

For the case of Fig. 2.2, this interpretation also holds under conditions of small strains, displacements, and rotations. We have without approximation:

$$\tan\theta = \frac{\Delta u_2}{\Delta x_1 + \Delta u_1}, \tag{2.13}$$

and under the condition that u_1 and u_2 are small compared with x_1 and thus Δu_1 and Δu_2 are small compared with Δx_1, we have:

$$\theta \approx \frac{\Delta u_2}{\Delta x_1} = \epsilon_{21}, \tag{2.14}$$

and the same arguments hold for ϵ_{12}. This shows that the intuitive relation to angle changes exhibited in the simple shear case described by eq. (2.12), is retained in the case of more complex deformations when the dispalcements and strains are small.

However, regardless of strain and displacement sizes, we see that this interpretation of ϵ_{ij} breaks down when rotations are introduced. Take for example the rigid body rotation given by the

transformation:

$$\begin{aligned} x' &= x\ \cos\theta - y\ \sin\theta, \\ y' &= x\ \sin\theta + y\ \cos\theta. \end{aligned} \tag{2.15}$$

In this rigid body rotation no lengths have changed, and the shape of the material is the same, i.e. it is not *deformed* or *strained* it is only rotated. However, the deformation gradient in this case is given by:

$$\mathbf{F} = \begin{pmatrix} \cos\theta & -\sin\theta \\ \sin\theta & \cos\theta \end{pmatrix}. \tag{2.16}$$

It is clear that the ϵ_{ij} defined from this $\mathbf{F}$ are nonzero for this case of zero strain; it cannot, therefore, be used to measure the strain state in a material. Furthermore, it will be shown later that the interpretation of ϵ_{ij} as a measure of realtive length changes and relative angle changes depended on the complexity of the deformation, and also on the magnitude of the strains involved. For this reason, in going from ϵ_{ij} to a more robust strain measure, the magnitude of the strains involved is important.

In the next two sections we present two different formulations of strain: in sec. 2.1.1.3 one valid only in the realm of small strains but which offers great conceptual and computational simplicity; and in sec. 2.1.1.4 another which is generally valid, but which loses to some extent the intuitive physical interpretation.

2.1.1.3 Infinitesimal strains

For the case of small strains, and small rotations, the tensor ϵ_{ij}, for a rigid body rotation, is given by:

$$\epsilon = \begin{pmatrix} 0 & -\theta \\ \theta & 0 \end{pmatrix}. \tag{2.17}$$

This is obtained by reference to eq. (2.16) and (2.7) in the regime of $\theta << 1$.

To arrive at a reasonable definition of strain, the part of ϵ_{ij} corresponding to rotation must be eliminated. We observe in eq. (2.17), that in the regime of small strains, a pure rotation is given by an antisymmetrical tensor. Furthermore, it is the case that any second-rank tensor can be expressed as the sum of a symmetric, ε, and an anti-symmetric, ϖ_{ij}, tensor [50]. Thus:

$$\epsilon_{ij} = \varepsilon_{ij} + \varpi_{ij}, \tag{2.18}$$

where

$$\varepsilon_{ij} = \frac{1}{2}\left(\epsilon_{ij} + \epsilon_{ji}\right) \qquad \text{and} \qquad \varpi = \frac{1}{2}\left(\epsilon_{ij} - \epsilon_{ji}\right). \tag{2.19}$$

In separating out the symmetric from the anti-symmetric parts of ϵ_{ij} we have separated out rotation from strain. Therefore, the symmetric part of ϵ_{ij}, ε_{ij}, represents the strain in the

material, and is unaffected by either translation or rotation, within the regime of small strains. In terms of the derivatives of the displacements, it is given (in 2D, the 3D case being similar):

$$\varepsilon = \begin{pmatrix} \frac{\partial u_1}{\partial x_1} & \frac{1}{2}\left(\frac{\partial u_1}{\partial x_2} + \frac{\partial u_2}{\partial x_1}\right) \\ \frac{1}{2}\left(\frac{\partial u_2}{\partial x_1} + \frac{\partial u_1}{\partial x_2}\right) & \frac{\partial u_2}{\partial x_2} \end{pmatrix}. \tag{2.20}$$

And in terms of the deformation gradient tensor, this tensor is given by:

$$\varepsilon = \frac{1}{2}\left(\mathbf{F}^T + \mathbf{F}\right) - \mathbf{I}. \tag{2.21}$$

Because of the assumptions made in its derivation, ε is referred to as the "small strain tensor" or the "infinitesimal strain tensor".

This strain measure has the advantage of computational simplicity, and also a very intuitive interpretation; referring to Fig. 2.2, we have:

$$\begin{aligned} \varepsilon_{11} &= \frac{\Delta L_{x_1}}{L_{x_1 0}}, & \varepsilon_{12} &= \theta_{12}, \\ \varepsilon_{21} &= \theta_{21}, & \varepsilon_{22} &= \frac{\Delta L_{x_2}}{L_{x_2 0}}, \end{aligned} \tag{2.22}$$

where we have that $\theta_{12} = \theta_{21}$, as a result of the removal of pure rotations. These quantities represent the change, after strain, in the angle between lines of the object originally parallel to x_1 and the x_2 axis, and the change in the angle between lines originally parallel to x_2 and the x_2 axis, respectively. $\frac{\Delta L_{x_1}}{L_{x_1 0}}$ and $\varepsilon_{22} = \frac{\Delta L_{x_2}}{L_{x_2 0}}$ represent the relative length changes in the x and y directions in the material.

For all its advantages in the regime of small strain, this strain tensor becomes an increasingly inappropriate measure of strain as the magnitudes of the strains and rotations increase. For example, without making the approximation of small angles, and using eq. (2.21), the strain tensor, for an unstrained body rotated through an angle θ, is given by:

$$\varepsilon = \begin{pmatrix} 1 - \cos\theta & 0 \\ 0 & 1 - \cos\theta \end{pmatrix}. \tag{2.23}$$

This implies that by simply rotating a body we are stretching it in its x and y directions, which is not acceptable. This result highlights the fact that a rotation matrix being a purely anti-symmetric matrix is an approximation which depends on a small magnitude of rotation.

Futhermore, if we consider the deformation of Fig. 2.3, we would note that the length PQ_1 is actually changed on shearing, becoming $\sqrt{\Delta x_1^2 + \Delta u_2^2}$, rather than simply Δx_1. This is not recorded in the infinitesimal strain tensor however, which would only tell us what the tangents of the angle changes between the lines in the sheet are. So the interpretation of the ε_{ij} terms has changed, and also it is apparent that for large shear strains even the relative length changes

are no longer fully described. The more complicated the combination of strains applied, the less appropriate the infinitesimal strain tensor is.

In the next section a strain measure which does not make any approximations about the magnitudes of the deformations applied to a material is introduced.

2.1.1.4 Finite strains

In the previous section, use was made of the approximation of small angles to eliminate rotations from the deformation gradient by its decomposition into symmetric and anti-symmetric parts. Here, we make no restriction to a particular region of strain or rotation, but rely instead on the general property of rotation matrices that: [51]

$$\mathbf{R}^T = \mathbf{R}^{-1} \qquad \text{or} \qquad \mathbf{R}^T\mathbf{R} = \mathbf{I}. \tag{2.24}$$

Now, returning to the definition of $\mathbf{F}$ given in eq. (2.5), we note that this deformation gradient tensor captures not only strain but also rotation, and that we would like to remove rotations from it so that we have a pure measure of strain. To do this we make use of the property of rotation matrices in eq. (2.24), and note that $\mathbf{F}^T\mathbf{F}$ is therefore a quantity which depends only on the state of strain of the body in question. We further note that for the unstrained case this function of strain will be $\mathbf{I}$. This leads to the Green-Lagrange or finite strain tensor, η, defined as: [52]

$$\eta = \frac{1}{2}\left(\mathbf{F}^T\mathbf{F} - \mathbf{I}\right), \tag{2.25}$$

where the factor $\frac{1}{2}$ ensures that η reduces to ε in the limit of infinitesimal strain. We will from now on refer to η as the Lagrangian strain.

Given the initial state of a body, and the Lagrangian strain tensor, a relation between the initial coordinates and the strain tensor give an exact expression for the changes of length of line elements in the body [52, 53]. The relation is most easily expressed in the simple tensor notation of Landau and Lifshitz [53]. The distance between two close together points in the material, are before deformation (dl), and after deformation (dl'):

$$dl = \sqrt{dx_1^2 + dx_2^2 + dx_3^2} \qquad \text{and} \qquad dl' = \sqrt{(dx_1 + du_1)^2 + (dx_2 + du_2)^2 + (dx_3 + du_3)^2}, \tag{2.26}$$

with the difference between these then being given in terms of the finite strain and the initial distances as:

$$dl'^2 - dl^2 = 2\eta_{ij}dx_i dx_j. \tag{2.27}$$

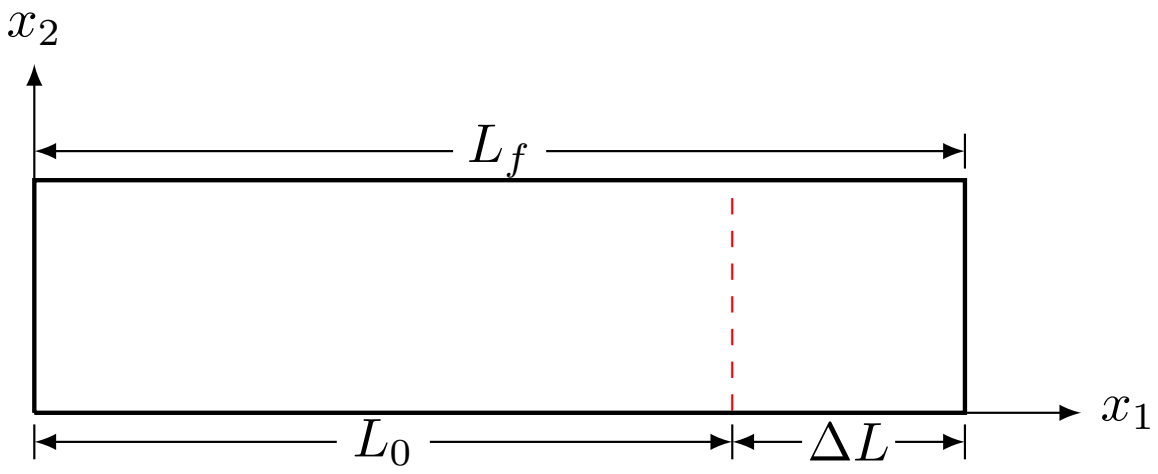

FIGURE 2.4: Simple finite strain of a 2D body.

In terms of the familiar displacement gradients, the components of the Lagrangian strain are given by:

$$
\begin{aligned}
\eta_{11} &= \frac{\partial u_1}{\partial x_1} + \frac{1}{2}\left(\left(\frac{\partial u_1}{\partial x_1}\right)^2 + \left(\frac{\partial u_2}{\partial x_1}\right)^2 + \left(\frac{\partial u_3}{\partial x_1}\right)^2\right), \\
\eta_{22} &= \frac{\partial u_2}{\partial x_2} + \frac{1}{2}\left(\left(\frac{\partial u_1}{\partial x_2}\right)^2 + \left(\frac{\partial u_2}{\partial x_2}\right)^2 + \left(\frac{\partial u_3}{\partial x_2}\right)^2\right), \\
\eta_{33} &= \frac{\partial u_3}{\partial x_3} + \frac{1}{2}\left(\left(\frac{\partial u_1}{\partial x_3}\right)^2 + \left(\frac{\partial u_2}{\partial x_3}\right)^2 + \left(\frac{\partial u_3}{\partial x_3}\right)^2\right), \\
\eta_{23} &= \frac{1}{2}\left(\frac{\partial u_2}{\partial x_3} + \frac{\partial u_3}{\partial x_2}\right) + \frac{1}{2}\left(\frac{\partial u_1}{\partial x_2}\frac{\partial u_1}{\partial x_3} + \frac{\partial u_2}{\partial x_2}\frac{\partial u_2}{\partial x_3} + \frac{\partial u_3}{\partial x_2}\frac{\partial u_3}{\partial x_3}\right), \\
\eta_{13} &= \frac{1}{2}\left(\frac{\partial u_1}{\partial x_3} + \frac{\partial u_3}{\partial x_1}\right) + \frac{1}{2}\left(\frac{\partial u_1}{\partial x_1}\frac{\partial u_1}{\partial x_3} + \frac{\partial u_2}{\partial x_1}\frac{\partial u_2}{\partial x_3} + \frac{\partial u_3}{\partial x_1}\frac{\partial u_3}{\partial x_3}\right), \\
\eta_{12} &= \frac{1}{2}\left(\frac{\partial u_1}{\partial x_2} + \frac{\partial u_2}{\partial x_1}\right) + \frac{1}{2}\left(\frac{\partial u_1}{\partial x_1}\frac{\partial u_2}{\partial x_3} + \frac{\partial u_2}{\partial x_1}\frac{\partial u_2}{\partial x_3} + \frac{\partial u_3}{\partial x_1}\frac{\partial u_2}{\partial x_3}\right).
\end{aligned}
\tag{2.28}
$$

Comparing this with eq. (2.20), we confirm that in the case of small displacements and strains, the Lagrangian strain components, η_{ij}, become equal to those of the infinitesimal strain tensor, ε_{ij}, i.e., the infinitesimal strains are the linearised version of the Lagrangian strains.

To illustrate the advantages (exact relation to relative length changes in a material and rotational invariance) and disadvantages (lack of simple intuitive physical interpretation) in this strain measure, we consider two simple deformations. In Fig. 2.4, a simple stretching in the x_1 direction is applied to a 2D sheet. We recall that in this situation the infinitesimal strain has the very simple and intuitive form:

$$
\varepsilon_{11} = \frac{\partial u}{\partial x} = \frac{\Delta L}{L_0}; \tag{2.29}
$$

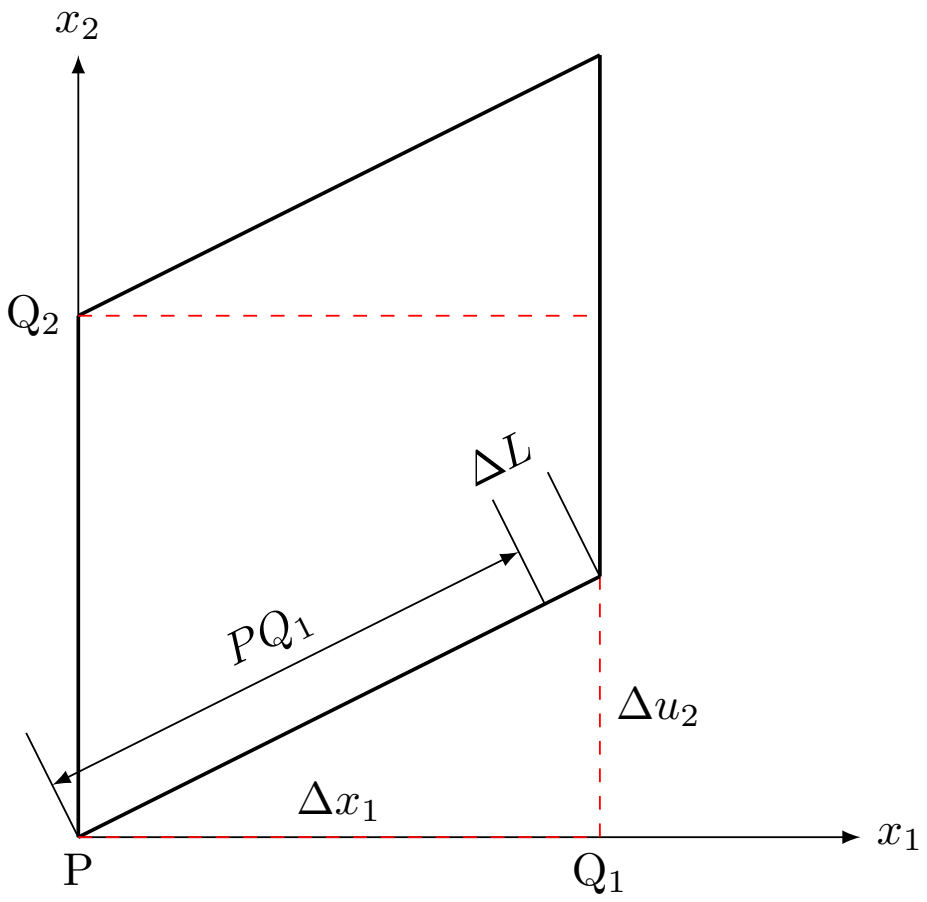

FIGURE 2.5: Simple finite strain of a 2D body: stretching associated with shear indicated.

the Lagrangian strain, however, is given by:

$$\eta_{11} = \frac{\partial u}{\partial x} + \frac{1}{2}\left(\frac{\partial u}{\partial x}\right)^2 = \frac{\Delta L}{L_0} + \frac{1}{2}\left(\frac{\Delta L}{L_0}\right)^2. \tag{2.30}$$

The difference between these two measures shows that, for simple strains, the Lagrangian strains lose the one to one correpsondance with the relative length changes in the material.

However, the complicated relation of the Lagrangian strains to the relative length changes, holds for all types of deformation, which is not true for the infinitesimal case. The Lagrangian strain thus offers a continuous, unique and monotonic function of the displacement gradients, and relative length changes which can be used to characterise the strain state of the material.

An illustration of an aspect of strain captured by the Lagrangian strain tensor but missed by the infinitesimal tensor is shown in Fig. 2.5, where a simple shear (which comprises a pure shear and a rotation) is applied to a 2D body. In this case, the infinitesimal shear strain is given by:

$$\varepsilon_{12} = \frac{1}{2}\left(\frac{\partial u_1}{\partial x_2} + \frac{\partial u_2}{\partial x_1}\right) = \frac{1}{2}\frac{D}{L}, \tag{2.31}$$

where we have written $\Delta x_1 = L$ and $\Delta u_2 = D$, to show the infinitesimal strain tensors correspondence with the "engineering shear" in this context. However, as we have seen before, the interpretation of this strain component as the change in angles between two orthogonal lines in the material is dependent on the amount of strain. In this simple case, the Lagrangian shear strain has the same form:

$$\eta_{12} = \frac{1}{2}\frac{\partial u_2}{\partial x} = \frac{1}{2}\frac{D}{L}. \tag{2.32}$$

However, the Lagrangian strain also captures an effect not descirbed by the infinitesimal tensor: the stretching of the line segment PQ. From Fig. 2.5 is is clear that the simple shear deformation applied involves not only a change in the angles between lines in the material, but also a stretching of lines; the line PQ, which was originally of length L, is stretched to length $\sqrt{L^2 + D^2}$. The η_{11} component of the Lagrangian strain tensor describes this stretching:

$$\eta_{11} = \frac{1}{2}\left(\frac{\partial u_2}{\partial x_2}\right)^2 = \frac{1}{2}\left(\frac{D}{L}\right)^2. \tag{2.33}$$

We may interpret this by considering the relative length change:

$$\frac{\Delta L}{L_0} = \frac{\sqrt{L^2 + D^2} - L}{L} = \sqrt{1 + \left(\frac{D}{L}\right)^2} - 1, \tag{2.34}$$

which, Taylor expanding to second order, yields:

$$\frac{\Delta L}{L_0} \approx \frac{1}{2}\left(\frac{D}{L}\right)^2, \tag{2.35}$$

showing that the Lagrangian strain captures aspects of stretching which are missed by the infinitesimal strain tensor.

For these reasons the Lagrangian strain tensor is to be preferred when dealing with larger strains.

2.1.2 The relation between stress and strain

When a body is put into a state of strain, it ceases to be in equilibrium and forces arise in the body which tend to return it to equilibrium. These internal forces which occur in a body when it is deformed are described in terms of *stresses*. In the macroscopic theory of elasticity, these internal forces are considered "near-action" forces, which act from any point only to neighbouring points. From this it follows that the forces exerted on any part of a body by surrounding parts act only on the surface of that part, and stresses may be defined as the internal forces per unit area on a part of a body.

Because for each surface of a body there can be forces in three directions, the *stress* is described mathematically by a second order tensor, denoted by σ:

$$\sigma = \begin{pmatrix} \sigma_{11} & \sigma_{12} & \sigma_{13} \\ \sigma_{21} & \sigma_{22} & \sigma_{23} \\ \sigma_{31} & \sigma_{32} & \sigma_{33} \end{pmatrix}. \tag{2.36}$$

The stress component σ_{ij} refers to the force in the x_i direction on the face of the material segment perpendicular to the x_j axis. From the condition of zero net moment of forces on a portion of the body, it can be shown [53] that $\sigma_{ij} = \sigma_{ji}$. This stress tensor, comprising the forces per unit area on each surface of a deformed body, is called the Cauchy stress.

Associated with this departure from equilibrium is also an increase in the free energy of the body, which depends on the amount of strain. The Helmholz free energy can thus be expanded in the Lagrangian strain as [54, 55]:

$$\rho_0 \psi = \frac{1}{2!} C_{ijkl} \eta_{ij} \eta_{kl} + \frac{1}{3!} C_{ijklmn} \eta_{ij} \eta_{kl} \eta_{mn}. \tag{2.37}$$

Here the function ψ is the Helmholtz free energy per unit mass, and ρ_0 is the unstrained mass density. Note that all considerations of the Helmholtz free energy are made here under conditions of constant temperature. The constants C_{ijkl} measure the strength of the material's response to strain, and are called the elastic constants.

Within the regime of infinitesimal strains, rotations and displacements, the assumption that the deformed configuration is the same as the undeformed configuration is valid. Using this approximation, the above energy can be derived using the small strain, ε, and the Cauchy stress, σ, and provides a relation between them. The free energy is determind by considering the work done per unit volume by the internal stresses when the state of deformation of a body is changed. This furnishes the expression for the incremental work done, and thus the incremental change in the free energy (per unit volume), of [53]:

$$\rho_0 d\psi = \sigma_{ij} d\varepsilon_{ij} \Longrightarrow \sigma_{ij} = \rho_0 \frac{\partial \psi}{\partial \varepsilon_{ij}}. \tag{2.38}$$

Considering then eq. (2.37) within the small strain regime ($\eta = \varepsilon$; expansion only to second order). We obtain:

$$\rho_0 \psi = \frac{1}{2} C_{ijkl} \varepsilon_{ij} \varepsilon_{kl}, \tag{2.39}$$

which from eq. (2.38), furnishes an expression for Hooke's law:

$$\sigma_{ij} = C_{ijkl} \varepsilon_{kl}. \tag{2.40}$$

Following from the symmetry of the ε and σ tensors [50, 56], we have also that $C_{ijkl} = C_{jikl} = C_{ijlk}$, and the Voigt contraction can be employed also for the elastic constants.

In this work we treat two crystal systems, zincblende (ZB) and wurtzite (WZ). For ZB the elastic stiffness tensor has the form (in contracted Voigt notation) [50]:

$$\mathbf{C}^{\mathrm{ZB}} = \begin{pmatrix} C_{11} & C_{12} & C_{12} & 0 & 0 & 0 \\ C_{12} & C_{11} & C_{12} & 0 & 0 & 0 \\ C_{12} & C_{12} & C_{11} & 0 & 0 & 0 \\ 0 & 0 & 0 & C_{44} & 0 & 0 \\ 0 & 0 & 0 & 0 & C_{44} & 0 \\ 0 & 0 & 0 & 0 & 0 & C_{44} \end{pmatrix}, \tag{2.41}$$

whilst for WZ, we have [50]:

$$\mathbf{C}^{\mathrm{WZ}} = \begin{pmatrix} C_{11} & C_{12} & C_{13} & 0 & 0 & 0 \\ C_{12} & C_{11} & C_{12} & 0 & 0 & 0 \\ C_{13} & C_{12} & C_{33} & 0 & 0 & 0 \\ 0 & 0 & 0 & C_{44} & 0 & 0 \\ 0 & 0 & 0 & 0 & C_{44} & 0 \\ 0 & 0 & 0 & 0 & 0 & \frac{C_{11}-C_{12}}{2} \end{pmatrix}. \tag{2.42}$$

If one would like to treat larger strains, and non-linear elasticity, one must accept that the approximations used to derive eqs. (2.40) and (2.39) become invalid when non-linear effects become important; this is because the small-strain tensor is defined in the undeformed configuration, and the Cauchy stress is defined in the deformed configuration. As these configurations become increasingly different, the small-strain and Cauchy stress become decreasingly work-conjugate [52] (The work done on the system when the strain state is changed by a stress is no longer well described by the product of the Cauchy stress and the small-strain [57]). Furthermore, the Lagrangian strain, which is appropriate for large deformations, is also defined in the undeformed configuration. So the Lagrangian strain is also not work-conjugate to the Cauchy stress, i.e. the Cauchy stress is not given as the derivative of the energy with respect to the Lagrangian strain.

The relationship between the Cauchy stress and the Lagrangian strain has, however, been presented by Murnaghan [52]. Following a rather more lengthy derivation than that in which small strains are assumed, the stress-strain relation obtained is given by:

$$\sigma = \frac{1}{det(\mathbf{F})} \mathbf{F} \frac{\partial \psi}{\partial \eta_{ij}} \mathbf{F}^T. \tag{2.43}$$

The tensor $\frac{\partial \psi}{\partial \eta_{ij}}$ is from here denoted by $\mathbf{t}$, and is known as the 2nd Piola-Kirchoff stress tensor [57], which is defined in the undeformed configuration. Because it is defined in the undeformed configuration, and because it is appropriate to large strains, we shall refer to $\mathbf{t}$ as the Lagrangian stress from here on.

Further details of the theory of finite strain, as well as third order elastic constants, are provided as needed in Chapter 5

2.1.3 Internal strain

For crystals whose atoms occupy sites with inversion symmetry, the position of every atom in the crystal under a deformation is given by eq. (2.6). However, for crystals whose atoms sit on sites lacking inversion symmetry, the transformation given by eq. (2.6) does not fully specify the positions, and the atoms of the crystal exhibit an additional sublattice displacement. This may be accounted for with the amended transformation:

$$\mathbf{r}' = \mathbf{F}\ \mathbf{r} + \mathbf{u}. \tag{2.44}$$

We note that only the relative displacement of the sublattices are important, and therefore, in the case of a two atom ZB cell, eq. (2.44) need be applied to only atoms of one of the sublattices, conventionally chosen to be that which corresponds to the central atom of the tetrahedron of a primitive cell. For crystals with many different sublattices, many $\mathbf{u}$ vectors will need to be specified. This vector $\mathbf{u}$ is known as the *internal strain* [58].

While this phenomenon has been studied from as early as 1954, as described in Born and Huang's seminal "Dynamical Theory of Crystal Lattices" [58], it was the popular 1962 paper by Kleinman [59], that motivated the first experimental measurements [60].

In his work, Kleinman sought to determine the deformation potential associated with shear strain in silicon, but was faced with the indeterminacy of the separation between the two atoms of the primitive cell, for a given shear. While the applied macroscopic shear strain will give the position of every atom at a lattice point, without knowing the nature of the bonds and forces on the central atom (the second basis atom), its equilibrium position cannot be known. The situation is shown in Fig. 2.6. Here the applied strain, in Voigt notation, is: $\varepsilon = \left(0, 0, 0, \frac{\beta}{2}, \frac{\beta}{2}, \frac{\beta}{2}\right)$.

To circumvent this indeterminacy, Kleinman estimates the internal strain via the assumption of a "bond-bending" model. This model assumes that "all shears take place through the mechanism of bond-bending", and as such, only the angles between the bonds change, but the lengths do not change. Thus, in the left hand side of Fig. 2.6, the forces on the unit cell associated with the shear are shown as green arrows along the cell faces, tending to bend the

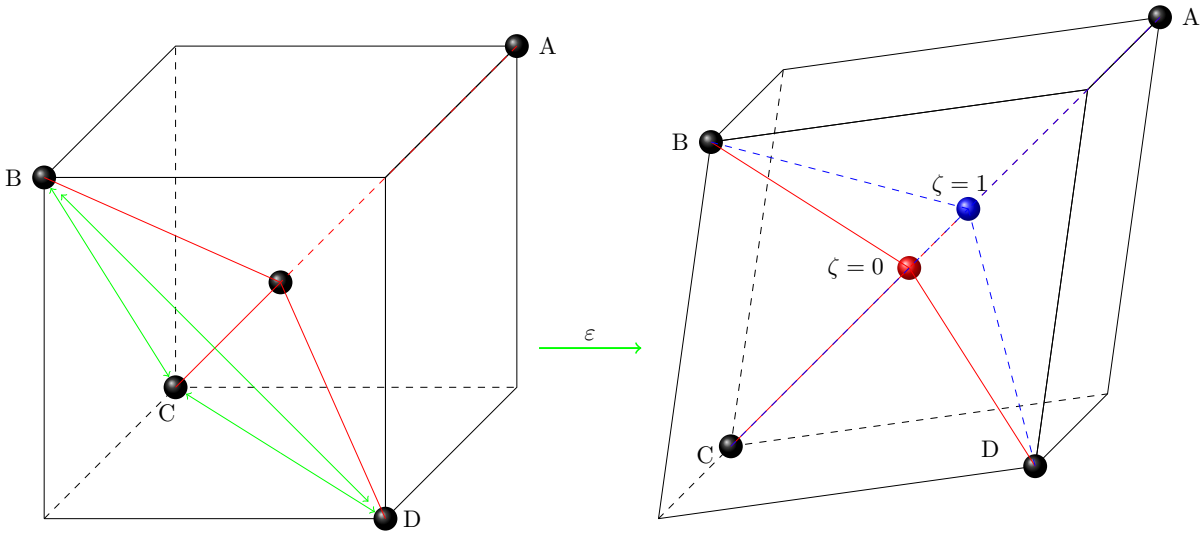

FIGURE 2.6: Effect of uniform shear strain on single ZB tetrahedron. (left) Shears are shown as bond bending forces represented by green lines, bonds between atoms represented by red lines before cell is deformed. (right) Deformed cell with different internal strain corresponding to $\eta = 0$ or $\eta = 1$.

bonds. Under this assumption of shear leading only to a bending of the bonds, the internal strain $\mathbf{u}$ is such that the distance between the central atom and atom A of Fig. 2.6 is the same as that between the central atom and the others, B, C, and D. This is shown on the right side of Fig. 2.6, where the bonds in question are shown in blue.

Kleinman also investigated the situation where the atom remains in the centre of the tetrahedron, i.e. the bonds resist bending so strongly that instead of bending, some bonds elongate and others contract. This is shown by the red bonds on the right figure of Fig. 2.6. This scenario, which contradicts the predictions of most interatomic potentials, yielded a deformation potential with the incorrect sign compared to the experimental one, validating the bond-bending assumption and the predictions of interatomic potentials [59].

In reality, it is rarely the case that the bonding in a solid is such that the forces resisting bond bending are completely overwhelmed by the forces resisting bond stretching/compressing, or vice-versa. The amount by which the central atom moves along the threefold axis along which the strain is applied depends on the relative strengths of bond-bending to bond-stretching forces. Kleinman characterised this distance, and the ratio of the forces, with the dimensionless parameter ζ, which has since become known as the "Kleinman parameter". Using this, the sublattice displacement in a ZB crystal is described to first order in the strain by [59, 61]:

$$\mathbf{u}^{\mathrm{ZB}} = \left(\frac{a_0}{4}\zeta\varepsilon_4, \frac{a_0}{4}\zeta\varepsilon_5, \frac{a_0}{4}\zeta\varepsilon_6\right). \tag{2.45}$$

In crystals with a larger basis there will be the possibility of internal strains leading to sublattice displacements between each of the basis atoms/sublattices. The four-atom WZ unit cell is

shown in Fig. 2.7. The atomic positions in this unit cell will be given after strain (utilising

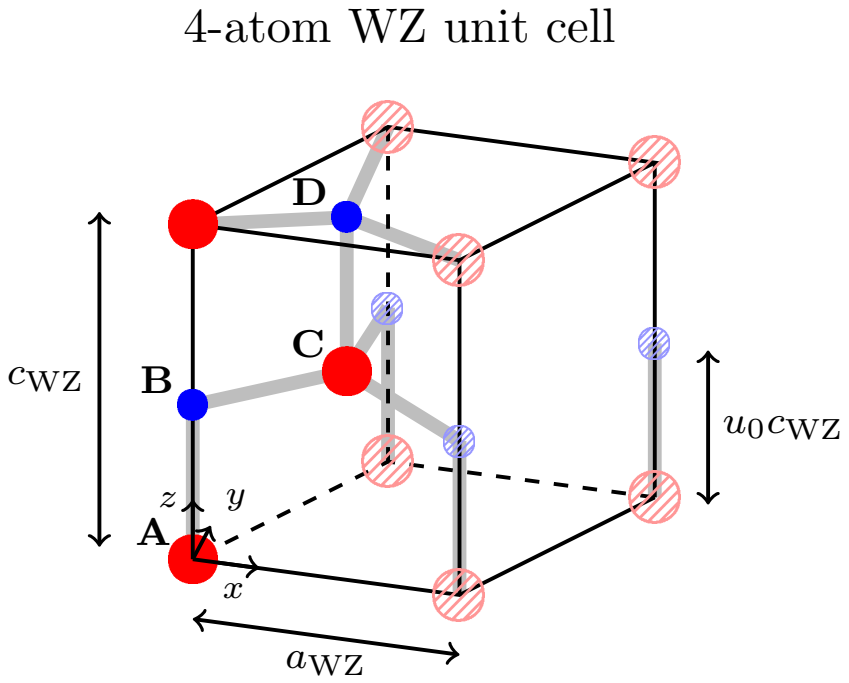

FIGURE 2.7: 4-atom WZ unit cell.

notation in figure and ref. [62]) by:

$$\begin{aligned}
\mathbf{r}_A^{\mathrm{WZ}} &= [0,0,0]\,, \\
\mathbf{r}_B^{\mathrm{WZ}} &= (\mathbf{I}+\varepsilon)\,\mathbf{r}_{B,0}^{\mathrm{WZ}} + \mathbf{u}_1^{\mathrm{WZ}}, \\
\mathbf{r}_C^{\mathrm{WZ}} &= (\mathbf{I}+\varepsilon)\,\mathbf{r}_{C,0}^{\mathrm{WZ}} + \mathbf{u}_2^{\mathrm{WZ}}, \\
\mathbf{r}_D^{\mathrm{WZ}} &= (\mathbf{I}+\varepsilon)\,\mathbf{r}_{D,0}^{\mathrm{WZ}} + \mathbf{u}_3^{\mathrm{WZ}},
\end{aligned} \tag{2.46}$$

where there are three unique sublattice displacements, $\mathbf{u}_i^{\mathrm{WZ}}$. These internal strains have the form: [62]

$$\begin{aligned}
\mathbf{u}_1^{\mathrm{WZ}} &= c_0 \left[\zeta_1\varepsilon_{xz} + \zeta_5\varepsilon_{xy},\ \zeta_1\varepsilon_{yz} + \zeta_5\frac{(\varepsilon_{xx}-\varepsilon_{yy})}{2},\ \zeta_2\left(\varepsilon_{xx}+\varepsilon_{yy}\right) - \zeta_3\varepsilon_{zz}\right], \\
\mathbf{u}_2^{\mathrm{WZ}} &= a_0 \left[-\zeta_4\varepsilon_{xy},\ -\frac{(\varepsilon_{xx}-\varepsilon_{yy})}{2}\zeta_4,\ 0\right], \\
\mathbf{u}_3^{\mathrm{WZ}} &= \mathbf{u}_1^{WZ} + \mathbf{u}_2^{WZ} - 2c_0 \left[\zeta_5\varepsilon_{xy},\ \zeta_5\frac{(\varepsilon_{xx}-\varepsilon_{yy})}{2},\ 0\right].
\end{aligned} \tag{2.47}$$

A full, thermodynamically rigourous development for all crystal structures of the theory of internal strain has been given by Cousins [63, 64]. This more rigourous development will be drawn on in chapter 5, building on the introduction of internal strain and Kleinman's description for ZB materials presented in this section.

2.1.4 Piezoelectricity and spontaneous polarisation

Piezoelectricity is the production of an internal polarization within a material in response to the presence of a strain. In general, the piezoelectric response of a material to a strain will be aniosotropic, with the direction of the produced polarisation depending on the symmetry properties of the material in question.

Up to first-order, the piezoelectric polarisation, which is a tensor of the first rank, will be related to the strain, which is a tensor of the second rank, by a tensor of third rank. This relation is given below [50]:

$$P_i = e_{ijk}\varepsilon_{jk}, \tag{2.48}$$

where P_i is the component of the polarisation vector along the i axis, and e_{ijk} are the components of the *piezoelectric tensor*.

This tensor will be subject to a reduction in the number of independent variables due to the symmetries of the tensors it relates, as well as crystal symmetries and physical considerations [50]; the Voigt contraction can thus be utilised to facilitate a concise matrix notation. In the two crystal systems that will be studied in this work, these matrices are given, with the contracted Voigt notation of $(jk) \rightarrow J$, by:

$$e_{iJ}^{(\mathrm{ZB})} = \begin{pmatrix} 0 & 0 & 0 & e_{14} & 0 & 0 \\ 0 & 0 & 0 & 0 & e_{14} & 0 \\ 0 & 0 & 0 & 0 & 0 & e_{14} \end{pmatrix}, \tag{2.49}$$

and

$$e_{iJ}^{(\mathrm{WZ})} = \begin{pmatrix} 0 & 0 & 0 & 0 & e_{15} & 0 \\ 0 & 0 & 0 & e_{15} & 0 & 0 \\ e_{31} & e_{31} & e_{33} & 0 & 0 & 0 \end{pmatrix}, \tag{2.50}$$

for ZB and WZ crystals, respectively.

Further details of the piezoelectricity in these crystals at a microscopic level, its incorporation into the tight binding formalism, and its relation to internal strain, can be found elsewhere [58, 65–67].

In addition to the polarisation due to piezoelectricity, we note also that in wurtzite III-N materials in equillibrium, the asymmetry of the bonds results in a spontaneous polarisation in the c-axis direction. In the three nitrides the spontaneous polarisation increases on magnitude going from GaN to AlN [68].

2.2 Tight binding method

To study the electronic properties of a solid, the time-independent Schrodinger equation must be solved for the single particle energies and wavefunctions:

$$\hat{H}\psi_{n\mathbf{k}} = E_n(\mathbf{k})\,\psi_{n\mathbf{k}}. \tag{2.51}$$

Here $\hat{H}$ is the Hamiltonian operator, $\psi_{n\mathbf{k}}$ is the wavefunction associated with wavevector $\mathbf{k}$ in the n^{th} band, and $E_n(\mathbf{k})$ is its energy.

For the case where spin-orbit coupling is neglected (justified for the nitride systems treated in this work [66]), the single electron Hamiltonian is given:

$$\hat{H} = -\frac{\hbar^2}{2m_0}\nabla^2 + V(\mathbf{r}), \tag{2.52}$$

with the first term representing the kinetic energy of an electron, and the second term, $V(\mathbf{r})$, representing the crystal potential as a function of position. Within the one-electron approximation this potential includes the averaged effects of all other electrons as well as the nuclei making up the solid. Because the nuclei and orbiting electrons are positioned at the sites of the crystal which are periodic in space, the potential, $V(\mathbf{r})$, is also periodic in space, i.e. $V(\mathbf{r}) = V(\mathbf{r}+\mathbf{R})$, where $\mathbf{R}$ is a Bravais lattice vector. And because the potential has this periodicity, so too do the electronic charge densities. This result is known as Bloch's theorem, which states that the crystal eigenstates, $\psi_{n\mathbf{k}}$, can be written in the form:

$$\psi_{n\mathbf{k}} = e^{i\mathbf{k}\cdot\mathbf{r}}u_{n\mathbf{k}}(\mathbf{r}), \tag{2.53}$$

where $u_{n\mathbf{k}}(\mathbf{r})$ shares the periodicity of the lattice, i.e. $u_{n\mathbf{k}}(\mathbf{r}) = u_{n\mathbf{k}}(\mathbf{r}+\mathbf{R})$, and $e^{i\mathbf{k}\cdot\mathbf{r}}$ is a plane wave which describes the symmetry of a crystal, as well as the delocalised nature of electrons in a solid.

In the tight binding model it is assumed that these extended states can be accurately described using a linear combination of the atomic orbitals of the atoms that make up the solid. A natural choice for this linear combination is a collection of Bloch sums of atomic orbitals.

A Bloch sum over a given atomic orbital, ϕ_α, associated with the basis atom, l, can be written as:

$$\phi_{\alpha l}(\mathbf{r},\mathbf{k}) = \frac{1}{\sqrt{N}}\sum_j e^{i\mathbf{k}\cdot\mathbf{r}_{jl}}\phi_\alpha(\mathbf{r}-\mathbf{r}_{jl}) \tag{2.54}$$

where α represents the different types of atomic orbitals (s,p,d etc.), the sum over j is a sum over all unit cells in the crystal, with the position vector, $\mathbf{r}_{jl}$, being the position of the basis

atom l in the unit cell j, and N refers to the total number of primitive cells included in the sum.

The cell periodic eigenstates of the crystal Hamiltonian $\hat{H}$ are expressed in a basis of these Bloch sums as:

$$\psi_{n\mathbf{k}}(\mathbf{r}) = \sum_{\alpha,l} a_{n\alpha l}(\mathbf{k})\, \phi_{\alpha l}(\mathbf{r},\mathbf{k})\,. \tag{2.55}$$

To express the Hamiltonian in terms of this basis and arrive at a means to obtain the crystal wave functions we substitute eq. (2.55) into eq. (2.51), and multiply on the left by the conjugate of the Bloch sum of an arbitrary orbital at the basis atom m, $\phi^*_{\beta m}(\mathbf{r},\mathbf{k})$, where the superscript '*' represents the complex conjugate operation. Then integrating over the whole crystal and using Dirac bracket notation to represent the resulting inner products, we obtain:

$$\sum_{\alpha,l} a_{n\alpha l}\left(\langle\phi_{\beta m}|\hat{H}|\phi_{\alpha l}\rangle - E_n\langle\phi_{\beta m}|\phi_{\alpha l}\rangle\right) = 0. \tag{2.56}$$

Note that we have left the position $\mathbf{r}$, and wave vector $\mathbf{k}$ dependence implicit, for the sake of a more concise notation. This equation is usefully described in terms of the Hamiltonian and overlap matrices, where: [69]

$$H_{\beta m\alpha l}(\mathbf{k}) = \langle\phi_{\beta m}|\hat{H}|\phi_{\alpha l}\rangle \qquad \text{and} \qquad S_{\beta m\alpha l}(\mathbf{k}) = \langle\phi_{\beta m}|\phi_{\alpha l}\rangle, \tag{2.57}$$

are the Hamiltonian and overlap matricies, respectively.

To make this solvable, we draw on the following propositions for the simplification of the overlap matrix:

1. The orbitals on a given atomic site are orthogonal.
2. Atom-like orbitals are orthogonal with respect to those on neighboring sites.

The first is a standard result of the fact that the eigenfunctions of a given Hamiltonian are orthogonal, and the atomic orbitals are eigenfunctions of the atomic Hamiltonians. The second, the assertion that the overlap between orbitals on different atomic sites is negligible, is justified given the decay of an orbital away from the site it is centred on and can in any case be guaranteed by the procedure of Löwdin orthogonalisation [70]. Using these assumptions, the overlap matrix is greatly simplified:

$$S_{\beta m\alpha l}(\mathbf{k}) = \delta_{\alpha\beta}\delta_{ml}, \tag{2.58}$$

where δ_{ij} is the Kronecker delta.

Turning now to the Hamiltonian expressed in the tight binding basis, we substitute eq. (2.54) into the expression for $H_{\beta m\alpha l}$ in eq. (2.57), and after performing some manipulation of the sums [69], obtain:

$$H_{\beta m\alpha l}\left(\mathbf{k}\right) = \sum_{jj'} e^{i\mathbf{k}\cdot\left(\mathbf{r}_{jl}-\mathbf{r}_{j'm}\right)} \langle \phi_\beta\left(\mathbf{r}-\mathbf{r}_{j'm}\right)|\hat{H}|\phi_\alpha\left(\mathbf{r}-\mathbf{r}_{jl}\right)\rangle, \tag{2.59}$$

where $\langle \phi_\beta\left(\mathbf{r}-\mathbf{r}_{j'm}\right)|\hat{H}|\phi_\alpha\left(\mathbf{r}-\mathbf{r}_{jl}\right)\rangle$ make up the matrix elements of the crystal Hamiltonian between the atomic orbitals ϕ_α and ϕ_β, situated in the j and j'^{th} unit cell, on the atomic sites l and m, respectively.

Because the atomic-like basis functions used, ϕ_α, decay exponentially outside of the atomic site upon which they are centred, $H_{\beta m\alpha l}$ becomes very small for cases where the atom denoted l is far from that denoted by m. This allows for the simplification of treating only interactions between orbitals situated on nearest neighbour atoms. Thus the sum in eq. (2.59) can be restricted to run over only pairs of nearest neighbours. With these approximations made to $H_{\beta m\alpha l}(\mathbf{k})$ and $S_{\beta m\alpha l}(\mathbf{k})$, the secular equation, eq. 2.56, may be written in an explicitly nearest neighbour formulation:

$$\sum_{\alpha,l} a_{n\alpha l}\left(\sum_{j=0}^{nn} e^{i\mathbf{k}\cdot\left(\mathbf{r}_{0l}-\mathbf{r}_{jl}\right)} \langle \phi_\beta\left(\mathbf{r}-\mathbf{r}_{0m}\right)|\hat{H}|\phi_\alpha\left(\mathbf{r}-\mathbf{r}_{jl}\right)\rangle - E_n\delta_{nm}\delta_{\alpha\beta}\right) = 0. \tag{2.60}$$

In eq. 2.60, the sum over j includes now 0, describing a self interaction, and nearest neighbour atoms, with the $\mathbf{k}$-dependence of the Hamiltonian depending on the geometry of the crystal being modelled. For example, in a simple cubic crystal, this will be a sum over the six nearest neighbours, whilst in a tetrahedral solid there are four terms.

In the semi-empirical tight binding approach employed in this work, the interaction elements, $\langle \phi_\beta\left(\mathbf{r}-\mathbf{r}_{0m}\right)|\hat{H}|\phi_\alpha\left(\mathbf{r}-\mathbf{r}_{jl}\right)\rangle$, are treated as adjustable parameters which are set and optimised according to the results of *ab initio* calculations or experiment. To begin the discussion of fitting these elements, we note that the diagonal '*on-site*' elements have a different meaning and fitting procedure to those of the off diagonal elements. These are elements of the kind $H_{\alpha l\alpha l} \sim \langle \phi_\alpha\left(\mathbf{r}-\mathbf{r}_{0l}\right)|\hat{H}|\phi_\alpha\left(\mathbf{r}-\mathbf{r}_{0l}\right)\rangle$, and since the Hamiltonian in the part of the crystal over which the $\phi_{\alpha l}$ will have a large magnitude will be strongly determined by the isolated atomic Hamiltonian for the atom located at that point, these self energies follow similar trends to the atomic eigenvalues. And while they will not be identical due to the effect of other atoms and electrons in the crystal, the atomic eigenvalues serve as a good starting point in the fitting of these matrix elements.

Since different orbitals on the same site are orthogonal, we have:

$$H_{\alpha l\beta l} = E_\alpha\delta_{\alpha\beta} \tag{2.61}$$

In supercell calculations, the effects of external potentials, strain, or crystal asymmetries are normally incorporated via adjustements to these eigenvalues. Details of the particular methodologies used for these adjustments are given in chapter 3.

For orbitals on different sites, the interaction terms $\langle\phi_{\alpha l}|H|\phi_{\beta m}\rangle$, are not so easily assigned. Because these inner products are related to the probability of an electron with the atomic wave function ϕ_α on the site l transfering to the atomic orbital ϕ_β on site m, they are also known as 'hopping' matrix elements. In the assignment of these hopping matrix elements, we make use of the approximation introduced by Slater and Koster [71], whereby the three centre integrals involved in these matrix elements are characterised in terms of simpler two centre integrals, and direction cosines.

For the sp^3 basis utilised in this work, there are two types of interaction between the atomic orbitals: σ interactions, which involve a head-on overlap between two orbitals, or π interactions, which involve sideways overlaps. These are illustrated graphically in Fig. 2.8. The different types of these interactions are:

- $V_{ss\sigma}$ - interaction between any two s orbitals on neighbouring atoms
- $V_{s_a p_c \sigma}$ - an s orbital on an anion in a σ bond with a p orbital on a cation
- $V_{s_c p_a \sigma}$ - an s orbital on a cation in a σ bond with a p orbital on an anion
- $V_{pp\sigma}$ - σ bond between two p orbitals on neighbouring atoms
- $V_{pp\pi}$ - π bond between two p orbitals on neighbouring atoms

However, unless we are dealing with a simple cubic crystal, the atoms and bonds will not be so oriented that they can all be described as either σ or π bonds. The orbitals must thus be resolved along the bond vector joining the atoms, and perpendicular to it. The interaction between a p state and another p state, can then be split into $V_{pp\sigma}$ and $V_{pp\pi}$ using direction cosines. This is illustrated in Fig. 2.9.

If we denote the direction cosines of the bond vector joining the atomic sites on which two states sit, as l_x, l_y and l_z, then the Slater Koster formalism gives the interaction parameters for any crystal as:

$$\langle s|\hat{H}|s\rangle = V_{ss\sigma}, \tag{2.62}$$

$$\langle s|\hat{H}|p_x\rangle = l_x(V_{sp\sigma}), \tag{2.63}$$

$$\langle p_x|\hat{H}|p_x\rangle = l_x^2(V_{pp\sigma}) + (1 - l_x^2)(V_{pp\pi}), \tag{2.64}$$

$$\langle p_x|\hat{H}|p_y\rangle = l_x l_y(V_{pp\sigma}) - l_x l_y(V_{pp\pi}). \tag{2.65}$$

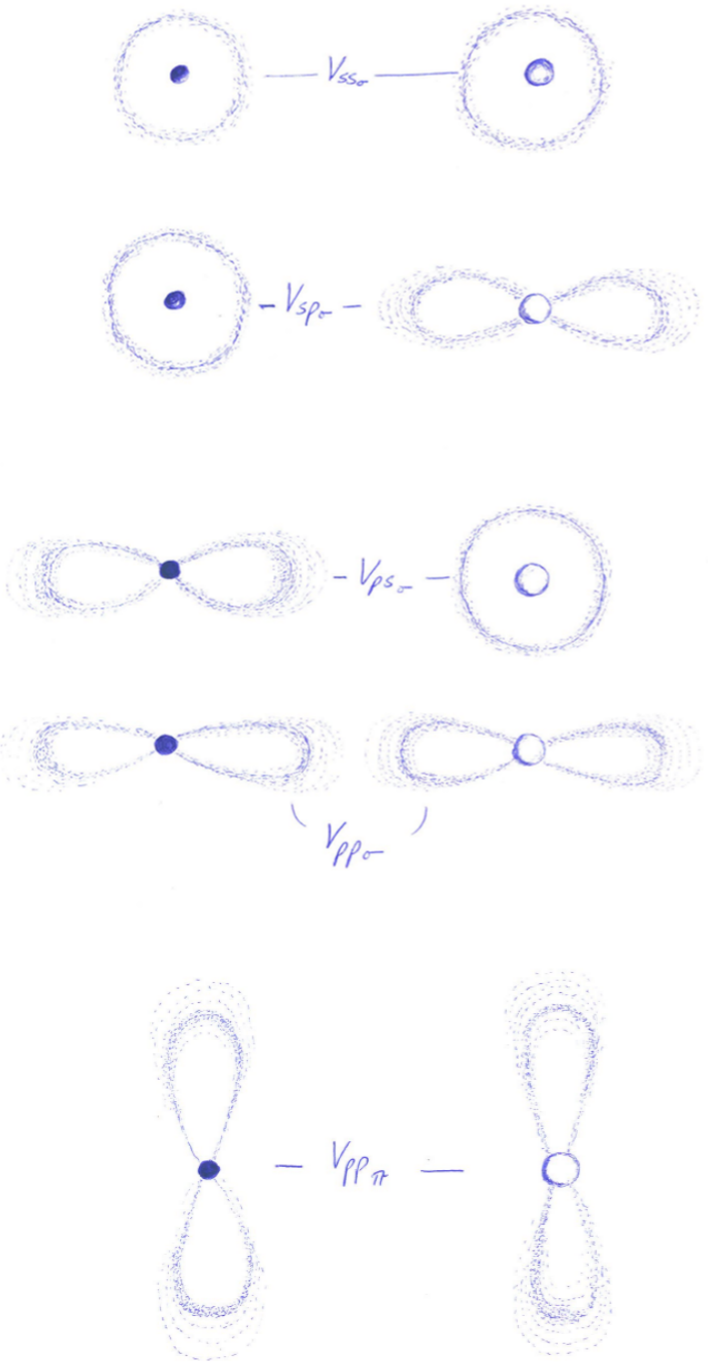

FIGURE 2.8: Two centre integral parameters for s and p type orbitals. Taken with permission from C.Coughlan [72].

With the interactions between different orbitals at neighbouring sites in the crystal thus characterised, the Hamiltonian of the bulk crystal, $H_{\alpha l \beta m}$ can be written down. For the wurtzite structures considered in this work, this Hamiltonian wil be comprise interactions between 4 orbitals on 4 basis atom sites, and will therefore have 16x16 elements. This hamiltonian can be diagonalised analytically at each k-point giving the energy dispersion $E_n(\mathbf{k})$, for each band,

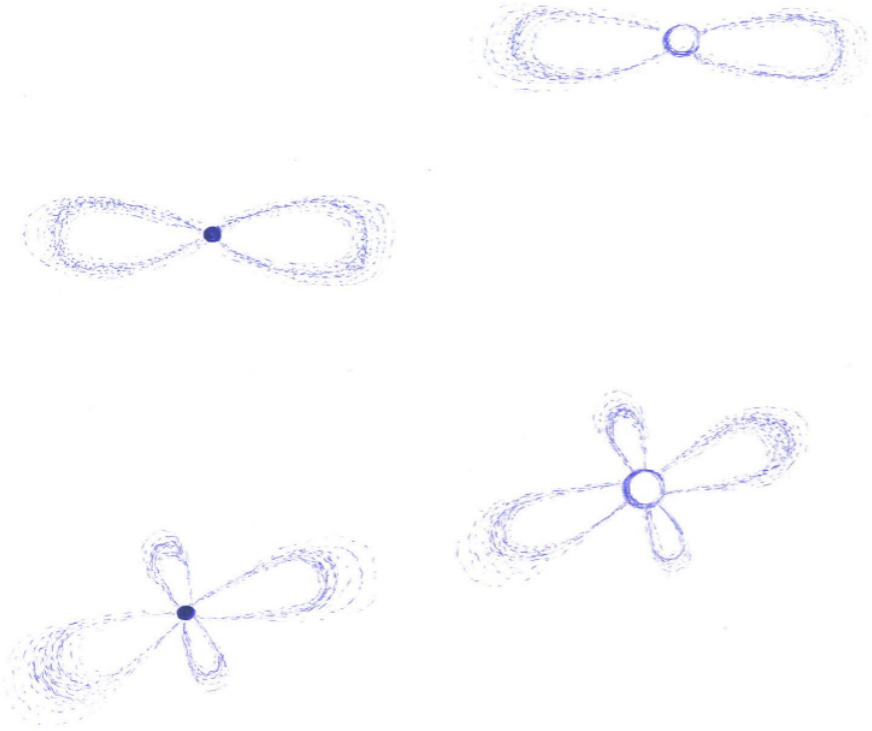

FIGURE 2.9: The resolution of two p_x orbitals into components with directions normal and parallel to the bond vector. Taken with permission from C.Coughlan [72].

as a function of the tight binding parameters. The parameters are then varied to obtain values of $E_n(\mathbf{k})$ which agree with experimntal or *ab. inito* band structures at chosen values of n and $\mathbf{k}$, i.e. to reproduce featuers of chosen bands at chosen k-points. The parameters used in this work were obtained via fitting to band structures calculated using density functional theory (DFT) within the Heyd-Scuseria-Ernzerhof (HSE) screen exchange hybrid functional scheme [73], whilst also taking into account experimentally determined band gaps. Generally, and in this work, the fitting is such that the most weight is put on the fittings around $\mathbf{k} = 0$, particularly at the valence band edge, given the importance of the energies in this region in determining the optical properties of semiconductors. The splittings between the different bands and the effective masses in these regions are thus reproduced by the optimised tight binding parameters.

The method by which the different parameterised bulk tight-binding models are applied to large alloy supercells, incorporating effects of local strain, built in field and local polarisation flucutations, is detailed with references in chapter 3.

Chapter 3

Electronic properties of c-plane InGaN/GaN Quantum Wells

In this chapter we present a detailed theoretical analysis of the electronic structure of c-plane InGaN/GaN quantum wells with indium contents varying between 10% and 25%. The electronic structure of the quantum wells is treated by means of an atomistic tight-binding model, accounting for variations in strain and built-in field due to random alloy fluctuations. Our analysis reveals strong localisation effects in the hole states. These effects are found not only in the ground states, but also the excited states. We conclude that localisation effects persist to of order 100 meV into the valence band, for as little as 10% indium in the quantum well, giving rise to a significant density of localised states. We find, from an examination of the modulus overlap of the wave functions, that the hole states can be divided into three regimes of localisation. Our results also show that localisation effects due to random alloy fluctuations are far less pronounced for electron states. However, the combination of electrostatic built-in field, alloy fluctuations and structural inhomogeneities, such as well-width fluctuations, can nevertheless lead to significant localisation effects in the electron states, especially at higher indium contents. Overall, our results are indicative of individually localised electron and hole states, consistent with the experimentally proposed explanation of time-dependent photoluminescence results in c-plane InGaN/GaN QWs.

3.1 Introduction

Nitride semiconductors have attracted considerable interest for a variety of different applications, ranging from photovoltaic cells up to optoelectronic devices such as light-emitting devices (LEDs) [74]. For instance, the cornerstone of modern light-emitting devices (LEDs) operating

in the blue to green spectral region are InGaN/GaN quantum wells (QWs) grown along the crystallographic c axis [1, 3, 75, 76]. The success of these devices is remarkable given the extremely high defect densities ($> 10^8$ cm^{-2}) in InGaN/GaN materials, which mainly originate from the large lattice mismatch between GaN and the underlying substrate, sapphire (16%) [11, 77]. The widely accepted explanation for the defect-insensitive efficiency of InGaN - based devices is that carrier localisation effects introduced by alloy fluctuations prevent diffusion to non-radiative recombination centres. Using positron annihilation measurements, Chichibu *et al.* [77] demonstrated the presence of such carrier localisation effects in nitride-based alloys. In addition to these measurements, photoluminescence (PL) spectroscopy studies by different groups also gave clear indications that the optical properties of c-plane InGaN/GaN QWs are significantly affected by localisation phenomena. For example, temperature dependent PL measurements have shown that the PL peak energy follows an "S-shaped" temperature dependence [16–18, 76]. This particular form of the shift of the PL peak position is attributed to the redistribution of carriers between different localised states [17, 78, 79]. Furthermore, time-dependent PL measurements revealed non-exponential decay transients and that the decay times extracted from the curves vary across the PL curve [16, 19, 34]. Morel *et al.* [80] proposed as an explanation for this that the radiative recombination process in c-plane InGaN/GaN QWs is dominated by individually localised carriers. The varying spatial separations of these separately localised carriers, both in the c-plane and perpendicular to it, lead to variations in the radiative recombination time. Using this assumption, Morel *et al.* [80] were able to obtain a good agreement between theoretical predictions and the experimental data.

Even though, as discussed above, there is considerable experimental evidence for the importance and presence of localisation effects due to alloy fluctuations, it is only recently that these effects have been considered in theoretical studies. The applied theoretical frameworks range from modified continuum-based descriptions [48, 81], which account for alloy fluctuations via spatial variation of material properties, such as the effective mass or band offsets, up to fully atomistic models [31, 44, 45]. These studies have focused mainly on ground state properties, which are important to understand and explain experimental studies at low temperature; however, in order to understand the results of experiments conducted at ambient temperature, as well as the transport properties of the system, many excited states must be considered. Already the "S-shaped" temperature dependence of the PL peak position indicates that excited states exhibit localisation features. These localised states modify the form of the density of states in such a way that there is a smooth tail of states at the low energy end of the density of states in a QW structure [82, 83]. Because of this, these states are often referred to as "tail states" [21].

In this chapter we address the impact of random alloy fluctuations on the localisation features of both ground and excited states in c-plane InGaN/GaN QWs systems. To cover the experimentally relevant indium composition ranges, we analyse InGaN/GaN QWs with indium contents of 10%, 15% and 25%. Furthermore, since experimental studies highlight also that

structural inhomogeneities, such as well width fluctuations, impact the electronic and optical properties of nitride-based heterostructures significantly [27], we include these effects in our atomistic analysis. Our theoretical framework is based on an atomistic sp^3 tight-binding (TB) model, which includes effects such as strain and polarisation field variations due to the considered random alloy fluctuations.

Our calculations reveal that random alloy fluctuations lead to strong hole wave function localisation effects in both ground and excited states. We find here that over an energy range of order 100 meV a significant density of localised valence states is expected. The presented data also indicates that these localised states significantly affect the probability for transferring carriers from one site/state to another. When studying whether or not the hole wave functions overlap with each other, three different regimes become apparent. The first corresponds to "strongly localised states" with almost no spatial overlap with all other states considered. The second and third regimes consist of what we refer to as "semi-localised states" and "delocalised states", respectively, where the spatial overlap is significantly increased with respect to the "strongly localised" states. Our data also shows that the number of states, and therefore the energy range, constituting each of these regimes, depends on the indium content of the system in question.

While our calculations reveal that random alloy fluctuations lead to very strong hole wave function localisation effects, the situation is different for the electron states. Compared with the hole states, the alloy fluctuations lead to much less pronounced electron wave function perturbations. The primary sources of the localisation of electron states are the electrostatic built-in field, and well width fluctuations, present in *c*-plane InGaN/GaN heterostructures. Also for the excited electron states, localisation effects are strongly reduced compared with the holes.

The combination of macroscopic built-in field, random alloy and well width fluctuations leads to a spatial separation of electron and hole wave functions both in the *c* plane and perpendicular to it. In standard continuum-based models, InGaN/GaN QWs are treated as ideal one-dimensional systems, which can be described by averaged material parameters. These approaches can account only for the spatial separation of electron and hole wave functions along the growth direction due to the presence of the built-in field. Thus, in contrast to the here applied fully atomistic three-dimensional approach, in-plane spatial separations are not captured. Our results indicate that electrons and holes are individually localised and that the wave function overlap should therefore also depend on the relative in-plane position of the carriers. Therefore, the here obtained findings are consistent with the "pseudo 2-D donor-acceptor pair system" proposed by Morel *et al.* [80] to explain time-dependent PL results of *c*-plane InGaN/GaN QWs.

The chapter is organised as follows. In Sec. 3.2, we introduce the components of our theoretical framework. In Sec. 3.3 we discuss the QW model system under consideration and the input from available experimental structural data. The results of our calculations are presented in Sec. 3.4. We first address ground state properties in Sec. 3.4.1 before turning to the excited states in Sec. 3.4.2. We relate our theoretical data to experimental findings in Sec. 3.5, before summarising our work in Sec. 3.6.

3.2 Theoretical Framework

In this section we briefly introduce the atomistic theoretical framework used to study the electronic structure of *c*-plane InGaN/GaN QWs with varying indium content. The approach can be divided into three main components.

First, the large lattice mismatch between InN and GaN (approx. 11%) gives rise to a strain field in InGaN/GaN heterostructures. To treat this strain field on an atomistic level, and thus account for the microscopic random alloy fluctuations, we employ a valence-force-field (VFF) model based on that introduced by Martin [84]. The energy per atom in this model is given by:

$$\begin{aligned} V_i = &\frac{1}{2}\sum_{j\neq i}\frac{1}{2}k_r\left(r_{ij}-r_{ij}^0\right)^2 + \sum_{j\neq i}\sum_{k\neq i,k>j}\left\{\frac{1}{2}k_\theta^i r_{ij}^0 r_{ik}^0\left(\theta_{ijk}-\theta_{ijk}^0\right)^2\right. \\ &\left. + k_{r\theta}^i\left[r_{ij}^0\left(r_{ij}-r_{ij}^0\right)+r_{ik}^0\left(r_{ik}-r_{ik}^0\right)\right]\left(\theta_{ijk}-\theta_{ijk}^0\right) + k_{rr}^i\left(r_{ij}-r_{ij}^0\right)\left(r_{ik}-r_{ik}^0\right)\right\} \\ &+ {\sum_{j\neq i}}'\frac{Z_i^* Z_j^* e^2}{4\pi\epsilon_r\epsilon_0 r_{ij}} - \frac{1}{2}\sum_{j\neq i}\frac{1}{4}\alpha_M\frac{Z_i^* Z_j^* e^2}{4\pi\epsilon_r\epsilon_0 {r_{ij}^0}^2}\left(r_{ij}-r_{ij}^0\right). \end{aligned} \tag{3.1}$$

In this equation, the r_{ij} and r_{ij}^0 are the strained an equillibrium bond lengths between atoms i and j, and θ_{ijk} and θ_{ijk}^0 are the strained and equillibrium bond angles, centred on atom i, between bonds r_{ij} and r_{ik}. The force constants, k_r, k_θ represent resistance to changes in bond lengths and angles away from their equillibrium values. k_{rr} and $k_{r\theta}$ describe forces that tend to change one bond length in response to the change of a neighbouring bond, or to change the angle between two bonds in response to the change in length of one of those bonds, respectively. The sums over j involving these force constants, are sums over 4 tetrahedral neighbours for k_r, and sums over the 6 angles about atom i, for k_θ, k_{rr} and $k_{r\theta}$. Z_i^* is the effective charge of atom i, e is the elementary charge, ϵ_0 is the permitivity of free space, ϵ_r is the dielectric constant of the material in question, and α_M is the Madelung constant. The last two terms represent the Coulombic interactions in the crystal, with the prime on the first electrostatic sum indicating that the summation is taken over all atoms in the infinite crystal, and not just nearest neighbours. The second term on the last line is a linear repulsive term, whose purpose is

to screen the linear part of the Coulomb interaction between nearest neighbours, and preserve the symmetry of the elastic constants, and stability of the crystal [84].

After fitting the force constants and effective charges to correctly reproduce elastic constants and internal strains (using the method of Keting [61], as described in Chapter 5), our VFF includes electrostatic effects explicitly and reproduces important real-wurtzite system attributes such as non-ideal c/a ratios and internal parameters u. More details of the model are given in Ref. [44]. We have implemented this model in the software package LAMMPS [85], minimising the energy to obtain the relaxed atomic positions and correct strain state of the system under investigation.

Second, the strong intrinsic electrostatic built-in fields in nitride heterostructures have to be included to achieve a realistic description of the electronic structure of c-plane InGaN/GaN QWs. In wurtzite III-N materials the lack of inversion symmetry leads to a non-vanishing sum of electric dipole moments and thus to a macroscopic electric polarisation. This polarisation has two contributions, one of which is strain *independent*, known as the spontaneous polarisation, and the other of which is the strain *dependent* piezoelectric polarisation [30]. In addition to the macroscopic polarisation, random alloy fluctuations lead also to local polarisation variations. To account for these local variations, we utilise a recently developed local polarisation theory [66], capable of accounting for both the macroscopic and local intrinsic polarisation. The model receives input for its material parameters from HSE DFT calculations [66]. The starting point for this approach is to split the wurtzite polarisation vector, made up of spontaneous and piezoelectric contributions, into macroscopic and microscopic terms:

$$P_i = \overbrace{\sum_{j=1}^{6} e_{ij}^{0}\varepsilon_j}^{macroscopic} + \overbrace{P_i^{sp} - \frac{e}{V_0}\frac{Z_i^0}{N_{coor}^0}\left(\mu_i - \sum_{j=1}^{3}\left(\delta_{ij}+\varepsilon_{ij}\right)\mu_{j,0}\right)}^{microscopic} \tag{3.2}$$

The macroscopic term is the so called clamped-ion contribution where ions are not allowed to move and this part is related to the piezoelectric coefficients e_{ij}^0 [30]. The local contribution involves the deformation of the nearest neighbor environment around the atom under consideration. With this a dipole moment for each tetrahedron can be defined over the entire cell. From this the corresponding polarisation (dipole moment/volume) can be calculated.

The final step is to calculate the related built-in potential. Usually this is done by solving Poisson's equation, $\nabla\cdot(\epsilon\nabla\psi) = \nabla\cdot\mathbf{P}$. However, since we are dealing with an atomic wurtzite grid this becomes difficult. Firstly because the discretisation of the medium is irregular, given the strain in the crystal. And secondly, because we solve Poisson's equation using a a finite difference or polynomial interpolation scheme, the solution involves the calculation of derivatives requiring the use of interpolations which smear out the effects of the abrupt local discontinuities in the polarisation, which motivated the developement of the local polarisation model in the

first place. To circumvent this problem use is made of the multipole expansion of a distribution of electric charges, from which the the electrostatic potential at position $\mathbf{r}$ due to the presence of a point dipole at $\mathbf{r}'$ can be calculated. In doing so we avoid the aforementioned numerical problems arising from solving Possion's equation by, for instance, a finite difference method on a strained wurtzite crystal structure. Consequently, we find the situation that the macroscopic component of the built-in potential, which is effectively the potential one would expect in a capacitor, is modified in the QW region by local fluctuations superimposed on the potential slope in the QW region. The details of the local polarisation and point dipole method are described in Ref. [66].

Thirdly, to determine the effects of alloy, strain and built-in potential fluctuations on the electronic structure of InGaN/GaN QWs, we use an atomistic, nearest neighbor sp^3 TB model. Here we use an atomic basis of 4 orbitals on each of the 4 atoms in the wurtzite basis, these have the symmetries of s, p_x, p_y, and p_z, in accordance with the outermost valence orbitals of InN and GaN. Because we are dealing with light atoms, spin-orbit coupling introduces energetic shifts of only a few meV, and is therefore neglected. Before treating the InGaN alloy we start from the binary materials InN and GaN. The required TB parameters are determined by fitting the TB bulk band structures of InN and GaN to those calculated using HSE hybrid-functional DFT, as described in Chapter 2. The details of this fitting, and the parameters obtained, along with the HSE DFT bandstructures, are provided in Ref. [66]. Due to the minimal basis used in sp^3 TB, the description of the conduction band at the L- and M-valleys is less accurate. However, from our HSE-DFT calculations we find that, for the nitrides, there is a very large energetic separation between the conduction band minimum at the Γ-point and the M and L valleys [66]. Because of this, the evolution of the energy gap is dominated by the band structure around $\mathbf{k} = \mathbf{0}$; thus, since the TB model used here captures well the valence band and the conduction band at Γ, it is particularly suitable for treating nitride semiconductors.

Equipped with this knowledge about the binary materials, we can then treat the InGaN alloy on a microscopic level. To this end, at each atomic site, the TB parameters are set according to the bulk values of their constituent atoms. For the cation sites (Ga,In), there is no ambiguity in assigning the on-site and nearest neighbor TB matrix elements, since these always have nitrogen atoms as their nearest neighbors. However, the nearest neighbor environment of the anions (N) will vary depending on the local indium distribution. To treat this effect, different approaches have been used in the literature. One ansatz is to start already at the bulk band structure level and use the same on-site TB matrix elements for N in InN and GaN. In doing so the ambiguity for the N-atom on-site energies in an InGaN alloy is removed. However, by assuming the same N-atom on-site energies in InN and GaN, one effectively fixes the band offset between InN and GaN. Such an approach limits the transferability of the TB parameters to other systems. Given these arguments, we apply here another widely used approach to treat the on-site energies of a common atom species in an alloy. The assignment here is performed using

weighted averages for the on-site energies, where the weights are determined by the number of nearest neighbor In or Ga atoms. This is a widely used and benchmarked approach to treat alloys in an atomistic TB framework [44, 86–88]. The band offset is included by shifting the InN on-site TB parameters by the valence band offset $\Delta E_{\mathrm{VB}} = 0.62$ eV. The value for ΔE_{VB} is taken from HSE-DFT calculations [89].

Strain and built-in potential effects are included in the description as on-site corrections to the TB Hamiltonian. The procedure is detailed in Ref. [66].

Finally, having determined the TB Hamiltonian for an alloyed supercell, the task remains to obtain the energies and states of interest. However, to accurately treat random alloy effects, very large supercells are needed, and the tight binding Hamiltonian will be of size 4Nx4N, N is the total number of atoms in the system. As N increases to accomodate the size of a typical InGaN QW, the diagonalisation problem becomes increasingly intractable. Furthermore, given that the optical properties of the InGaN QWs are governed by the states near the band gap, the calculation of all the valence states from bands below those at the valence band edge is a waste of computational resources. To circumnavigate this misuse of resources we use the folded spectrum method [90]. This method avoids solving the conventional Schordinger equation:

$$H|\psi_n\rangle = E_n|\psi_n\rangle; \tag{3.3}$$

in favour of:

$$(H - E_{ref}I)^2\,|\psi\rangle = (E_n - E_{ref})^2\,|\psi_n\rangle. \tag{3.4}$$

The lowest eigenstate, and the first obtained via the variational method, is now the eigenstate closest to E_{ref}. Using this method, the single particle states are obtained in the band gap region for $\mathbf{k} = 0$.

This framework has already been successfully applied to other wurtzite III-N alloys, such as AlGaN and AlInN [91, 92]. And similar approaches have been used also to effectively describe other alloy systems, such as GaBiAs/GaAs QWs [93].

Having discussed the theoretical framework, we introduce the model *c*-plane InGaN/GaN QW systems in the next section.

3.3 InGaN/GaN QW System

Here we introduce the QW systems to which we apply our theoretical framework. The QW structures being studied are similar in indium contents to QWs studied experimentally in Ref. 26. To model *c*-plane $In_xGa_{1-x}N$/GaN QWs we use $\approx$ 82,000 atom supercells (equivalent to a system size of $\approx 10\,\mathrm{nm} \times 9\,\mathrm{nm} \times 10\,\mathrm{nm}$) with periodic boundary conditions. The QW in

these supercells is around 3.5 nm wide. These supercell dimensions have been chosen such that the experimentally reported carrier localisation lengths of 1.1 – 3.1 nm [26] can be accommodated within the cell without spurious coupling to periodic replicas. Following Refs. [22–24, 94], we assume that InGaN is a random alloy and distribute indium atoms at the cation sites of the active region with a probability given by the nominal indium content of the alloy composition in question. In doing so we do not assume any preferential orientation or correlation of indium atoms. To examine the impact of the microscopic indium configuration on the electronic structure, we consider twenty different random atomic configurations for each composition studied. These configurations are generated for nominal indium contents of 10% , 15% and 25% , which cover the experimentally relevant range of indium contents [26]. It should be noted that we are interested here in general trends rather than a detailed statistical analysis of the results. Such an analysis would require significantly more random configurations. However, for our purposes, to shed light on trends and basic properties of the InGaN/GaN QWs with varying indium content, including effects of random alloy fluctuations, a sample of twenty different configurations per alloy content is sufficient.

In Refs. [26] and [95], well-width fluctuations were observed at the upper interface [GaN on InGaN] of *c*-plane InGaN/GaN QWs. The reported diameters range from 5 to 10 nm and heights of one to two monolayers are observed. We include a well-width fluctuation with a diameter of 5 nm and a height of two monolayers sitting in the center of the upper region of our QW. Consistent with previous approaches to the modeling of these features, the shape of the well-width fluctuation is assumed to be disk-like [44, 48]. We are mainly interested in the impact of random alloy fluctuations on the electronic properties, therefore, we do not attempt to study the effects of well width fluctuations varying in size and shape. This would require very detailed experimental information as input into our model and is beyond the scope of the present work. However, assuming a single type of well width fluctuation does give an indication of the mechanisms by which any well-width fluctuation, in combination with random alloy and built-in field effects, could affect carrier localisation features.

3.4 Results

In this section we present the results of our theoretical analysis. We start with ground state properties in Sec. 3.4.1, and focus then in detail on excited states in Sec. 3.4.2.

3.4.1 Ground state properties

A first quantitative measure for the impact of alloy fluctuations on the electronic structure of *c*-plane InGaN/GaN QW systems is given by the variation in ground state transition energies

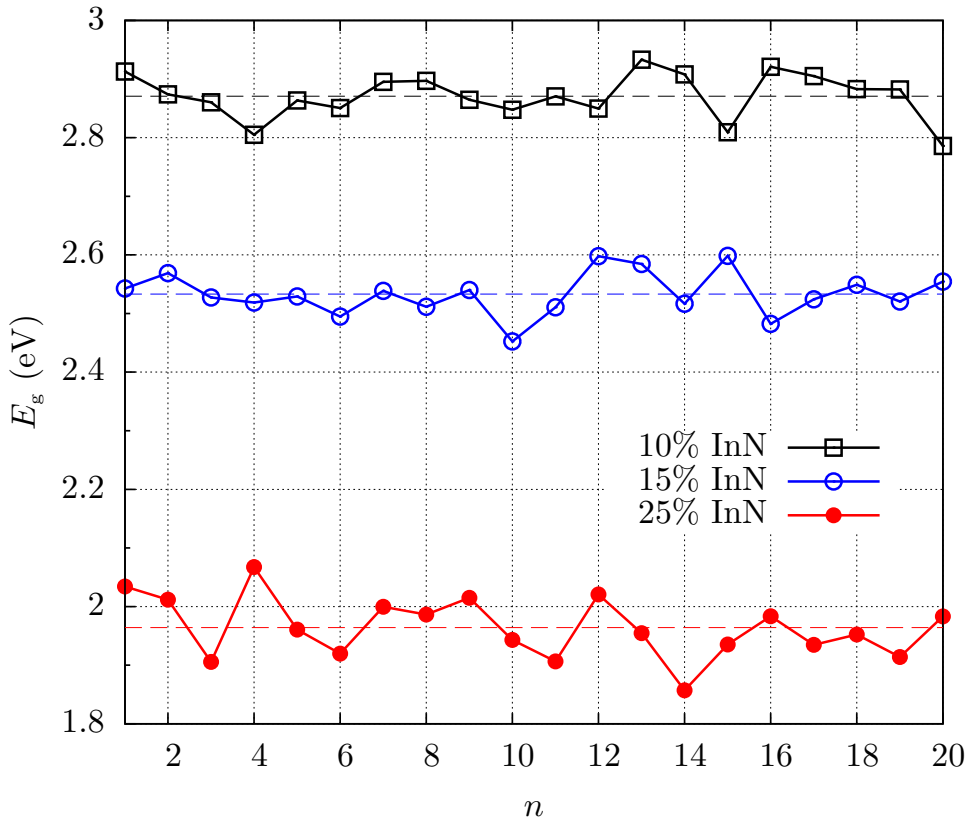

FIGURE 3.1: Single-particle ground state transition energies (band gap) in the here-considered c-plane $In_xGa_{1-x}N/GaN$ QWs for the n different random microscopic configurations. The indium content in the well is $x = 0.1$ (10%, black square), $x = 0.15$ (15%, open blue circle) and $x = 0.25$ (25%, red solid circle). The average transition energies for each indium content are indicated by the dashed lines.

about their configurational average. In Fig. 3.1, the energy of the ground state transition, E_g, is plotted against the configuration number, n, for each nominal indium concentration [10%, 15% and 25%]. For each case the average transition energy is indicated by a dashed line. The values obtained for the 10% (black square), 15% (open blue circle) and 25% (solid red circle) indium systems are 2.871 eV, 2.533 eV and 1.964 eV, respectively. As expected, the transition energy shifts to lower energies with increasing indium content, due to the lower band gap of InN with respect to GaN. Apparent from Fig. 3.1 is the significant spread in transition energies about their averages across all indium contents. This demonstrates that random alloy effects are important for as little as 10% indium in the well. The fluctuations in E_g are also consistent with the large PL linewidths observed experimentally [15, 19, 26, 96, 97]. These calculated average transition energies will be compared to experimental PL peak energies reported in the literature in Sec. 3.5.

To investigate the origin of the variance of the transition energies, we look now to the variation of the corresponding electron and hole ground state energies about their respective averages. In Fig. 3.2 the electron ground state energies, E^{e}_{GS} [Fig. 3.2 (a)], and hole ground state energies, E^{h}_{GS} [Fig. 3.2 (b)], are plotted as a function of the configuration number, n. The average ground

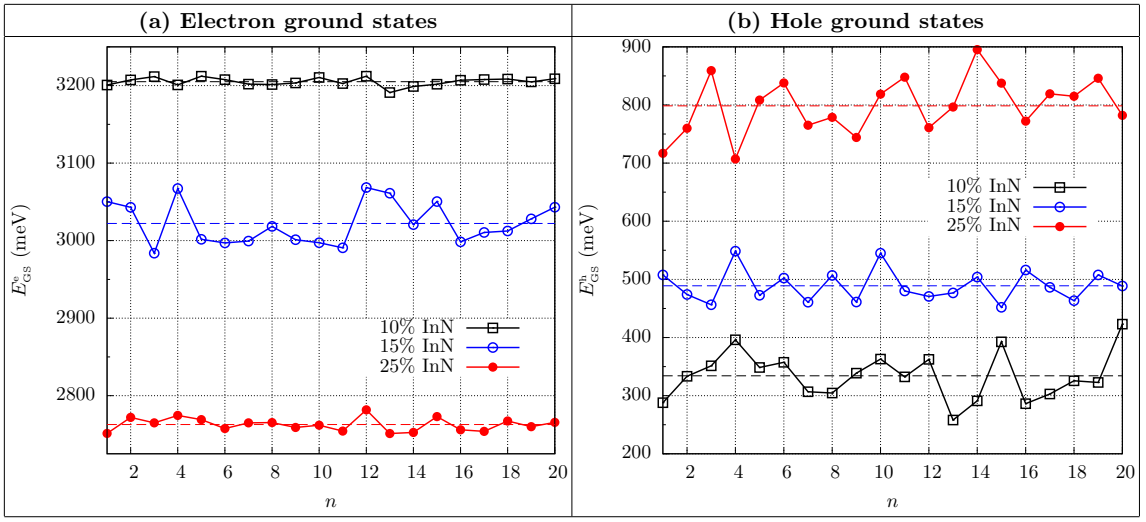

FIGURE 3.2: (a), Electron ground state energy, E^{e}_{GS}, and (b), hole ground state energy, E^{h}_{GS}, in an $In_xGa_{1-x}N$/GaN QW as function of the different random microscopic configurations, n. The indium content x in the well is $x = 0.10$ (10%, black square), $x = 0.15$ (15%, blue circle) and $x = 0.25$ (25%, red solid circle). The average ground state energies are indicated by dashed lines.

state energies are again indicated as dashed lines. The data are shown for the different indium contents x. The average hole ground state energy increases with increasing indium content since the valence band offset increases. For 10% [$x = 0.1$, black square], 15% [$x = 0.15$, blue circle] and 25% [$x = 0.25$, red solid circle] indium the average energies are 334 meV, 489 meV and 785 meV, respectively [cf. Fig. 3.2 (b)]. The zero of energy is taken as the valence band edge of the unstrained bulk GaN. However, due to the macroscopic built-in potential and random alloy fluctuations, the valence and conduction band edges will vary with position across the QW structure, with the calculated hole energies then including a contribution from these factors. For the comparison with the experiment only the transition energies are relevant, which are independent of the choice of the zero of energy. The average ground state energies of the electrons likewise decrease with increasing indium content, since the conduction band offset is increased [cf. Fig. 3.2 (a)]. The average electron ground state energies are 3.205 eV, 3.022 eV and 2.763 eV for 10%, 15% and 25% indium, respectively.

On comparison of the variations in Fig. 3.2 (a) and (b), in general, it is evident that the hole ground state energy, E^{h}_{GS}, is very sensitive to the configuration number, n. This further indicates that the alloy microstructure plays an important role for the valence band states. More specifically, from Fig. 3.2 we find that the E^{h}_{GS} values vary between $\sim \pm 100$ meV around their average energies whilst the electron ground state energies, E^{e}_{GS}, vary at most from the average by $\sim \pm 50$ meV. However, for the electron ground states, the large value of ± 50 meV arises mainly from the 15% indium case while for 10% and 25% indium we find only $\sim \pm 10$ meV and $\sim \pm 20$ meV, respectively. Furthermore, for the 15% indium case, the spread in the

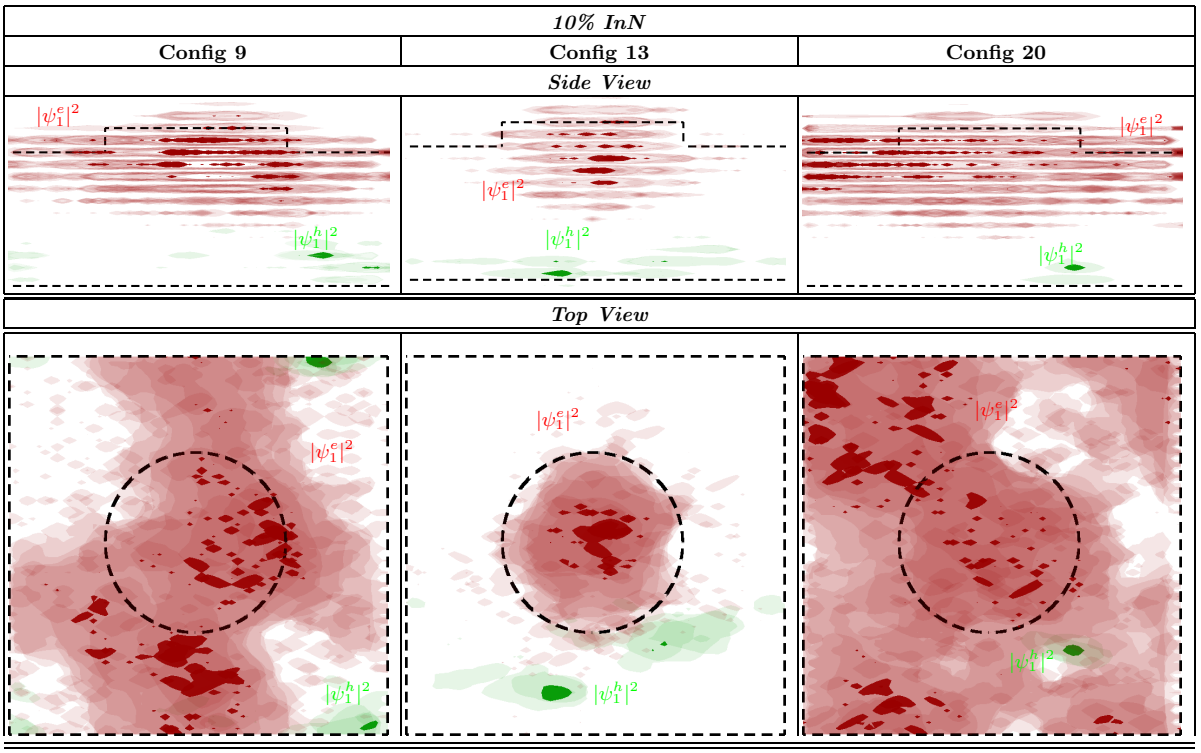

FIGURE 3.3: Isosurface plots of the electron (red), $|\psi_1^e|^2$, and hole (green), $|\psi_1^e|^2$, ground state charge densities in the $In_{0.10}Ga_{0.90}N/GaN$ QW. The light (dark) isosurface corresponds to 10% (50%) of the maximum charge density. The results are shown perpendicular ("Side View") and parallel ("Top View") to the *c*-axis. In this and the following two figures, the dashed lines in the side view indicate the QW interfaces; as a guide to the eye, the circular well width fluctuation is also given by the dashed line in the "Top View". The results are shown for three different random microscopic configurations (Configs 9, 13, and 20).

electron ground state energies about their average energy is comparable with the spread in the energies of the hole states.

To shed more light on the results shown in Fig. 3.2 (a) and (b), Figs. 3.3, 3.4 and 3.5 show isosurfaces of the electron (red) and hole (green) ground state charge densities for selected configurations in the case of 10%, 25% and 15% indium in the QW, respectively. The "Side View" for each of these cases is a view perpendicular to the *c*-axis, while the "Top View" is a view looking down the *c*-axis. The light and dark isosurfaces correspond to 10% and 50% of the respective maximum charge density values. The selected configurations correspond to situations with positive and negative deviations from the average ground state energy plus one configuration that is close to the average value.

We analyse in a first step configurations $n = 9, 13$ and 20 of the 10% indium case. The corresponding charge densities are displayed in Fig. 3.3. In general we find that the electron and hole wave functions are spatially separated along the *c*-axis due to the presence of the electrostatic built-in field. Looking at configurations 9 and 20, we see from the electron charge densities that they are almost spread across the entire *c*-plane in the QW region. However, a closer inspection also reveals that the ground state electron wave functions are affected by the

presence of the random alloy fluctuations. This is evinced by the lower probability densities in certain parts of the QW region. For configurations 9 and 20 we find also that the assumed well width fluctuation is of secondary importance. A different behaviour in our calculations is observed when looking at configuration 13, where the charge density is localised very strongly in the well-width fluctuation. This particularity of the ground state wave function, confined in the well-width fluctuation, is also reflected in the energy value, which shows the largest absolute deviation from the average [cf. Fig. 3.2 (a)]. However, we stress here again that we have assumed only a particular type of well-width fluctuation. We will discuss the importance of the well-width fluctuation in more detail below.

For the hole ground states the situation is different. Looking at the charge densities (green isosurfaces) in Fig. 3.3, much stronger localisation effects are visible for all configurations. The "strength" and spatial position of the localisation changes greatly from configuration to configuration. This behaviour reflects the sensitivity of the hole ground state energies to a particular microscopic configuration, as seen in Fig. 3.2 (b). In general this sensitivity to the alloy microstructure can be attributed to the larger effective mass of the holes [98, 99], when compared to the electrons, and their associated tendency to be localised at In-N-In chains, as shown by DFT calculations [45, 100]. It is important to note that the observed hole localisation features both in-plane as well as along the *c*-axis are vastly different from a standard continuum-based description. When looking at configuration 13, the hole wave function localises near the bottom QW/barrier interface. This situation might be expected from a continuum-based description. However, a fully continuum-based description would not account for the clearly visible in-plane localisation effect, since in such an approach InGaN/GaN QWs are usually treated as one dimensional systems. For configurations 9 and 20, the wave functions are localised in regions clearly above the bottom QW interface. This would also not be expected from a continuum description. This strong localisation experienced by the holes validates the aforementioned conclusion that random alloy fluctuations significantly impact the system properties for as little as 10% indium in the QW. The results shown in Fig. 3.3 also indicate that the wave function overlap between electron and hole ground states is not only affected by the spatial separation along the growth direction but also by the spatial separation in the *c*-plane. We will come back to this observation in Sec. 3.5 where we discuss the observed results with respect to experimental data.

Before turning to the 15% indium case, we focus on the 25% indium results, shown in Fig. 3.4, in the next step. When looking at the electron charge densities (red) of the here displayed configurations 4, 13 and 15, it is evident that the electron wave functions are all localised by the well-width fluctuation. This results from the increased built-in field in the 25% indium case when compared with the 10% indium case [cf. Fig. 3.3]. Since the well-width fluctuation introduces an extra in-plane/lateral confinement for the electron wave functions, one could expect larger variations in the corresponding electron ground state energies when compared

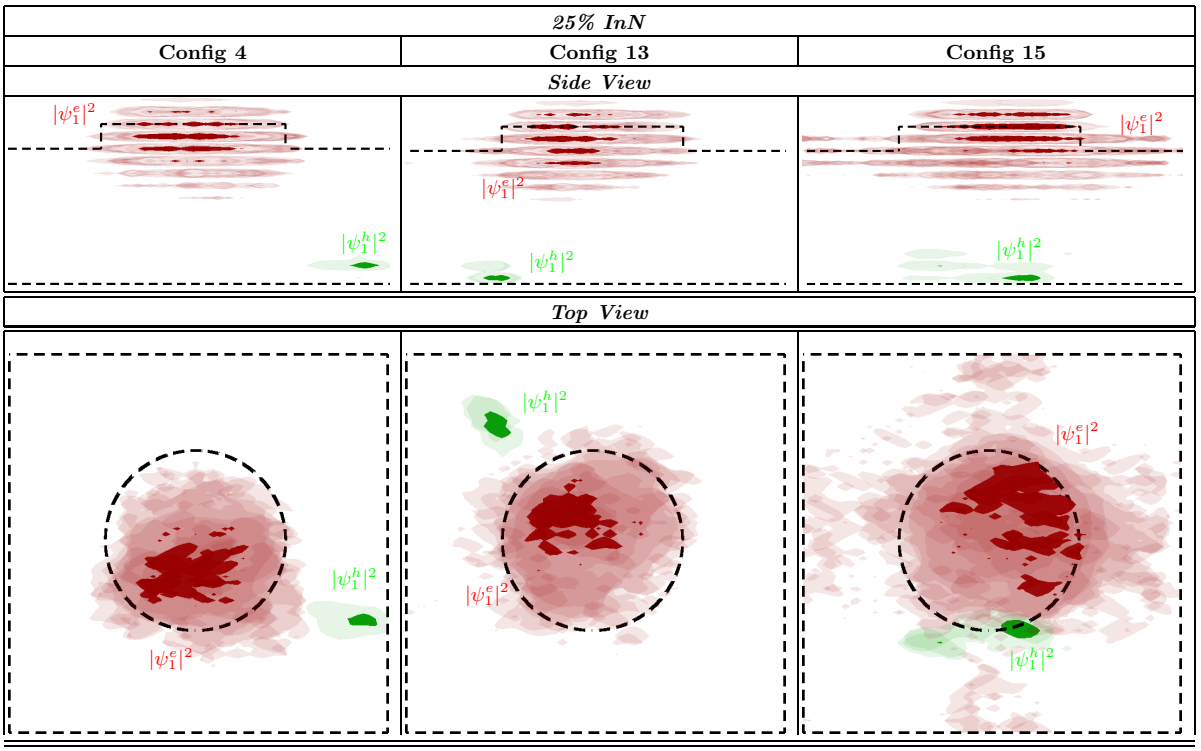

FIGURE 3.4: Isosurface plots of the electron (red), $|\psi_1^e|^2$, and hole (green), $|\psi_1^h|^2$, ground state charge densities in the $In_{0.25}Ga_{0.75}N/GaN$ QW. The light (dark) isosurface corresponds to 10% (50%) of the maximum charge density. The results are shown perpendicular ("Side View") and parallel ("Top View") to the *c*-axis for three different random microscopic configurations (Config 4, 13, and 15).

with the 10% indium system, where the considered well-width fluctuations are only of secondary importance. This is because different microscopic configurations of the indium atoms in the well-width fluctuation will lead to different effective confining regions for the electrons. For instance, a concentration of indium in the centre of the well width fluctuation (configuration 13) can lead to a ground state with a very different energy from that of a configuration where the indium is concentrated near the barrier material (configuration 15); the state near the barrier is effectively confined in a smaller region and will have its energy increased by the effects of the barrier. This picture of small changes in indium content leading to large changes in confinement and energy is consistent with the data shown in Fig. 3.2 (a), and discussed above. Turning to the hole ground states, we find a similar behaviour as in the 10% indium case with strong localisation features for each configuration. In configurations 13 and 15 the hole wave function is localised close to the bottom QW interface, while the hole ground state wave function in configuration 4 is localised two monolayers above the lower QW interface. Due to the increased built-in field in the 25% indium case one would expect that the hole wave functions are localised near the bottom interface. In this sense, with the hole wave function not being localised near the bottom QW interface, one could expect that configuration 4 represents an extreme case. This is confirmed in the large deviation of its ground state energy from the average ground state energy, as displayed in Fig. 3.2 (b). When looking at the "Top View"

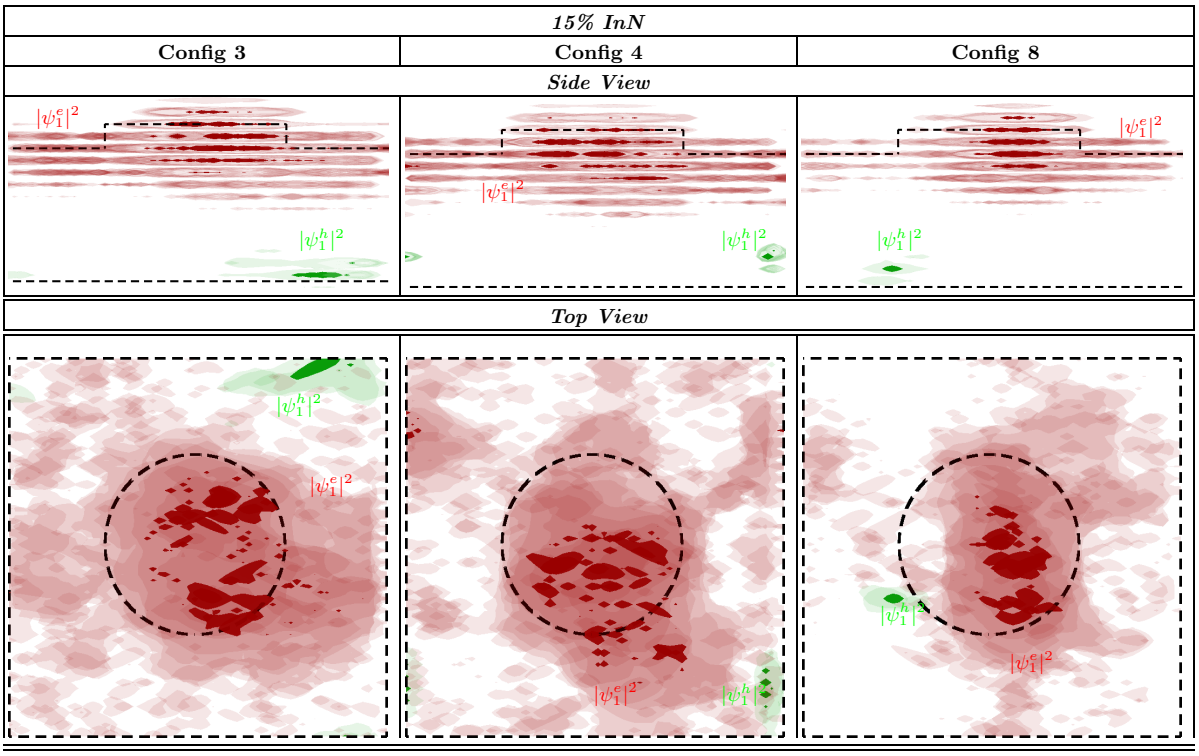

FIGURE 3.5: Isosurface plots of the electron (red), $|\psi_1^e|^2$, and hole (green), $|\psi_1^e|^2$, ground state charge densities in the $In_{0.15}Ga_{0.85}N/GaN$ QW. The light (dark) isosurface corresponds to 10% (50%) of the maximum charge density. The results are shown perpendicular ("Side View") and parallel ("Top View") to the *c*-axis for three different random microscopic configurations (Config 3, Config 4, Config 8).

of the electron and hole ground state charge densities, we find that electron and hole wave functions are separately localised due to the built-in field, random alloy fluctuations and well width fluctuations. Again, the wave function overlap between electrons and holes is not only affected by the spatial separation along the growth direction but also in the *c*-plane. When looking, for instance, at the charge densities of the electron and hole wave functions from configuration 15, we find that electron and hole wave functions are localised at similar in-plane positions. This is in contrast to configuration 4 and 13, where we are left with a clear spatial separation also *in* the *c*-plane. Again, we will come back to the importance of these properties in Sec. 3.5.

We now turn to the 15% indium case. Here we have selected configurations 3, 4 and 8. The corresponding electron and hole ground state charge densities are displayed in Fig. 3.5. As discussed above, the variation in the hole ground state energies [cf. Fig. 3.2 (b)] is comparable to the variations observed in the 10% and 25% indium case, respectively. The isosurfaces of the hole charge densities (green) displayed in Fig. 3.5, show also a similar behaviour as in the 10% and 25% indium systems. However, in comparison with the 10% or 25% indium case, the electron ground state energies in the 15% indium system show much larger variations [cf. Fig. 3.2 (a)]. When looking at the isosurfaces of the electron charge densities (red) for

configurations 3, 4 and 8, the origin of this behaviour becomes clear. In terms of the importance of the well-width fluctuation, the 15% indium case represents an intermediate situation. For example, in the case of configuration 8, the electron wave function is mainly localised inside the well width fluctuation, while configuration 4 shows still significant charge density contributions outside the well-width fluctuation. From this one could expect that the energies of these different configurations are very different, and indeed this is confirmed by Fig 3.2 (a). In summary, the presence of the well-width fluctuation in combination with the built-in field explains the initially surprising result of the stronger variation in the electron ground state energies for the 15% indium case in our calculations.

Overall, even though we have considered here only one particular type of well-width fluctuation, our results clearly demonstrate that their presence can contribute significantly to variations in both transition energies and localisation effects. It should also be mentioned that our results for electrons are consistent with the work by Watson-Parris *et al.* [48, 101], who studied the impact of well-width fluctuations on the electronic structure of InGaN QWs in the framework of a modified effective mass approach. In the study by Watson-Parris *et al.* [48, 101], disk-shaped well-width fluctuations with diameters ranging from 5 nm to 20 nm have been studied. The influence of these fluctuations on the electron wave function localisation characteristics has been analysed for *c*-plane InGaN/GaN QWs with indium contents between 5% and 25%. At 10% indium content, the results with and without well-width fluctuations are similar in terms of the electron ground state localisation length. Only a slight decrease in the localisation length is observed when the well-width fluctuations are included, indicating that well-width fluctuations for lower indium contents are of secondary importance, consistently with our results [cf. Fig. 3.3]. Watson-Parris *et al.* [48, 101] showed also that at 25% indium, well width fluctuations lead to a significant reduction of the electron ground state localisation length, when compared to a calculation without well width fluctuations. This corroborates our earlier mentioned conclusion that the importance of well width fluctuations in localising the electron wave functions will depend on the indium content. Therefore, even though we have assumed only one particular type of well-width fluctuation, our presented results provide a first indication of the importance of well-width fluctuations on the electronic structure of *c*-plane InGaN/GaN QWs with different indium contents.

So far our discussion of localisation effects has been based on inspecting the charge densities of the electron and hole ground state wave functions. To study localisation effects now on a more quantitative basis we use the metric of the inverse participation ratio (IPR) [102]. This provides a more objective measure of localisation and also allows the examination and comparison of the localisation characteristics of many states at once. The participation ratio was first introduced by Bell [103] to assess the localisation properties of atomic vibrations. In that context it gave insights into the fraction of the total number of atoms in the system which participate effectively in the vibrations of a particular normal mode. The IPR is the inverse of

this quantity, and is commonly used as a measure of localisation in TB models [102, 104]. In our TB formalism, a carrier wave function, ψ, is given by:

$$\psi = \sum_{i}^{N} \sum_{\alpha}^{N_\alpha} a_{i\alpha} \phi_{i\alpha} \ , \tag{3.5}$$

where the index i runs over the N lattice sites, and the index α denotes the different orbitals in our sp^3 TB basis at each site. The term $a_{i\alpha}$ represents the amplitude of the wavefuntion, ψ, constructed with the basis $\phi_{i\alpha}$, at the site i. On the basis of Eq. (3.5) the IPR may be defined as:

$$\mathrm{IPR} = \sum_{i=1}^{N} \left(\sum_{\alpha} |a_{i\alpha}|^2 \right)^2 / \left(\sum_{i=1}^{N} \sum_{\alpha} |a_{i\alpha}|^2 \right)^2 \ . \tag{3.6}$$

For a *completely localised* state, which will be expressible in terms of orbitals at only one atomic site, the IPR will be one; for a *completely delocalised* state, which is comprised of a linear combination of equal parts of orbitals at all atomic sites, the IPR will be N^{-1}; and for a state which is intermediate between localised and delocalised, the IPR varies continuously between one and N^{-1}.

In the following we have normalised the calculated IPR values to the IPR value of the electron ground state with the largest IPR value ($1.529\text{x}10^{-4}$) in the 10% indium case, which is configuration 13, shown in Fig. 3.3 (b). Therefore, the normalised IPR values, $\widetilde{\mathrm{IPR}}$, can exceed values of one and can be interpreted as giving the extent to which the state under consideration is more or less localised than the electron ground state of configuration 13 shown in Fig. 3.3. Normalising the IPR values in this way gives a more intuitive and visual picture of the localisation properties of the state in question.

The ground state electron and hole $\widetilde{\mathrm{IPR}}$ values are shown as a function of their respective energies in Fig. 3.6. Figure 3.6 (a), (b) and (c) correspond to the electron ground states in the 10%, 15% and 25% indium content systems, respectively. The data for the holes is depicted in Fig. 3.6 (d), (e) and (f). Figure 3.6 confirms that the hole states are, in general, far more localised than the electron states [*please note the different scales*]. More specifically, we find hole states which are up to 350 times more localised than the electron ground state to which they are normalised, and never less than 5 times more localised. Furthermore, Fig. 3.6 reveals that the $\widetilde{\mathrm{IPR}}$ values of the hole states significantly vary between different configurations, highlighting again that the hole ground states are very sensitive to the microscopic alloy structure.

To discuss the results in more detail, we start with the $\widetilde{\mathrm{IPR}}$ values of the electron ground states [Fig. 3.6 (a), (b), and (c)]. When comparing the electron $\widetilde{\mathrm{IPR}}$ values for the different indium contents, we find that in general the $\widetilde{\mathrm{IPR}}$ values increase with increasing indium content. Since the macroscopic strain increases with increasing indium content, the piezoelectric built-in field increases as well. Thus, with increasing indium content an increasing confinement (along the

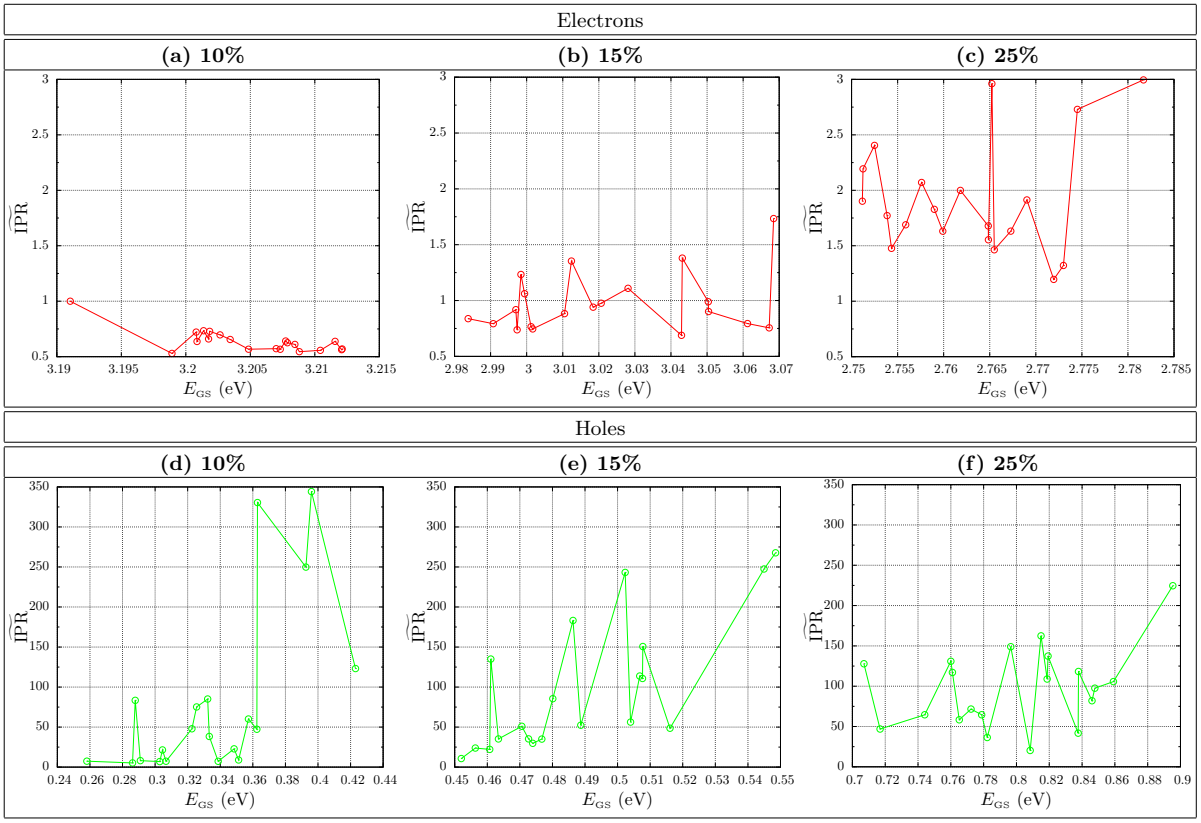

FIGURE 3.6: Electron and hole ground state normalised inverse participation ratios ($\widetilde{\mathrm{IPR}}$) plotted as a function of the ground state energies, E_{GS}, of each of the 20 microscopically different configurations, for nominal indium contents of 10%, 15% and 25%. The IPRs are normalised to that of the 10% electron ground state with the higest IPR, which is Config 13 (cf. Fig. 3.3). [*Note different scales*]

c-axis) for the electron ground state can be expected. Additionally, with increasing indium content, the considered well-width fluctuation becomes increasingly important and adds an extra in-plane confinement. This is consistent with the trends observed across Fig. 3.6(a-c) for the electron $\widetilde{\mathrm{IPR}}$ values.

However, when looking at the holes [Fig. 3.6 (d), (e), and (f)], we see that this trend is not as clearly visible as in the electron case. This arises from several factors. For instance, in the 10% indium case [cf. Fig. 3.6 (d)], we have three exceptionally strongly localised states. Their $\widetilde{\mathrm{IPR}}$ values are of the order of, or even exceed, the maximum values of the 15% [Fig. 3.6 (e)] and 25% [Fig. 3.6 (f)] indium case. Therefore, to treat these exceptional states accurately, a larger number of configurations would have to be considered to perform more reliable statistical averages. However, this is beyond the scope of the present study. Here we are mainly interested in identifying general trends and to gain first insights into the effects of random alloy fluctuations on the electronic structure of *c*-plane InGaN/GaN QWs with varying indium contents.

Based on the results presented, the argument of an increased built-in field with increased indium content, used to explain the trends in the electron ground states, cannot be directly

applied to the hole states. The reason for this is that the hole states show not only a strong localisation along the growth direction, it is also evident from Figs. 3.3, 3.4 and 3.5 that the hole localisation has a very strong in-plane localisation component. This component is not greatly affected by the presence of the *macroscopic* built-in field along the growth direction. Thus the localisation behaviour of the hole states is less dominated by the macroscopic built-in field and governed more by fluctuations in the local indium environment. Consistent with this, we find very large changes in the $\widetilde{\mathrm{IPR}}$ values of the ground state hole wave functions between different configurations at nominally the same indium content, even though the macroscopic built-in field should be very similar for a fixed indium content. Further to this, we note a tendency for localisation ($\widetilde{\mathrm{IPR}}$) to increase as the holes become more strongly confined, with a general rise from left to right in each of Fig. 3.6 (d),(e), and (f); nevertheless, the fluctuations in the $\widetilde{\mathrm{IPR}}$ values are about as large as the trend itself.

So far we have focused our attention on localisation effects in ground state properties. This provides key information for experiments performed at low temperatures. However, when the optical properties of *c*-plane InGaN/GaN QWs are studied experimentally at ambient temperature, or when InGaN based devices are operating at room temperature, excited states become relevant. Thus a knowledge of the localisation characteristics of excited electron and hole states is also important for understanding *c*-plane InGaN QWs. This is the focus of the next section.

3.4.2 Excited states

After studying the ground state localisation properties by means of the $\widetilde{\mathrm{IPR}}$ values, here we apply the same metric to the excited states. We start by investigating, in Fig. 3.7, selected configurations for 10%, 15% and 25% indium before looking at results averaged over the 20 different random configurations, considered for each composition. The benefit of studying selected configurations first is that we can then display the results both as a function of the energy and the state number. This is not possible for the averaged data where the data is best displayed as a function of the state number. This stems from the fact that the ground state energies fluctuate significantly between different configurations [cf. Fig. 3.2,3.6]. The configurations selected here have a ground state $\widetilde{\mathrm{IPR}}$ value which is close to the average $\widetilde{\mathrm{IPR}}$ of all the ground states of that indium content, for electrons and holes. Figure 3.7 shows the $\widetilde{\mathrm{IPR}}$ values for the first 60 electron and hole states as a function of the energy, measured with respect to the corresponding ground state energy. We take the absolute value of this energy difference so that with increasing energy the states move deeper into the valence or conduction band. The state numbers are given on the second x-axis at the top of each figure. Figure 3.7 reveals a greater energy range covered by the first 60 electron states than by the 60 hole states. This is due to the larger hole effective mass in comparison with the electron effective mass.

This results in a smaller spacing between two sequential hole states than for electrons and consequently 60 hole states cover a smaller energy range than 60 electron states.

Looking at the electron states first, we note that in general the $\widetilde{\text{IPR}}$ values for the first few excited states increase with increasing indium content [Fig. 3.7(a), (b) and (c)]. We attribute this effect to the increasing piezoelectric built-in field with increasing indium content. A similar trend is also observed for the hole states [Fig. 3.7 (d), (e) and (f)]. For instance, the $\widetilde{\text{IPR}}$ values of the first 5 hole states increase with increasing indium content. Thus, one can expect that for the holes, the energy depth into the valence band to which there are still localised states found, increases with increasing indium content. This is consitent with the experimentally observed increase of the PL width, stokes shift, and absorption edge broadening with indium content [15, 26, 28, 105, 106]. The localised states in this energy range are sometimes referred to as "tail states" due to the manner in which they modify the form of the density of states; the localised states appear as an added tail at the begining of the ideally step-like form of the density of states [82, 107]. In order to gain some first insights into the relation between localisation effects and energy, we note that for 10% indium [Fig. 3.7 (d)] up to 40 meV into

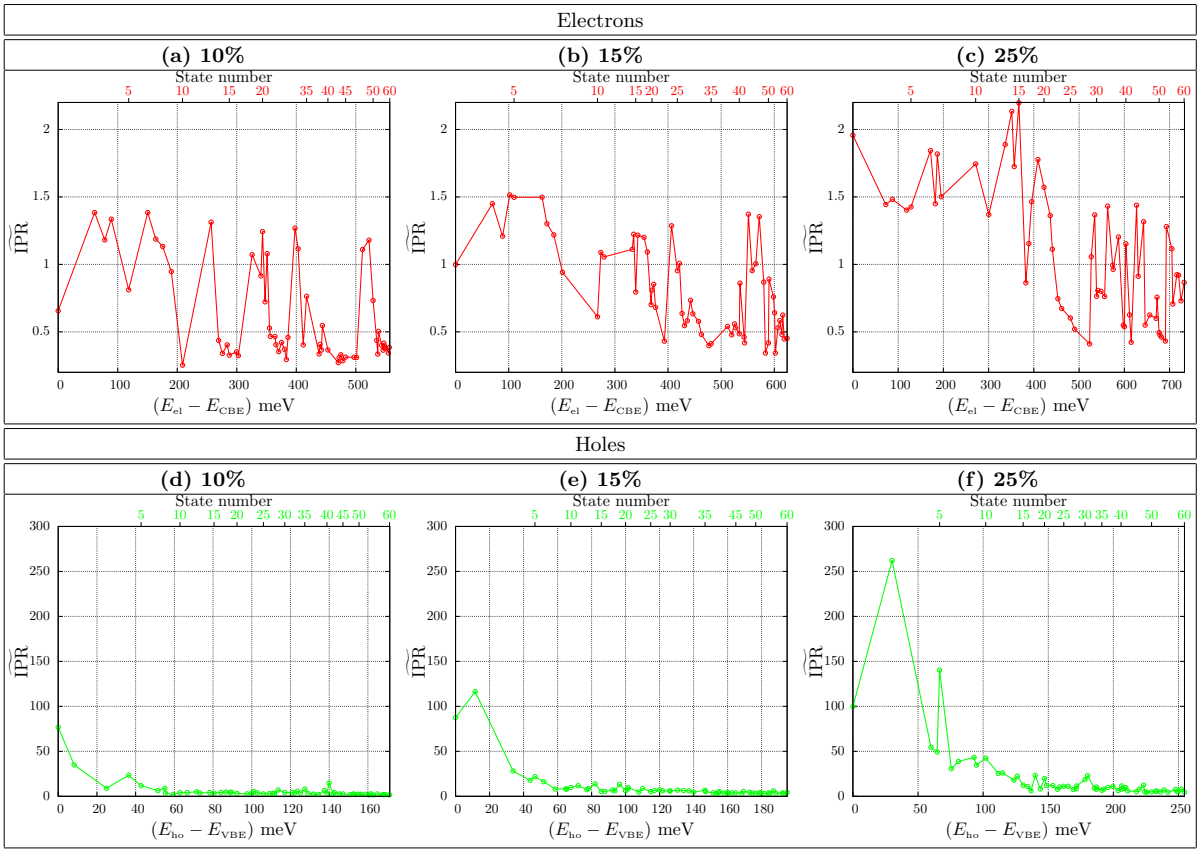

FIGURE 3.7: Normalised electron (top row) and hole (bottom row) inverse participation ratios ($\widetilde{\text{IPR}}$) plotted against the state energy as measured from the conduction or valence band edge. The results are given for particular representative configurations with indium contents of 10%, 15% and 25% (see text for selection criteria). The IPRs are normalised with respect to the IPR of the most localised 10% electron ground state, which is configuration 13.

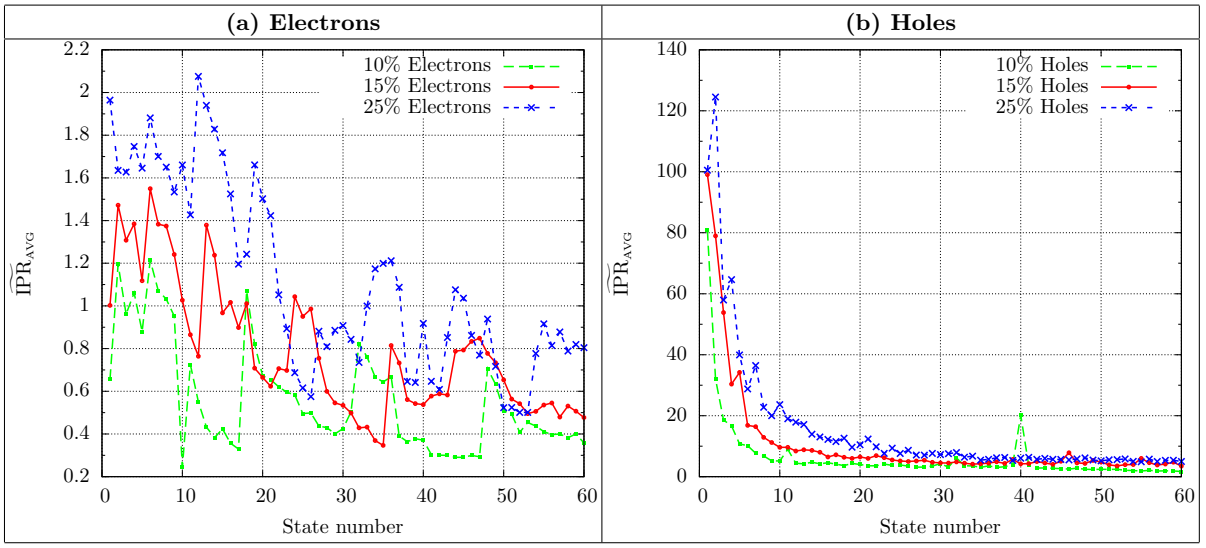

FIGURE 3.8: Normalised inverse participation ratios of increasing electron (a) and hole (b) states averaged over all microscopic configurations, $\widetilde{\mathrm{IPR}}_{\mathrm{AVG}}$, plotted against state number. The results are shown for three different indium contents, 10%, 15%, and 25%, and the normalisation is taken with respect to the most localised 10% electron ground state, which is that of configuration 13, shown in Fig. 3.3 (b).

the valence band (state number 5) the holes have still an $\widetilde{\mathrm{IPR}}$ value which is approximately 10 times larger than that of the highest $\widetilde{\mathrm{IPR}}$ value of the electron ground state for the 10% indium case. Noting that this electron ground state shows considerable localisation [cf. Fig. 3.3, Config 13], we can safely say that a state 10 times more localised than this is strongly localised. For 15% indium [Fig. 3.7 (e)], again using $\widetilde{\mathrm{IPR}} \approx 10$ as an arbitrary threshold, this lasts up to 100 meV (state number 20), and for 25% indium [Fig. 3.7 (f)] there are still states with $\widetilde{\mathrm{IPR}} \approx 10$ past 165 meV at state 26. This behaviour, combined with the wide variation in calculated ground state energy observed in Fig. 3.2, implies that a significant density of localised states is present in *c*-plane InGaN/GaN QWs, which should measurably affect the optical properties of these systems at elevated temperatures.

So far we have focused our attention only on selected configurations. To illustrate the generality of the observed behaviour in the excited states, Fig. 3.8 displays the $\widetilde{\mathrm{IPR}}$ values for the first 60 (a) electron and (b) hole states averaged over the 20 different configurations. These averaged normalised IPR values are denoted by $\widetilde{\mathrm{IPR}}_{\mathrm{AVG}}$. The results are shown for 10% (dashed green line), 15% (red solid line), and 25% (dashed-crossed blue line) indium. Overall it is evident that the hole states show much stronger localisation effects [higher $\widetilde{\mathrm{IPR}}$ values] when compared with the electrons. Figure 3.8 also corroborates the earlier observed trend that with increasing indium content there is an increased persistence of localisation effects into the valence and conduction bands.

In an infinite system, the energy beyond which there are no more localised states can be expected at a definite energy, E_{mob}, referred to as the mobility edge. However, even when using

periodic boundary conditions, one is left with a system of finite size. While each of these systems represents a portion of the real QW, there remain finite-size effects that would not be present in the real, laterally infinite, QW. For example, even though the highest valence state generally has a very high IPR value in our finite-sized supercells, the most weakly bound of these states may be resonant with delocalised QW states in the infinite system. We refer to such states of our finite systems as "quasi-localised" states. These states should be excluded in estimations of the energy range of localisation. Taking this into consideration, we can nevertheless combine the results obtained for the ground and excited states in order to gain a first estimate of the energy range of localised states which exist in the valence band before the onset of delocalisation. We refer first to Fig. 3.6 where it is evident that the ground state energies for the holes vary by at least 100 meV across different random indium confgurations. We further note from Fig. 3.6 that all of these hole states have very high IPR values and can thus be considered strongly localised in comparison with the electrons. Taking a conservative measure for the localisation depth and keeping in mind the "quasi-localisation" effect described above, we consider only the four energetically highest valence states for each indium concentration studied to estimate the depth of localisation in the valence band. This gives us approximately an energy spread of 50-60 meV.

Turning now to the excited state data, we see, from the selected configurations studied in Fig. 3.7, that, for instance, in the 10% indium case strong localisation effects ($\widetilde{\mathrm{IPR}}_{\mathrm{AVG}} > 10$) extend for at least an energy range of 40 to 50 meV below the hole ground state. With increasing indium content this range further extends [cf. Figs. 3.7 (e) and (f)]. That these are not atypical behaviours in our ensemble is supported by reference to Fig. 3.8. Hence, combining the conservative estimate for the energy range of localised states inferred from our ground state data and the insights from the excited state studies, we estimate that already in case of 10% indium a total energy spread of localised states amounts to $\approx$ 100 meV. Thus, we expect an energy range of at least 100 meV over which there will be a significant density of localised valence states in *c*-plane InGaN/GaN QWs with indium contents at above or equal to 10%.

Even though we cannot determine the density of localised states exactly, we can still analyse how the wave function overlap between carriers in different states is affected by alloy fluctuations. This question is, for example, relevant for transport through *c*-plane InGaN/GaN QWs, since it gives a first indication of the probability of a carrier transferring from one site/state to another. To gain some insight into the carrier overlap we study in the following the *modulus overlap* of the wave functions of different states. In our TB formalism the modulus overlap σ_{nm} between two states ψ_m and ψ_n can be defined by:

$$\sigma_{nm} = \sum_{i}^{N} |\psi_{n,i}||\psi_{m,i}| \ , \tag{3.7}$$

where i denotes the lattice site. For $n = m$, this will be the overlap of a state with itself, $\sigma_{nn} = 1$, since the wave functions are normalised. A state ψ_j with a large σ_{jm} value for many states ψ_m will then have a widely spread out wave function. Conversely, if a state ψ_j has a small σ_{jm} for many other states, ψ_m, it means that the wave function ψ_j is localised in a particular spatial region of the QW. Note that we are dealing here with the *modulus* overlap; our definition for the overlap does not take into account the parity of the respective wave functions. Our metric simply indicates the extent to which the densities of the involved carriers are spatially coincident.

Figure 3.9 (a),(b), and (c) show, for the same configurations chosen in Fig. 3.7, the modulus overlaps, σ^e_{nm}, of each electron state with every other electron state. The data for the hole states are displayed in Fig. 3.9 (d),(e) and (f). We have considered the first 40 electron and hole states. The left column, (a) and (d), contains the results for 10% indium, the middle column, (b) and (d), the data for the 15% indium case while the right column, (c) and (f), depicts the situation for the QW with 25% indium.

We begin our analysis by focusing on the modulus hole wave function overlap σ^h_{nm} [Fig. 3.9 (d), (e) and (f)]. In the 25% case, (f), there are three distinct regimes in σ^h_{nm} visible. Over the first five states a dark region of very poor overlap [small σ^h_{nm} value] is visible. This indicates a region of strongly localised states, with the hole localisation length well below the supercell size (10 nm) considered here. This is consistent with the very high $\widetilde{\text{IPR}}$ values shown in Fig. 3.6. After the first five states, from state 6 to 10, we find a region of "semi-localised" states, with σ^h_{nm} values around 0.3 to 0.7. Beyond these states we find an area in the σ^h_{nm} plot that has values between 0.7 and 1. We classify these states as "delocalised states". Looking at the 15% indium case [Fig. 3.9 (e)] we find again these three regions but with the "delocalised" region being much larger, and both the "semi-localised" and "localised" region being greatly reduced. For the 10% indium case it is very hard to discern a region which could be described as "strongly localised" in the same sense as for 25% indium, but there is still clearly visible a "semi-localised" region. Consistent with our discussion of Figs. 3.7 and 3.8, it can be concluded that for the holes the location of the "mobility edge" depends on the indium content.

Looking at the electron states, in the upper row of Fig. 3.9, the minimum values of σ^e_{nm} are much larger [$\sigma^e_{nm} \approx 0.4$] when compared to the holes [$\sigma^h_{nm} \approx 0.05$]. We attribute this to the fact that the electron states, as discussed in Sec. 3.4.1 and demonstrated in Fig. 3.7, are less perturbed by the alloy fluctuations. The light and dark overlap "bands" of the figure correspond to the overlaps between states localised inside the QW and states which start to spread into the GaN barrier material. When looking at the positions (state numbers) of the dark regions with low σ^e_{nm} values, we find that these regions in general move to higher state numbers with increasing indium content. The different positions (state numbers) of these "bands" for the different indium contents can be imputed to changes in the conduction band confinement

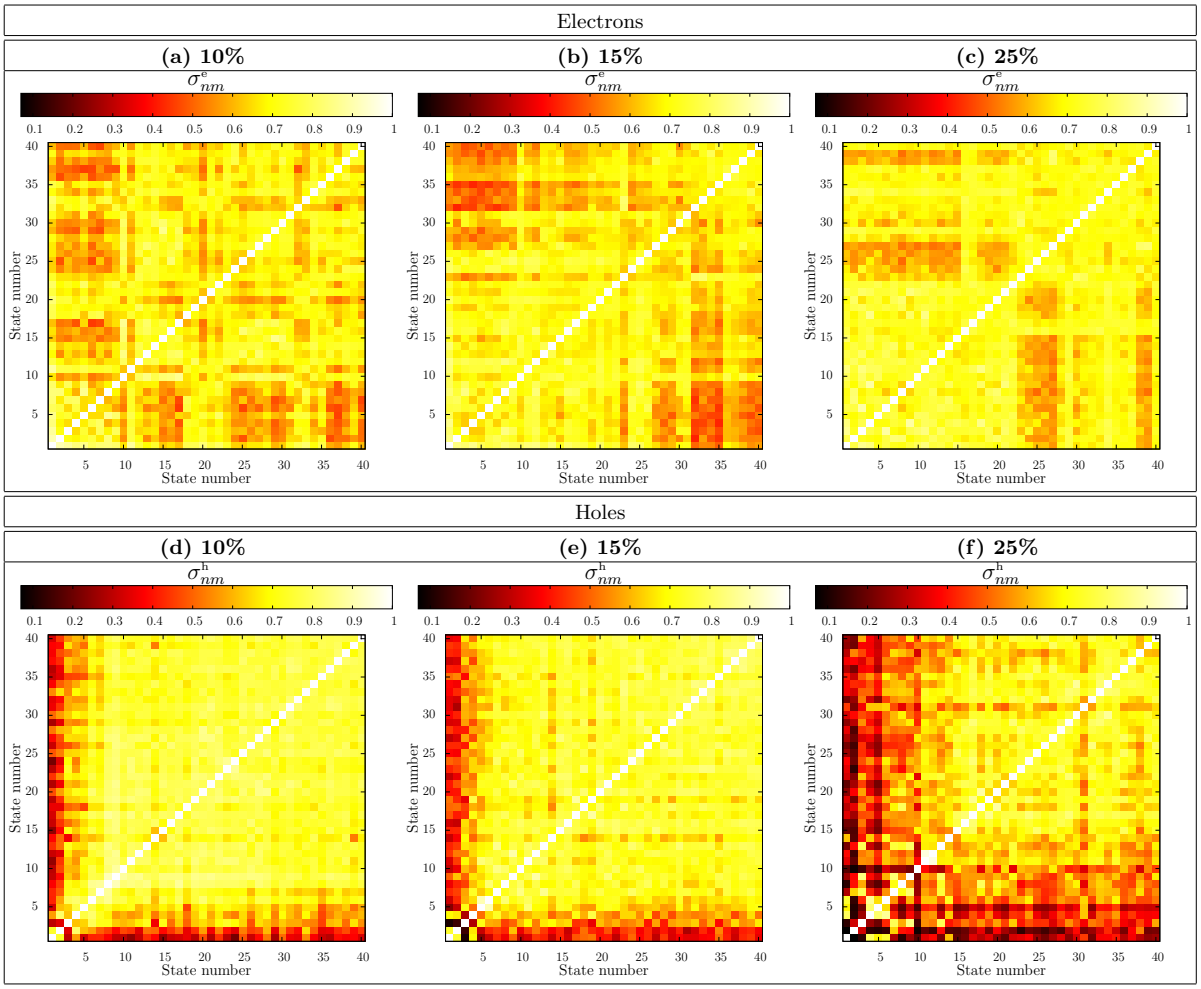

FIGURE 3.9: Modulus wave function overlaps, $\sigma^{e,h}_{nm}$, of the first 40 states for electrons and holes in particular configurations of $In_xGa_{1-x}N$/GaN QWs with indium contents of 10% (x=0.1), 15% (x=0.15), and 25% (x=0.25). The magnitude of the modulus overlap between state n and m is indicated by the colour of the point (n,m) on the plot.

potential. Please note that with increasing indium content, the electron wave functions also begin to become localised by the well-width fluctuations, which then also affects σ^e_{nm}.

To support these arguments and to further clarify the features seen in the σ^e_{nm} values, we now present the planar integrated probability density, P_i, of each state ψ_i:

$$P_i(z_m) = \sum_{k,l} |\psi_i(x_k, y_l, z_m)|^2 \ , \tag{3.8}$$

where x_k and y_l are the in-plane (c-plane) indices and z_m denotes the layer index along the c axis. The quantity $P_i(z_m)$ gives the probability that the electron or hole state i be found in the layer specified by the index z_m. This allows us to shed light on the localisation characteristic of the different states along the c axis.

Figure 3.10 shows $P_i(z_m)$ plotted for the first 40 electron [upper row] and hole states [lower row] for 10%, 15% and 25% indium [left to right in Fig. 3.10]. In each figure, the horizontal

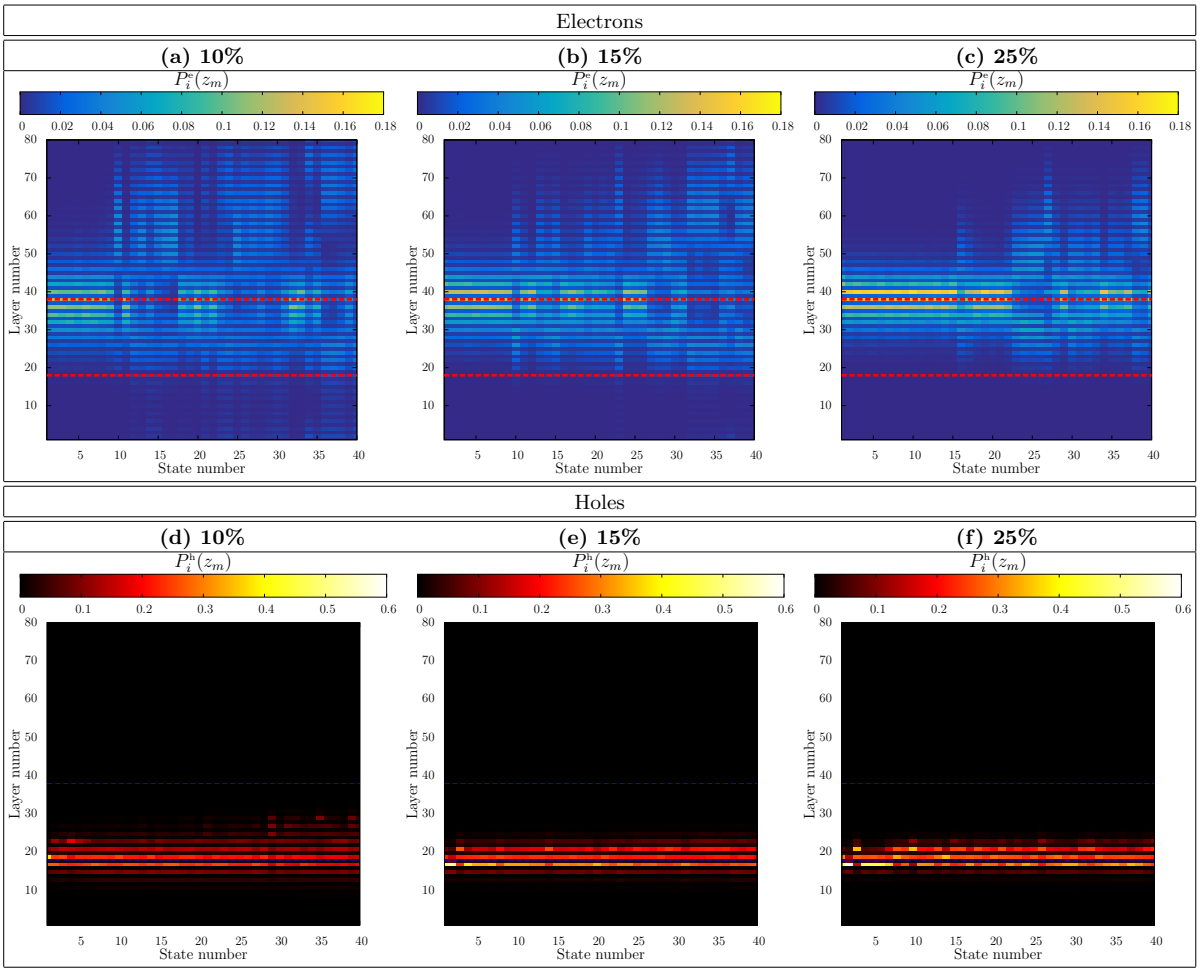

FIGURE 3.10: Planar integrated probability densities of electrons, $P_i^{\mathrm{e}}(z_m)$, [(a),(b) and (c)] and holes, $P_i^{\mathrm{h}}(z_m)$, [(d),(e) and (f)] in c-plane InGaN quantum wells with indium contents of 10%, 15% and 25%, for the first 40 states. The index i refers to the state number, and the index m refers to the layer of the quantum well. The boundaries of the quantum well active region are indicated by red dashed lines on the figure. To emphasise the different colour scales, a different colour scheme has been used for electrons and holes.

axis denotes the state number and $P_i(z_m)$ is given on the vertical axis. Thus the point (1,2) will give the probability that the electron/hole described by the first eigenstate be found in the second layer of the supercell. As a guide to the eye we indicate the QW boundaries as (red) dashed lines. Figure 3.10 confirms that much of the structure observed in the σ^e_{nm} values displayed in Figs. 3.9 (a-c), arises from variations in overlap with increasing height, z_m, in the QW. Conversely, Fig. 3.10 indicates that for the holes it is primarily the in-plane separation and in-plane variation in overlap, rather than the separation in z_m, that leads to the structure observed in σ^h_{nm} shown in Figs. 3.9 (d-f).

So far we have focused our discussion on selected configurations to illustrate trends in the localisation characteristics of ground and excited states. In order to demonstrate the generality of these results we have calculated the modulus wave function overlap averaged over all configurations for each of the indium contents considered here. This is denoted by $\bar{\sigma}^e_{nm}$ for electrons,

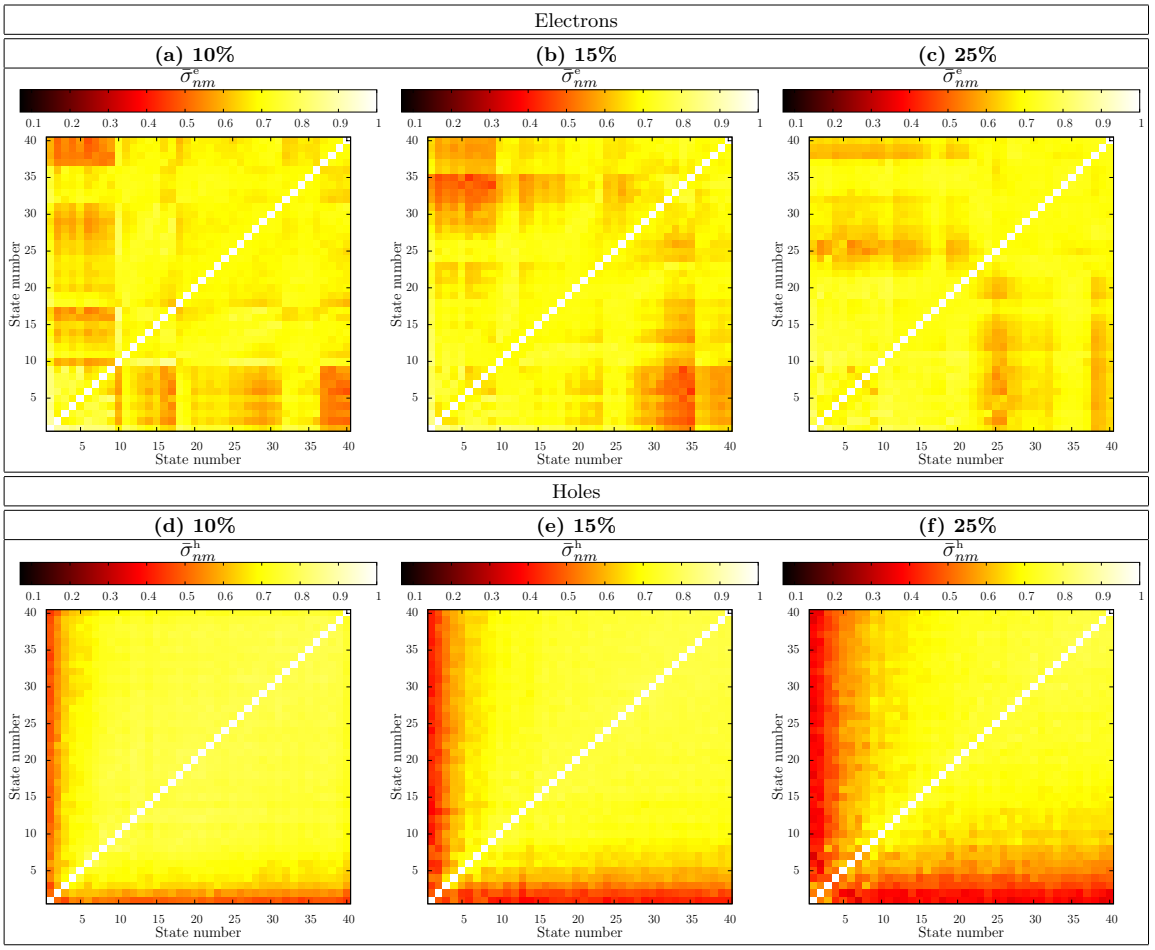

FIGURE 3.11: Modulus wave function overlaps of the 40 electron (top row) and hole (bottom row) states, of $In_xGa_{1-x}N$/GaN quantum well systems averaged over 20 different microscopic configurations. The averaged overlaps are denoted by $\bar{\sigma}^{e,h}_{nm}$. The data are shown for three different indium contents, 10%, 15% and 25%.

and $\bar{\sigma}^{h}_{nm}$ for holes. The $\bar{\sigma}^{e,h}_{nm}$ results are displayed in Fig. 3.11, which shows that $\bar{\sigma}^{e,h}_{nm}$ reflects the trends observed in the selected configurations [cf. Fig. 3.9]. Notably, the overlap structure in the electrons is preserved. For the holes the different regimes of localisation are again apparent across the different indium contents, especially the increasing width of the "strong-localisation" region with increasing indium content.

To gain further insight into the impact of random alloy fluctuations and varying indium content on the electronic and optical properties of *c*-plane InGaN/GaN QWs, we analyse in a next step the modulus overlap, σ^{eh}_{nm}, of the first 40 electron and hole wave functions. The results are shown in Fig. 3.12. The data give first indications of how the emission efficiency of the QWs are affected by changes in the indium content. Our results reveal that with increasing indium content the electron and hole modulus wave function overlap decreases. This effect can be attributed primarily to the increasing strain-dependent macroscopic piezoelectric polarization field in the QW. Consequently, one observes a stronger spatial separation of the electron and hole wave functions along the *c*-axis. However, the increasing in-plane localisation introduced

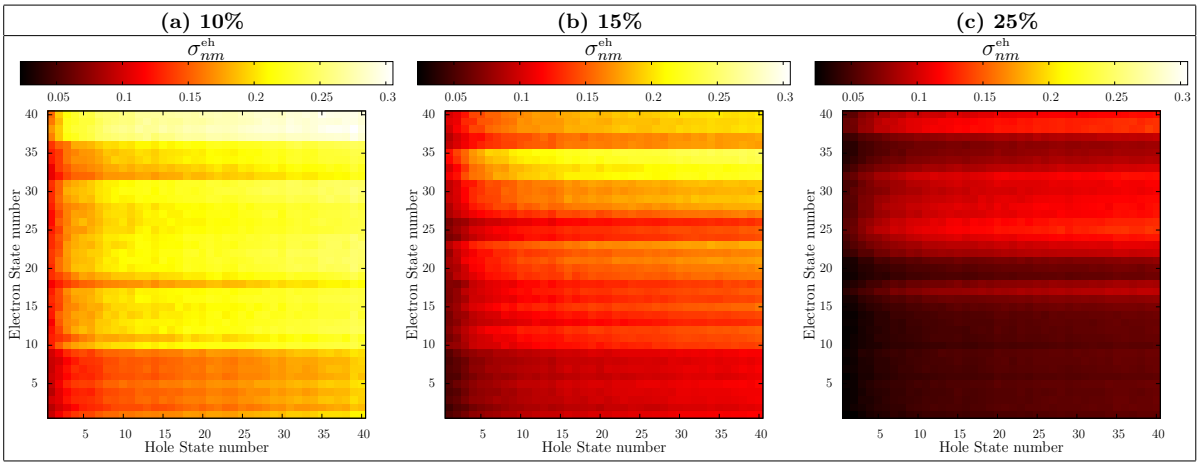

FIGURE 3.12: Modulus wave function overlaps of the 40 electron and hole states, in $In_xGa_{1-x}N/GaN$ quantum well systems averaged over 20 different microscopic configurations. The averaged overlaps are denoted by $\bar{\sigma}^{eh}_{nm}$. The data are shown for three different indium contents, 10%, 15% and 25%.

by well width and alloy fluctuations, which also increase with increasing indium content (from 10% to 25%), as shown earlier, will also contribute to an increasing reduction in overlap. This finding is consistent with previous experimental studies on InGaN/GaN QWs, wherein the internal quantum efficiency decreases rapidly with increasing indium content for long emmission wavelengths [108]. However, our data indicates also that when looking at σ^{eh}_{nm} for a fixed indium content, the modulus overlap is state number dependent and increases in general with increasing state number. For instance, when looking at the electron ground state, $n = 1$, in the in 10% In case, we find a low σ^{eh}_{1m} value for hole states with $m < 5$, while the value is clearly larger when $m > 35$. This indicates a more efficient radiative recombination rate for transitions involving the electron ground states and excited hole states. We attribute this behavior to the effect observed in Fig. 3.11, wherein regions of "delocalised hole states" are found.

3.5 Comparison With Experimental Data

To begin our theory-experiment correlation, we analyse the calculated average ground state transition energies and compare them with measured PL peak energies from the literature [26]. The data are summarised in Table 3.1. The here considered indium contents x are very close to the experimental values; however, we have kept the well width L constant, while in the experiment this quantity varies between the different samples. Nevertheless, the reported theoretical data is in good agreement with the experimental values, and given that our well width in general is larger than the experimental value, we slightly underestimate the PL peak energies.

Our theoretical findings on the nature of the localisation in these systems also support several experimental studies and their proposed explanations. For instance, the experimentally observed shift in the PL peak position with temperature, usually referred to as the "S-shape" dependence, is normally attributed to the existence of localised carriers in *c*-plane InGaN/GaN QWs. Based on our data we can conclude that localisation effects play not only a significant role in ground but also in excited hole states. This is even the case in *c*-plane InGaN/GaN QWs with as little as 10% indium. From our data we expect an energy range of order 100 meV over which there will be a significant density of localised valence states in *c*-plane InGaN/GaN QWs. This is consistent with the minimum energy ranges which can be inferred from the blue shift due to thermal redistribution amongst localised states in temperature dependent PL and electroluminescence (EL) experiments, which ranges from $55 - 200$ meV [16, 17] for different QW structures.

In addition to the "S-shape" dependence of the PL and EL spectra, time dependent PL spectra of *c*-plane InGaN/GaN QWs show non-exponential decay transitions and the measured decay times vary across the spectrum [19, 34]. An explanation for this behaviour has been put forward by Morel *et al.* [80], using a model of independently localised electron and hole wave functions. Under this assumption, Morel *et al.* [80] were able to achieve very good agreement between theoretical predictions and experimentally observed data. Our results support the assumption of individually localised carriers as demonstrated in Sec. 3.4.1. Furthermore, the fact that slower decay times are observed with decreasing detection energy [34], is consistent with the trends observed in Figs. 3.7 and 3.12, where hole localisation is seen to increase with increasing energy, and overlap with other hole states and conduction band states is seen to decrease with increasing hole energy. We show here that this behaviour is independent of the considered indium content, since even at 10% indium both electron and hole charge densities show indications of localisation effects. We have also shown in Ref. 44 that localisation effects and built-in fields dominate over Coulomb effects and thus a single-particle picture should already provide a reliable description of the localisation features in *c*-plane InGaN systems. It is important to note that the spatial separation between electron and hole wave functions is

	x	L (nm)	E_g (eV)
Exp	0.25	3.3	2.162
Calc	0.25	3.5	1.964
Exp	0.15	2.9	2.707
Calc	0.15	3.5	2.533
Exp	0.12	2.7	2.994
Calc	0.10	3.5	2.871

TABLE 3.1: Comparison between calculated average ground state transition energies (Calc) and experimental PL peak energies (Exp) obtained at low temperatures ($T = 6K$) in $In_xGa_{1-x}N$/GaN *c*-plane QWs [26]. The QW well width is denoted by L and the transition energies/PL peak position energies are given by E_g.

not only affected by the presence of the macroscopic built-in field but also by the localisation characteristics of the wave functions in the c-plane. Thus, while in a continuum based c-plane QW description, dipole matrix elements are determined by the spatial separation along the growth direction only, in our atomistic calculation the relative position of the electron and hole wave functions within the c-plane also plays an important role. As the relative in-plane positions of electrons and holes change as a function of the configuration [cf. Figs. 3.3 - 3.5] the dipole matrix elements will change between different configurations, as demonstrated in Ref. 44. This behaviour is consistent with the non-exponential PL decay curves and the variation of decay time across the spectrum.

3.6 Conclusions

In summary, we have presented a detailed analysis of the electronic structure of c-plane $In_xGa_{1-x}N$/GaN QWs with indium contents of $x = 0.1$, 0.15 and 0.25, covering the experimentally relevant range. To perform this analysis we have used a fully atomistic description, including local alloy, strain and built-in field variations arising from random alloy fluctuations. In addition to going beyond the usually applied continuum-based description for these systems, we give insight into not only ground state properties but also excited state properties.

From our analysis we conclude that for as little as 10% indium in the QW, the valence band structure is strongly affected by localisation effects. Our results indicate that well width fluctuations could lead to electron wave function localisation effects in addition to localisation effects introduced by random alloy fluctuations. These observations hold not only for ground states but also for excited states. From an initial estimate of our data, we conclude that even at 10% indium in the well, we are left with an energy range of order 100 meV into the valence band that should be dominated by strongly localised states. Our data also indicate that this energy range increases with increasing indium content. Experimental data, such as the "S-shape" dependence of the PL peak position with temperature gives clear experimental evidence of the presence of such (excited) localised states. Our theoretical findings are therefore consistent with experimental observations.

Moreover, by looking at (modulus) wave function overlaps between the first 40 hole or electron states, we gained initial insights into the probability of transferring carriers from one site/state to another. Our investigations indicated different regimes ranging from strongly "localised states" up to "delocalised states". While the localised states have very little overlap with all other states, the delocalised states reveal a high overlap with most of the other considered states. These features are relevant for experimental studies at ambient temperature and transport properties. In particular, the strong hole wave function localisation should affect the hole transport in c-plane InGaN-based multi-QW LEDs significantly. The observed localisation

effects will impact both the vertical transport along the c-axis through the different QWs, and also the lateral transport and thus how the carriers spread within the growth plane of the QW. Thus, these localisation features are relevant in general for InGaN-based devices operating at room temperature and above. The obtained data will now form the basis for more detailed transport and in general device-related calculations.

Finally, our theoretical study showed that built-in field, random alloy and well width fluctuations lead to the situation of independently localised electron and hole wave functions in c-plane InGan/GaN QWs. This holds for as little as 10% indium in the QW. This finding is consistent with the "pseudo 2-D donor-acceptor pair" model proposed by Morel *et al.* [80] to explain time resolved PL measurements of c-plane InGaN/GaN QWs.

Chapter 4

Electronic properties of m-plane InGaN/GaN Quantum Wells

Having discussed c-plane systems in the previous chapter, we turn now and present here a detailed atomistic analysis of the electronic properties of m-plane InGaN/GaN QWs. To achieve a microscopic description of these systems, we apply the tight-binding model introduced in Chapter 3 to treat realistically sized systems atomistically (supercells with ∼82,000 atoms), accounting for compositional and structural inhomogeneities in the absence of the built-in field. Local variation in strain and built-in potential arising from random alloy fluctuations are explicitly included in the model. Many energy states of the supercells considered are calculated in order to determine the impact of the alloy fluctuations on the electronic structure of the system under investigation. Similar to the c-plane situation, we find that while the electrons are relatively insensitive to the local indium environment, the hole states are highly sensitive to it and are subject to very strong localisation effects. These effects persist over an energy range of order 100 meV into the valence band. This strong localisation of the hole states leads to a very broad distribution of ground state energies in different random configurations. Again, we see that the localisation leads to poor overlap between different hole states resulting in a reduced probability of transfer of carriers between different states; this feature should play an important role for transport properties in m-plane InGaN/GaN QWs. To obtain a closer comparison with experiment, excitonic properties are calculated within the configuration interaction scheme. In agreement with experiment, and in contrast to the single particle picture which neglects Coulomb effects, these show that the electron wavefunction localises about the hole wavefunction due to the Coulomb interaction. In addition, the calculated photoluminescence spectrum elucidates the impact of alloy fluctuations on the optical properties.

4.1 Introduction

As discussed in the previous chapter, QWs based on InGaN alloys have applications in highly efficient light emitting devices. To attain three colour LEDs and thus an all-LED white light source, the emission wavelength in these devices must be shifted from blue to green. However, the addition of indium to tune the emission to the desirable green/yellow spectral region introduces a number of phenomena whose deleterious effects on efficiency inhibit the successful realisation of such devices. One consequence of adding indium is that the strain dependent piezoelectric polarisation field is strongly increased in c-plane InGaN QWs. As we have seen in Chapter 4, this built-in field draws the electrons and holes to opposite surfaces of the QW. The resulting spatial separation of electron and hole wave functions leads to a reduced radiative recombination rate and thus to reduced device efficiency [109]. Since these built-in fields are due to the inherent properties of c-plane growth, recent research has been directed towards growth along different crystallographic directions in order to mitigate these effects [110, 111]. When grown on a plane perpendicular to the c-plane, such as the m-plane, the built-in field would be, ideally, completely removed [112]. Furthermore, these non-polar InGaN QWs possess the potential to act as efficient sources of light with a high degree of optical linear polarisation [113] (DOLP). This has valuable applications such as back-lit liquid crystal displays [36], where the ability to control polarisation would result in power savings of up to 50% [2].

Despite the recent interest in non-polar m-plane InGaN QWs and the promising applications they offer, the impact of random alloy fluctuations on their electronic, optical and transport properties has received little attention. Previous theoretical work has treated mainly c-plane InGaN QWs, and mostly using modified continuum approaches [48, 81], which account for compositional fluctuations by . While these methods do demonstrate the localisation produced by random alloy effects, they do not fully elucidate their fundamentally atomistic origin. DFT studies [45, 100, 114] undertaken on small bulk systems have shown the importance of In-N-In-N chains in localising the hole states. As highlighted in the previous chapter, while these DFT studies are capable of analysing atomistic effects, the method is too computationally expensive to study full QW systems, where the interplay of atomistic and larger scale inhomogeneities may be important, nor do they provide information about the distribution of localised states.

We present here the results of the tight binding (TB) model introduced in the previous chapter, capable of describing realistically sized InGaN/GaN QWs on an atomistic scale, explicitly including local alloy, strain and built-in potential fluctuations [44, 66]. The model is therefore ideally suited to study the physics of m-plane InGaN/GaN QW systems. To analyse the impact of the alloy fluctuations, not just ground states but several excited states are calculated. Coulomb effects are included via the configuration interaction [44, 115] (CI) scheme based on the calculated single particle electron and hole wave functions.

Overall, the atomistic analysis presented here indicates that random alloy effects play a significant role in the determination of the system attributes of InGaN/GaN m-plane QWs. We find that in particular the hole states are strongly influenced by the potential fluctuations introduced by the randomness of the indium distribution. The results show very strong hole ground state as well as excited state localisation whilst the single-particle electron states are only weakly affected by the fluctuations. This localisation of the hole states is shown also to lead to poor wave function overlap between different hole states, hindering therefore the hole carrier mobility. The hole localisation is found to persist for several states into the valence band of the supercells considered, and a first estimation of the energy ranges over which these states are localised is obtained from the data. The inclusion of the Coulomb interaction between electrons and holes reveals that electron wave functions localise about the hole wave functions, resulting in localised excitons. This is consistent with the experimentally observed single-exponential decay transients in m-plane QWs [34]. Results of the CI calculations show very good agreement with PL measurements performed by Manchester (Dawson's group) on m-plane samples from Cambridge (Humphrey's and Oliver's groups), [116] and the theoretical results elucidate the origin of the different features in the optical spectra. In summary, this analysis provides a clear picture of the impact of alloy fluctuations on m-plane InGaN/GaN QWs and serves as a base from which to launch further investigations.

The chapter is organised as follows. The details of the theoretical framework used to calculate the wave functions, energies and system attributes are given in Section 4.2. Our results are then presented in section 4.3 and broken into two subsections, the ground states in Section 4.3.1 and the excited states in Section 4.3.2. Further calculations are then provided for the purposes of direct comparison to experiment in Section 4.3.3. Finally we summarise our results and conclude in Section 4.4.

The work in this chapter comes from two papers, ref. [117] and ref. [116]. My contribution to these works was the generation and relaxation of the supercells, as well as the calculation of the single-particle states from the tight binding Hamiltonian, and the subsequent analysis of these single particle states. Stefan Schulz performed all CI calculations, and all post-analysis on the CI wavefunctions and energies (excitonic binding energies, charge densities of correlated wave functions, photoluminescence spectra).

4.2 Theoretical framework and model QW system

As mentioned above, in order to determine the electronic and optical properties of m-plane InGaN-based QWs, we use the same atomistic TB model presented in Chapter 3. On top of this, for the purposes of comparison with experiment, Coulomb interactions have been included via the CI scheme. The details of the CI calculations have been previously presented [44].

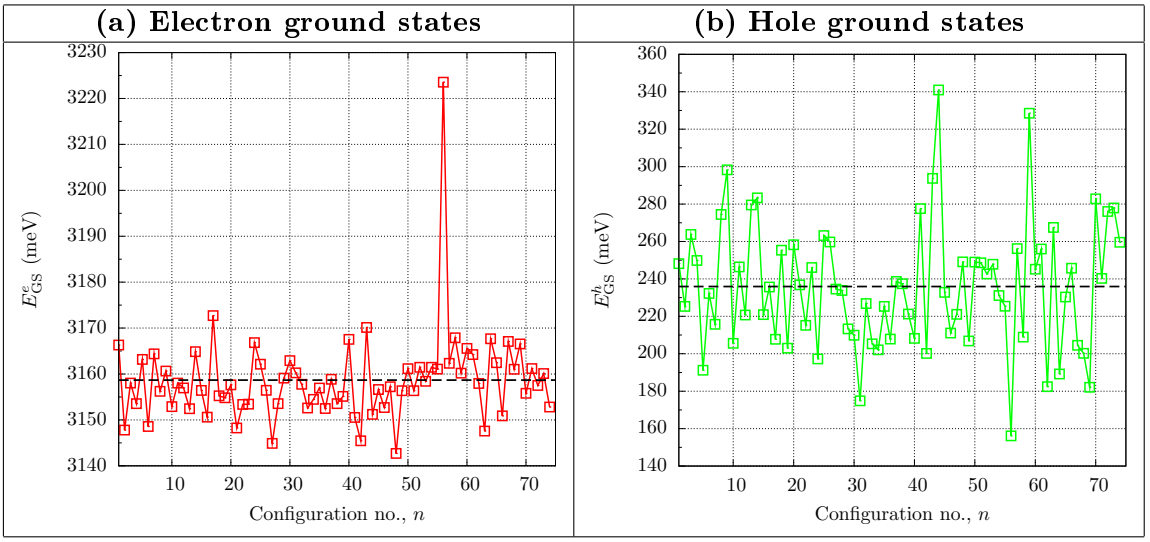

FIGURE 4.1: Ground state energies for (a) electrons and (b) holes as a function of the configuration number n. The horizontal dashed lines indicate the average energies.

The QW to which we apply this theoretical framework has been characterised experimentally by the groups of Prof. P. Dawson (Manchester), Sir Prof. C. J. Humphreys and Dr. R. A. Olver (Cambridge); more details on the experimental results are given in Ref. [116]. Building on the experimental data, we assume an indium content of 17%, and a well width of 2 nm, with disk-like well width fluctuations. The well width fluctuations are of base diameter 5 nm and two monolayers in height. For each calculation the indium atoms are randomly distributed on the cation sites in the QW region. The calculations have been repeated 75 times to realise different microscopic arrangements of the atoms. The supercell contains approximately 82,000 atoms corresponding to a supercell size of 10 nm $\times$ 9 nm $\times$ 10 nm.

4.3 Results

Having introduced the theoretical framework we present in the following the results of our calculations. In a first step, in Sec. 4.3.1, we discuss ground state properties before turning to the excited states in Sec. 4.3.2. Section 4.3.3 is dedicated to a theory experiment comparison.

4.3.1 Ground State Properties

As a first quantitative demonstration of the effect of alloy fluctuations on the electronic structure of the considered m-plane system, Fig. 4.1 shows the ground state energies of electrons and holes as a function of the (microscopic) configuration n. In Fig 4.1 (a) the electron ground state energies are shown while in (b) the results for hole ground state energies are given. The dashed lines indicate the average ground state energies. For the electrons we find an average

ground state energy of 3159 meV and for the holes it is 236 meV, where the unstrained bulk GaN valence band edge is the energy reference. A schematic illustration of the band edge diagram is given in Fig. 4.2. The standard deviation, σ, indicates the impact random alloy fluctuations have on the electron or hole ground states. We calculate that the hole states are considerably more sensitive to the fluctuations, having a standard deviation of $\sigma^h = 34$ meV compared to $\sigma^e = 10$ meV for the electrons. This increased sensitivity of the hole states to potential fluctuations caused by the random alloy has been reported before in alloyed bulk [29] and QW systems (see previous chapter and refs. [44, 48]). Similar to our c-plane analysis, these strong variations lead to a broadening of the resulting single-particle transition energies (shown in Fig. 4.5), which is consistent with the large experimentally observed linewidths of PL spectra of m-plane QWs [116, 118]. We will return to this feature in Sec. 4.3.3.

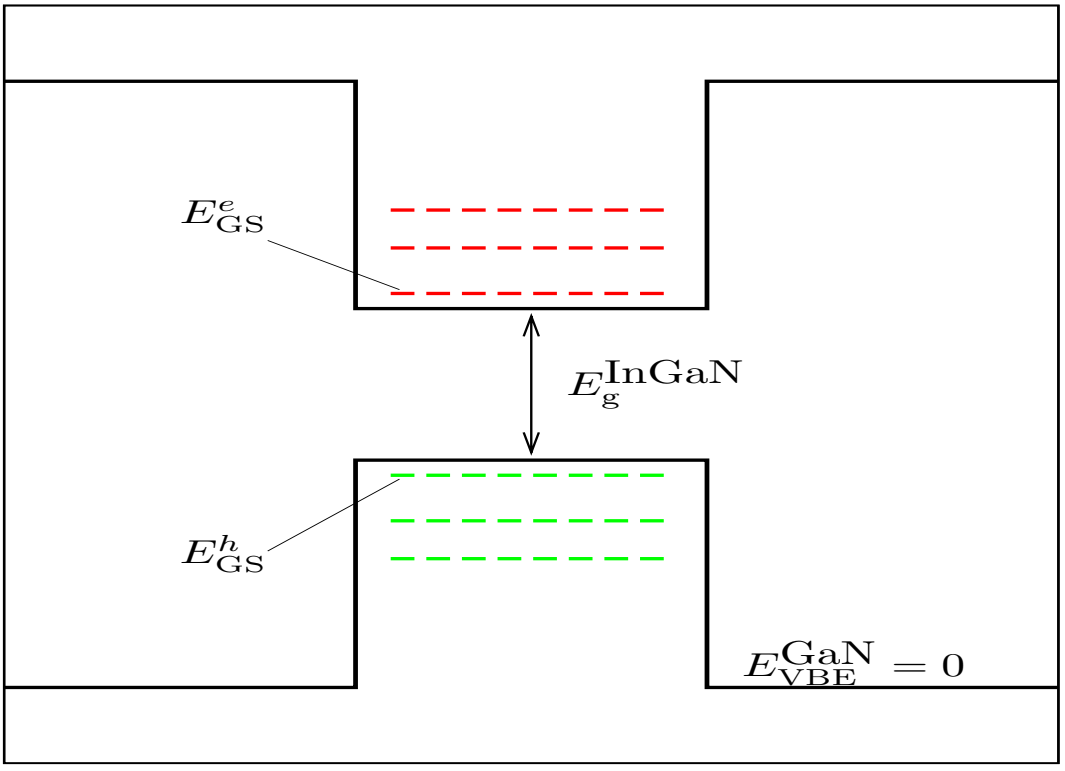

FIGURE 4.2: Schematic band edge diagram along the m-axis of an ideal QW, neglecting potential variations due to fluctuations in the local indium content. The reference energy is the VBE of the barrier material GaN ($E_{\mathrm{VBE}}^{\mathrm{GaN}} = 0$). The ground state energies of electron and hole are denoted by E^e_{GS} and E^h_{GS}, respectively. The band gap of the InGaN QW is denoted by E_g^{InGaN}.

This variance of the ground state energies shows that the electronic and optical properties of m-plane systems are indeed sensitive to the alloy fluctuations present. The particular manner in which the electrons and holes are affected by the alloy fluctuations can be ascertained through an examination of the ground state wave functions. Figure 4.3 displays the isosurfaces

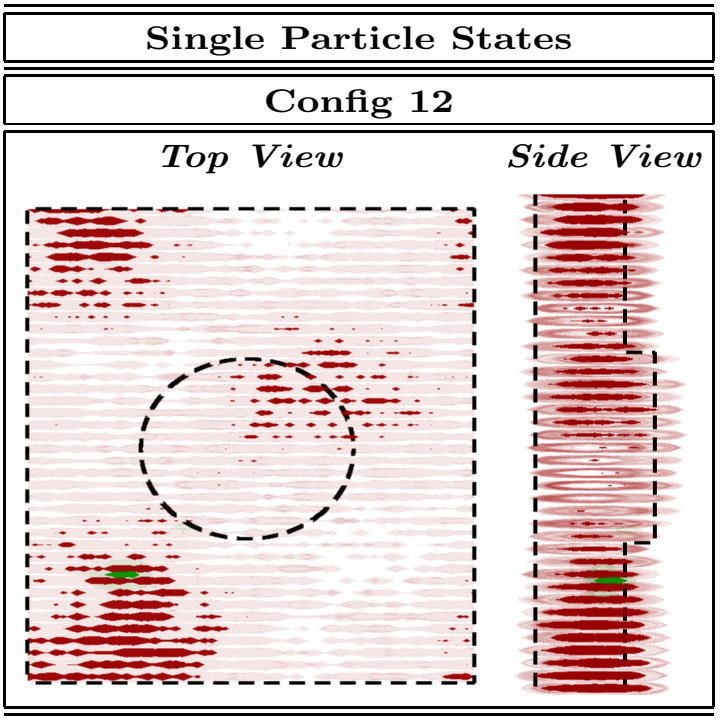

FIGURE 4.3: Isosurface plots of the electron and hole ground state charge densities in the m-plane quantum well of configuration n=12. Configuration 12 is chosen because the electron and hole ground state energies are close to the configurational averages. Isosurfaces of electron ground state charge densities are given in red and the hole ground state charge densities are coloured green. The dark (light) isosurfaces correspond to 25% (5%) of the maximum charge density.

of ground state electron and hole charge densities of configuration $n = 12$. We have chosen this configuration because it represents an average configuration in terms of electron and hole ground state energies (cf. Fig. 4.1). The 'Top View' is a view from a direction parallel to the m-plane axis, looking down on the quantum well. This view shows the lateral distribution of charge densities. The 'Side View' is a view from a direction perpendicular to that of the m-axis and shows the distribution of charge densities along the growth direction in the QW region. Isosurfaces of electron ground state charge densities are given in red while the hole ground state charge densities are coloured green. The dark (light) isosurfaces correspond to 25% (5%) of the maximum charge density. Figure 4.3 serves as a visual indication of the heightened sensitivity of the hole states, when compared to the electron states, to alloy fluctuations. The hole state is strongly localised both laterally and vertically in a small region of the QW. The electron charge density, however, is only slightly affected by the alloy fluctuations, resulting therefore in a situation where the electron wave function is spread out over the entire QW region. This asymmetry is consistent with DFT and empirical pseudopotential calculations on bulk systems [29, 114] and also in general with results on c-plane systems (cf. Chapter 3 and refs. [44, 48]). However, the main difference to c-plane systems is the absence here of the macroscopic built-in field, which creates further localisation for the c-plane electrons and holes.

While these results are consistent with most experimental anlyses of m-plane InGaN QWs, we note that the picture of localised hole states and delocalised electron states is not compatible with the experimentally observed single exponential decay times observed in PL spectra of m-plane QWs [34, 116]. This differs from the case of c-plane QWs where time-dependent PL studies show decay times that vary across the PL spectrum, consistently with the picture of individually localised electrons and holes, as discussed in Chapter 3. This is due to the increased importance of Coulomb interactions between electrons and holes in m-plane systems.

To include Coulombic effects we use the CI scheme described in detail in Ref. [44]. We consider here only a single electron hole pair. Thus, electron-electron and hole-hole Coulomb interactions are not included. We neglect electron-hole exchange contributions since these are small corrections on the energy scale relevant for the discussion of our results. To describe the excitonic many-body wave function we include 5 electron and 15 hole states in the CI expansion.

To visualise the electron and hole densities under the influence of the Coulomb interaction, we use reduced electron and hole density matrices. In general, the excitonic many-body wave function $|\psi^X\rangle$ can be written as a *linear combination* of electron-hole basis states:

$$|\psi^X\rangle = \sum_{i,j} c_{ij}^X \hat{e}_i^\dagger \hat{h}_j^\dagger |0\rangle \,. \tag{4.1}$$

Here $|0\rangle$ is the vacuum state, c_{ij}^X the expansion coefficient and $\hat{e}_i^\dagger$ ($\hat{h}_i^\dagger$) denotes the electron (hole) creation operator. Electron and hole states are denoted by i and j, respectively. We can then define reduced density matrices for electrons and holes. For instance, for the electrons the density operator $\hat{\rho}^e$ is given by:

$$\hat{\rho}^e = \sum_{i,i'} |i\rangle \sum_j c_{ij}^X c_{i'j}^{X*} \langle i'| = \sum_{i,i'} |i\rangle \rho_{ii'}^e \langle i'| \,. \tag{4.2}$$

The corresponding electron and hole densities are given by $\rho^e = \langle R|\hat{\rho}^e|R\rangle$ and $\rho^h = \langle R|\hat{\rho}^h|R\rangle$, respectively. The right side of Fig. 4.4 depicts the calculated electron ρ^e and hole ρ^h densities for the configurations 5, 20 and 75.

The effect of including the Coulomb interaction between electrons and holes is shown by comparing in Fig. 4.4, the single particle charge densities on the left (without Coulomb), with the CI charge densities on the right (with Coulomb). From Fig. 4.4 we see that, compared to the single particle description, the hole charge density is not changed in any immediately appreciable manner, but that the electron charge density is significantly affected by the attractive Coulomb interaction with the holes. For each configuration, we see that the electron is drawn to the hole state and localised about it. This localisation of the electron state about the hole state also occurs for all other configurations. This exciton localisation is consistent with the single exponential decays observed in PL studies [116].

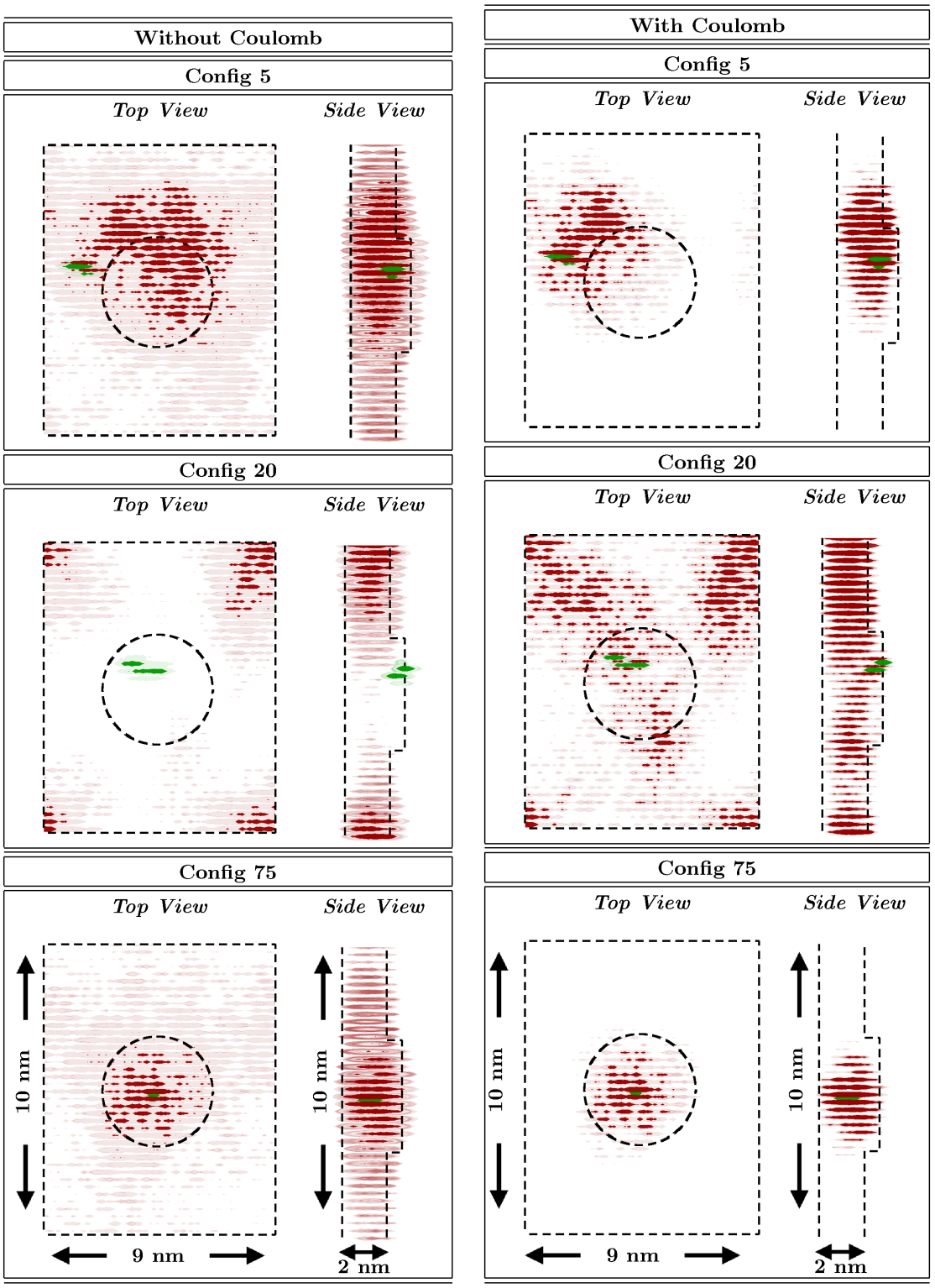

FIGURE 4.4: Ground state electron (red) and hole (green) charge densities with (right) and without (left) Coulomb effects included for configurations 5 (Config 5), 20 (Config 20) and 75 (Config 75). Results are shown for different view points. Light (dark) isosurfaces correspond to 5% (25%) of the maximum charge density value. Dashed lines indicate the QW interfaces.

The impact of the Coulomb interaction on the transition energies is shown in Fig. 4.5. The figure shows that the Coulomb effects result in a shift in the average transition energy, as well

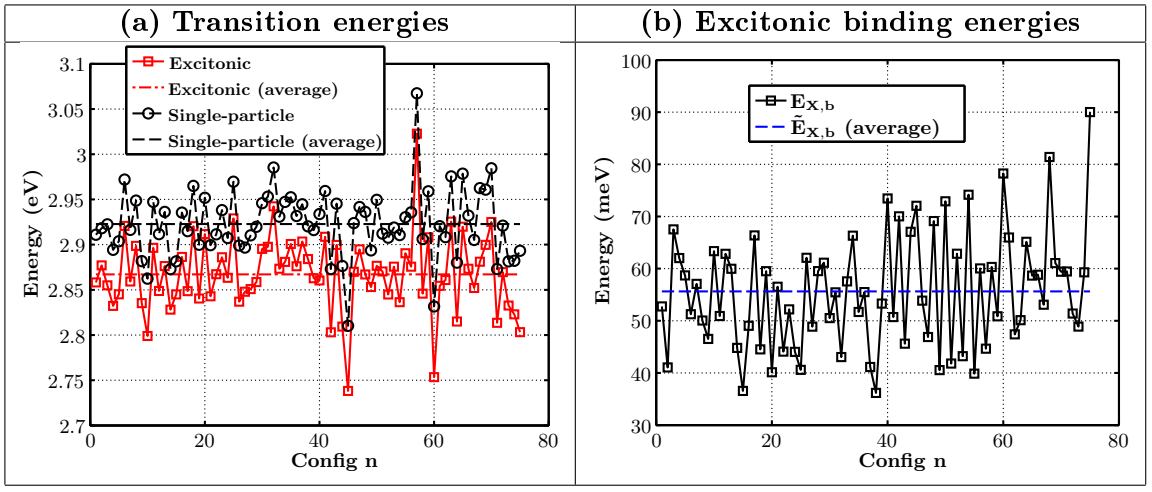

FIGURE 4.5: (a) Single-particle (black circles) and excitonic (red squares) groundstate transition energies as a function of the configuration number, n. The average transition energies are indicated in each case by a dashed line the same colour as the points. (b) Excitonic binding energy, $E_{X,b}$, as a function of the configuration number. The excitonic binding energy is caluclated as the difference between Coulombic and non-Coulombic groundstate transition energies.

as a broadening of the spectrum. The average single-particle transition energy is 2.93 eV whilst the average excitonic transition energy is 2.87 eV, giving an average binding energy of 56 meV. The fluctuations in the binding energies seen in Fig. 4.5 can be understood by reference to the single particle wave functions of Fig. 4.4. Taking configuration 20 as an example, we see that the electron wave function has very little overlap with the hole wave function, compared to the electron-hole overlaps of configurations 5 and 75. This leads to a lower exciton binding energy. Configuration 75, on the other hand, exhibits a very good electron hole overlap in the single particle picture, and from this one would expect a large binding energy, and looking at Fig. 4.5 we see that this is the case. A situation of intermediate single-particle overlap is exhibitted in configuration 5, and we thus expect an intermediate binding energy, which is affirmed in Fig. 4.5. We find it to be generally true that the excitonic binding energies are much higher in m-plane QWs than c-plane QWs [44].

While Figs 4.3 and 4.4 give a first visual impression of localisation effects, to measure the localisation of different states more quantitatively, we utilise the metric of the inverse participation ratio (IPR) [102]. This is defined in Chapter 3 in eq. (3.6). In what follows we focus on the localisation characteristics of single-particle states, and pay particular attention to the hole states. This is justified by the fact that, even in the many-body picture, it is the spatial extent of the single-particle hole states that sets the limit for how localised the many body will be.

Instead of plotting the IPR values with respect to the configuration number, n, we show the data now as a function of the ground state energy. The results of our analysis are depicted in Fig. 4.6. Here, we normalise the IPR values with respect to the average electron ground state IPR value. We will denote these renormalised IPR values by $\widetilde{\text{IPR}}$. This renormalisation allows

direct comparison between the localisation of these states and that of the electron wavefunction in Fig. 4.3, which was chosen on the basis that it had the closest IPR of all electron states to the average. Thus a state with a $\widetilde{\text{IPR}}$ value of one will have the same spatial extent as the electron wavefunction shown in Fig. 4.3, a state with a $\widetilde{\text{IPR}}$ value of 5 will be 5 times more localised and thus occupy a fifth of the space occupied by the reference wavefunction. The electron $\widetilde{\text{IPR}}$ values are shown in Fig. 4.6 (a). Due to the very high groundstate energy in configuration 56, cf. Fig. 4.1 (a), it is difficult to extract trends from Fig. 4.6 (a). Therefore, the inset focuses on a reduced energy range, neglecting configuration 56. The $\widetilde{\text{IPR}}$ values for the hole ground states as a function of the energy are displayed in Fig. 4.6 (b).

On comparing Fig. 4.6 (a) and (b) one sees that the particular asymmetry of localisation strength between electrons and holes evidenced in Fig. 4.3 is reflected generally in differences in the magnitudes of the electron and hole $\widetilde{\text{IPR}}$ values for all configurations. Therefore, the charge densities depicted in Fig. 4.3 reflect the general properties of the localisation characteristics in the here considered m-plane QW system. More specifically, from Fig. 4.6 one can infer that the hole ground states can be to 650 times more localised than the average electron ground state. Discernible also in Fig. 4.6 (b) is a trend of increasing $\widetilde{\text{IPR}}$ with increasing energy. This is due to the fact that the mechanism of localisation is that of potential energy fluctuations. An indium rich region corresponds to an energetically favourable region in which a carrier becomes localised. A higher indium content leads to a deeper potential fluctuation and a more localised carrier. So for the hole states increasing energy should lead to a stronger localisation effect and therefore a larger $\widetilde{\text{IPR}}$ value. On average the data in Fig. 4.6 (b) bears out this trend. For the electron states one expects that with decreasing ground state energy the $\widetilde{\text{IPR}}$ value should

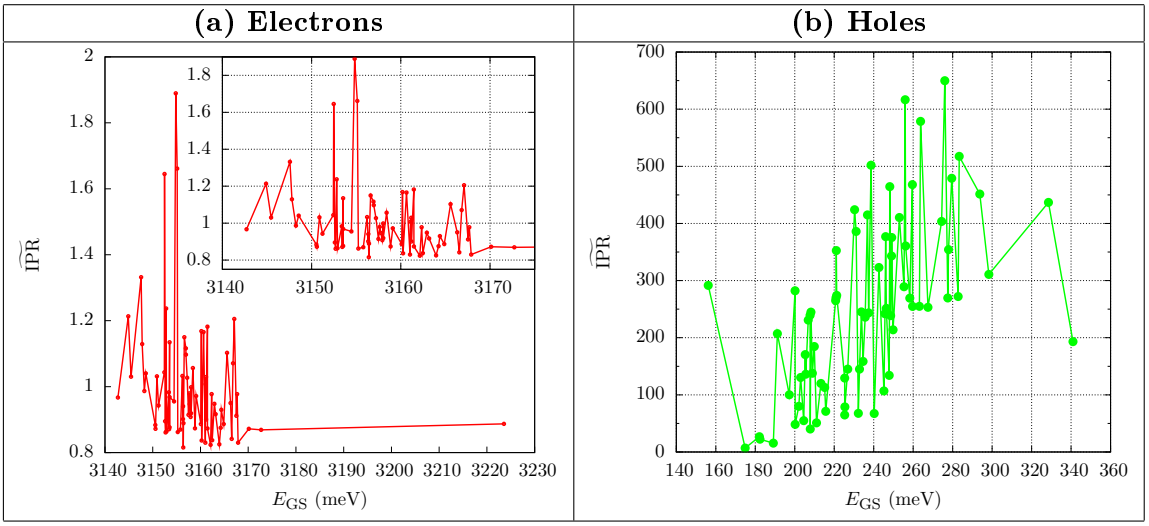

FIGURE 4.6: (a) Electron and (b) hole ground state relative inverse participation ratios (IPRs) plotted as a function of the ground state energy for the 75 different microscopic configurations considered. The IPRs are normalised (denoted by $\widetilde{\ }$) to the average electron groundstate IPR which describes a wavefunction with the same localisation characteristics as the electron wave function in Fig. 4.3.

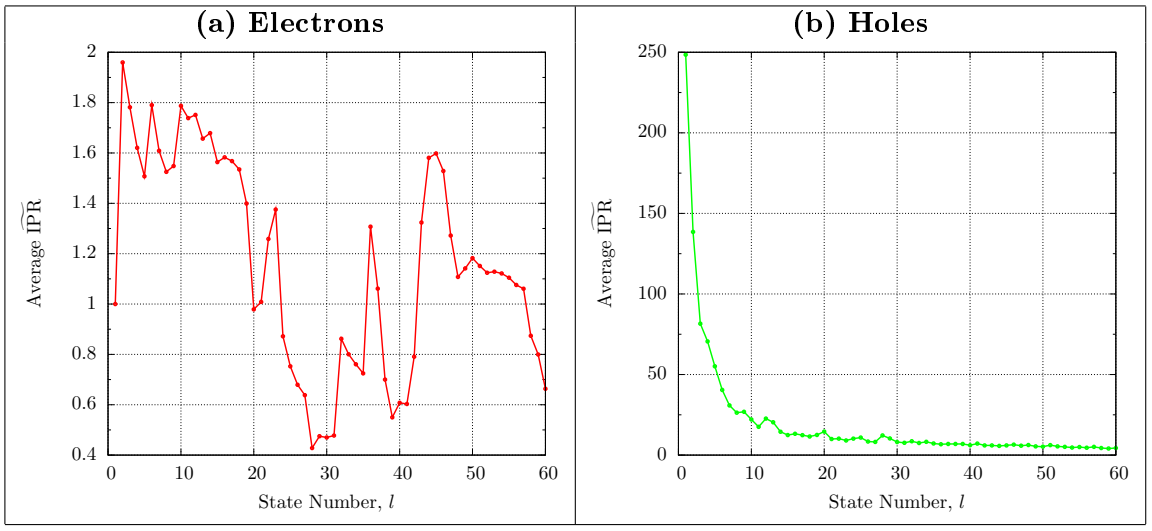

FIGURE 4.7: Average inverse participation ratio values for the first 60 (a) electron and (b) hole states. The data is normalised to the average inverse participation ratio of the electron ground states.

increase. However, one needs to keep in mind that electron ground state wave functions and energies (cf. Figs. 4.1 and 4.3), are far less affected by alloy fluctuations. From the inset of Fig. 4.6 (a) we find in general that the trend is indeed of increasing $\widetilde{\text{IPR}}$ with decreasing energy, though less marked than in the hole case, as expected from the above discussion.

Having studied the ground state properties we turn now to analyse the localisation characteristics of the excited states. This study will elucidate the extent to which alloy fluctuations affect these excited states. This allows the determination of whether these states, too, are localised, or if they could be described with a continuum picture.

4.3.2 Excited State Properties

To study the impact of random alloy fluctuations on the localisation characteristics of the excited states, Fig. 4.7 shows the $\widetilde{\text{IPR}}$ values of the first 60 electron and hole states averaged over the 75 microscopic configurations. The results for electrons are shown in Fig. 4.7 (a) while (b) displays the data for holes. Again, a striking difference between electron and hole localisation effects is that, consistent with our analysis of the ground states, the holes are in general far more localised than the electrons. Additionally, one can infer from Fig. 4.7 that the hole states maintain this higher degree of localisation deep into the valence band, i.e. to higher state numbers. Consequently, when performing experiments at elevated temperatures, localisation effects in the valence band should still be important.

There is also a marked difference between electrons and holes when studying how the $\widetilde{\text{IPR}}$ values change with increasing state number. We see that while the holes become gradually and monotonically less localised with increasing state number, the $\widetilde{\text{IPR}}$s of the electrons show an

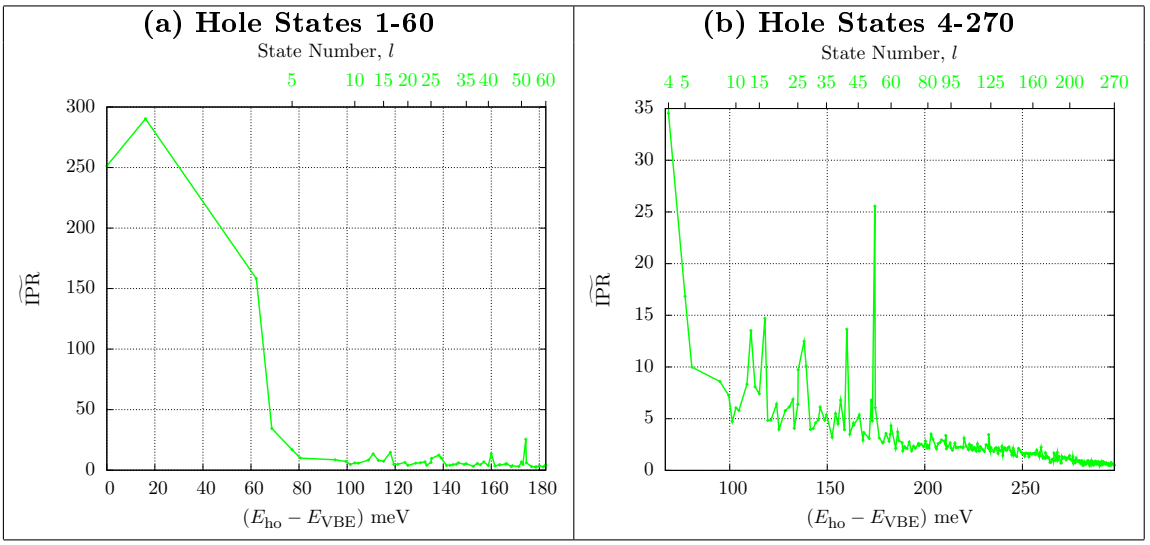

FIGURE 4.8: Normalised hole inverse participation ratio values ($\widetilde{\text{IPR}}$) as function of the energy measured with respect to the valence band edge (hole ground state energy E_{VBE}) for configuration $n = 12$. (a) Full spectrum for 60 hole states considered; (b) Same spectrum as in (a) but this time for states with state numbers larger than three.

almost flat behaviour. The dip in the $\widetilde{\text{IPR}}$ values for electrons around state 28 is due to the fact that here the electron energy is larger than the energy of the unstrained GaN conduction band edge, resulting in a spreading of the wave function into the GaN barrier material. Given that the behaviour of the electrons can be understood, to a first approximation, by a continuum-based QW description, we focus our analysis of excited state properties solely on the hole states.

To obtain an estimation of the energy range over which localisation persists in the valence band, we draw now upon a similar argument to that made in sec. 3.4.2 of Chapter 3. A mobility edge can be expected at a well-defined energy, E_{mob}, in the valence band of an infinite system, which separates localised states above E_{mob} from delocalised states below the edge. It is not however possible to directly identify such an energy in the finite systems considered here. Firstly, because of finite size effects, there is no clear transition point in the data in Fig. 4.7 (or Fig. 4.8, discussed further below) which can be chosen to definitively separate localised and delocalised states. In addition, it can be seen from Fig. 4.6 that the hole ground state energy varies by over 100 meV between different random configurations of indium atoms in the 82,000-atom supercells considered. Hence states at a given energy may be localised in one supercell, but delocalised in another supercell. The average $\widetilde{\text{IPR}}$ values of the hole states, shown in Fig. 4.7 (b), reveal strong hole localisation of many excited states. While these *average* values give a first indication of the general decay of the localisation of the hole states, they do not indicate the energy ranges over which this decay occurs. Since the energy of a given state fluctuates between different microscopic configurations, we cannot directly plot the average $\widetilde{\text{IPR}}$ values against energy. For further studies we have therefore chosen a particular configuration

close to the average behaviour observed in Fig. 4.7. Consequently, we are now able to visualise the dependence of the $\widetilde{\text{IPR}}$ values on energy instead of state number. Here we have chosen configuration $n = 12$ and the $\widetilde{\text{IPR}}$ values are displayed in Fig. 4.8 as a function of the energy. The energy is measured relative to the valence band edge (hole ground state energy) of this configuration. Similar to Fig. 4.7, we have taken 60 hole states into consideration. Due to the large differences in magnitude between the $\widetilde{\text{IPR}}$s of the first four states, and those for all subsequent states, Fig. 4.8 (b) shows the data for only those states above the fourth. This allows for a closer examination of the behaviour of these states in terms of $\widetilde{\text{IPR}}$ values and energy separation. Please note that configuration $n = 12$ has also been used for the visualisation of the hole ground state charge densities depicted in Fig. 4.3, allowing one therefore to connect the calculated high $\widetilde{\text{IPR}}$ value of the ground state with an illustration of the spatial extent of its wave function. From Fig. 4.8, one can infer strong localisation of the states within 60 meV of the valence band edge in this configuration, with evidence of some other states being highly localised at energies which are over 150 meV below the highest valence state. We note in addition from Fig. 4.6 that there is a spread of about 100 meV between the calculated ground state energy in the different supercells considered. Thus, based on the results presented in Figs. 4.6 to 4.8, we conclude that there will be a broad energy range ($>\sim$ 100 meV) over which there will be a significant density of localised valence states in m-plane InGaN QWs similar to those considered here.

Having discussed the localisation characteristics of the ground and excited hole states, we now introduce a second approach to analyse their localisation. As a metric we use again the *modulus* overlap of the wave functions of different states, introduced in Chapter 3, which is given in our TB formalism as:

$$\Omega_{lk} = \sum_{i}^{N} |\psi_{l,i}||\psi_{k,i}| \ . \tag{4.3}$$

Following Fig. 4.8, we start with the analysis of Ω_{lk} for configuration $n = 12$. The results for Ω_{lk} are displayed in Fig. 4.9 for again 60 hole states. From Fig. 4.9 we see that the strong localisation of the hole states observed in Fig. 4.8 is also reflected in the Ω_{lk} data. Evident in the plot is the very poor overlap of the first two hole states with most other hole states; these having Ω_{lk} values between 0.1 and 0.35. This will result in a scenario where it will be very unlikely for a hole in these states to move from one state to another through the material. We could therefore consider these states as 'strongly localised', given their high $\widetilde{\text{IPR}}$ values and their low overlaps with other states. Furthermore, we see that as the states become higher in energy, and therefore less localised (cf. Fig. 4.8), the overlap between different states increases on average. Transport involving these states becomes as a result more likely. Looking at the overlaps of states three and four reveal magnitudes between 0.3 and 0.5. For states beyond state five $\Omega_{lk} > 0.5$, so the carriers share more regions in common than they do not. Transfer will be therefore more likely between these states.

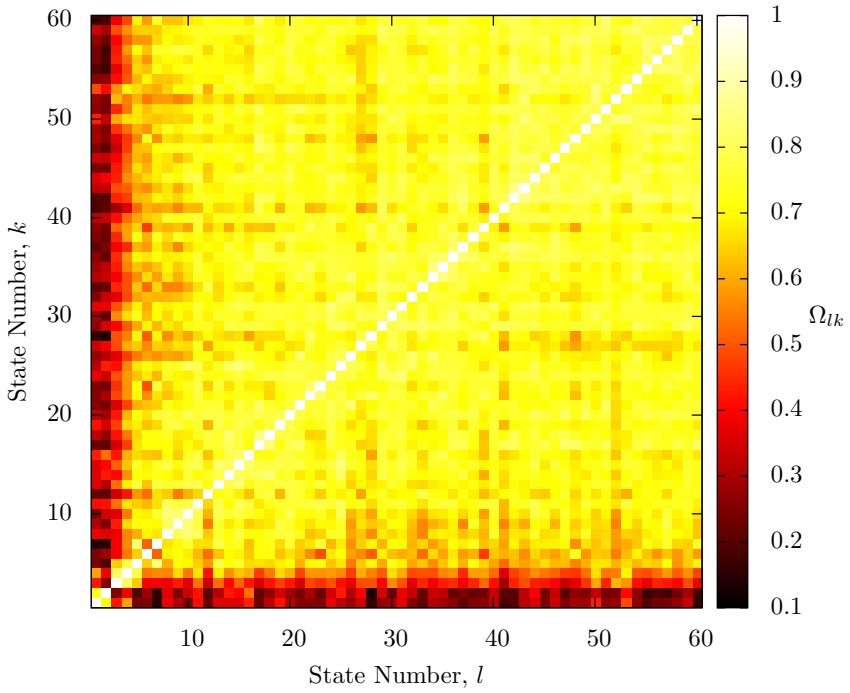

FIGURE 4.9: Modulus wave function overlap Ω_{lk} between the 60 highest hole states. The result is shown for the microscopic configuration $n = 12$.

In order to demonstrate the generality of these results and to show that the trends observed are not particular to configuration $n = 12$, Fig. 4.10 displays the modulus overlaps, $\bar{\Omega}_{lk}$, obtained via averaging over all configurations. We see reflected here in all configurations the behaviours observed in Fig. 4.9 for configuration $n = 12$. Notably, the different regimes of localisation are again apparent, but with smoother and softer profile. We find again a region of strong localisation, consisting of the first two states, with overlaps from below 0.2 to just above 0.3, followed by a transition region that includes on average the states 3 to 5, where $\bar{\Omega}_{lk}$ ranges from 0.35 to 0.5, and then the delocalised region, consisting of states with state numbers above 5 and overlaps in excess of 0.5.

Overall, further studies are now required to obtain a clearer picture and more stringent criteria to determine at which values of Ω one has a crossover from localised to delocalised states. It would be worthwhile target this in future studies and analysis, and examine also how localisation effects affect transport properties both in the vertical and in the lateral direction of the QW. This is beyond the scope of the present study.

Having discussed our theoretical findings and shown their consistency with and explanation of, the experimental results generally, we turn in the next section and make explicit comparison

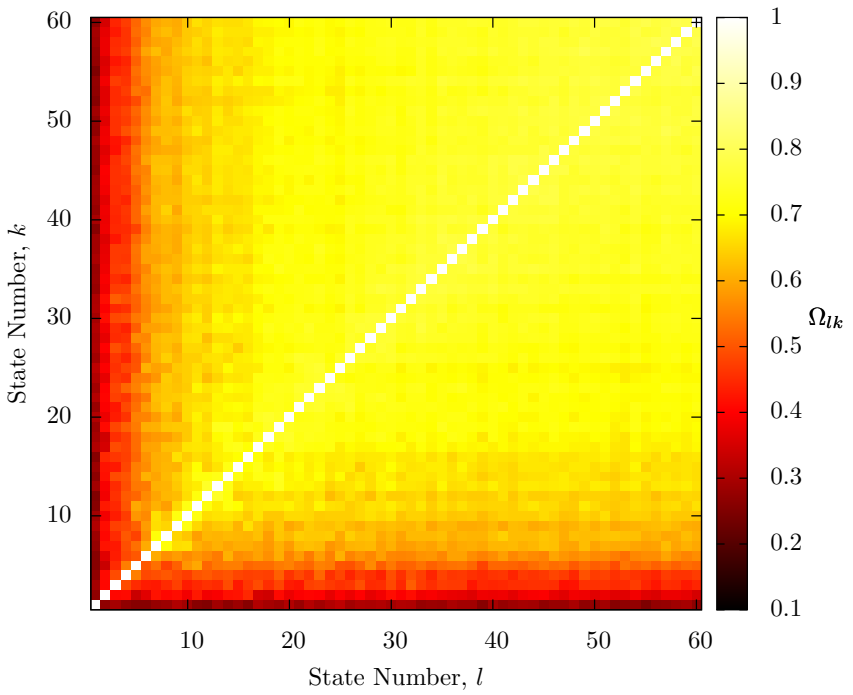

FIGURE 4.10: Average modulus wave function overlap $\bar{\Omega}_{lk}$ between the 60 highest hole states. The result shown here are averaged over the 75 microscopic configurations considered.

of these results with experimental data from Manchester and Cambridge [116]. Here, we make a direct comparison with experimental results by calculating the photoluminescence spectrum associated with our 75 configurations.

4.3.3 Comparison to experiment

To compare our results more closely with the experimental PL data, we have calculated the excitonic ground state emission spectrum. This is obtained via the evaluation of dipole transitions between the Coulomb-correlated states, using the methodolgy detailed in Ref. [44]. To investigate the large degree of linear polarisation ($> 90\%$) observed in the experimental PL [116], spectra are calculated for two different light polarisation vectors $\mathbf{e}_{p,i}$, i.e. $\mathbf{e}_{p,\perp} = (1,0,0)^T$ and $\mathbf{e}_{p,\parallel} = (0,0,1)^T$. This means that the selected electric field $\mathbf{E}$ is perpendicular to the c-axis ($\mathbf{e}_{p,\perp}$) and parallel to the c-axis ($\mathbf{e}_{p,\parallel}$), respectively. In the calculations we have assumed growth along the y-axis, therefore the chosen light polarisation vectors reflect the experimental set up described in detail in Ref. [116].

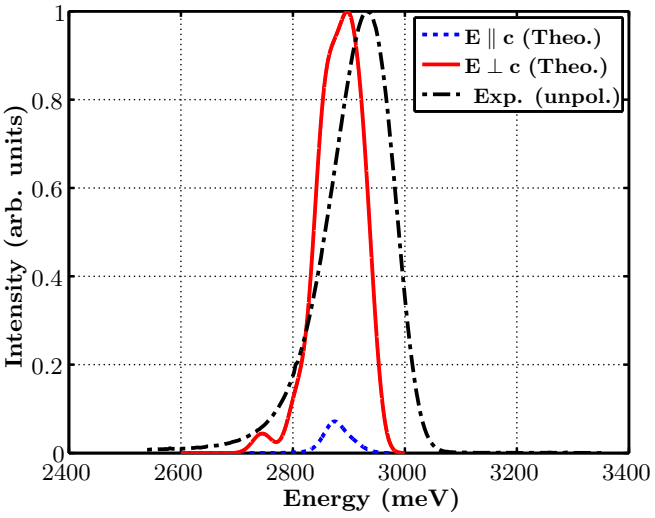

FIGURE 4.11: Calculated excitonic ground state emission spectrum with light polarisation vectors parallel ($\mathbf{E} \parallel c$) and perpendicular ($\mathbf{E} \perp c$) to the c-axis. The (black) dashed dotted line shows the experimental (unpolarised) PL spectrum.

The calculated excitonic ground state emission spectrum is shown in Fig. 4.11 for $\mathbf{e}_{p,\perp}$ (red solid line) and $\mathbf{e}_{p,\parallel}$ (blue dashed line) together with the experimental (unpolarised) PL emission spectrum (black dashed-dotted line). Several different features are visible in Fig. 4.11.

First of all we find good agreement between the calculated (solid red) and the experimentally determined emission energy (black dashed-dotted line), in particular, given the slight uncertainties in the experimental indium content and well width as discussed in Ref. [116].

Secondly, we find also theoretically a very broad emission spectrum. For $\mathbf{E} \perp c$ ($\mathbf{e}_{p,\perp}$), the theoretically determined full width at half maximum (FWHM) is 101 meV. The experimentally reported value for the FWHM is 135 meV [116]. Different factors might contribute to the observed differences between theory and experiment. For example, even though 75 different microscopic different structures may appear a large number, it could be the case that even more configurations have to be considered to fully resolve the measured FWHM, bearing in mind the large variations between different microscopic configurations (cf. Fig. 4.5). Additionally, if subtle non-random clustering effects exist, they may contribute to the broadening of the PL line width. However, the theoretically determined value of 101 meV for the FWHM is in reasonable agreement with the experimental data [116].

Thirdly, Fig. 4.11 shows that there is a large difference in the calculated intensities for $\mathbf{e}_{p,\perp}$ and $\mathbf{e}_{p,\parallel}$. In the theoretical analysis, the intensities are normalised to the intensity of $\mathbf{e}_{p,\perp}$. We may calculate the degree of linear polarisation (DOLP) from our theoretical spectrum via the equation:[119]

$$\mathrm{DOLP} = \frac{I_\perp - I_\parallel}{I_\perp + I_\parallel} \,. \tag{4.4}$$

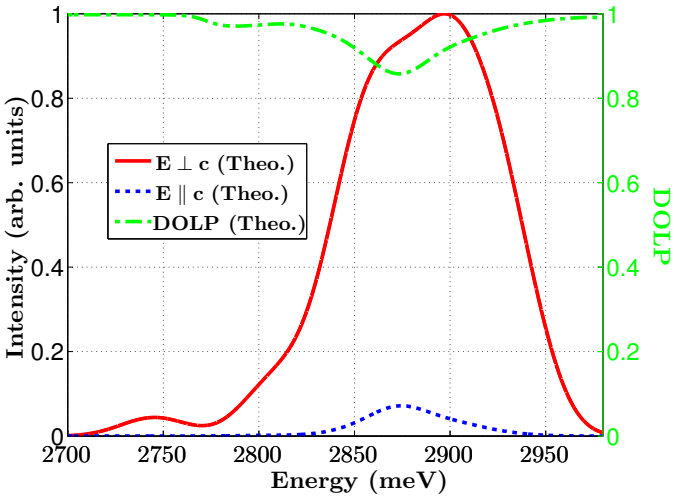

FIGURE 4.12: Calculated excitonic emission spectrum for the light polarisation perpendicular (red solid line) and parallel (blue dashed-dotted line) to the c-axis. The spectral dependence of the corresponding DOLP, calculated according to eq. (4.4), is shown by the (green) dashed-dotted line.

Based on the maximum intensities for $\mathbf{e}_{p,\perp}$ and $\mathbf{e}_{p,\|}$, we find a value for the DOLP of approximately 87%, which is slightly smaller than the experimental values ($> 90\%$).

For further comparison with experiment, we have also calculated the spectral dependence of the DOLP from our theoretical emission spectra for the two light polarisation configurations depicted in Fig. 4.11. Using eq. (4.4), our theoretical results for the spectral dependence of the DOLP are depicted in Fig. 4.12. The DOLP (green dashed-dotted line) is shown as a function of energy together with the excitonic emission spectrum for $\mathbf{E} \perp \mathbf{c}$ (red solid line) and $\mathbf{E} \parallel \mathbf{c}$ (blue dashed line). When comparing our theoretical data with experimental DOLP, which exhibits an almost constant high DOLP $> 90\%$, across the spectrum [116], the theoretical results show slightly lower values than the experiment plus that the calculated DOLP is not as constant as the experimental data across the spectrum. Again, even though 75 configurations may appear a large number, we show below that some of the structure in the DOLP spectrum of Fig. 4.12 is due to a small number of exceptional states; more configurations would be required to reliably treat the importance of such states. This is beyond the scope of the present study, since the present analysis gives already, in general, a good description of the experimentally observed spectral dependence of the DOLP.

The origin of the calculated high DOLP can be further understood by looking at the orbital character of the hole ground state/valence band edge (VBE) state. The outcome of such an analysis is displayed in Fig. 4.13, where the orbital contributions to the VBE are shown as a function of the configuration number n. From a continuum-based calculation, neglecting the weak spin-orbit coupling, one would expect, due to the differences in the valence band effective masses along the growth direction and the positive crystal field splitting energy in GaN and InN, that the VBE is dominated by a single-orbital type (p_x- or p_y-like orbitals). Obviously such an

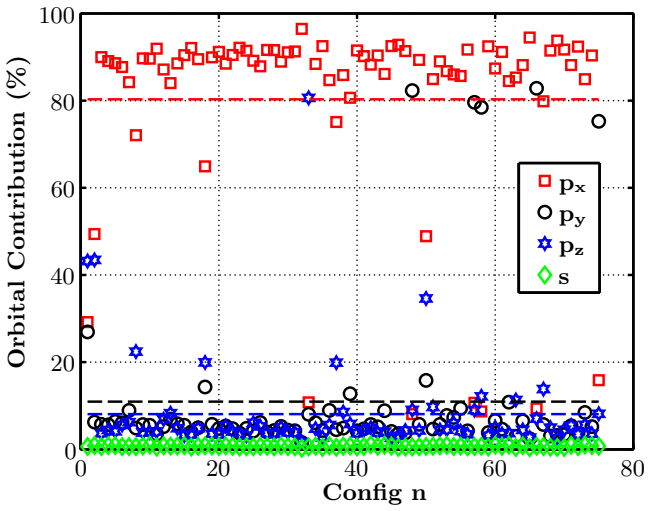

FIGURE 4.13: Orbital contributions to the VBE as a function of the n different microscopic configurations considered here.

analysis neglects the effects of alloy fluctuations. However, we can infer from Fig. 4.13 that the VBE state in the different microscopic configurations is mainly made up of contributions from a single orbital type, in this case from p_x-like orbitals. Thus, we may conclude from the general agreement of our atomistic results with what would be expected from a simple continuum picture, that, for the orbital character of the hole ground state the microscopic configuration is, in general, of secondary importance. However, we note that there is an enhanced p_z-like character and a very low p_x-like character in about 10%-20% of the structures studied. The dominance of the p_x character of the VBE explains the calculated high DOLP, which is in good agreement with the experimental data. Furthermore, as we know from Fig. 4.5 the hole ground state energies vary significantly between different configurations. This gives rise to the broad emission spectrum shown in Fig. 4.11. Since Fig. 4.13 reveals that the orbital contribution to the VBE state is for the most part independent of the configuration number n, all these findings in combination explain why we observe only a weak spectral dependence of the DOLP displayed in Fig. 4.12, in line with the experimental results [116].

4.4 Conclusion

We have presented a detailed analysis of carrier localisation effects in m-plane InGaN/GaN QWs. Our study of the electronic structure of these systems is based on an atomistic theoretical framework, accounting for strain and built-in field variations arising from random alloy fluctuations. We find that electron states, to a first approximation, can be described by a continuum-like picture, with deviations arising from the continuum picture due to the specific indium atom distribution in the different structures considered. However, such a continuum-based description fails completely for the hole states. Our investigation reveals that random

alloy fluctuations lead to strong hole wave function localisation effects both in the ground and in the lowest excited states. We estimate that these localisation effects extend over an energy range of at least 100 meV into the valence band, making them also relevant to experimental studies at elevated temperatures.

The many-body wavefunctions derived from the single particle states in a CI calculation reveal the importance of Coulomb effects in m-plane QWs; under the influence of the Coulomb attraction, the electron localises around the hole state, leading to large excitonic binding energies, and single exponential time decay transients in the time resolved PL spectra. When compared directly with experiment, we find that the theoretically calculated PL matches the experimental quite well, reproducing the large FWHM and DOLP within a good degree or accuracy. Furthermore, the high experimental DOLP is explained by reference to the orbital character of the single particle states. In a complementary approach, we have also studied the modulus wave function overlap between 60 hole states averaged over 75 different microscopic configurations to gain further insight into the characteristics of different hole states. This allows for information on the probability of transferring carriers from one site/state to another. Our initial analysis reveals different regimes ranging from strongly localised states with very little overlap with all other states, up to a delocalised regime where the carriers have strong overlap with most of the other considered states. Having access to all this data on an atomistic level forms now a good starting point for further and detailed transport studies.

Chapter 5

Elastic Properties of zincblende III-V semiconductors

In this chapter, we investigate the elastic properties of selected zincblende III-V semiconductors. This is motivated in part by the desirable electronic properties of the cubic nitrides. Inacccuracies in the ubiquitous valence force field models of Keating and Martin are quantified for Ga, In and Al containing III-V compounds, providing the impetus for an improved description of the elasticity of these materials in both the harmonic and anharmonic strain regimes. Following the extraction of second and third order elastic constants, and first and second order internal strain tensor components, improved microscopic elastic models are introduced, and in the case of a harmonic strain energy, parameterised and tested.

5.1 Introduction

While the growth and study of nitride devices on non-polar wurzite planes continues to progress, another means by which the deleterious effects of the built-in field may be circumvented has recently returned to prominence: the use of nitride devices grown in the meta-stable cubic phase [120–122]. The cubic nitrides have resurfaced as a possible means to all-LED white light emitters due to improvements in growth techniques; where formerly devices based on these materials were hampered by a high density of stacking faults, cubic GaN systems are now grown with >90% cubic phase [123].

Like wurtzite nitride crystals grown on the m-plane and a-plane, the crystal symmetry in the cubic nitrides produces no built-in field in the [001] growth direction. This allows for increased colour stability with current and the possibility of efficient wider QWs. These wider wells present a larger area for the carriers to travel through, lowering the carrier density and the losses due to Auger recombination associated with higher densities.

However, unlike nitrides grown on any of the non-polar hexagonal planes, the cubic phase of GaN has a band gap narrower by 0.2 eV [39]. This 30 nm headstart towards the longer wavelengths means less indium need be incorporated in order to shift the wavelength to the green and yellow spectral region. This in turn allows for the developement of longer wavelength nitride devices without the myriad problems associated with indium incorporation [38] and the high defect densities [124] due to the large lattice mismatch between GaN and InN by which non-polar nitride systems in particular are plagued. In addition to this significant advantage, the bandstructure of the cubic phase of GaN is such that the carriers have smaller effective masses, higher carrier mobilities, higher doping efficiency, and smaller Auger losses [37, 40]. Early theoretical studies also indicate that these differences between the bandstructure of the cubic and wurtzite nitrides also manifest in attractive advantages like better momentum matrix elements between conduction and valence band minima and maxima, and higher optical gain in general [47]. With these notable advantages over the wurtzite phases, and the latest advances in growth techniques, the solution of the green gap problem through use of the cubic III-nitrides seems more feasible than ever. Thus there is a renewed need to study cubic nitride systems from the ground up.

Previous theoretical studies on cubic nitrides have mainly focussed on small bulk alloys using density functional theory (DFT) with the local density approximation (LDA) [100], empirical pseudopotential [29, 125] methods, or, if structures of realistic sizes are treated, it is with continuum models [47], which normally do not account for the atomistic effects shown to be important by other theoretical studies [29] and experiment [123]. The aim of this chapter is to lay the base for a theoretical framework suitable to describe cubic nitride heterostructures on an atomistic level. As before, the tight binding method is an appropriate electronic structure method to describe the cubic nitrides. The localised basis set is suitable for the local phenomena present, and the computational efficiency of the method is such that large structures can be studied. Likewise for the local strain and atomic relaxation of cubic nitride systems, our earlier used VFF model is again appropriate. The structural properties of cubic nitride structures and alloys have already been studied using valence force field models [125, 126]. However, an examination of the valence force field model of Keating, as well as other models used, reveals a lack of suitability for the study of the cubic nitrides, or indeed, heteropolar zincblende crystals in general. In particular, the Kleinman parameter is often neglected in the fitting of many VFF models and other interatomic potentials [127–131]. Furthermore, for the case of the predominantly used Keating model [61, 132, 133], the structural relaxation will suffer from inaccuracies due to the inherent incapacity of the model to fit even the three cubic elastic constants at once.

Furthermore, in nitride and other III-V heterostructures (and in particular quantum dots), very large local strains of up to 10% can develop in the system (The lattice mismatch between InN and GaN is 11%). This 10% strain well exceeds the harmonic regime in which most existing VFF

models are parameterised. We therefore cannot take for granted that in all heterostructures of the highly lattice-mismatched nitride alloys with which we would like to deal, conventional VFFs are sufficient to fully describe the relaxation properties in the regions of high strain. To describe such structures, new VFF models, taking into account more than the harmonic elastic properties of the material, will need to be developed. The anharmonic elastic properties must be determined as a necessary first step to this.

Thus, motivated initially by the desire to establish a theoretical framework with which to analyse the next generation of nitride devices, and secondly by the more general need for improved VFF models for structural relaxation and calculation of strain in all III-V materials, a new implementation of the VFF method is introduced in this chapter. This is based on a simplified version of the model of Musgrave and Pople [134], which was introduced by Martin [84]. Relations between the elastic constants, Kleinman parameter and force constants of a cubic crystal are obtained, and these are then used to derive simple analytic expressions for the force constants needed to describe a given material using the model. Furthermore, criteria for the suitability of the model for a given material are given. The VFF implementation shares all of the advantages and simplicity of the early Keating model, but with more force terms, is able to simultaneously and exactly describe the three elastic constants and Kleinman parameter of zincblende materials. When compared with more sophisticated and transferable (e.g. across material phases) interatomic potentials, the presented implementation offers advantages of greater accuracy within the regime of interest for structural relaxation, greater scalability to larger systems, and markedly more easily determined force constants. Additionally, second and third order elastic properties are extracted from previously calculated DFT data [135]. The elastic constants extracted from these data can be considered more accurate than those calculated in previous studies because of the highly accurate Heyd-Scuseria-Ernzerhof (HSE) [73] screened exchange hybrid functional scheme used. These constants are then used to parameterise the present harmonic VFF model and can be used to parameterise future anharmonic models.

In the next section, section 5.2, calculated values for the second order elastic properties of a host of III-V materials are presented. We then discuss in section 5.3 shortcomings in the reproduction of these properties by widely used VFF models. In section 5.4, a VFF model capable of fitting all the properties calculated is introduced; equations determining the force constants directly in terms of these elastic properties are provided; and the range of materials for which this model is appropriate are provided, along with estimations of the optical phonon frequencies. Third order elastic constants for the same set of III-V materials are then presented in section 5.5, again extracted from HSE DFT data, and a discussion is presented as to the best routes towards at third order VFF model. Finally, in section 5.6, we draw conclusions and comment on the outlook for future work.

5.2 Elastic Properties of III-V materials to second order

Before the treatment of the harmonic elasticity of III-V heterostructures and alloys using semi-empirical methods is possible, it is necessary to obtain accurate *ab initio* or experimental measures of the elastic properties of their constituent binary materials. In this work, the desired properties are theoretically determined. This is justified by the general difficulty of extraction of certain properties experimentally i.e. shear moduli [62, 136], internal strain parameters [137, 138], or any parameters at all for those materials for which a sufficiently large single crystal cannot be obtained; and agreement with experiment where reliable experimental values are available (values for C_{11} and C_{12} for example). These experimental difficulties are compounded by the metastability of the cubic III-nitrides. We thus extract for ourselves a full consistent set of all those needed elastic properties of the III-V materials under consideration.

Contemporary theoretical determination of elastic properties normally involves the use of some variant of DFT to calculate the total energy [139], stress [140, 141] and internal strain [59, 62] of a given unit cell as a function of applied macroscopic strain. In particular, the equillibrium lattice constant in a zincblende unit cell is determined by finding the cell size for which the total energy is minimised; or, alternatively, finding the cell size for which all stresses on the cell vanish. Likewise, the sub lattice displacement, given by the atomic positions, for which the total energy is a minimum for a given macroscopic strain, determines the Kleinman parameter and internal strain properties. The elastic constants are extracted via a calculation of the stress or energy as a function of strain, and fitting these to known energy-strain or stress-strain relations (i.e. eqs.2.40 and 2.39).

In this work, for the determination of second and third order macroscopic elastic and internal strain properties, use is made of data from HSE DFT calculations performed by Miguel Caro [135, 141]. DFT within the HSE scheme offers improved accuracy over standard Kohn-sham approaches to the exchange energy [142]. For instance, it circumvents the well known band gap problem of LDA and generalised gradient approximation (GGA) implementations. Moreover, HSE-DFT has been shown to give improved predictions elastic and lattice properties of solids [143].

The data used consist of the total energy, the six components of the stress tensor, and the atomic positions in the two atom basis, as a function of different applied strains. The internal degrees of freedom are optimised to acheive the minimum energy for each strain, and thus the relative sublattice displacement offers a means to extract the Kleinman parameter, and the stress-strain/energy-strain curves give the physical, relaxed, elastic constants.

These quantities are calculated for five different strain branches, given in [135]:

$$\begin{aligned}
\epsilon^{(1)} &\equiv (0,0,0,\beta,\beta,\beta)\,,\\
\epsilon^{(2)} &\equiv (\alpha,0,0,\beta,0,0)\,,\\
\epsilon^{(3)} &\equiv (0,\alpha,0,\beta,0,0)\,,\\
\epsilon^{(4)} &\equiv (0,\alpha,\alpha,\beta,0,0)\,,\\
\epsilon^{(5)} &\equiv (\alpha,\alpha,\alpha,\beta,\beta,\beta)\,.
\end{aligned} \tag{5.1}$$

For each of these strain branches α (β) is varied from -0.02 (-0.04) to 0.02 (0.04) in steps of 0.01 (0.02). Each value of α and β is associated with six stress components, a total energy value, and atomic positions, which by fitting to eqs. 2.40, 2.39 and 2.45, will yield values for the elastic constants and Kleinman parameter.

For the determination of elastic constants, we choose to fit to the stress/strain equations for reasons of greater accuracy and efficiency [140]. The stress method is suited to efficient calculation of the elastic constant tensor, because the different stress components obtained from a single calculation each yield an equation from which different elastic constants may be obtained. Thus the elastic constants can be obtained via the stress method efficiently from one calculation whereas from the energy method several separate calculations would be needed. Furthermore, in terms of accuracy, the equations relating these elastic constants to the strains will be linear, and therefore easier to fit when dealing with very small strains. Finally, the number of k-points needed in a given calculation to obtain converged values of the elastic constants is lower for those elastic constants calulated via the stresses than for those calculated via the total energy method [141], meaning that a desired accuracy can be achieved more efficiently using the stress method.

The high symmetry of zincblende crystals results in their having only three independent second order elastic constants. Taking the second strain branch, $\epsilon^{(2)}$, as an example, these three independent elastic constants may be obtained from eq.(2.40) for the different stress components. Equation (5.2) below, relates the stress components σ_1, σ_2, and σ_3 to the components of the second strain branch of eq. (5.1).

$$\begin{aligned}
\sigma_1 &= C_{11}\alpha,\\
\sigma_2 &= C_{12}\alpha,\\
\sigma_3 &= C_{44}\beta.
\end{aligned} \tag{5.2}$$

The fittings to eq. (5.2) are shown in Fig. 5.1. In order to show the limits of the linear elastic theory in treating the material properties, we plot the stresses corresponding not just to $\alpha = -0.02 : 0.02$ with $\beta = 0$, but include those data points corresponding to different values of

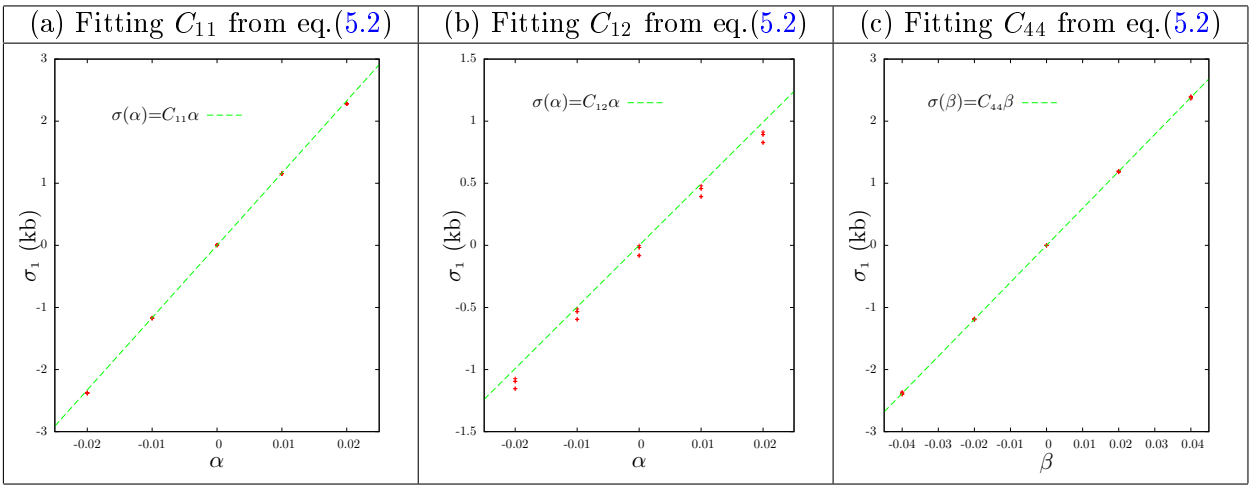

FIGURE 5.1: Illustrative fittings of eq.(5.2) to HSE DFT stress/strain data for GaAs. For each value of α, β is varied, showing the the linear approximation where shear strains have no effect on axial stresses leads to a decrease in fit quality even at lower strains.

β for a given value of α. According to eq. (5.2) the values of σ_2 for example, should only depend on α, but Fig. 5.1 (b) shows that the stress deviates from this behaviour with increasing β. The decreasing accuracy of the linear approximation with strain can also be seen in Fig. 5.1 (a) where the fit detiorates slightly as the strain increases. The quantitative source of these errors is apparent when one uses the non-linear Lagrangian strain formulation. This will be discussed further in section 5.5.2, here the linear equations and fittings are given for illustrative purposes only.

Fitting to the other strain branches of eq. (5.1) will yield additional, similarly simple equations for the same three elastic constants; thus in the uncomplicated case of extracting the harmonic elastic constants, the given strain branches and their corresponding stresses, produce an over-abundance of data from which we can extract highly accurate elastic constant values, obtained through, and averaged across, many independent fittings.

Each α and β is associated also with a sublattice displacement, which by fitting to eq. 2.45, yields a value for the Kleinman parameter. The second order elastic and structural properties of Al, Ga, and In containing III-V compounds, extracted from our HSE DFT data are summarised in Table 5.1. For convenience the lattice constants as well as equillibrium bond lengths are also given. (Note: to acheive more accurate and less ambiguously defined second order elastic constants, the values in Table 5.1 are actually obtained from third order elastic equations)

In the next section the values in table 5.1 are compared with the predictions of the popular VFF models of Martin [84] and [61], revealing possibilities for their improvement for the purposes of structural relaxation in materials within the regime of small strains.

	C_{11}(GPa)	C_{12}(GPa)	C_{44}(GPa)	ζ	a_0(Å)	r_0(Å)
AlN	309.47	166.06	196.90	0.5385	4.3647	1.8900
AlP	138.25	67.73	66.52	0.5759	5.4713	2.3691
AlAs	116.64	55.62	56.96	0.5746	5.6865	2.4623
AlSb	86.39	40.65	40.71	0.5893	6.1877	2.6794
GaN	288.35	152.98	166.68	0.5678	4.4925	1.9453
GaP	142.16	60.47	72.58	0.5333	5.4600	2.3642
GaAs	116.81	49.64	59.76	0.5288	5.6859	2.4620
GaSb	86.37	36.55	43.44	0.5517	6.1524	2.6641
InN	185.20	121.72	91.49	0.7474	4.9908	2.1611
InP	100.42	53.72	47.39	0.6520	5.9035	2.5562
InAs	84.28	44.72	39.66	0.6378	6.1160	2.6483
InSb	64.97	33.00	30.42	0.6337	6.5632	2.8419

TABLE 5.1: Elastic and structural properties of III-V compounds, where C_{11}, C_{12}, and C_{44} are the second order elastic constants, ζ is the Kleinman parameter, a_0 and r_0 are the equilibrium lattice constant and bond length, respectively.

5.3 Shortcomings of current Valence Force Field Implementations in the harmonic regime

The ultimate test of the suitability of a particular interatomic potential energy functional for the description of selected properties of a given material is whether or not the potential reproduces those targeted properties during numerical simulations of the dynamics or relaxation behaviour of the material in question.

However, a simpler and more insightful test, which obviates the need for any extraneous simulations, is to examine the elastic constant relations predicted by a given functional form. This method was used as early as the 19th century when Saint-Venant [144] showed that a crystal comprising atoms interacting only via central pairwise forces in a cubic lattice (which atoms of a central pairwise potential will tend to crystalise in e.g. the ionic NaCl), exhibits the relation $C_{12} = C_{44}$. [56, 145] That this relation does not at all hold for tetrahedral semiconductor materials, means that such a functional form will never be able to accurately describe their properties.

This failing of a purely central force field to describe tetrahedrally bonded materials motivated M. Born to develop a potential with, in addition to a central force term, a term which depends on the angles between the bonds joining the atoms. Combined with the central force term, such an angular dependence of the energy allows for the possibility of a tetrahedrally bonded crystal to have a lower energy than the close-packed crystal structures. From this two-term potential Born derived the new relation [146, 147]:

$$\frac{4C_{11}\left(C_{11}-C_{44}\right)}{\left(C_{11}+C_{12}\right)^2}=1. \tag{5.3}$$

Thirty one years after the publication of this paper, when the first measurements of the elastic constants of diamond were made, the ratio was found to be 1.1 [146], showing good agreement and pointing to the greater suitability of Born's two term potential over the simple central force model.

While the agreement of eq. (5.3) with experiment was encouraging, the potential was nevertheless found to suffer serious shortcomings. Keating [61] showed the model produced a bulk modulus which depends on angular force constants, an unadmissible result given a hydrostatic compression involves no changes in the angles between atoms. Furthermore, the compliance constant s_{11} was found to be negative or in certain cases infinite, depending on the values of the force constants. These issues illustrate that the satisfaction by a given material of the elastic constant relations for a particular potential is a necessary, but not sufficient, condition for the suitability of that potential to describe the material in question.

The failings of Born's potential gave the impetus for Keating's introduction of what would become one of the most widely used VFF potentials for the structural analysis of semiconductors. In particular, as well as being used to model group IV crystals, it has been the primary potential used, or forms the basis of potentials used, for the dynamics, structural relaxation and analysis of a host of III-V materials, including the III-nitrides, in both thier cubic and wurtzite phases [128, 131–133, 148–150]. The functional form of Keating's potential for a pure zincblende crystal is given below in eq. (5.4):

$$V = \frac{1}{2}\sum_{l}\left[\frac{\alpha}{4a}\sum_{i=1}^{4}\left(r_{0i}^2(l) - 3a^2\right)^2 + \frac{\beta}{2a^2}\sum_{i,j>i}^{4}\left(\mathbf{r}_{0i}(l)\cdot\mathbf{r}_{0j}(l) + a^2\right)^2\right], \tag{5.4}$$

Where $a = \frac{a_0}{4}$, the equillibrium lattice constant divided by 4, α and β are the bond stretching and bond-bending force constants, respectively. The sum over l is a sum over all the primitive unit cells in the crystal, and $\mathbf{r}_{0i}$ is the displacement vector between atom i and atom 0, the central atom in the tetrahedron.

The explicit imposition of rotational invariance is evident in the dependence of eq. (5.4) on only scalar products of the interatomic displacements. Given the popularity of this model and the availability of parameter sets for III-V materials, it is a natural place to start if one wishes to describe their structural properties. However, the elastic constant relations predicted by the model indicate that there is much room for improvement.

The relations between the force constants of this potential and the elastic constants and Kleinman parameter of the material whose properties are to be described are given below:

$$C_{11} = \frac{\alpha + 3\beta}{4a}, \tag{5.5}$$

$$C_{12} = \frac{\alpha - \beta}{4a}, \tag{5.6}$$

$$C_{44} = \frac{\alpha\beta}{a(\alpha + \beta)}, \tag{5.7}$$

$$\zeta = \frac{\alpha - \beta}{\alpha + \beta}. \tag{5.8}$$

Rearranging the terms in this underdetermined system leads to relations amongst the elastic constants. Adding three times eq. (5.6) to (5.5) yields eq. (5.9) , whilst subtracting eq. (5.6) from eq. (5.5) gives an expression for β.

$$\alpha = a(C_{11} + 3C_{12}), \tag{5.9}$$

$$\beta = a(C_{11} - C_{12}). \tag{5.10}$$

Substituting eqs. (5.9) and (5.10) into eq. (5.7), gives an expression for C_{44} related through the fitted values of α and β to C_{11} and C_{12}. We denote this by:

$$C_{44}^{\mathrm{VFF}} = \frac{(C_{11} - C_{12})(C_{11} + 3C_{12})}{2(C_{11} + C_{12})}. \tag{5.11}$$

The ratio between the actual value of C_{44} (determined experimentally or from *ab-initio* theory), and that predicted via the force constants in terms of C_{11} and C_{12}, serves as a measure of how accurately the elastic constants of a given material can be described using the Keating model:

$$R_{C_{44}} = \frac{C_{44}}{C_{44}^{\mathrm{VFF}}} = \frac{2C_{44}(C_{11} + C_{12})}{(C_{11} - C_{12})(C_{11} + 3C_{12})}. \tag{5.12}$$

Where the nature of the error described by this equation depends on the parameters fitted to. Many implementations of Keating's model fit only to C_{11} and C_{12} [61, 84, 126, 148, 151] and thus eq. (5.12) describes the fractional error in C_{44}. In other fitting schemes, the force constants are fitted simiultaneously to all three elastic constants using a least squares method [126, 128]; in this case the ratio describes the cumulative error distributed over the three constants, with the errors in each particular constant depending on the weights and method of fitting. Table 5.2 below shows, for a host of III-V materials, the value of the ratio of $R_{C_{44}}$ and the error corresponding to this value, respectively.

An examination of table 5.2 shows, that with errors of at least 8% for the III-V materials, either all in C_{44} or spread across the three elastic constant values, care should be taken before using Keating's model for the structural relaxation of their heterostructures, and that there is

	N	P	As	Sb
Al	1.617 (-38%)	1.138 (-12%)	1.134 (-12%)	1.085 (-8%)
Ga	1.454 (-31%)	1.113 (-10%)	1.115 (-10%)	1.093 (-9%)
In	1.607 (-38%)	1.196 (-16%)	1.184 (-16%)	1.137 (-12%)

TABLE 5.2: Value of ratio $R_{C_{44}}$ of eq. (5.12) for selected III-V materials. The error corresponding to this value is given in brackets, and indicates the error in C_{44} when fitting is made to C_{11} and C_{12}.

room for an improved model. This is particularly the case for the ZB nitrides which motivate this section, with these suffering from errors of up to a 38% underestimation of C_{44}.

In addition to the ratio of eq. (5.12), which Keating gave in his original paper [61], another ratio can be used to further examine the accuracy with which the potential can describe a given material. This ratio is obtained by substituting eqs. (5.9) and (5.10) into eq. (5.8) and is a measure of the ability of the potential to capture the Kleinman parameter:

$$R_\zeta = \frac{\zeta}{\zeta^{\text{VFF}}} = \frac{\zeta\left(C_{11}+C_{12}\right)}{2C_{12}}. \tag{5.13}$$

The value of the ratio of eq. (5.13), and the corresponding error in ζ (when α and β are fitted to C_{11} and C_{12}), for different materials are shown is shown in Table 5.3 below:

	N	P	As	Sb
Al	0.771 (30%)	0.881 (14%)	0.890 (12%)	0.921 (9%)
Ga	0.819 (22%)	0.894 (12%)	0.887 (13%)	0.927 (8%)
In	0.942 (6%)	0.935 (7%)	0.920 (9%)	0.941 (6%)

TABLE 5.3: Value of ratio R_ζ of eq. (5.13) for selected III-V materials. The error corresponding to this value is given in brackets, and indicates the error in ζ when fitting is made to C_{11} and C_{12}.

Table 5.3 shows that not only does the model give an incomplete description of the macroscopic properties via C_{44}, but that the internal relaxation within a supercell is also not fully captured, with an overestimation of at least 6%, and as much as 30%. The sublattice displacement with shear strain, controlled by the Kleinman parameter, is an integral quantity in the calculation of piezoelectric effects in a structure [66, 67, 135], therefore, the fact that the error in the Kleinman parameter tends generally to increase with increasing ionicity, where piezoelectric effects also become increasingly important is a significant failing of the model.

Noticing that these errors tended to increase with ionicity, Keating himself stated [61] that his original potential was not suitable for the heteropolar III-V materials due to the increasing importance of the long range Coulomb forces (though it is nevertheless still widely used in its original form). The trends in error with ionicity were noted by Martin [84], who sought to improve them by the addition of an electrostatic interaction between partially charged rigid ions, which he described in his paper (in C.G.S units) as: $\pm Z^{*2}e^2/\epsilon R$. This interaction is

characterised by the effective charge, Z^*, for which Martin uses the dynamic definition [69, 152], which sets the charge via the optic mode splitting:

$$S = \frac{Z^{*2}}{\epsilon_\infty} = \left(\frac{\Omega}{4\pi e^2}\right) \mu \left(\omega_l^2 - \omega_t^2\right) . \tag{5.14}$$

Here the quantity S is used for later convenience. ϵ_∞ is the high frequency dielectric constant of the material in question, Ω is the volume of the primitive cell, e is the electronic charge, ω_l and ω_t are the longitudinal and transverse optical phonon frequencies, respectively, and μ is the reduced mass of the basis of anion and cation.

With the addition of this interaction, Martin derives equations relating the force constants, α and β, to the elastic constants, C_{ij} [84]:

$$C_{11} + 2C_{12} = \frac{\sqrt{3}}{4r}(3\alpha + \beta) - 0.355SC_0 , \tag{5.15}$$

$$C_{11} - C_{12} = \frac{\sqrt{3}}{r}\beta + 0.053SC_0 , \tag{5.16}$$

$$C_{44} = \frac{\sqrt{3}}{4r}(\alpha + \beta) - 0.136SC_0 - C\zeta^2 , \tag{5.17}$$

$$C = \frac{\sqrt{3}}{4r}(\alpha + \beta) - 0.266SC_0 , \tag{5.18}$$

$$\zeta = C^{-1}\left[\frac{\sqrt{3}}{4r}(\alpha - \beta) - 0.294SC_0\right] , \tag{5.19}$$

$$C_0 = \frac{e^2}{r^4} . \tag{5.20}$$

Here the numerical prefactor to SC_0 in eqs. (5.15-5.19) are the results of calculated Ewald summations [153] over the infinite crystal when subjected to different strains; it represents the second-order coefficient of the expansion in strain of the total Coulomb energy of an atom.

To determine if this Coulombic addition of Martin's sufficiently improves the accuracy of the description of the selected III-Vs, ratios similar to eqs. (5.12) and (5.13) can be derived from eqs. (5.15-5.19). For C_{44} the following relation ensues:

$$R^M_{C_{44}} = \frac{C_{44}}{C^{\mathrm{VFF}}_{44}} = \frac{2C_{44}\left(C_{11} + C_{12} - C'\right)}{\left(C_{11} - C_{12}\right)\left(C_{11} + 3C_{12} - 2C'\right) + 0.831C'\left(C_{11} + C_{12} - C'\right)}, \tag{5.21}$$

where Martin uses the simplifying notation $C' = 0.314SC_0$. The value of eq. (5.21) for different materials and the attendant errors are given in Table 5.4.

It is evident from Table 5.4 that while the inclusion of Coulombic forces yields significant improvement over the purely covalent model of Keating, there remain non-negligible inaccuracies in the description of the properties of the listed materials. The cubic nitrides incur the largest errors, with up to 20% for AlN, whilst the other materials have an average error of about 5%

	N	P	As	Sb
Al	1.255[a] (-20%)	1.028[b] (-3%)	1.040[c] (-4%)	1.031[d] (-6%)
Ga	1.192[a] (-16%)	1.043[d] (-4%)	1.052[d] (-5%)	1.092[d] (-8%)
In	1.073[a] (-7%)	1.069[d] (-6%)	1.073[d] (-7%)	1.071[d] (-7%)

TABLE 5.4: Value of ratio $R^M_{C_{44}}$ of eq. (5.21) for selected III-V materials; superscript refers to the source of phonon frequencies used to calculate S, eq. (5.14): a = Ref [126], b = Ref [154], c = Ref [155], d = Ref [84]. Values for the elastic constants are extracted from HSE DFT data and presented in Table 5.1.

In addition to the errors in C_{44}, inaccuracies accrue to the internal relaxation through the fitting to the Kleinman parameter, ζ. Within Martin's formalism, the ratio which describes these errors is:

$$R^M_\zeta = \frac{\zeta}{\zeta^{\text{VFF}}} = \frac{\zeta\,(C_{11}+C_{12}-C')}{2C_{12}-C'}. \tag{5.22}$$

The value of eq. (5.22) for different materials and the corresponding errors are given in Table 5.5 below:

	N	P	As	Sb
Al	0.868 (15%)	0.926 (8%)	0.932 (7%)	0.946 (6%)
Ga	0.894 (12%)	0.938 (7%)	0.925 (8%)	0.928 (8%)
In	1.026 (-3%)	0.974 (3%)	0.954 (5%)	0.963 (4%)

TABLE 5.5: Value of ratio R^M_ζ of eq. (5.22) for selected III-V materials calculated using elastic constant and Kleinman parameter values extracted from HSE DFT data presented in Table 5.1, with the phonon frequencies used to calculate S given in Table 5.4.

This table indicates that for the Kleinman parameter too, a general improvement is acheived with the inclusion of the electrostatic forces, but that a finite error nevertheless remains for all materials. Apart from the anomalous case of InN, the Kleinman parameter is overestimated by $> 10\%$ for the nitrides and an average of 6% for the other materials.

In summary then, Tables 5.4 and 5.5 reveal that, despite the electrostatic amendments of Martin, there are still significant shortcomings in the ability of this functional form to describe the properties of many III-V materials. This implies that while the ionic effects are indeed important, either there remain subtleties of the covalent bonding that are not captured by the simple two term form of eq. (5.4); or that the parameterisation of the Coulomb interaction via the splitting in the optic phonon modes is not a good one. Either way, improvements are needed to describe the cubic nitrides and other III-V materials.

A natural first step on the path towards this improvement is to include more nearest neighbour valence interactions to allow a broader description of the variation of the energetics with changes in the local bonding environment. To complement this approach use can now be made of the much larger data-base of *ab initio* results. For example, even the value of the ratios of eqs. (5.13) and (5.22) were not calculable in Keating's time. Indeed, the equations (5.8) and

(5.19) (and similar equations derived from other interatomic potentials) served as some of the first theoretical estimations of the Kleinman parameter [138]; here the force constants would be determined from the limited macroscopic elastic constant data, and the Kleinman parameter in turn calculated from the force constants. Now, however, availability of accurate first principles calculations of the still experimentally elusive Kleinman parameter allow not only for additional validity checks, but serve also as an additional material property with which to parameterise future potentials. Better still, in addition to the relaxed elastic properties of crystals, modern DFT calculations give access to the elastic properties of unrelaxed unit cells. This gives access to a larger parameter set by which VFF potentials may be parameterised.

In the next section we describe a VFF model with additional terms and better able to make use of the modern abundance of first principles data, whilst retaining the attractive simplicity of Keating's model and its electrostatic successor.

5.4 Improved description of harmonic elasticity

In this section we seek to address the shortcomings pointed out in section 5.3, by use of a VFF model with additional interaction terms to accommodate those structural properties neglected by previous implementations. In section 5.4.1, the interatomic potential which will be used is introduced and its terms discussed. Then in section 5.4.2, the fitting of the potential parameters to elastic properties is detailed, and finally in section 5.4.3, the suitability of this model for different materials is examined, and its ability to model properties not included in the fitting is tested; for those materials for which the potential is suitable, VFF force constants are provided.

5.4.1 Interatomic Potential

To improve upon the aforementioned shortcomings, we take up, as with the VFF potential used in chapters 1 and 2 for wurzite, the thread left by Martin in his 1970 paper [84]. In this paper Martin draws attention to the original VFF model of Musgrave and Pople [134] and points out that the valence coordinates used and their accompanying force constants maintain the translational and rotational invariance lacking in those of the models identified by Keating [61]. This functional form was well justified by Musgrave and Pople in their original work [134], deriving the valence force terms by considering the forces in every direction on a given atom due to movements of neighbouring atoms in every direction. Discarding a purportedly unimportant cross angle term, Martin gives the form of the potential which will be the subject of this section.

For each atom in a ZB crystal Martin's potential is given by:

$$V_i = \frac{1}{2}\sum_{j\neq i}\frac{1}{2}k_r\left(r_{ij}-r_{ij}^0\right)^2 + \sum_{j\neq i}\sum_{k\neq i,k>j}\left\{\frac{1}{2}k_\theta^i r_{ij}^0 r_{ik}^0\left(\theta_{ijk}-\theta_{ijk}^0\right)^2 + k_{r\theta}^i\left[r_{ij}^0\left(r_{ij}-r_{ij}^0\right)+r_{ik}^0\left(r_{ik}-r_{ik}^0\right)\right]\left(\theta_{ijk}-\theta_{ijk}^0\right)+k_{rr}^i\left(r_{ij}-r_{ij}^0\right)\left(r_{ik}-r_{ik}^0\right)\right\}. \tag{5.23}$$

Here i refers to the central atom being considered, while j and k run over the 4 nearest neighbours for each i. This means that for the potential of a zincblende primitive cell 8 bond lengths and 12 angles will be treated. The half preceeding the first term prevents double counting when summing over i. $r_{ij} = (\mathbf{r_{ij}}\cdot\mathbf{r_{ij}})^{\frac{1}{2}}$ refers to the bond length between atom i and j, $\theta_{ijk} = \cos^{-1}\left(\frac{\mathbf{r}_{ij}\cdot\mathbf{r}_{ik}}{|\mathbf{r}_{ij}||\mathbf{r}_{ik}|}\right)$ refers to the angle between the bonds r_{ij} and r_{ik}, and r_{ij}^0 and θ_{ijk}^0 refer to the equillibrium bond lengths and bond angles, respectively.

The potential terms of eq. (5.23) are shown graphically in Fig. 5.2. The term k_r captures the resistance of any bond to length changes away from the equillibrium length, likewise k_θ describes the harmonic resistance to changes in angle. The term k_{rr}^i describes the relation between neighbouring bonds which share an atom (atom i); how one bond will tend to increase in length if another is decreased. $k_{r\theta}^i$ describes the interaction between the angle between two bonds, and each of the two bonds; this will, for example, make it energetically favourable for bond lengths to increase when bond angles decrease. This energetic favourability can be imputed to changes in the s-p mixing on the orbitals sitting on the central atom [156]. The amount by which the energy changes due to this rehybridisation would of course depend on the species of the central atom; which in turn would imply different 3-body terms are needed for the cation and the anion, hence the superscript i on these terms. However, Martin justifies the exclusion of this effect by emphasising that the potential is being used to study only phenomena in the long-wavelength regime: elastic properties, as well as zone centre optic and acoustic modes. In this case the force constants for the two atoms in the unit cell always enter the energy and frequency equations together, and thus could not be separated (See appendix A, eq. (A.8): angles about atoms 0 of the primitive cell are equivalent to those about atom 1). He thus treats anion-centred and cation-centred angular terms as the same, and this equality is imposed also in the present work.

We part ways with Martin's method when he applies further approximations and dependencies to the force constants such that eq. (5.23) becomes equivalent to the Keating potential in eq. (5.4). In this work no dependencies amongst the force constants are imposed, and there are thus four force constants with which we can fit the elastic properties. Furthermore, we do not at present include Coulombic effects amongst our terms, studying first the effects of the inclusion of additional valence interactions.

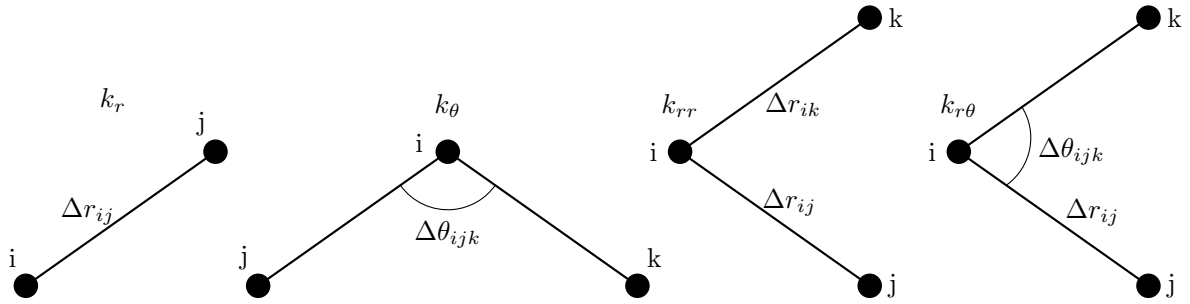

FIGURE 5.2: Valence force field interaction terms contributing to eq. (5.23). From left to right: bond stretch, k_r; bond bending, k_θ; bond-bond, k_{rr}; bond-angle, $k_{r\theta}$.

In the next section we discuss the fitting of the force constants to reproduce the elastic properties of Al, In, and Ga containing III-V semicondcutors.

5.4.2 Force constant fitting

In this section the primary focus is on the results of the expansion of eq.(5.23) in strain, and the subsequent fitting. For a more detailed description of the expansion, see appendix A.

To parameterise the VFF model of eq. (5.23), the interatomic bond lengths and the angles between these bonds must be expressed in terms of the strain and the internal strain.

The two atom zincblende primitive cell is shown in Fig. 5.3 below, the two basis atoms and the lattice vectors transform as:

$$\begin{aligned} \mathbf{a} &= T\mathbf{a}^0, \\ \mathbf{b} &= T\mathbf{b}^0, \\ \mathbf{c} &= T\mathbf{c}^0, \\ \mathbf{r}_1 &= T\mathbf{r}_1^0, \\ \mathbf{r}_0 &= T\mathbf{r}_0^0 + \mathbf{u}. \end{aligned} \tag{5.24}$$

Where $T = (1+\varepsilon)$ is the deformation matrix written in terms of the strain, and $\mathbf{t}$ represents the displacement between two sublattices, the internal strain. Taking into account the symmetry of the zincblende crystal, eq. (5.24) gives the dependence on strain of all the relevant atomic coordinates in the cell.

Having the position vectors of the atoms thus in terms of strain, a Taylor expansion of eq. (5.23) to second order in the nine strain components, $(\varepsilon_{11}, \varepsilon_{22}, \varepsilon_{33}, \varepsilon_{32}, \varepsilon_{13}, \varepsilon_{12}, u_x, u_y, u_z)$, results in an expression for the energy which is a second order polynomial in the strain variables. Subsequently minimising this expression with respect to the internal strain, and comparing with the well known expression for the macroscopic energy density of cubic crystals [50], yields equations

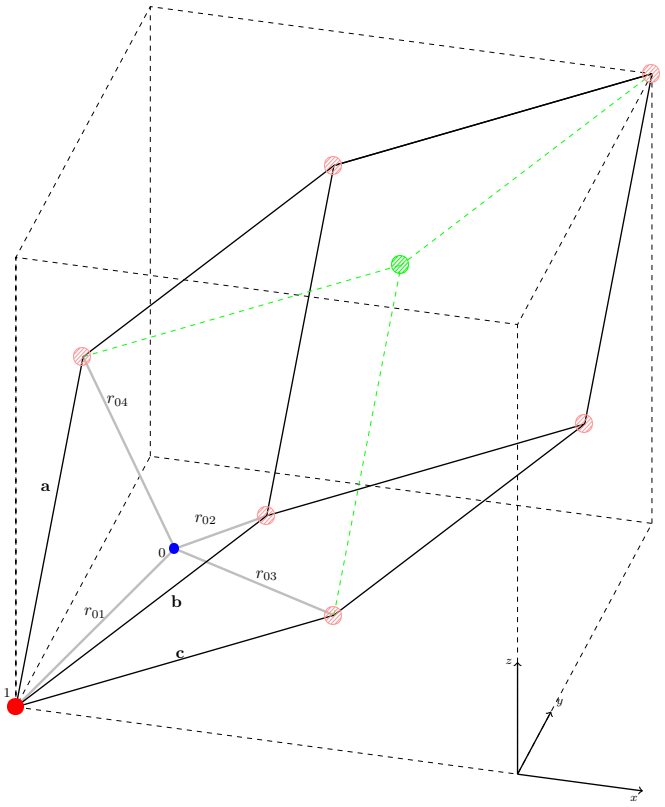

FIGURE 5.3: Zincblende primitive cell.

(5.25-5.28), relating the force constants of eq. (5.23) to the elastic properties of Table 5.1:

$$C_{11} = \frac{\sqrt{3}}{12 r_0}\left(k_r + 6k_{rr} + 12k_\theta\right), \tag{5.25}$$

$$C_{12} = \frac{\sqrt{3}}{12 r_0}\left(k_r + 6k_{rr} - 6k_\theta\right), \tag{5.26}$$

$$C_{44} = \frac{3\sqrt{3}}{2 r_0}\frac{k_r k_\theta - 2k_{rr}k_\theta - 4k_{r\theta}^2}{k_r - 2k_{rr} - 8\sqrt{2}k_{r\theta} + 8k_\theta}, \tag{5.27}$$

$$\zeta = \frac{k_r - 2k_{rr} - 2\sqrt{2}k_{r\theta} - 4k_\theta}{k_r - 2k_{rr} - 8\sqrt{2}k_{r\theta} + 8k_\theta}. \tag{5.28}$$

Inverting these equations, and taking care to eliminate the extraneous root (see Appendix A), we obtain direct expressions for the force constants in terms of the second order elastic constants. These are given in eqs. (5.29) to (5.32) below:

$$k_\theta = \frac{2\left(C_{11}-C_{12}\right)r_0}{3\sqrt{3}}, \tag{5.29}$$

$$k_r = \frac{r_0}{\sqrt{3}\left(1-\zeta\right)^2}\left[C_{11}\left(2+2\zeta+5\zeta^2\right)+C_{12}\left(1-8\zeta-2\zeta^2\right)+3C_{44}\left(1-4\zeta\right)\right], \tag{5.30}$$

$$k_{rr} = \frac{r_0}{6\sqrt{3}\left(1-\zeta\right)^2}\left[C_{11}\left(2-10\zeta-\zeta^2\right)+C_{12}\left(7-8\zeta+10\zeta^2\right)-3C_{44}\left(1-4\zeta\right)\right], \tag{5.31}$$

$$k_{r\theta} = \frac{r_0}{3}\sqrt{\frac{2}{3}}\frac{\left(C_{11}-C_{12}\right)\left(1+2\zeta\right)-3C_{44}}{\zeta-1}. \tag{5.32}$$

Having this one-to-one analytic relation between the force constants and the elastic constants has several advantages. Like the Keating model we have direct expressions for the force constants with no numerical fitting procedures required. These simple expressions make the explanation of different trends in elastic properties in terms of the force constants a straight forward procedure; having only equations of the type of eqs.(5.25-5.28), predictions of elastic properties in terms of trends in the force constants, and vice versa, would be very difficult. Unlike the Keating model, however, with the four force terms, the full elastic constant tensor and Kleinman parameter can be fit to exactly. With respect to other more sophisticated potentials, this parameterisation of the VFF model offers all the advantages of the much used Keating model, as well as greater accuracy in the regime to which it is parameterised.

In the next section an analysis of the model is made in terms of stability and suitability to different materials.

5.4.3 Suitability of Model

To ascertain the suitability of these potentials for the materials we seek to model, we may examine their prediction of properties to which they are not fitted. One such readily available prediction is the value of the transverse optical phonon at the Γ point; while the potential does not purport to accurately describe dynamical properties, such quantities will nevertheless give an indication of whether or not the energetics of internal strain are reasonable.

The quantity B_{xx} is related to the transverse optical phonon at Γ for ZB structures by [137, 140]:

$$B_{xx} = 4\mu\omega_{\mathrm{TO}}^2/a_0^3, \tag{5.33}$$

where μ is the reduced mass of the anion and cation system, ω_{TO} is the transverse optical phonon frequency at Γ, and a_0 is the lattice constant. From equations (5.29) to (5.32) and (A.15) the following relation between B_{xx} and the known elastic properties is derived:

$$B_{xx} = \frac{16\left(C_{11}-C_{12}-C_{44}\right)}{\left(1-\zeta\right)^2 a_0^2}. \tag{5.34}$$

A negative B_{xx} would lead to two undesirable results: imaginary ω_{TO}, and worse, the scenario that the energy density has a stationary point which is a maximum rather than a minimum in the internal strain (See eqs.(A.9) and (A.10)). This latter consequence invalidates the basis of the whole procedure by which the relaxed elastic constants are derived, wherein the assumption that the energy is being *minimised* with respect to the internal strain must hold for the parameterisation via the Kleinman parameter to be reasonable.

An inspection of the terms in the numerator of eq. (5.34) reveals that only those crystals for which:

$$A = \frac{2C_{44}}{C_{11} - C_{12}} < 2, \tag{5.35}$$

where A is the anisotropy parameter [153], are stable against sublattice displacements.

The values of B_{xx} predicted from eq.(5.34), and the transverse optical phonon frequencies corresponding to these are shown in tables 5.6 and 5.7. Table 5.6 shows that the potential is

	N	P	As	Sb
Al	-210.92	12.06	11.09	12.45
Ga	-132.85	22.45	16.52	13.40
In	-282.01	-2.62	-0.321	4.28

TABLE 5.6: Value of B_{xx} predicted from eq.(5.34) given in units of GPa Å^{-2}.

not suitable for the cubic III-N or any of the indium containing III-Vs other than InSb. While simulations of these crystals with negative B_{xx} using this potential will exhibit the correct elastic constant tensor, the crystals will be unstable with respect to internal displacements for a fixed shear strain.

The transverse optical phonon frequencies, ω_0, predicted from the values of B_{xx} above are given in Table 5.7. Tables 5.6,5.7,B.2 and condition (5.35) indicate that the VFF potential (eq.(5.23)) parameterised via eqs. (5.29-5.32), is suitable for neither the structural relaxation nor the dynamics of materials for which $A > 2$, whilst for materials with $A < 2$ the potential describes the parameters of the structural relaxation very well (C_{ij} and ζ), but does not accurately describe the Γ point phonons. These results have been further corroborated by actual structural relaxations, where materials with $A < 2$ relax to the correct equillibrium state and respond correctly to different strains.

The force constants for the materials whose structural relaxation is suitably described by the VFF model are given in Table 5.8 below:

	N	P	As	Sb
Al	N/A	241 (454[a], -46%)	209 (360[b], -42%)	238 (318[c], -25%)
Ga	N/A	269 (366[d], -27%)	189 (273[d], -30%)	173 (231[c], -25%)
In	N/A	N/A	N/A	93 (185[c], -49%)

TABLE 5.7: Value of ω_{TO} predicted from eq.(5.33) given in units of cm^{-1}. Experimental values are given in brackets, followed by the error with respect to this experimental value. a= Ref [154]; b=Ref [155]; c=Ref [69]; d=Ref [157]

	k_r(eV $\mathring{A}^{-2}$)	k_θ(eV rad^{-2}))	k_{rr}(eV $\mathring{A}^{-2}$)	$k_{r\theta}$ (eV $\mathring{A}^{-1}\mathrm{rad}^{-1}$)	r_0(Å)
AlP	5.505	0.401	0.640	0.453	2.3691
AlAs	4.962	0.361	0.521	0.391	2.4623
AlSb	4.557	0.294	0.320	0.249	2.6794
GaP	6.237	0.464	0.455	0.421	2.3642
GaAs	5.292	0.397	0.396	0.364	2.4620
GaSb	4.542	0.319	0.264	0.258	2.6641
InSb	3.194	0.218	0.362	0.248	2.8419

TABLE 5.8: Force constant values of VFF model for selected III-V semicondcutors.

5.5 Description of third-order elasticity

The necessity of a third order description of elasticity, and the insufficiency of classical continuum and atomistic strain models in acheiving such a description, has been well established by various studies on the technologically important InAs/GaAs quantum dot system. Because of the nature of the Stransky-Krastanov growth of these heterostructures, they are normally modelled as pure InAs embedded in a GaAs matrix. With the lattice mistmatch between these binaries being about 7%, they are firmly outside of the region of linear strain theory.

Ellaway and Faux [158] demonstrated the considerable overestimation of the hydrostatic strain made by continuum models based on the linear strain theory. Deriving the strain dependence of the effective harmonic elastic constants (i.e. the third and higher order elastic constants) from an atomistic Stillinger Weber potential, they showed that a continuum model with and without taking this strain dependence into account, produced hydrostatic strains which differed by 16%.

Previous to this, Pryor [133] had delineated various advantages of calculating the strain field via the Keating or other atomistic models over continuum models. The most pertinent of these advantages is that atomistic models retain the atomic level symmetry that is lost in continuum models. However, Pryor also points out the divergence of the two models at large strains, and by claiming that "harmonicity is not assumed" in the Keating model in a list of advantages, implies that the Keating model can be relied upon to produce meaningful anharmonic behaviour. However, while the Keating model indeed involves terms which are higher than second order in the strain, this does not imply that the model has the ability to accurately capture energetics at these higher orders. Indeed, the derivatives of the Keating model to third order in the linear

strains is 0, and the derivatives to fourth order are equal to the second order derivatives (the harmonic elastic constants), and thus contribute negligibly to the strain. So while the two models diverge in the region of non-linear strain, there is no reason to suppose that either method can be trusted in these strain regimes outside of which they were parameterised. Nevertheless, this work clearly illustrated the need to account for departures from the small strain regime, and to do so atomistically.

This issue was then addressed by Lazarenkova *et. al* [159], who recognised not only the importance of the large strains present in these systems, but also the inability of the quasi-harmonic Keating model to take them accurately into account. In their work they sought to extend the Keating model to describe anharmonicity in the strain, via the inclusion of anharmonic bond length dependent adjustments to the two harmonic parameters. These adjustments were parameterised using the pressure depedence of phonon frequencies. While this model is widely used to treat nanostructures in which large strains are present, there are many means by which a more accurate description could be attained. To begin with, Table 5.2 shows that in terms of shear strains even in the harmonic regime, this model will suffer from errors of around 16%. In addition to this, fitting to the anharmonic dynamic properties does not guarantee that the anharmonic elasticity will be fully captured, and vice versa. To infer that the simple bond-bending and bond-stretching model can model static propeties when fitted to dynamic properties, is to assume a greater physical justification for the functional form of the Keating potential than its derivation warrants. This point is illustrated by Cousins [160], where in table 6.1, of this work, it is shown that the classic two parameter Keating model fitted only to elastic constants suffers a 17% error in the Raman frequency, and this same model fitted to C_{11} and the Raman frequency, will produce a value for C_{12} which is negative, and a value for C_{44} which is considerably inaccurate. These errors were associated with a fitting to diamond, for which the Keating model is more suited than any other material [61], thus the errors discussed here will be greater for other materials.

Thus, following Cousins, and a remarkably successful paper by Keating [156], we pursue the accurate atomistic description of third order elasticity by direct determination of the third order elastic properties, and direct parameterisation of a third order VFF model by these properties. This method does not make any assumptions about the physical verisimilitude of our simple potentials, nor their applicability outside of their fitting range. Of course, the third order elastic properties are not readily available for many semiconductors of interest (which perhaps motivated more indirect means of capturing the behaviour they determine), so in this section we first extract these properties using highly accurate HSE DFT methods, before considering their implementation in a VFF model.

5.5.1 Finite strain theory for cubic crystals

In order to rigourously describe third order elastic properties, the assumption of infinitesimal strains must be dropped and the Lagrangian strain formalism must be adopted. Murnaghan's finite strain theory has been applied to cubic crystals by Birch [55].

A useful matrix relation between the Lagrangian strain tensor and the small strain tensor will allow for easy determination of the Lagrangian strains in cases where the small strain tensor, or simply the deformation gradient tensor are specified:

$$\eta = \varepsilon + \frac{1}{2}\varepsilon^2. \tag{5.36}$$

The third order elastic constants are conventionally defined in terms of the expansion of the elastic energy density in terms of these Lagrangian strains; for a cubic crystal, this energy density is given by [54, 55, 161]:

$$\begin{aligned} U = {} & \frac{1}{2}C_{11}\left(\eta_1^2+\eta_2^2+\eta_3^2\right) + \frac{1}{2}C_{44}\left(\eta_4^2+\eta_5^2+\eta_6^2\right) + C_{12}\left(\eta_1\eta_2+\eta_1\eta_3+\eta_2\eta_3\right) \\ & + \frac{1}{6}C_{111}\left(\eta_1^3+\eta_2^3+\eta_3^3\right) + \frac{1}{2}C_{112}\left(\eta_2\eta_1^2+\eta_3\eta_1^2+\eta_2^2\eta_1+\eta_3^2\eta_1+\eta_2\eta_3^2+\eta_2^2\eta_3\right) + C_{123}\eta_1\eta_2\eta_3 \\ & + \frac{1}{2}C_{144}\left(\eta_1\eta_4^2+\eta_2\eta_5^2+\eta_3\eta_6^2\right) + \frac{1}{2}C_{155}\left(\eta_2\eta_4^2+\eta_3\eta_4^2+\eta_1\eta_5^2+\eta_3\eta_5^2+\eta_1\eta_6^2+\eta_2\eta_6^2\right) + C_{456}\eta_4\eta_5\eta_6. \end{aligned} \tag{5.37}$$

The derivatives of this energy with respect to the η_{ij} provide equations relating the Lagrangian strains to the stresses, via the elastic consnats:

$$t_i = \frac{\partial U}{\partial \eta_i} \tag{5.38}$$

Thus, the general expressions for each of the six Voigt components of the Lagrangian stress in terms of an arbitrary Lagrangian strain on a cubic crystal are:

$$\begin{aligned}
t_1 &= C_{11}\eta_1 + C_{12}\left(\eta_2+\eta_3\right) + \frac{1}{2}C_{111}\eta_1^2 + \frac{1}{2}C_{112}\left(2\eta_2\eta_1 + 2\eta_3\eta_1 + \eta_2^2 + \eta_3^2\right) \\
&\quad + C_{123}\eta_2\eta_3 + \frac{1}{2}C_{144}\eta_4^2 + \frac{1}{2}C_{155}\left(\eta_5^2+\eta_6^2\right), \\
t_2 &= C_{11}\eta_2 + C_{12}\left(\eta_1+\eta_3\right) + \frac{1}{2}C_{111}\eta_2^2 + \frac{1}{2}C_{112}\left(\eta_1^2 + 2\eta_2\eta_1 + \eta_3^2 + 2\eta_2\eta_3\right) \\
&\quad + C_{123}\eta_1\eta_3 + \frac{1}{2}C_{144}\eta_5^2 + \frac{1}{2}C_{155}\left(\eta_4^2+\eta_6^2\right), \\
t_3 &= C_{11}\eta_3 + C_{12}\left(\eta_2+\eta_1\right) + \frac{1}{2}C_{111}\eta_3^2 + \frac{1}{2}C_{112}\left(\eta_1^2 + \eta_2^2 + 2\eta_1\eta_3 + 2\eta_2\eta_3\right) \\
&\quad + C_{123}\eta_1\eta_2 + \frac{1}{2}C_{155}\left(\eta_4^2+\eta_5^2\right) + \frac{1}{2}C_{144}\eta_6^2, \\
t_4 &= C_{44}\eta_4 + C_{144}\eta_1\eta_4 + C_{155}\left(\eta_2\eta_4+\eta_3\eta_4\right) + C_{456}\eta_5\eta_6, \\
t_5 &= C_{44}\eta_5 + C_{144}\eta_5\eta_2 + C_{155}\left(\eta_5\eta_3+\eta_{55}\eta_1\right) + C_{456}\eta_4\eta_6, \\
t_6 &= C_{44}\eta_6 + C_{144}\eta_3\eta_6 + C_{155}\left(\eta_1\eta_6+\eta_2\eta_6\right) + C_{456}\eta_4\eta_5.
\end{aligned} \tag{5.39}$$

However, when the stresses on a strained supercell are measured in a DFT calculation using the Hellman Feynman theorem, or from an interatomic potential calculation, it is the stresses on the faces of the deformed configuration that are obtained. This is the Cauchy stress. Thus in order the use eqs.(5.39) we invert eq.2.43 to obtain:

$$\mathbf{t} = det\left(\mathbf{J}\right)\mathbf{J}^{-1}\sigma\left(\mathbf{J}^T\right)^{-1}, \tag{5.40}$$

where σ is the Cauchy stress, the superscript $^{\mathrm{T}}$ denotes a matrix transpose, and the superscript $^{-1}$ denotes the matrix inverse.

As well as improving the description of the macroscopic elastic properties, the precision with which the internal strain is described may also be improved; this involves a second, rather than first, order description of the internal strain. Taking, then, the zincblende cell shown in Fig. 5.3, the atom at the origin remains fixed, and the position of the central atom is given by:

$$\mathbf{r}_0 = J\mathbf{r}_0^0 + \mathbf{u} \tag{5.41}$$

Although this transformation completely specifies the deformed positions geometrically, the $\mathbf{u}$ are not suitable parameters in which to expand the scalar energy because they lack rotational invariance. Thus the Lagrangian strain, η, is used in place of J, and a rotationally invariant description of the internal strain is obtained through use of what Cousins [63, 137] calls the *inner displacement*, rather than simply the vector displacement between the two sublattices, denoted by $\mathbf{u}$. This is given by:

$$\zeta = J^T\mathbf{u}. \tag{5.42}$$

Because this inner displacement occurs in response to internal forces arising from the application of finite strain, each inner displacement can be expressed as a Taylor series in the components of the finite strain:

$$\zeta_i = A_{iJ}\eta_J + \frac{1}{2}A_{iJK}\eta_J\eta_K, \tag{5.43}$$

Here Voigt notation has been employed for the elements of the finite strain, and the subscripts relating to the strain are denoted by capitals, whilst those relating to the cartesian coordinate of the inner displacement are denoted by the lower-case i. The A_{iJ} and A_{iJK} are the first and second order *internal strain tensors*, respectively. Cousins [64, 137] gives the form of these tensors for a ZB crystal. The first order internal strain tensor may be expressed conveniently in matrix notation:

$$A_{iJ} = \begin{pmatrix} 0 & 0 & 0 & A_{14} & 0 & 0 \\ 0 & 0 & 0 & 0 & A_{14} & 0 \\ 0 & 0 & 0 & 0 & 0 & A_{14} \end{pmatrix}. \tag{5.44}$$

A matrix representation is not possible for A_{iJK}, but there are only three independent non-zero components. These are the components:

$$A_{114} = A_{225} = A_{336} \tag{5.45}$$

$$A_{156} = A_{246} = A_{345} \tag{5.46}$$

$$A_{124} = A_{235} = A_{316} = A_{134} = A_{215} = A_{326}. \tag{5.47}$$

Substituting eqs. (5.44) and (5.45) into eq. (5.43) yields an expression for the value of $\mathbf{r}_0$ which minimises the strain energy of a ZB crystal for a given applied finite strain:

$$\zeta = A_{14}\begin{pmatrix}\eta_4\\ \eta_5\\ \eta_6\end{pmatrix} + \frac{1}{2}\left[A_{114}\begin{pmatrix}\eta_1\eta_4\\ \eta_2\eta_5\\ \eta_3\eta_6\end{pmatrix} + A_{124}\begin{pmatrix}\eta_4\left(\eta_2+\eta_3\right)\\ \eta_5\left(\eta_3+\eta_1\right)\\ \eta_6\left(\eta_1+\eta_2\right)\end{pmatrix} + A_{156}\begin{pmatrix}\eta_5\eta_6\\ \eta_4\eta_6\\ \eta_4\eta_5\end{pmatrix}\right] \tag{5.48}$$

From eqs. (5.48) and (5.39) the values for the elastic and internal strain constants can be extracted if the stress, strain, and relaxed atomic positions are known. The details of this extraction form the content of the next section.

5.5.2 Extraction of third order elastic constants

For the extraction of third or higher order elastic constants, where the use of Lagrangian strains is needed, the deformation J_{ij} is normally chosen such that the Lagrangian strains have as simple a form as possible [161–163] so that the relations arising from eq. (5.38) are not overly complicated. While this strategy has not been executed here, the strain branches of eq. (5.1), with two independently variable parameters, and the abundance of fitting options provided by

the different stress components, ensure that the Lagrangian strains used, though complicated, are more than sufficient to determine all independent third order elastic constants and internal strain tensor components.

In what follows, whenever a strain is written in vector form, Voigt notation is used. Voigt notation will be used for the simplification of the fitting equations involving energy and strain, and the standard notation will be used where matrices can be used to simplify calculations, as in eq. (5.36). GaAs results will be shown as a particular case of the fitting method.

5.5.2.1 Lagrangian strains and elastic constants from $\varepsilon^{(1)}$

For strain branch $\epsilon^{(1)}$, of eq. (5.1) we have:

$$\epsilon^{(1)} = (0, 0, 0, \beta, \beta, \beta) = \begin{pmatrix} 0 & \frac{\beta}{2} & \frac{\beta}{2} \\ \frac{\beta}{2} & 0 & \frac{\beta}{2} \\ \frac{\beta}{2} & \frac{\beta}{2} & 0 \end{pmatrix}. \tag{5.49}$$

Utilising eq. (5.36) yields:

$$\eta^{(1)} = \begin{pmatrix} \frac{\beta^2}{4} & \frac{\beta}{2}+\frac{\beta^2}{8} & \frac{\beta}{2}+\frac{\beta^2}{8} \\ \frac{\beta}{2}+\frac{\beta^2}{8} & \frac{\beta^2}{4} & \frac{\beta}{2}+\frac{\beta^2}{8} \\ \frac{\beta}{2}+\frac{\beta^2}{8} & \frac{\beta}{2}+\frac{\beta^2}{8} & \frac{\beta^2}{4} \end{pmatrix} = \left(\frac{\beta^2}{4}, \frac{\beta^2}{4}, \frac{\beta^2}{4}, \beta+\frac{\beta^2}{4}, \beta+\frac{\beta^2}{4}, \beta+\frac{\beta^2}{4}\right). \tag{5.50}$$

Looking at eq. (5.39), then, one obtains the equations relating the Lagrangian stress to strain for this branch. t_1, t_2, and t_3 are produced solely by nonlinear strain effects, and are equal by symmetry. They are given by:

$$t_1 = t_2 = t_3 = \left(\frac{1}{32}C_{111} + \frac{3}{16}C_{112} + \frac{1}{16}C_{123} + \frac{1}{32}C_{144}\right)\beta^4 + \left(\frac{1}{4}C_{144} + \frac{1}{2}C_{155}\right)\beta^3 + \left(\frac{1}{4}C_{11} + \frac{1}{2}C_{12} + \frac{1}{2}C_{144} + C_{155}\right)\beta^2. \tag{5.51}$$

Without already knowing C_{11}, C_{12} and either C_{144} or C_{155}, eq. (5.51) cannot be used to reliably determine either. The coefficients to third order and higher in β tend to be too difficult to extract due to the relatively small contribution these higher powers and their coefficients make to the total stress. However, fixing these higher order terms, and inputting values for C_{11}, C_{12} and C_{155} determined through subsequent strain branches, a value for C_{144} can be obtained:

$$C_{144} = -12 \pm 4(34\%) \text{ GPa}. \tag{5.52}$$

The error given here is that associated with the least squares fitting. The largeness of the error in this quantity reflects the fact that it is being extracted as a relatively small component in

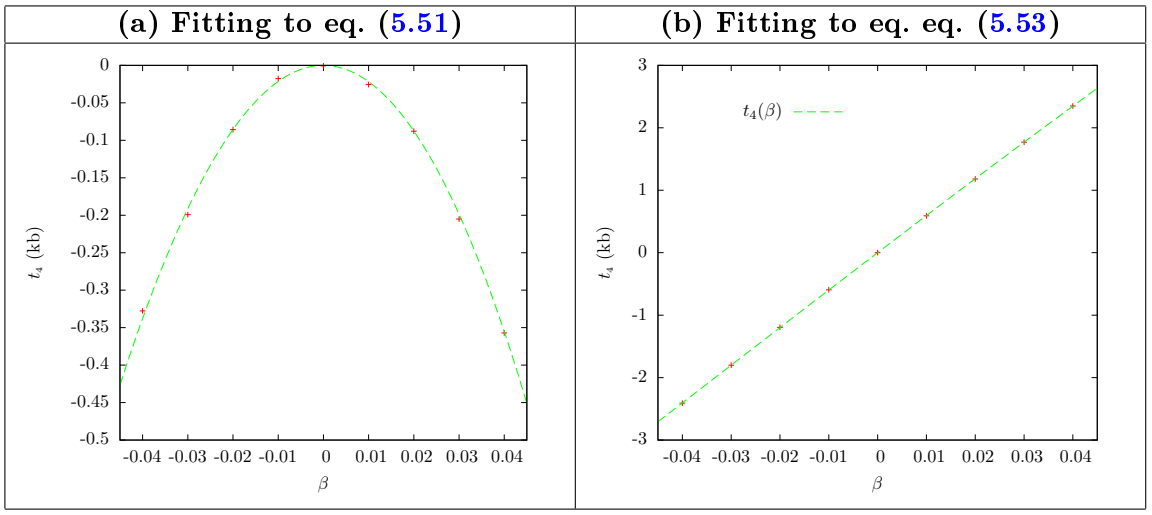

FIGURE 5.4: Fitting elastic constants to Lagrangian stress-strain equations for strain branch $\varepsilon^{(1)}$ applied to a GaAs primitive unit cell. (a) fitting to stress component t_1, t_2 and t_3 to obtain C_{144}(b) fitting to stress component t_4, t_5 and t_6 to obtain C_{456}

a prefactor to a small quantity. This difficulty is compounded by the cumulative errors in the values of the other constants which are substituted in. Nevertheless, this value agrees within the error with other estimations of C_{144}, and serves as a corroboration of other independent determinations of this quantity, as well as a validation for those constants used to determine it.

t_4, t_5, and t_6 are likewise equal by symmetry and given by:

$$t_4 = t_5 = t_6 = \left(\frac{1}{16}C_{144} + \frac{1}{8}C_{155} + \frac{1}{16}C_{456}\right)\beta^4 + \left(\frac{1}{4}C_{144} + \frac{1}{2}C_{155} + \frac{1}{2}C_{456}\right)\beta^3 + \left(\frac{1}{4}C_{44} + C_{456}\right)\beta^2 + C_{44}\beta. \quad (5.53)$$

Equation 5.53 can be used to obtain values for C_{44} (already presented in Table 5.1), and C_{456} independently of any knowledge of other constants. Again, the prefactors to higher powers of β are harder to accurately extract, and especially to decompose into the individual elastic coefficients given also the large differences in the magnitudes of these different factors. Fixing C_{155} (to the value determined independently from a later strain branch) and C_{144} (to anything with the correct order of magnitude), and fitting to eq. (5.53) the values for C_{44} and C_{456} can be optimised for the best fit. The results of these fittings are shown graphically in Fig. 5.4.

The results of the parameter optimisation are:

$$C_{44} = 59.65 \pm 0.04(0.07\%)\ \text{GPa}, \quad (5.54)$$

$$C_{456} = -33 \pm 1(4\%)\ \text{GPa}. \quad (5.55)$$

C_{44} and C_{456} are optimised to produce a very good fit to the data, and can be trusted as accurate values.

In addition to the elastic constants, the relaxed atomic positions give access to the non-zero components of the internal strain tensor. Substituting eq. (5.50) into eq. (5.48) reveals one non-zero component of the inner displacemnt:

$$\zeta_x = \frac{1}{32}\left(A_{114} + 2A_{124} + A_{156}\right)\beta^4 + \frac{1}{4}\left(\frac{1}{2}A_{114} + A_{124} + A_{156}\right)\beta^3 + \frac{1}{4}\left(A_{14} + 2A_{156}\right)\beta^2 + A_{14}\beta. \quad (5.56)$$

Fixing the coefficients to terms of order 2, this provides the internal strain tensor components:

$$A_{14} = -0.753 \pm 0.001(0.2\%)\ \text{Å}, \quad (5.57)$$

$$A_{156} = 2.38 \pm 0.08(3\%)\ \text{Å}. \quad (5.58)$$

In the same fashion, for the other branches, the Lagrangian strains are derived; however, for these cases there are two independent strain variables which necessitates a two dimensional fitting.

5.5.2.2 Lagrangian strains and elastic constants from $\varepsilon^{(2)}$

For strain branch $\epsilon^{(2)}$, of eq. (5.1) we have, from eq. (5.36):

$$\epsilon^{(2)} = (\alpha, 0, 0, \beta, 0, 0) = \begin{pmatrix} \alpha & 0 & 0 \\ 0 & 0 & \frac{\beta}{2} \\ 0 & \frac{\beta}{2} & 0 \end{pmatrix}$$
$$\Rightarrow \eta^{(2)} = \begin{pmatrix} \alpha + \frac{\alpha^2}{2} & 0 & 0 \\ 0 & \frac{\beta^2}{8} & \frac{\beta}{2} \\ 0 & \frac{\beta}{2} & \frac{\beta^2}{8} \end{pmatrix} = \left(\alpha + \frac{\alpha^2}{2}, \frac{\beta^2}{8}, \frac{\beta^2}{8}, \beta, 0, 0\right). \quad (5.59)$$

Substituting the strain of eq. (5.59) into eq. (5.39) the equations relating the two independent strain parameters, α and β to the Lagrangian stress, via the elastic constants are obtained. For t_1 we find:

$$t_1 = \frac{1}{8}C_{111}\alpha^4 + \frac{1}{2}C_{111}\alpha^3 + \frac{1}{8}C_{112}\alpha^2\beta^2 + \frac{1}{4}C_{112}\alpha\beta^2 + \frac{1}{64}\left(C_{112} + C_{123}\right)\beta^4 + \frac{1}{2}\left(C_{11} + C_{111}\right)\alpha^2 + C_{11}\alpha + \left(\frac{1}{4}C_{12} + \frac{1}{2}C_{144}\right)\beta^2. \quad (5.60)$$

From the form of eq. (5.60), and earlier mentioned considerations regarding the size of the terms of higher powers, it can be expected that accurate vales for C_{11} and C_{111} may be obtained, with a value for C_{144} possible if C_{12} is known, and if the sum of these two prefactors of β^2 is not too small. Fitting to eq. (5.60), with C_{112}, C_{123} and C_{12} fixed (to known values or values with the correct order of magnitude), the values and errors in the remaining constants are given:

$$C_{11} = 116.67 \pm 0.04\ (0.03\%)\ \text{GPa}, \tag{5.61}$$

$$C_{111} = -611 \pm 5\ (0.9\%)\ \text{GPa}, \tag{5.62}$$

$$C_{144} = -15.5 \pm 1.3\ (8.6\%)\ \text{GPa}. \tag{5.63}$$

We note that while very low errors are incurred for C_{11} and C_{111}, the percentage error in C_{144} is larger; this is to be expected for a constant of such small magnitude occuring at second order in the strain. However, the value is within the errors of the previous determination, eq. (5.52).

The Lagrangian stresses t_2 and t_3 are equal by symmetry and given by:

$$\begin{aligned} t_2 = t_3 = \frac{1}{8}C_{112}\alpha^4 + \frac{1}{2}C_{112}\alpha^3 + \frac{1}{128}\left(C_{111} + 3C_{112}\right)\beta^4 + \\ \frac{1}{16}\left(C_{112} + C_{123}\right)\alpha^2\beta^2 + \frac{1}{8}\left(C_{112} + C_{123}\right)\alpha\beta^2 + \\ \frac{1}{2}\left(C_{12} + C_{112}\right)\alpha^2 + C_{12}\alpha + \frac{1}{8}\left(C_{11} + C_{12} + 4C_{155}\right)\beta^2 \end{aligned} \tag{5.64}$$

From this equation, values for C_{12}, C_{155}, and C_{112} may be obtained, provided C_{11} is known accurately, and the other constants are fixed to reasonable values.

$$C_{12} = 49.58 \pm 0.04\ (0.07\%)\ \text{GPa}, \tag{5.65}$$

$$C_{112} = -353 \pm 4\ (1\%)\ \text{GPa}, \tag{5.66}$$

$$C_{155} = -263 \pm 1\ (0.4\%)\ \text{GPa}. \tag{5.67}$$

The only remaining non-zero stress, t_4, is given by:

$$t_4 = \frac{1}{2}C_{144}\alpha^2\beta + C_{144}\alpha\beta + \frac{1}{4}C_{155}\beta^3 + C_{44}\beta. \tag{5.68}$$

Associated with this stress are three elastic constants. Attempting to optimise all three will lead to a C_{155} value which is three times larger than its actual value and with the wrong sign, and with a huge error. While this value is not to be trusted, it can also not be tolerated as such a large spurious term would interfere with the fitting of the other terms. Therefore, C_{155} is fixed to a value known from other strain branches/stresses and values for C_{44} and C_{144} are

obtained:

$$C_{44} = 59.79 \pm 0.02\ (0.07\%)\ \text{GPa}\,, \tag{5.69}$$

$$C_{144} = -15 \pm 2\ (11\%)\ \text{GPa}\,. \tag{5.70}$$

Here again agreement is obtained for the inherently difficult to determine constant C_{144} with previous values, whilst C_{44} is optimised to a very good fit which is extremely close to the value of eq. (5.54).

For the inner displacement, substituting eq. (5.59) into eq. (5.48) reveals one non-zero component:

$$\zeta_x = A_{14}\beta + \frac{1}{2}\left(A_{114}\left(\alpha\beta + \frac{\alpha^2\beta}{2}\right) + A_{124}\frac{\beta^3}{4}\right). \tag{5.71}$$

This gives:

$$A_{14} = -0.75314 \pm 0.00006\ (0.009\%)\ \text{Å}\,, \tag{5.72}$$

$$A_{114} = 3.583 \pm 0.009\ (0.3\%)\ \text{Å}\,, \tag{5.73}$$

where the error ridden prefactor to the cubic $\frac{\beta^3}{4}$ is omitted here in favour of later more accurate determinations.

5.5.2.3 Lagrangian strains and elastic constants from $\varepsilon^{(3)}$

For strain branch $\epsilon^{(3)}$, of eq. (5.1) we have, from eq. (5.36):

$$\begin{aligned} \epsilon^{(3)} = (0,\alpha,0,\beta,0,0) &= \begin{pmatrix} 0 & 0 & 0 \\ 0 & \alpha & \frac{\beta}{2} \\ 0 & \frac{\beta}{2} & 0 \end{pmatrix} \\ \Rightarrow \eta^{(3)} &= \begin{pmatrix} 0 & 0 & 0 \\ 0 & \alpha + \frac{\alpha^2}{2} + \frac{\beta^2}{8} & \frac{\beta}{2} + \frac{\alpha\beta}{4} \\ 0 & \frac{\beta}{2} + \frac{\alpha\beta}{4} & \frac{\beta^2}{8} \end{pmatrix} = \left(0, \alpha + \frac{\alpha^2}{2} + \frac{\beta^2}{8}, \frac{\beta^2}{8}, \beta + \frac{\alpha\beta}{2}, 0, 0\right). \end{aligned} \tag{5.74}$$

Substituting the strain of eq. (5.74) into eq. (5.39) the equations relating the two independent strain parameters, α and β to the Lagrangian stress, via the elastic constants are obtained.

The equation relating t_1 to the two independent strain parameters is shown below:

$$t_1 = \frac{1}{8}C_{112}\alpha^4 + \frac{1}{64}\left(C_{112}+C_{123}\right)\beta^4 + \frac{1}{16}\left(C_{112}+C_{123}+2C_{144}\right)\alpha^2\beta^2 + \frac{1}{8}\left(C_{112}+C_{123}+4C_{144}\right)\alpha\beta^2 + \frac{1}{2}C_{112}\alpha^3 + \frac{1}{2}\left(C_{12}+C_{112}\right)\alpha^2 + C_{12}\alpha + \left(\frac{1}{4}C_{12}+\frac{1}{2}C_{144}\right)\beta^2. \quad (5.75)$$

The elastic constants obtained from this fitting are:

$$C_{12} = 49.51 \pm 0.04\ (0.09\%)\ \text{GPa}, \quad (5.76)$$

$$C_{112} = -350 \pm 6\ (2\%)\ \text{GPa}, \quad (5.77)$$

$$C_{144} = -15 \pm 1\ (9\%)\ \text{GPa}, \quad (5.78)$$

where agreement with previous fittings is again achieved.

For t_2 the relation is:

$$t_2 = \frac{1}{8}C_{111}\alpha^4 + \frac{1}{16}\left(C_{111}+C_{112}+2C_{155}\right)\alpha^2\beta^2 + \frac{1}{128}\left(C_{111}+3C_{112}\right)\beta^4 + \frac{1}{8}\left(C_{111}+C_{112}+4C_{155}\right)\alpha\beta^2 + \frac{1}{2}C_{111}\alpha^3 + \frac{1}{2}\left(C_{11}+C_{111}\right)\alpha^2 + C_{11}\alpha + \frac{1}{8}\left(C_{11}+C_{12}+4C155\right)\beta^2. \quad (5.79)$$

This provides values for C_{11}, C_{111} and C_{155} of:

$$C_{11} = 117.09 \pm 0.06\ (0.05\%)\ \text{GPa}, \quad (5.80)$$

$$C_{111} = -612 \pm 8\ (1\%)\ \text{GPa}, \quad (5.81)$$

$$C_{155} = -264 \pm 2\ (0.8\%)\ \text{GPa}. \quad (5.82)$$

We note that while C_{111} and C_{155} agree within error to previous determinations, this is not the case for C_{11}. This is not a problem, since the two values are still extremely close; but it does point out that the errors associated with the fitting should not be taken to give the whole of the uncertainty in the value. In this case, and in subsequent similar cases, where the disagreement between the values is larger than the errors in their fittings, we use instead the standard deviation between the values as the error in the final value, which can be considered to be less of an underestimation in the uncertainty.

For t_3 the relation is:

$$t_3 = \frac{1}{8}C_{112}\alpha^4 + \frac{1}{128}\left(C_{111} + 3C_{112}\right)\beta^4 + \frac{1}{8}\left(C_{112} + C_{155}\right)\alpha^2\beta^2 + \left(\frac{1}{4}C_{112} + \frac{1}{2}C_{155}\right)\alpha\beta^2 + \frac{1}{2}C_{112}\alpha^3 + \frac{1}{2}\left(C_{12} + C_{112}\right)\alpha^2 + C_{12}\alpha + \frac{1}{8}\left(C_{11} + C_{12} + 4C_{155}\right)\beta^2. \quad (5.83)$$

This differs little from t_1, with differences arising due to the higher order effects of the shear strain; it thus serves as a good consistentcy check for the constants derived above. This stress component gives values for C_{12}, C_{112} and C_{155} of:

$$C_{12} = 49.99 \pm 0.07\ (0.14\%)\ \text{GPa}, \quad (5.84)$$

$$C_{112} = -351 \pm 9\ (3\%)\ \text{GPa}, \quad (5.85)$$

$$C_{155} = -264 \pm 1\ (9\%)\ \text{GPa}. \quad (5.86)$$

Due to the sole shear component η_4 of the strain, t_4 is again the only non-zero shear stress:

$$t_4 = \frac{1}{4}C_{155}\alpha^3\beta + \frac{1}{8}C_{155}\alpha\beta^3 + C_{155}\alpha^2\beta + \frac{1}{4}C_{155}\beta^3 + \left(\frac{1}{2}C_{44} + C_{155}\right)\alpha\beta + C_{44}\beta. \quad (5.87)$$

With only two constants involved, this gives the values:

$$C_{44} = 59.94 \pm 0.03\ (0.04\%)\ \text{GPa}, \quad (5.88)$$

$$C_{155} = -265 \pm 2\ (9\%)\ \text{GPa}. \quad (5.89)$$

The equation describing the inner displacement for this branch is:

$$\zeta_x = A_{14}\beta + \frac{1}{2}\left(A_{14} + A_{124}\right)\alpha\beta + \frac{1}{8}A_{124}\beta^3 + \frac{1}{2}A_{124}\alpha^2\beta + \frac{1}{8}A_{124}\alpha^3\beta + \frac{1}{16}A_{124}\alpha\beta^3 \quad (5.90)$$

From this is obtained another value for A_{14} and the first value for A_{124}:

$$A_{14} = -0.75345 \pm 0.00008\ (0.01\%)\ \text{Å}, \quad (5.91)$$

$$A_{124} = 5.55 \pm 0.01\ (0.2\%)\ \text{Å}. \quad (5.92)$$

5.5.2.4 Lagrangian strains and elastic constants from $\varepsilon^{(4)}$

For strain branch $\epsilon^{(4)}$, of eq. (5.1) we have, from eq. (5.36):

$$\epsilon^{(4)} = (0, \alpha, \alpha, \beta, 0, 0) = \begin{pmatrix} 0 & 0 & 0 \\ 0 & \alpha & \frac{\beta}{2} \\ 0 & \frac{\beta}{2} & \alpha \end{pmatrix}$$
$$\Rightarrow \eta^{(4)} = \begin{pmatrix} 0 & 0 & 0 \\ 0 & \alpha + \frac{\alpha^2}{2} + \frac{\beta^2}{8} & \frac{\beta}{2} + \frac{\alpha\beta}{2} \\ 0 & \frac{\beta}{2} + \frac{\alpha\beta}{2} & \alpha + \frac{\alpha^2}{2} + \frac{\beta^2}{8} \end{pmatrix} = \left(0, \alpha + \frac{\alpha^2}{2} + \frac{\beta^2}{8}, \alpha + \frac{\alpha^2}{2} + \frac{\beta^2}{8}, \beta + \alpha\beta, 0, 0\right). \tag{5.93}$$

Substituting the strain of eq. (5.93) into eq. (5.39) the equations relating the two independent strain parameters, α and β to the stress, via the elastic constants are obtained. The equation relating t_1 to the two independent strain parameters is shown below:

$$\begin{aligned} t_1 = {} & \frac{1}{4}\left(C_{112} + C_{123}\right)\alpha^4 + \frac{1}{64}\left(C_{112} + C_{123}\right)\beta^4 + \frac{1}{8}\left(C_{112} + C_{123} + 4C_{144}\right)\alpha^2\beta^2 \\ & + \frac{1}{4}\left(C_{112} + C_{123} + 4C_{144}\right)\alpha\beta^2 + \left(C_{112} + C_{123}\right)\alpha^3 \\ & + \left(C_{12} + C_{112} + C_{123}\right)\alpha^2 + 2C_{12}\alpha + \left(\frac{1}{4}C_{12} + \frac{1}{2}C_{144}\right)\beta^2. \end{aligned} \tag{5.94}$$

From this fitting we obtain the first value for C_{123}. This value can be considered to be reliable before fitting: the term occurs as a prefactor to a low order polynomial term and the other constants which make up the prefactor, C_{12} and C_{112}, are well known from previous fittings. The elastic constants obtained from this fitting are:

$$C_{12} = 49.62 \pm 0.04\ (0.08\%)\ \text{GPa}, \tag{5.95}$$
$$C_{123} = -86 \pm 5\ (6\%)\ \text{GPa}, \tag{5.96}$$
$$C_{144} = -15 \pm 2.5\ (17\%)\ \text{GPa}. \tag{5.97}$$

For t_2 and t_3, which are equal by symmetry of the applied strain and crystal, the relation is:

$$\begin{aligned} t_2 = t_3 = {} & \frac{1}{8}\left(C_{111} + 3C_{112}\right)\alpha^4 + \frac{1}{128}\left(C_{111} + 3C_{112}\right)\beta^4 + \frac{1}{16}\left(C_{111} + 3C_{112} + 8C_{155}\right)\alpha^2\beta^2 \\ & + \frac{1}{8}\left(C_{111} + 3C_{112} + 8C_{155}\right)\alpha\beta^2 + \frac{1}{2}\left(C_{111} + 3C_{112}\right)\alpha^3 \\ & + \frac{1}{2}\left(C_{11} + C_{12} + C_{111} + 3C_{112}\right)\alpha^2 + \left(C_{11} + C_{12}\right)\alpha + \frac{1}{8}\left(C_{11} + C_{12} + 4C_{155}\right)\beta^2. \end{aligned} \tag{5.98}$$

The elastic constants obtained from this fitting are:

$$C_{111} = -662 \pm 40\ (6\%)\ \text{GPa}\,, \tag{5.99}$$

$$C_{155} = -263 \pm 10\ (4\%)\ \text{GPa}\,. \tag{5.100}$$

The value of C_{111} is within error of previous extractions, but the accuracy with which it can be determined is inherently limited by its heavy dependence on other constants. Thus this value for C_{111} is a useful confirmation of the accuracy of previous determinations, but will not be used in the final averaged value.

For t_4 the stress-strain relation is:

$$t_4 = C_{155}\alpha^3\beta + \frac{1}{4}C_{155}\alpha\beta^3 + \frac{1}{4}C_{155}\beta^3 + 3C_{155}\alpha^2\beta + (C_{44} + 2C_{155})\,\alpha\beta + C_{44}\beta. \tag{5.101}$$

The elastic constants obtained from this fitting are:

$$C_{44} = 60.18 \pm 0.06\ (0.1\%)\ \text{GPa}\,, \tag{5.102}$$

$$C_{155} = -264 \pm 2\ (0.8\%)\ \text{GPa}\,. \tag{5.103}$$

In addition to the elastic constants, the relaxed atomic positions give access to the non-zero components of the internal strain tensor. Substituting eq. (5.74) into eq. (5.48) reveals one non-zero component of the inner displacemnt:

$$\zeta_x = \frac{1}{2}A_{124}\alpha^3\beta + \frac{1}{8}A_{124}\alpha\beta^3 + \frac{1}{8}A_{124}\beta^3 + \frac{3}{2}A_{124}\alpha^2\beta + (A_{14} + A_{124})\,\alpha\beta + A_{14}\beta, \tag{5.104}$$

from which we obtain:

$$A_{14} = -0.7532 \pm 0.0006\ (0.08288\%)\ \text{Å}\,, \tag{5.105}$$

$$A_{124} = 5.55 \pm 0.04\ (0.8\%)\ \text{Å}\,. \tag{5.106}$$

5.5.2.5 Lagrangian strains and elastic constants from $\varepsilon^{(5)}$

$$\epsilon^{(5)} = (\alpha, \alpha, \alpha, \beta, \beta, \beta) = \begin{pmatrix} \alpha & \frac{\beta}{2} & \frac{\beta}{2} \\ \frac{\beta}{2} & \alpha & \frac{\beta}{2} \\ \frac{\beta}{2} & \frac{\beta}{2} & \alpha \end{pmatrix}$$

$$\Rightarrow \eta^{(5)} = \begin{pmatrix} \alpha + \frac{\alpha^2}{2} + \frac{\beta^2}{8} & \frac{\beta}{2} + \frac{\beta^2}{8} + \frac{\alpha\beta}{2} & \frac{\beta}{2} + \frac{\beta^2}{8} + \frac{\alpha\beta}{2} \\ \frac{\beta}{2} + \frac{\beta^2}{8} + \frac{\alpha\beta}{2} & \alpha + \frac{\alpha^2}{2} + \frac{\beta^2}{8} & \frac{\beta}{2} + \frac{\beta^2}{8} + \frac{\alpha\beta}{2} \\ \frac{\beta}{2} + \frac{\beta^2}{8} + \frac{\alpha\beta}{2} & \frac{\beta}{2} + \frac{\beta^2}{8} + \frac{\alpha\beta}{2} & \alpha + \frac{\alpha^2}{2} + \frac{\beta^2}{8} \end{pmatrix}$$

$$= \left(\alpha + \frac{\alpha^2}{2} + \frac{\beta^2}{8}, \alpha + \frac{\alpha^2}{2} + \frac{\beta^2}{8}, \alpha + \frac{\alpha^2}{2} + \frac{\beta^2}{8}, \beta + \frac{\beta^2}{4} + \alpha\beta, \beta + \frac{\beta^2}{4} + \alpha\beta, \beta + \frac{\beta^2}{4} + \alpha\beta \right). \tag{5.107}$$

Substituting the strain of eq. (5.107) into eq. (5.39) the equations relating stress to strain, via the elastic constants are obtained.

Under this strain branch t_1, t_2, and t_3 are equal by symmetry. These are given by:

$$\begin{aligned} t_1 = t_2 = t_3 = {} & \frac{1}{4}\left(\frac{1}{2}C_{111} + 3C_{112} + C_{123}\right)\alpha^4 + \frac{1}{32}\left(C_{111} + 6C_{112} + 2C_{123} + C_{144} + 2C_{155}\right)\beta^4 \\ & + \frac{1}{4}\left(\frac{1}{2}C_{111} + 3C_{112} + C_{123} + 2C_{144} + 4C_{155}\right)\alpha^2\beta^2 + \frac{1}{4}\left(C_{144} + 2C_{155}\right)\alpha\beta^3 \\ & + \left(\frac{1}{2}C_{111} + 3C_{112} + C_{123}\right)\alpha^3 + \frac{1}{4}\left(C_{144} + 2C_{155}\right)\beta^3 + \left(\frac{1}{4}C_{111} + \frac{3}{2}C_{112}\right) + \frac{1}{2}C_{123} + C_{144} + 2C_{155}\Big)\alpha\beta^2 \\ & + \left(\frac{1}{2}C_{11} + C_{12} + \frac{1}{2}C_{111} + 3C_{112} + C_{123}\right)\alpha^2 + \left(\frac{1}{4}C_{11} + \frac{1}{2}C_{12} + \frac{1}{2}C_{144} + C_{155}\right)\beta^2 + \left(C_{11} + 2C_{12}\right)\alpha. \end{aligned} \tag{5.108}$$

While this strain branch is overly complex to rely on for initial values of any of the elastic constants, it can be used for consistency checks, or to examine pure hydrostatic or pure shear strain behaviour. Below is an example of a consistency check, where the constants C_{123} and C_{144} are examined, for the reason that there is only one prior determination of C_{123} and C_{144} has larger percentage errors than most other constants.

$$C_{144} = -4.39511 \pm 17.96 \ (408.7\%) \ \text{GPa}, \tag{5.109}$$

$$C_{123} = -109.682 \pm 35.9 \ (32.73\%) \ \text{GPa}. \tag{5.110}$$

Given that the errors in this fitting are due not only to the fit itself, but are also compunded by the errors in each of the determined constants which must be used in the fitting, these two values show encouraging agreement with earlier determinations. Due to their large errors however, the values determined from this strain branch will serve only as checks, and not determinations, of the values of any of the elastic constants.

The Lagrangian stress components, t_4, t_5 and t_6 are also equal by symmetry and are given by:

$$\begin{aligned} t_4 = t_5 = t_6 = {} & \frac{1}{16}\left(C_{144} + 2C_{155} + C_{456}\right)\beta^4 + \left(\frac{1}{2}C_{144} + C_{155}\right)\alpha^3\beta \\ & + \left(\frac{1}{8}C_{144} + \frac{1}{4}C_{155} + C_{456}\right)\alpha^2\beta^2 + \frac{1}{2}\left(\frac{1}{2}C_{144} + C_{155} + C_{456}\right)\alpha\beta^3 \\ & + \frac{1}{2}\left(\frac{1}{2}C_{144} + C_{155} + C_{456}\right)\beta^3 + \left(\frac{3}{2}C_{144} + 3C_{155}\right)\alpha^2\beta + \left(\frac{1}{4}C_{144} + \frac{1}{2}C_{155} + 2C_{456}\right)\alpha\beta^2 \\ & + \left(\frac{1}{4}C_{44} + C_{456}\right)\beta^2 + \left(C_{44} + C_{144} + 2C_{155}\right)\alpha\beta + C_{44}\beta. \end{aligned} \tag{5.111}$$

From this branch we can determine C_{44} independently of any other values, and we may use it to check the values for the error ridden C_{144} and the seldom seen C_{456}:

$$C_{44} = 59.87 \pm 0.06\ (0.1\%)\ \text{GPa}, \tag{5.112}$$

$$C_{456} = -34.51 \pm 1.54\ (4\%)\ \text{GPa}, \tag{5.113}$$

$$C_{144} = -3.59 \pm 4\ (112\%)\ \text{GPa}. \tag{5.114}$$

In addition to the elastic constants, the relaxed atomic positions give access to the non-zero components of the internal strain tensor. Substituting eq. (5.107) into eq. (5.48) reveals only one non-zero component of the inner displacement:

$$\begin{aligned} \zeta_x = {} & \frac{1}{16}\left(A_{114} + 2A_{124} + 8A_{156}\frac{1}{2}\right)\alpha^2\beta^2 + \frac{1}{8}\left(A_{114} + 2A_{124} + 2A_{156}\right)\alpha\beta^3 + \frac{1}{32}\left(A_{114} + 2A_{124} + A_{156}\right)\beta^4 \\ & + \frac{1}{4}\left(A_{114} + 2A_{124}\right)\alpha^3\beta + \frac{1}{4}\left(3A_{114} + 6A_{124}\right)\alpha^2\beta + \left(\frac{1}{8}A_{114} + \frac{1}{4}A_{124} + A_{156}\right)\alpha\beta^2 \\ & + \frac{1}{8}\left(A_{114} + 2A_{124} + 2A_{156}\right)\beta^3 + \left(A_{14} + \frac{1}{2}A_{114} + A_{124}\right)\alpha\beta + \left(\frac{1}{4}A_{14} + \frac{1}{2}A_{156}\right)\beta^2 + A_{14}\beta. \end{aligned} \tag{5.115}$$

This yields values against which earlier obtained values can be checked:

$$A_{14} = -0.751 \pm 0.002\ (0.3\%)\ \text{Å}, \tag{5.116}$$

$$A_{114} = 3.8 \pm 0.3\ (9\%)\ \text{Å}, \tag{5.117}$$

$$A_{156} = 2.3 \pm 0.1\ (6\%)\ \text{Å}. \tag{5.118}$$

These show good agreement with all previous fittings.

In the next section we present the third order elastic and second order internal strain constants for all materials considered. Each value is an average over selected individual fittings.

5.5.2.6 Third order elastic constants for selected III-V materials

The third order elastic constants, averaged over the different values obtained in the previous section, are gathered in Table 5.9. The errors assigned to the averaged values is given by the sum of the individual errors, for example:

$$\Delta C_{111} = \frac{\sqrt{\Delta C_{111\_a}^2 + \Delta C_{111\_b}^2}}{2}. \tag{5.119}$$

Here ΔC_{111} refers to the error in the final averaged value of C_{111} and ΔC_{111_a} and ΔC_{111_b} are the individual fitting errors in the extractions of C_{111} from different branches. For C_{111}, as indicated above, there are two independent values used to obtain the average value in Table 5.9. These are the values from strain branches $\varepsilon^{(2)}$ and $\varepsilon^{(3)}$ in eqs. (5.62) and (5.81). For all materials these values agreed with each other and with the third determination shown in the previous section. For C_{112}, all three independent determinations are used. For C_{155}, of which there are many determinations, the value presented is the average of all 6 determined values, with the errors in these values given by eq. (5.119), except for the cases of InSb and InAs, where the standard deviations are used for aforementioned reasons.

For C_{144}, only those three values extracted from strain branches $\varepsilon^{(2)}$ and $\varepsilon^{(3)}$ are used, with the other values, highly dependent on other terms with errors of their own, used only as checks. We note, however, that for the very soft materials, GaSb and InSb, the values of C_{144} fluctuated in values always very close to 0, with InSb values even changing sign. We may infer from this that the small magnitudes of C_{144} for these materials may require a higher resolution of calculation.

For C_{123}, the value given is the value obtained from $\varepsilon^{(4)}$, corroborated by the value from $\varepsilon^{(5)}$, with which an average was not made because of the large fitting errors. Likewise for C_{456}, only one value was used, with the other generally being in agreement, though not sufficiently well determined to include in the final presented value. In Table 5.10 experimental and theoretical values for GaAs, and just theoretical values for the cubic nitrides are presented for comparison. We find good agreement between these experimental values and our calculated values, taking into account the fact that these measurements are taken at room temperature where materials tend to be softer[161] (with some measured constants even changing sign with changes in temperature) than at the 0 K limit of temperature at which DFT calculations are made. Our theoretical determinations are to be trusted over the others presented based on their closer agreement with experiment (particularly for the second order elastic constants which can be much more accurately determined experimentally), and the use of the accurate HSE hybrid functional approach [62, 73] for the treatment of the exchange-correlation energy, over the less accurate LDA (Ref [167]) or GGA (Ref [161]).

	C_{111}(GPa)	C_{112}(GPa)	C_{155}(GPa)	C_{144}(GPa)	C_{123}(GPa)	C_{456}(GPa)
AlN	-1119 (14)	-1036 (8)	-789 (3)	51 (3)	-44(12)	-11.6 (0.7)
AlP	-595 (4)	-428 (4)	-243 (1)	14.9 (0.9)	-103 (6)	-33 (1)
AlAs	-526 (4)	-364 (3)	-220 (1)	7.1 (0.7)	-86 (4)	-27 (1)
AlSb	-416 (3)	-268 (2)	-156.9 (0.6)	6.4 (0.5)	-77 (3)	-21.4 (0.7)
GaN	-1277 (8)	-976 (4)	-647 (2)	-46 (1)	-252 (9)	-49 (1)
GaP	-753 (8)	-441 (7)	-295 (1)	-10 (1)	-73 (7)	-47 (1)
GaAs	-612 (5)	-351 (4)	-264 (1)	-15.2 (0.9)	-86 (5)	-33(1)
GaSb	-471 (6)	-260 (5)	-192 (1)	-2.81 (0.96)	-63 (4)	-19.34 (0.27)
InN	-786 (8)	-701 (8)	-290.41 (0.86)	28 (2)	-327 (12)	22 (1)
InP	-491 (2.5)	-336 (2)	-168.57 (0.56)	-5.17 (0.59)	-131 (3.5)	-13.6 (0.6)
InAs	-419 (5)	-276 (4)	-154.3 (0.6)	-5.9 (0.8)	-125 (4.5)	-7.89 (0.70)
InSb	-319 (13)	-186 (10)	-120 (1)	-3 (2)	-114 (6)	-6.79 (0.8)

TABLE 5.9: Third order elastic constants of zincblende III-V compounds, calculated using HSE DFT. Fitting errors are indicated in brackets.

	Experimental: (GaAs)	Previous theoretical: (GaAs)	(AlN)	(GaN)	(InN)
C_{111}(GPa)	-675[a], -622[b], -620[c]	-600[d], -561[e]	-1073[e]	-1213[e]	-756[e]
C_{112}(GPa)	-402[a], -387[b], -392[c]	-401[d], -318[e]	-965[e]	-867[e]	-636[e]
C_{155}(GPa)	-320[a], -269[b], -274[c]	10[d], -16[e]	-757[e]	-606[e]	-271[e]
C_{144}(GPa)	-70[a], 2[b], 8[c]	-305[d], -242[e]	57[e]	-46[e]	13[e]
C_{123}(GPa)	-4[a],-57[b],-62[c]	-94[d], -70[e]	-61[e]	-253[e]	-310[e]
C_{456}(GPa)	-69[a], -39[b], -43[c]	-43[d], -22[e]	-9[e]	-49[e]	15[e]

TABLE 5.10: Previous experimental and theoretical determinations of third order elastic constants of GaAs and the cubic III-nitride materials. a= Ref [164]; b=Ref [165]; c=Ref [166]; d=Ref [167]; e=Ref [161]

The non-zero components of the internal strain tensor are given in Table 5.11. For A_{14} the values from $\varepsilon^{(1)}$, $\varepsilon^{(2)}$ and $\varepsilon^{(3)}$ are averaged. Since there is not the same abundance of equations with which to describe the higher order internal strain tensor components as there is for the elastic constants, the values for the different A_{iJK} are set simply to those of the single independent determination of lowest error. For A_{114} the only independent determination is that from $\varepsilon^{(2)}$, for A_{156}, it is $\varepsilon^{(1)}$. For A_{124} there are two independent determinations, but we include in the table only the value from the uncomplicated $\varepsilon^{(3)}$ strain branch, rather than the complex and error prone $\varepsilon^{(4)}$ extraction.

A further sanity check for the obtained elastic constants is their convergence with the number of k-points used in the DFT calculations. The behaviour of the three second order and six third order elastic constants with k-point mesh resolution is shown for our exemplar material GaAs in Fig. 5.5. We note that in all cases the difference between subsequent values converges to a magnitude which is of the order of the errors in those quantities.

In the next section how best to use these newly extracted elastic constants in the context of a VFF model is discussed.

	A_{14} (Å)	A_{114} (Å)	A_{124} (Å)	A_{156} (Å)
AlN	-0.5888 (0.0002)	4.339 (0.008)	4.478 (0.009)	2.33 (0.03)
AlP	-0.7936 (0.0003)	4.01 (0.01)	5.32 (0.01)	1.81 (0.06)
AlAs	-0.8187 (0.0003)	3.959 (0.009)	5.385 (0.007)	1.95 (0.06)
AlSb	-0.9129 (0.0003)	3.95 (0.01)	5.53 (0.01)	1.72 (0.06)
GaN	-0.6394 (0.0002)	4.04 (0.02)	6.11 (0.02)	1.97 (0.02)
GaP	-0.7295 (0.0002)	3.417 (0.008)	5.65 (0.01)	1.98 (0.04)
GaAs	-0.7533 (0.0005)	3.584 (0.009)	5.55 (0.01)	2.38 (0.08)
InN	-0.9357 (0.0002)	5.12 (0.05)	6.61 (0.04)	1.23 (0.03)
InP	-0.9645 (0.0004)	3.86 (0.03)	6.72 (0.03)	1.44 (0.07)
InAs	-0.9777 (0.0004)	3.91 (0.05)	6.58 (0.07)	1.70 (0.06)
InSb	-1.0427 (0.0009)	3.19 (0.25)	6.61 (0.07)	1.8 (0.1)
GaSb	-0.8499 (0.0002)	3.48 (0.02)	5.38 (0.01)	2.20 (0.03)

TABLE 5.11: Internal strain tensor components extracted from HSE DFT data for Ga, In, and Al containing III-V compounds. Fitting errors are given in brackets.

5.5.3 Extended valence force field potential

Knowing the elastic properties of different materials to third order, the next step in their modelling is to incorporate these properties into an atomistic VFF model. Anharmonic properties are incorporated into VFF models in a variety of ways, some of which are: anharmonic corrections to the harmonic force constants [131, 159, 168, 169], expansion of VFF energy directly in terms of Lagrangian strains [137], or expanding the VFF energy in terms of the deformation tensor/infinitesimal strains, and then relating this to the third order expression for the macroscopic energy density expressed in terms of the Lagrangian strains [156, 170]. In implementations of the first method, the anharmonic adjustments to the harmonic models are normally parameterised via the strain dependence of the Raman frequencies; however, parameterisation via anharmonic dynamic properties does not necessarily mean that those parameters which govern the crystal relaxation will also be reproduced. Furthermore, treating the effects of larger strains without recourse to finite strain theory may lead to inaccuracies and inconsistencies. The rigourous method of Cousins [160] is eschewed here for the more algebraically tractable method of Gerlich [170], given the purpose of this section is to outline and discuss, rather than implement, a possible third order VFF model.

The use of Gerlich's method in this context involves the same sort of expansion detailed in Appendix A, but with the taylor expansion extended to third order. For the model described by eq. (5.23), terms involving any unsquared bond lengths will appear at every order of the Taylor expansion (because they have components of the form $\varepsilon^{\frac{1}{2}}$), as will terms involving the bond angles (as these involve components of the form $arccos(\varepsilon)$); however, the force constants associated with these terms will occur with ever diminishing magnitude as the order of the derivative increases, and their purpose is anyway to describe the harmonic properties. Thus, in order to model third order macroscopic properties, microscopic interaction terms which are

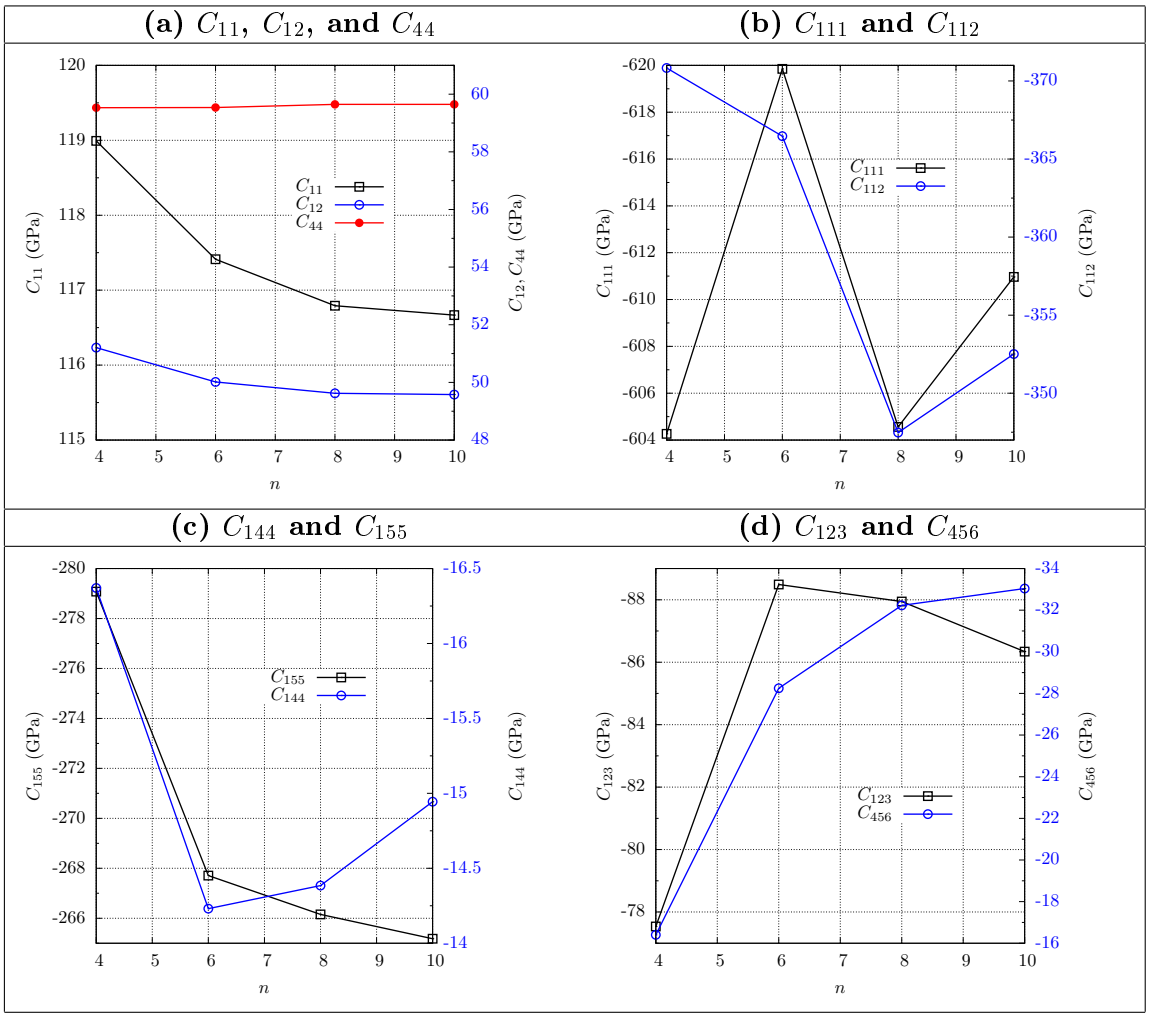

FIGURE 5.5: Convergence of different elastic constants of GaAs with increasing n x n x n k-point mesh.

third order in the bond lengths will need to be included, which will appear appreciably in an expansion to third order in the strain.

Given the success of Keating in matching the six third order elastic constants of germanium and silicon using only three force constants additional to his original model [156], a suitable starting point for the extension of our existing VFF model to third order, would be to include similar terms to eq. (5.23), but involving the more arithemtically abstruse but conceptually clear valence coordinates, rather than the easily expanded, but less simply interpretted, squared dot

products of Keating. Such a VFF model would be of the form:

$$\begin{aligned} V_i = & \frac{1}{2}\sum_{j\neq i}\frac{1}{2}k_r\left(r_{ij}-r_{ij}^0\right)^2+\frac{1}{2}\sum_{j\neq i}\frac{1}{6}k_{r3}\left(r_{ij}-r_{ij}^0\right)^3 \\ & +\sum_{j\neq i}\sum_{k\neq i,k>j}\left\{\frac{1}{2}k_\theta^i r_{ij}^0 r_{ik}^0\left(\theta_{ijk}-\theta_{ijk}^0\right)^2+\frac{1}{6}k_{\theta 3}^i r_{ij}^0 r_{ik}^0\left(\theta_{ijk}-\theta_{ijk}^0\right)^3\right. \\ & +k_{r\theta}^i\left[r_{ij}^0\left(r_{ij}-r_{ij}^0\right)+r_{ik}^0\left(r_{ik}-r_{ik}^0\right)\right]\left(\theta_{ijk}-\theta_{ijk}^0\right) \\ & \left.+k_{rr}^i\left(r_{ij}-r_{ij}^0\right)\left(r_{ik}-r_{ik}^0\right)+k_{r\theta^2}^i\left[r_{ij}^0\left(r_{ij}-r_{ij}^0\right)+r_{ik}^0\left(r_{ik}-r_{ik}^0\right)\right]\left(\theta_{ijk}-\theta_{ijk}^0\right)^2\right\} \end{aligned} \tag{5.120}$$

We note that this potential does not have all third order cross terms. A bond-squared-angle term could also be included. However, whether or not this is necessary will not be known until fittings are made and the resulting force constants and elastic constant predictions are tested. It is likely that the III-V semiconductors in which we are interested are not as well modelled by so few force constants as the group IV elements are. Nevertheless, eq. (5.120) makes a good starting point.

The expansion of eq. (5.120) in terms of the infinitesimal strain is straightforward. However, the third order elastic constants are the coefficients of the Lagrangian strains, as in eq. (5.37), and expressing eq. (5.120) in terms of these is less straight forward. To circumvent the difficulty of expanding the VFF model in terms of the Lagrangian strains, the general Lagrangian strain tensor can be expressed in terms of the infinitesimal strain tensor and substituted into eq. (5.37) [170]. Using eq. (5.36) as earlier, we obtain, for the general strain:

$$\begin{aligned} \eta_1 &= \varepsilon_1+\frac{1}{2}\left(\varepsilon_{11}^2+\varepsilon_{12}^2+\varepsilon_{13}^2\right) \\ \eta_2 &= \varepsilon_2+\frac{1}{2}\left(\varepsilon_{22}^2+\varepsilon_{23}^2+\varepsilon_{12}^2\right) \\ \eta_3 &= \varepsilon_3+\frac{1}{2}\left(\varepsilon_{33}^2+\varepsilon_{23}^2+\varepsilon_{13}^2\right) \\ \eta_4 &= \varepsilon_4+\left(\varepsilon_{23}\left(\varepsilon_{22}+\varepsilon_{33}\right)+\varepsilon_{12}\varepsilon_{13}\right) \\ \eta_5 &= \varepsilon_5+\left(\varepsilon_{13}\left(\varepsilon_{11}+\varepsilon_{33}\right)+\varepsilon_{12}\varepsilon_{23}\right) \\ \eta_6 &= \varepsilon_6+\left(\varepsilon_{12}\left(\varepsilon_{11}+\varepsilon_{22}\right)+\varepsilon_{13}\varepsilon_{23}\right). \end{aligned} \tag{5.121}$$

Substituting this into eq. (5.37) yields an expression for the energy to which the VFF model of eq. (5.120), expanded to third order in the infinitesimal strains, may be compared and fitted:

$$\begin{aligned} U = &\frac{1}{2}C_{11}\left(\varepsilon_1^2+\varepsilon_2^2+\varepsilon_3^2\right)+C_{12}\left(\varepsilon_1\varepsilon_2+\varepsilon_1\varepsilon_3+\varepsilon_2\varepsilon_3\right)+\frac{1}{2}C_{44}\left(\varepsilon_4^2+\varepsilon_5^2+\varepsilon_6^2\right)+\frac{1}{6}\left(3C_{11}+C_{111}\right)\left(\varepsilon_1^3+\varepsilon_2^3+\varepsilon_3^3\right) \\ &+C_{123}\varepsilon_1\varepsilon_2\varepsilon_3+\frac{1}{2}\left(C_{12}+C_{112}\right)\left(\varepsilon_1\left(\varepsilon_{22}^2+\varepsilon_{33}^2\right)+\varepsilon_{22}\left(\varepsilon_{11}^2+\varepsilon_{33}^2\right)+\varepsilon_{33}\left(\varepsilon_{11}^2+\varepsilon_{22}^2\right)\right) \\ &+\left(C_{12}+C_{144}\right)\left(\varepsilon_{11}\varepsilon_{23}^2+\varepsilon_{22}\varepsilon_{13}^2+\varepsilon_{33}\varepsilon_{12}^2\right) \\ &+\left(C_{11}+C_{12}+4C_{44}+4C_{155}\right)\left(\varepsilon_{11}\left(\varepsilon_{12}^2+\varepsilon_{13}^2\right)+\varepsilon_{11}\left(\varepsilon_{12}^2+\varepsilon_{13}^2\right)+\varepsilon_{33}\left(\varepsilon_{13}^2+\varepsilon_{23}^2\right)\right) \\ &+2\left(3C_{44}+4C_{456}\right)\varepsilon_{12}\varepsilon_{32}\varepsilon_{13} \end{aligned} \tag{5.122}$$

From the above expression, we see that, once the bond lengths and angles of any VFF model are expressed in terms of the infinitesimal strain, and minimised with respect to the internal strain, then the third order elastic constants may be related to the microscopic force constants via the third derivatives of the microscopic energy with respect to the strain. The conditions that the internal strain minimises the energy will determine equations relating the force constants to the components of the internal strain tensor.

Once these equations are obtained there are several ways to parameterise the VFF model. One would be a least squares fitting to all or some of the constants, which can be done however many interaction terms are included in the potential. Another is to increase the number of force constants until all the elastic and internal strain tensor components can be exactly fitted. Another still is to fit only to those elastic constants which are deemed significant for a particular material under particular circumstances.

As an example of a scenario where some elastic constants are more or less important than others, consider the stress t_1 in eq. 5.39, and consider a general applied strain of the form: $\varepsilon = (\alpha, \alpha, \alpha, \beta, \beta, \beta)$. In this notation, t_1, will have the form:

$$t_1 = C_{11}\alpha + 2C_{12}\alpha - \frac{C_{111}}{2}\alpha^2 - 3C_{112}\alpha^2 - C_{123}\alpha^2 - \frac{C_{144}\beta^2}{2} - C_{155}\beta^2, \tag{5.123}$$

Setting $\alpha = 0.1$ gives a 10% Lagrangian hydrostatic strain, and setting $\beta = 0.02$ gives a 2% shear strain. Substituting these values in and considering the t_1 which would be produced in GaAs, we may examine the contribution of the separate terms to the stress:

$$t_1 = 117(0.1) + 50(0.2) - \frac{612}{2}(0.01) - 351(0.03) - 86(0.01) - \frac{15}{2}(0.0004) - \frac{264}{2}(0.0008) = 7, \tag{5.124}$$

with contributions (in GPa) from the terms of: C_{11}: 12 ; C_{12}:10 ; C_{111}: -3 ; C_{112}: - 11 ; C_{123}: -0.9 ; C_{144}: - 0.003; C_{155}: - 0.05. While for the shear stress, t_4, we obtain:

$$t_4 = 60(0.02) - 15(0.002) - 264(0.004) - 33(0.0004) = 0.1, \tag{5.125}$$

with contributions from the terms of: C_{11}: 12 ; C_{12}:10 ; C_{111}: -3 ; C_{112} - 11 ; C_{123} -0.9 ; C_{144}: - 0.003; C_{155}: - 0.05. From this we see that a possible simplification of the fitting procedure for GaAs could be to neglect completely C_{144} and C_{456}, whilst possibly also neglecting C_{123}. We note that, by the similarity of the relative magnitudes of the second order to third order constants of GaAs and InAs, the large impact of C_{155} on the shear stress, casts doubt on the conclusion of Ellaway and Faux [158], where the effective C_{44} is said to be nearly constant with strain. Given their use of the Stillinger Weber potential[171] to calculate these properties, and given that the particular implementation used modelled the shear elastic constant inaccurately even in the harmonic regime, the description of third order properties given by our HSE DFT extracted elastic constants, is more reliable.

The details of the fitting procedure, and how this may lead to modifications of the potential form, will be the topic of a later work.

5.6 Conclusion and outlook

In this chapter, shortcomings in the commonly used descriptions of harmonic and third order elasticity were pointed out, and the ground work for their improvement was laid.

In the harmonic regime, a circumvention of these shortcomings was sought firstly via accurate determination of the elastic constants and the commonly neglected Kleinman parameter; and secondly by the implementation of a VFF model, originally due to Musgrave [134] and modified by Martin [84], which explicitly fits to the oft ill-described Kleinman parameter, as well as the three cubic elastic constants, of which C_{44} was often poorly represented in the popular Keating [61] model. By analysis of the anisotropy parameters of different III-V materials, a direct analytic relation amongst the force constants of this potential, and the elastic and Kleinman constants of the materials in question was obtained. It was determined that the model is suitable only for the description of those materials for which the anisotropy factor is < 2. Given that all the cubic nitrides and InAs have $A > 2$, this is a serious shortcoming for the model. However, an immediate next step in its developement is the inclusion of Coulombic effects. If Martin's [84] method for the parameterisation of the Coulomb interaction is implemented (via the transverse and longitudinal optical phonon splitting), then the direct analytic relation between microscopic force constants and experimental quantities can be maintained. Furthermore, different fitting schemes may be pursued even before the inclusion of Coulombic effects. Since it is the constant B_{xx} which determines whether or not the model posseses a minimum with respect to the internal strain, this quantity can be directly fitted to, with the value for B_{xx} derived either from the longitudinal optical phonon frequencies, or directly from DFT calculations. Finally, given the increased fitting parameter set provided by use of the bare, rather than relaxed, elastic constants, and the formerly unavailable means of their determination by

DFT calculation, the fifth parameter of Musgrave and Pople [134], excluded by Martin [84], may be tentatively reinstated, and all possible nearest-neighbour harmonic interactions then accounted for.

In the regime of large strains, previously unknown third order elastic and internal strain constants were extracted from accurate HSE DFT data. The elastic constants were extracted via stress-strain relations expressed within the formalism of finite strain, and found to agree well with experiment and previous theory (over which our extracted values are to be trusted, due to the higher quality of the exchange-correlation functional with which the data were calculated). The components of the second order internal strain tensor extracted here have not before been measured or calculated. With the anharmonic properties of many III-V materials thus suitably determined, a suggestion for their incorporation into an atomistic model is made with reference to previous studies. With the newly extracted accurate values for the elastic properties, it is expected that a VFF model, parameterised using these constants in the manner of Keating and Gerlich [156, 170], will offer significant advantages in modelling the relaxation of highly strained heterostructures.

The amelioration of the harmonic potential by the inclusion of the important Coulombic interaction, and the developement of a VFF made specifically to capture the elastic (and not phonon) properties of highly strained heterostructures, and thus their relaxation properties, will form the content of a later work.

Chapter 6

Conclusions and Outlook

6.1 Conclusions

This thesis has presented the results of a theoretical investigation into the electronic and optical properties of InGaN/GaN quantum wells (QWs). Detailed atomistic analyses were performed on both c-plane and m-plane QWs using an atomistic sp^3 tight-binding model, which includes effects such as strain and polarisation field variations due to random alloy effects. In particular, localisation effects related to random alloy fluctuations were analysed. For the case of metastable cubic nitride based systems, the beginnings of a theoretical framework in which to perform a similar analysis were laid out. This involved the determination of the fundamental elastic properties of cubic III-V compounds, including the III-N materials, and their use to establish atomistic valence force field models.

In Chapter 3 the impact of random alloy fluctuations on the localisation features of both ground and excited states in c-plane InGaN/GaN QW systems is addressed. To cover the experimentally relevant indium composition ranges, we analyse InGaN QWs with indium contents varying between 10% and 25%. The results show that for as little as 10% indium in the QWs, an energy range of localised hole states of order 100 meV is expected. In addition, our data shows that the extent and range of the hole localisation depends on the indium content of the system in question. We find that at higher indium contents states are more localised, and localised over a wider energy range in the valence band. For each indium content these localised states will therefore play an important role in determining device properties at ambient temperature. The calculations also reveal that in c-plane structures, the localisation of both electrons and holes is enhanced by the built-in field. In particular, we find that the built-in field in combination with structural inhomogeneities such as alloy fluctuations as well as well width fluctuations can lead to significant electron localisation. Furthermore, the built-in field acts against the Coulomb interaction to separate the electrons and holes along the growth axis, leading to the situation

of individually localised electrons and holes. This is consistent with the non-exponential decay transients measured in time-dependent photoluminescence (PL) experiments on c-plane structures and early models used to interpret them. A study of the overlaps between different hole states, different electron states, and electron and holes states, reveals that the localisation in these systems will be such that it limits transport amongst the well localised hole states, and hampers radiative recombination between the individually localised and separated electron and hole states, at least at low temperatures and low carrier densities.

In Chapter 4, where we treat the m-plane system and the built-in field is absent, we find that the Coulombic interaction becomes significant, and electrons and holes are localised together as excitons in indium rich regions of the QW. This is consistent with the experimentally measured single exponential decay transients found in time-resolved PL measurements performed on m-plane structures, and we show, by explicit calculation of optical properties that the experimental features are correctly attributed to random alloy effects. Similarly to the case of c-plane systems, we find that localisation effects in m-plane QWs persist into the valence band over an energy range of at least 100 meV, and that these localisation effects are such that they will significantly affect the overlap between hole states, and thus the transport properties of m-plane InGaN devices.

Considered together, our calculations on c- and m-plane InGaN QWs in chapters 3 and 4 reveal that random alloy fluctuations alone are sufficient to bring about carrier localization effects in both systems. This result is important in the context of earlier studies on nitride materials and devices, where it was believed that gross indium clustering, rather than simple random alloy fluctuations, were the source of carrier localisation. We also find generally that the localisation effects are much stronger for the hole states than for the electron states. In both cases, a significant density of localised hole states is observed. These results are consistent with the experimentally observed large full width at half maxium (FWHM) of PL spectra in both c- and m-plane systems. While the mechanism by which the random alloy fluctuations lead to localisation of the hole states is the same in each system, the different macroscopic properties associated with the two growth planes, lead to significant differences in the overall nature of carrier localisation in each system.

It is important to note that widely used standard continuum-based models do not capture these effects (in-plane separation, wave function localisation due to alloy fluctuations); and first principles studies are unable to treat the large number of atoms necessary to capture the interplay between microscopic random alloy effects, and the macroscopic structural properties, including the built-in field and well width fluctuations. Therefore, the semi-empirical fully atomistic approach presented offers a completeness of description lacking in previous studies.

In Chapter 5, motivated by a desire to study the cubic nitrides, the first components of the necessary theoretical framework were developed. In an initial step, the harmonic elastic properties

were extracted from HSE DFT data. Relations amongst the determined elastic constants and Kleinman parameter are used to illustrate shortcomings in the currently available valence force field (VFF) models used to calculate local strain and relaxed atomic positions in cubic III-V semiconductor alloys. This analysis revealed that widely used VFF models suffered cumulative errors of up to 38% in the description of some elastic constants, and 30% in the description of internal strain. Noting the importance of internal strain when treating piezoelectric properties, a new VFF implementation is introduced, based on that due to Martin, with additional parameters, allowing for an accurate description of the formerly neglected C_{44} elastic constant, and the Kleinman internal strain parameter, ζ. The implementation retains the benefit of a simple analytic relation between the VFF force constants and the elastic constants enjoyed by the popular Keating model, but does not share its inaccuracies. Unfortunately, the model was found to be suitable only for the description of those materials with an elastic anisotropy factor < 2, and this does not include the III-N materials. In a second step, recognising the large strains that may occur in the semiconductor devices made using higly lattice-mismatched materials such as InN and GaN, third order elastic properties are extracted from highly accurate HSE DFT data. This extration is performed by fitting to third order elastic formulae, using finite-strain theory. Some of these third order elastic constants are the first to be published for the materials in question, and most of the constants are determined to a higher degree of accuracy than those previously given in the literature. Finally, the utilisation of these properties in a VFF model is discussed, and an appropriate functional form is suggested.

6.2 Outlook

In chapters 3 and 4, we have investigated in detail of the localised states which dominate the properties of InGaN/GaN QWs. While we have made reliable conservative estimations of the energy range covered by these states, we were limited by finite size effects and time constraints from providing a more precise determination of this quantity.

An alternative possible means to determine when the states in the valence band become delocalised and governed by the overall geometry of the QW, would be to consider, using our calculated tight-binding wave functions, the expectation value of the in-plane components of the position vector, $\mathbf{r}$. That is, assuming growth in the z direction, to calculate $\langle\psi|x|\psi\rangle$ and $\langle\psi|y|\psi\rangle$ from the tight binding wavefunctions, ψ. When a state is delocalised it will be subject to the wider confining potential of the QW, and so will be approximately either symmetric or antisymetric about the centre of the QW. Its x and y expectation values will therefore be in the centre of the well. For consecutive localised states however, these quantities will vary greatly from one state to the next. The standard deviation of $\langle\psi|x|\psi\rangle$ and $\langle\psi|y|\psi\rangle$ will thus be large for the localised states, whilst for the delocalised states, the standard deviation will be approximately 0. We may thus define the point in energy beyond which the states, in a given

QW are no longer localised, E_{mob}, as the energy beyond which the standard deviation in the values of $\langle\psi|x|\psi\rangle$ and $\langle\psi|y|\psi\rangle$ has become sufficiently close to 0. Unlike localised states, the overlap behaviour of these states will depend on the nodal structure of subsequent states in the QW, and will not share the monotonic increase in overlap with energy which was identified in Chapter 3, as a property of localised states.

To determine whether or not E_{mob}, thus determined, is subject to finite-size effects, its variations across different configurations of the same supercell, can be examined. If this variation is large for different configurations, then finite size effects are playing a role. These finite size effects may be reduced by increasing the supercell size. If there is a small deviation between the E_{mob} values in different configurations, then we may infer that finite size effects have a smaller impact. Furthermore, when convergence is obtained with increasing supercell size of E_{mob}^{avg}, the average of E_{mob} over all random configurations for a given supercell size, then we may say that our supercell size is large enough that our study of the densitiy of localised states is suitably independent of cell-size. However, such a study would be extremely time consuming, as not only does increasing the cell size increase the size of the Hamiltonian which must be set up and diagonalised to calculate the states, an ever increasing amount of localised states would need to be calculated. This is because the number of localised states in a given QW will depend on its size. Having obtained this E_{mob}, we may use the number of localised states in a QW divided its area, to estimate the carrier densities at which saturation of localised states may occur.

Given that the efficiency droop in nitride systems has been variously linked to saturation of localised states at higher current densities [18, 20, 21] and to Auger recombination [41, 42], further theoretical studies would provide valuable insights. A precise estimate of the energy range and density of localised states could help to disentangle these two effects. On the one hand, improved knowledge of the localised state distribution could help to identify the carrier, and hence current density at which delocalisation occurs. On the other hand, the localised tight-binding wave functions could be used as input to calculate Auger matrix elements and hence the expected dependence of Auger recombination on carrier and current density in typical QW structures. Although these calculations would require large effort and computational resources, they could also give a significantly improved understanding of the relative importance of different loss mechanisms in III-N optical devices.

Building on the m-plane results, the properties of InGaN/GaN QWs grown on the a-plane or on semi-polar planes could be readily investigated with the same theoretical framework used here. In particular, the relation in semi-polar QWs, between the reduced built-in fields and the QW microstructure could be examined. The nature of the recombination in these systems, whether excitonic or non-excitonic, could be then assertained. These studies would be worthwhile given

the superior indium incorporation properties of certain semi-polar growth plains over the m-plane [38]. In the case of a-plane InGaN QWs, the origin of the lower DOLP with respect to the m-plane case [172] would make an interesting study.

With respect to the work of Chapter 5, and the study of cubic nitride systems, the immediate outlook is the improvement of the VFF model. The first step will be the inclusion of Coulombic effects. If Martin's [84] method for the parameterisation of the Coulomb interaction is implemented (via the transverse and longitudinal optical phonon splitting), then the direct analytic relation between microscopic force constants and experimental quantities can be retained.

Furthermore, different fitting schemes to the elastic properties may be pursued. Since it is the constant B_{xx} which determines whether or not the model posseses a minimum with respect to the internal strain, this quantity can be directly fitted to, with the value for B_{xx} derived either from the longitudinal optical phonon frequencies, or directly from DFT calculations. Finally, given the increased fitting parameter set provided by use of the bare, rather than relaxed, elastic constants, the fifth parameter of Musgrave and Pople [134], excluded by Martin [84], may be re-incorporated in the model, and all possible nearest-neighbour harmonic interactions then accounted for.

In the regime of large strains, with the newly extracted accurate values for the third order elastic properties, it is expected that a VFF model, parameterised using these constants in the manner of Keating and Gerlich [156, 170], will offer significant advantages in modelling the relaxation and local strain of highly lattice-mismatched heterostructures.

With the VFF model in place, attention may be turned to the parameterisation of a tight binding model for the study of the electronic properties of cubic InGaN/GaN QWs.

Overall, we conclude that the investigations presented in this thesis not only provide very useful insight into the properties of III-N heterostructures, but can also be used as the starting point for further studies to investigate a wide range of growth directions and cubic nitride growth, as well as to provide a better understanding of the dominant loss mechanisms in existing III-N devices.

Appendix A

Expansion of valence force field energy in terms of strain

The total energy associated with displacing an atom from equillibrium in a zincblende crystal is given in our model by:

$$V_i = \frac{1}{2}\sum_{j\neq i}\frac{1}{2}k_r\left(r_{ij}-r_{ij}^0\right)^2+\sum_{j\neq i}\sum_{k\neq i,k>j}\left\{\frac{1}{2}k_\theta^i r_{ij}^0 r_{ik}^0\left(\theta_{ijk}-\theta_{ijk}^0\right)^2 + k_{r\theta}^i\left[r_{ij}^0\left(r_{ij}-r_{ij}^0\right)+r_{ik}^0\left(r_{ik}-r_{ik}^0\right)\right]\left(\theta_{ijk}-\theta_{ijk}^0\right)+k_{rr}^i\left(r_{ij}-r_{ij}^0\right)\left(r_{ik}-r_{ik}^0\right)\right\} \tag{A.1}$$

where r_{ij}^0 (θ_{ijk}^0) and r_{ij} (θ_{ijk}) are the equillibrium and displaced bond lengths (bond angles), respectively.

In order to relate this microscopic expression for the energy to the macroscopic properties of the crystal, we treat the total energy of a single primitive cell. The atoms, bonds and angles involved are shown in fig. A.1.

The lattice vectors of the primitive cell are defined by:

$$\begin{aligned}\mathbf{a}^0 &= \{0,\frac{a_0}{2},\frac{a_0}{2}\},\\ \mathbf{b}^0 &= \{\frac{a_0}{2},0,\frac{a_0}{2}\},\\ \mathbf{c}^0 &= \{\frac{a_0}{2},\frac{a_0}{2},0\}.\end{aligned} \tag{A.2}$$

with the two basis atoms within the cell at positions:

$$\begin{aligned}\mathbf{r}_1^0 &= \{0,0,0\},\\ \mathbf{r}_0^0 &= \{\frac{a_0}{4},\frac{a_0}{4},\frac{a_0}{4}\}.\end{aligned} \tag{A.3}$$

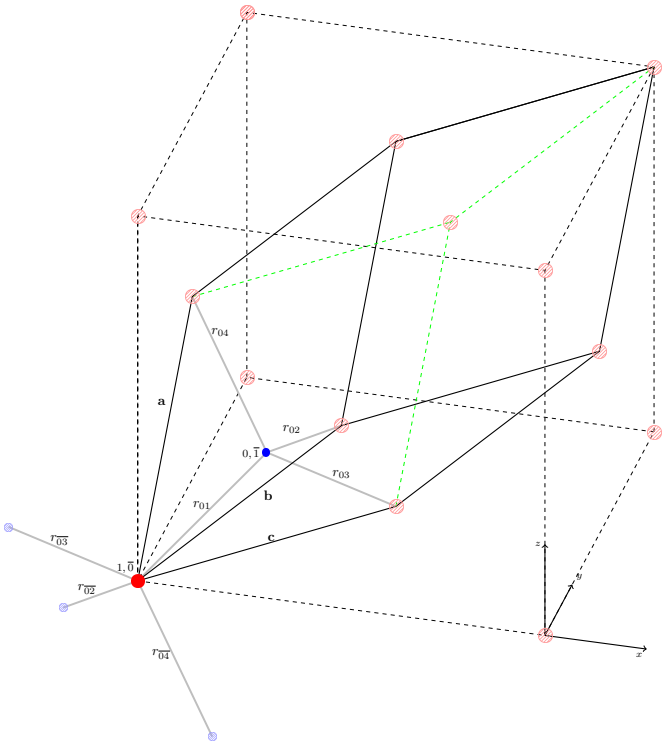

FIGURE A.1: Zincblende unit cell.

In a strained crystal with a monatomic basis, the displacement of all atoms in the lattice from the equillibrium positions can be described using, $T = (1 + \varepsilon)$, where ε is the strain tensor:

$$T = \begin{pmatrix} 1+\varepsilon_{11} & \varepsilon_{12} & \varepsilon_{13} \\ \varepsilon_{12} & 1+\varepsilon_{22} & \varepsilon_{23} \\ \varepsilon_{13} & \varepsilon_{23} & 1+\varepsilon_{33}. \end{pmatrix} \tag{A.4}$$

However, when dealing with a basis of two atoms, to fully describe the energetics of the system, and the positions of the atoms within it, we must include the effects of the sublattice displacement. We represent this internal strain by the vector **u**. Thus, after a uniform strain, our vectors are given by:

$$\begin{aligned} \mathbf{a} &= T\mathbf{a}^0, \\ \mathbf{b} &= T\mathbf{b}^0, \\ \mathbf{c} &= T\mathbf{c}^0, \\ \mathbf{r}_1 &= T\mathbf{r}_1^0, \\ \mathbf{r}_0 &= T\mathbf{r}_0^0 + \mathbf{u}. \end{aligned} \tag{A.5}$$

The angles and bonds associated with this primitive cell are identified in fig. A.1; we associate with the cell all of the bonds about atom 0, (bonds to atom 1 and its 3 periodic images) and the angles about both atoms 1 and 0.

The bond vectors about atom 0, which feature in the energy of the primitive cell, are given by:

$$\begin{aligned}
\mathbf{r}_{01} &= \mathbf{r}_1 - \mathbf{r}_0 = -\frac{a_0}{4}\begin{pmatrix} 1+\varepsilon_{11}+\varepsilon_{12}+\varepsilon_{13}-u'_x \\ \varepsilon_{12}+1+\varepsilon_{22}+\varepsilon_{23}-u'_y \\ \varepsilon_{13}+\varepsilon_{23}+1+\varepsilon_{33}-u'_z \end{pmatrix}, \\
\mathbf{r}_{02} &= T\mathbf{b} - \mathbf{r}_0 = -\frac{a_0}{4}\begin{pmatrix} 1+\varepsilon_{11}-\varepsilon_{12}+\varepsilon_{13}-u'_x \\ \varepsilon_{12}-1-\varepsilon_{22}+\varepsilon_{23}-u'_y \\ \varepsilon_{13}-\varepsilon_{23}+1+\varepsilon_{33}-u'_z \end{pmatrix}, \\
\mathbf{r}_{03} &= T\mathbf{c} - \mathbf{r}_0 = -\frac{a_0}{4}\begin{pmatrix} 1+\varepsilon_{11}+\varepsilon_{12}-\varepsilon_{13}-u'_x \\ \varepsilon_{12}+1+\varepsilon_{22}-\varepsilon_{23}-u'_y \\ \varepsilon_{12}+\varepsilon_{23}-1-\varepsilon_{33}-u'_z \end{pmatrix}, \\
\mathbf{r}_{04} &= T\mathbf{a} - \mathbf{r}_0 = -\frac{a_0}{4}\begin{pmatrix} -1-\varepsilon_{11}+\varepsilon_{12}+\varepsilon_{13}-u'_x \\ -\varepsilon_{12}+1+\varepsilon_{22}+\varepsilon_{23}-u'_y \\ -\varepsilon_{12}+\varepsilon_{23}+1+\varepsilon_{33}-u'_z \end{pmatrix}.
\end{aligned} \tag{A.6}$$

Here we have utilised $\mathbf{u}' = \frac{4}{a_0}\mathbf{u}$ for cleanliness. Through their dot products with with themselves and each other, these bond vectors determine all the bond lengths and bond angles of eq. (A.1).

To relate the interatomic energy to the macroscopic strain energy, these dot products are computed and the functions of them which occur in the energy (square roots, arc cosines and functions of these) are then taylor expanded to second order in the strain and internal strain variables. These dot products, and the taylor expansions of their functionals are very long expressions in the strain, and to minimise human error, their computation is best executed using software capable of analytic manipulation such as Matlab [173] or Mathematica [174], and here only the end results of the full expansion of the energy is shown.

The 6 angles about atom B to be taken into account are:

$$\begin{aligned}
&\theta_{012} = \cos^{-1}\left(\frac{\mathbf{r}_{01}\cdot\mathbf{r}_{02}}{|\mathbf{r}_{01}||\mathbf{r}_{02}|}\right), \quad \theta_{013} = \cos^{-1}\left(\frac{\mathbf{r}_{01}\cdot\mathbf{r}_{03}}{|\mathbf{r}_{01}||\mathbf{r}_{03}|}\right), \quad \theta_{014} = \cos^{-1}\left(\frac{\mathbf{r}_{01}\cdot\mathbf{r}_{04}}{|\mathbf{r}_{01}||\mathbf{r}_{04}|}\right), \\
&\theta_{023} = \cos^{-1}\left(\frac{\mathbf{r}_{02}\cdot\mathbf{r}_{03}}{|\mathbf{r}_{02}||\mathbf{r}_{03}|}\right), \quad \theta_{024} = \cos^{-1}\left(\frac{\mathbf{r}_{02}\cdot\mathbf{r}_{04}}{|\mathbf{r}_{02}||\mathbf{r}_{04}|}\right), \quad \theta_{034} = \cos^{-1}\left(\frac{\mathbf{r}_{03}\cdot\mathbf{r}_{04}}{|\mathbf{r}_{03}||\mathbf{r}_{04}|}\right).
\end{aligned} \tag{A.7}$$

The six angles about atom A are angles between the bonds joining atom A to the periodic images of atom B. These bonds are given below:

$$\begin{aligned}
\mathbf{r}_{\overline{01}} &= \mathbf{r}_0 = -\mathbf{r}_{01}, \\
\mathbf{r}_{\overline{02}} &= \mathbf{r}_0 - T\mathbf{b} = -\mathbf{r}_{02}, \\
\mathbf{r}_{\overline{03}} &= \mathbf{r}_0 - T\mathbf{c} = -\mathbf{r}_{03}, \\
\mathbf{r}_{\overline{04}} &= \mathbf{r}_0 - T\mathbf{a} = -\mathbf{r}_{04}.
\end{aligned} \tag{A.8}$$

Because $r_i = -r_{\bar{i}}$, it is also the case that $\theta_{A\bar{i}j} = \theta_{Bij}$, so the angles about atom A are equal to those about atom B. This equivalence of angles about A and B presents a limitation to this method of expanding the VFF energy in strain; it leads to the situation where it is not possible to assign and independently parameterise anion-centred and cation-centred angular force terms. This could possibly be circumvented by expanding the energy of a full conventional ZB unit cell in strain, but the approximation of $k_\theta^A = k_\theta^B$ has been justified in the context of structural relaxation [84], so its improvement is not sought here.

Having the VFF energy cast now as a complicated function of the strain, we perform a Taylor series expansion to second order in the strain and internal strain about the unstrained zero of energy. This will allow us to compare to different macroscopic expressions for the elastic energy density of the crystal. Additionally, to convert the energy of one unit cell to an energy density, we divide by the primitive cell volume, $V_0 = \left(\frac{r_0}{\sqrt{3}}\right)^3$. For convience and to comply with convention, Voight notation is adopted at this point. Thus, our microscopically derived energy density, to second order in strain, is given by:

$$\begin{aligned} U = &\frac{1}{2}\frac{\sqrt{3}}{12r_0}\left(k_r + 6k_{rr} + 12k_\theta\right)\left[\varepsilon_1^2 + \varepsilon_2^2 + \varepsilon_3^2\right] + \frac{\sqrt{3}}{12r_0}\left(k_r + 6k_{rr} - 6k_\theta\right)\left[\varepsilon_1\varepsilon_2 + \varepsilon_1\varepsilon_3 + \varepsilon_2\varepsilon_3\right] \\ &+\frac{1}{2}\frac{\sqrt{3}}{12r_0}\left(k_r - 2k_{rr} + 4\sqrt{2}k_{r\theta} + 2k_\theta\right)\left[\varepsilon_4^2 + \varepsilon_5^2 + \varepsilon_6^2\right] + \frac{1}{4r_0^2}\left(k_r - 2k_{rr} - 2\sqrt{2}k_{r\theta} - 4k_\theta\right)\left[u_x\varepsilon_1 + u_y\varepsilon_2 + u_z\varepsilon_3\right] \\ &+ \frac{1}{2}\frac{\sqrt{3}}{4r_0^3}\left(k_r - 2k_{rr} - 8\sqrt{2}k_{r\theta} + 8k_\theta\right)\left[u_x^2 + u_y^2 + u_z^2\right]. \end{aligned} \quad \text{(A.9)}$$

While this equation does not relate to the standard elastic energy density in which the physical (measured) elastic constants are found, it does relate to the 'bare'[175] elastic constants. These can be extracted in density functional theory calculations, or derived indirectly from experimental measurements of long wavelength optical phonon frequencies and the Kleinman parameter, and thus used to determine the force constants [137, 140, 175]. Assigning the force constants in this way has four notable advantages:

1. the bare elastic constants depend linearly on the force constants;
2. The bare elastic constants are less computationally demanding to determine because the cell need not be relaxed;
3. For a cubic crystal there are five bare elastic constants to fit to, whilst for the relaxed crystal there are only three elastic constants and the Kleinman parameter. Having more constants and an underdetermined system allows the possibility of *a priori* tests of the applicability of the potential to a given matieral.
4. The extra bare elastic constants offer the option to include more force constants in the potential without losing accuracy in fitting.

For these reasons, and for subsequent analysis, the relations between the VFF force constants and the bare elastic constants are worth explicit statement.

Vanderbilt *et. al.* [175] gave the elastic energy density of a macroscopic crystal in terms of the bare elastic constants as:

$$\begin{aligned} U = \frac{1}{2}B_{11}\left(\varepsilon_1^2+\varepsilon_2^2+\varepsilon_3^2\right) + B_{12}\left(\varepsilon_1\varepsilon_2+\varepsilon_1\varepsilon_3+\varepsilon_2\varepsilon_3\right) \\ + \frac{1}{2}B_{44}\left(\varepsilon_4^2+\varepsilon_5^2+\varepsilon_6^2\right) + B_{4x}\left(\varepsilon_4 u_x+\varepsilon_5 u_y+\varepsilon_6 u_z\right) \\ + \frac{1}{2}B_{xx}\left(u_x^2+u_y^2+u_z^2\right) \end{aligned} \tag{A.10}$$

Comparing eqs. (A.9) and (A.10) leads to five relations between our force constants and the bare elastic constants of:

$$B_{11} = \frac{\sqrt{3}}{12r_0}\left(k_r+6k_{rr}+12k_\theta\right), \tag{A.11}$$

$$B_{12} = \frac{\sqrt{3}}{12r_0}\left(k_r+6k_{rr}-6k_\theta\right), \tag{A.12}$$

$$B_{44} = \frac{\sqrt{3}}{3r_0}\left(k_r-2k_{rr}+4\sqrt{2}k_{r\theta}+2k_\theta\right), \tag{A.13}$$

$$B_{4x} = \frac{1}{4r_0^2}\left(k_r-2k_{rr}-2\sqrt{2}k_{r\theta}-4k_\theta\right), \tag{A.14}$$

$$B_{xx} = \frac{\sqrt{3}}{4r_0^3}\left(k_r-2k_{rr}-8\sqrt{2}k_{r\theta}+8k_\theta\right). \tag{A.15}$$

To obtain the relations amongst the force constants and the physical, relaxed, elastic constants, the energy must be minimised with respect to the internal strain, $\mathbf{u}$. Given the symmetry of the equations, this need be done only for the x component:

$$\begin{aligned} \frac{\partial U}{\partial u_x} &= 0, \\ \Rightarrow u_x^0(\varepsilon) &= -\frac{r_0}{\sqrt{3}}\frac{k_r-2k_{rr}-2\sqrt{2}k_{r\theta}-4k_\theta}{k_r-2k_{rr}-8\sqrt{2}k_{r\theta}+8k_\theta}\varepsilon_4. \end{aligned} \tag{A.16}$$

This internal strain which minimises the energy may be compared with experiment via the Kleinman parameter, which specifies, to first order, the sub lattice displacement as a function of shear strain:[59, 61]

$$\mathbf{u}^0 = \{-\frac{a_0}{4}\zeta\varepsilon_4, -\frac{a_0}{4}\zeta\varepsilon_5, -\frac{a_0}{4}\zeta\varepsilon_6\}. \tag{A.17}$$

A comparison of eq. (A.16) and (A.17) yields an expression for the the Kleinman parameter in terms of the VFF force constants:

$$\zeta = \frac{k_r-2k_{rr}-2\sqrt{2}k_{r\theta}-4k_\theta}{k_r-2k_{rr}-8\sqrt{2}k_{r\theta}+8k_\theta}. \tag{A.18}$$

Substituting $\{u_x^0, u_y^0, u_z^0\}$ into eq. (A.9), the final form of the VFF energy in terms of only the uniform macroscopic strain is obtained:

$$U = \frac{1}{2}\frac{\sqrt{3}}{12r_0}\left(k_r + 6k_{rr} + 12k_\theta\right)\left[\varepsilon_1^2 + \varepsilon_2^2 + \varepsilon_3^2\right] + \frac{\sqrt{3}}{12r_0}\left(k_r + 6k_{rr} - 6k_\theta\right)\left[\varepsilon_1\varepsilon_2 + \varepsilon_1\varepsilon_3 + \varepsilon_2\varepsilon_3\right] + \frac{3\sqrt{3}}{r_0}\frac{k_r k_\theta - 2k_{rr}k_\theta - 4k_{r\theta}^2}{k_r - 2k_{rr} - 8\sqrt{2}k_{r\theta} + 8k_\theta}\left[\varepsilon_4^2 + \varepsilon_5^2 + \varepsilon_6^2\right] \quad \text{(A.19)}$$

For cubic crystals, elastic energy density is given, to second order in strain, by:[50]

$$U = \frac{1}{2}C_{11}\left(\varepsilon_1^2 + \varepsilon_2^2 + \varepsilon_3^2\right) + C_{12}\left(\varepsilon_1\varepsilon_2 + \varepsilon_1\varepsilon_3 + \varepsilon_2\varepsilon_3\right) + \frac{1}{2}C_{44}\left(\varepsilon_4^2 + \varepsilon_5^2 + \varepsilon_6^2\right) \quad \text{(A.20)}$$

where C_{11}, C_{12}, and C_{44} are the macroscopic elastic constants of the material.

Finally, by comparison between equation (A.19) and (A.20), the equations relating the force constants to the experimentally measured physical elastic constants, and to the Kleinman parameter are given by:

$$C_{11} = \frac{\sqrt{3}}{12r_0}\left(k_r + 6k_{rr} + 12k_\theta\right), \quad \text{(A.21)}$$

$$C_{12} = \frac{\sqrt{3}}{12r_0}\left(k_r + 6k_{rr} - 6k_\theta\right), \quad \text{(A.22)}$$

$$C_{44} = \frac{3\sqrt{3}}{2r_0}\frac{k_r k_\theta - 2k_{rr}k_\theta - 4k_{r\theta}^2}{k_r - 2k_{rr} - 8\sqrt{2}k_{r\theta} + 8k_\theta}, \quad \text{(A.23)}$$

$$\zeta = \frac{k_r - 2k_{rr} - 2\sqrt{2}k_{r\theta} - 4k_\theta}{k_r - 2k_{rr} - 8\sqrt{2}k_{r\theta} + 8k_\theta}. \quad \text{(A.24)}$$

Appendix B

Analytic relation of force constants to elastic constants

The equations (A.21)-(A.24) which relate the elastic constants of ZB materials to sums over the force constants contained in the potential of eq. (5.23), were derived in the previous appendix and are repeated below:

$$\begin{aligned} C_{11} &= \frac{\sqrt{3}}{12 r_0}\left(k_r + 6k_{rr} + 12k_\theta\right) , \\ C_{12} &= \frac{\sqrt{3}}{12 r_0}\left(k_r + 6k_{rr} - 6k_\theta\right) , \\ C_{44} &= \frac{3\sqrt{3}}{2 r_0}\frac{k_r k_\theta - 2k_{rr}k_\theta - 4k_{r\theta}^2}{k_r - 2k_{rr} - 8\sqrt{2}k_{r\theta} + 8k_\theta} , \\ \zeta &= \frac{k_r - 2k_{rr} - 2\sqrt{2}k_{r\theta} - 4k_\theta}{k_r - 2k_{rr} - 8\sqrt{2}k_{r\theta} + 8k_\theta} . \end{aligned}$$

Subtracting eq. (A.22) from eq. (A.21) reveals immediately the unique determination of k_θ in terms of C_{11} and C_{12}:

$$k_\theta = \frac{2 r_0}{3\sqrt{3}}\left(C_{11} - C_{12}\right) . \tag{B.1}$$

To simplify later algebra the following notation is employed:

$$\xi = 8\zeta\sqrt{2} - 2\sqrt{2}\,, \tag{B.2}$$
$$\gamma = \frac{4}{3}(1-\zeta)\,, \tag{B.3}$$
$$\alpha = \frac{2r_0}{3\sqrt{3}}(C_{11}+2C_{12})\,, \tag{B.4}$$
$$\beta = (8\zeta+4)\,k_\theta + 2(1-\zeta)\,\alpha\,, \tag{B.5}$$
$$C_{44}\prime = \frac{2r_0 C_{44}}{3\sqrt{3}}\,, \tag{B.6}$$
$$\kappa = \frac{4}{3}(C_{44}\prime - k_\theta)\,. \tag{B.7}$$

Adding twice eq. (A.22) to eq. (A.21) reveals a linear expression for k_{rr} in terms of C_{11}, C_{12}, and k_r:

$$k_{rr} = \frac{2r_0}{3\sqrt{3}}(C_{11}+2C_{12}) - \frac{k_r}{6} = \alpha - \frac{k_r}{6}. \tag{B.8}$$

Multiplying out eq. (5.28) and utilising eq. (B.8), a linear expression relating $k_{r\theta}$ to k_r is obtained:

$$k_r = -\frac{\xi}{\gamma}k_{r\theta} + \frac{\beta}{\gamma}. \tag{B.9}$$

Having now expressions for k_{rr} in terms of k_r, and $k_{r\theta}$ in terms of k_r, the remaining quadratic equation eq. (A.23) can be cast in terms of only $k_{r\theta}$ and known elastic constants.

With this notation eq. (A.23) multiplies out to the quadratic equation:

$$\overbrace{4}^{a}k_{r\theta}^2 - \overbrace{\left(C_{44}\prime 8\sqrt{2} + \frac{\kappa\xi}{\gamma}\right)}^{b}k_{r\theta} + \overbrace{\frac{\kappa\beta}{\gamma} + C_{44}\prime(8k_\theta - 2\alpha) + 2\alpha k_\theta}^{c} = 0\,, \tag{B.10}$$

amenable to solution by the quadratic formula, $k_{r\theta} = \frac{-b\pm\sqrt{b^2-4ac}}{2a}$. Each of these solutions correspond to different values of k_{rr}, and k_r, with the same k_θ. However, numerical implementation of this formula reveals one of the solutions to be extraneous, and whether the extraneous solution is the plus or minus solution of the quadratic formula depends on the properties of the material being fitted to. We find that the critical material parameter determining the correct solution is the anisotropy parameter, given by: [153]

$$A = \frac{2C_{44}}{C_{11}-C_{12}}. \tag{B.11}$$

Table B.1 summarises which of the two solutions, + or -, in the quadratic formula, correctly reproduces the elastic constants used to parametrise the force constants for each III-V material considered.

TABLE B.1: Solution of eq. (B.10) consistent with elastic constants and Kleinman parameter.

	N	P	As	Sb
Al	+	-	-	-
Ga	+	-	-	-
In	+	+	+	-

TABLE B.2: Value of the anisotropy paramter for III-V materials based on DFT-extracted elastic constants

	N	P	As	Sb
Al	2.747	1.887	1.866	1.779
Ga	2.463	1.776	1.779	1.742
In	2.882	2.028	2.004	1.905

Tables B.1 and B.2 imply that the solutions to eq. (B.10) depend critically, on whether the anisotropy is greater or less than 2, or, more specifically, on whether $C_{44} > (C_{11} - C_{12})$. For easy assignment of force parameters, irrespective of material properties, and an understanding of the extraneous root, we pursue a single analytic solution.

Expanding out the terms we obtain:

$$-b = \frac{4}{3}\sqrt{\frac{2}{3}} r_0 \frac{(C_{11} - C_{12})(4\zeta - 1) - 3C_{44}}{\zeta - 1}, \tag{B.12}$$

$$b^2 - 4ac = \frac{32 r_0^2}{3} \frac{(C_{44} - (C_{11} - C_{12}))^2}{(\zeta - 1)^2}. \tag{B.13}$$

Putting these values into the quadratic formula and simplifying, we obtain:

$$k_{r\theta} = \frac{4}{3}\sqrt{\frac{2}{3}} \frac{r_0}{1-\zeta} \left[(C_{11} - C_{12})(1 - 4\zeta) + 3C_{44} \pm 3 \left[(C_{44} - (C_{11} - C_{12}))^2 \right]^{1/2} \right] \tag{B.14}$$

These two solutions simplify to:

$$k_{r\theta} = \frac{2}{3}\sqrt{\frac{2}{3}} r_0 (C_{11} - C_{12}) = \sqrt{2} k_\theta \qquad \text{and} \qquad k_{r\theta} = \frac{r_0}{3}\sqrt{\frac{2}{3}} \frac{(C_{11} - C_{12})(1 + 2\zeta) - 3C_{44}}{\zeta - 1} \tag{B.15}$$

By inspection of eq. (A.23) we can see that the extraneous solution is the the left in eq. (B.15), which would lead to the undefined scenario of 0/0. Furthermore, we see that whether this solution is the + or - solution depends on whether $C_{44} > (C_{11} - C_{12})$, or whether $\frac{A}{2} > 1$. Thus, the single correct analytic expression for the force constant $k_{r\theta}$ in terms of the elastic constants and the Kleinman parameter is the right hand solution in eq. (B.15). Via, eqs. (B.1), (B.8) and (B.9), we then obtain the full single set of force constants:

$$k_\theta = \frac{2(C_{11} - C_{12}) r_0}{3\sqrt{3}}, \tag{B.16}$$

$$k_r = \frac{r_0}{\sqrt{3}(1-\zeta)^2} \left[C_{11}(2 + 2\zeta + 5\zeta^2) + C_{12}(1 - 8\zeta - 2\zeta^2) + 3C_{44}(1 - 4\zeta) \right], \tag{B.17}$$

$$k_{rr} = \frac{r_0}{6\sqrt{3}(1-\zeta)^2} \left[C_{11}(2 - 10\zeta - \zeta^2) + C_{12}(7 - 8\zeta + 10\zeta^2) - 3C_{44}(1 - 4\zeta) \right], \tag{B.18}$$

$$k_{r\theta} = \frac{r_0}{3}\sqrt{\frac{2}{3}} \frac{(C_{11} - C_{12})(1 + 2\zeta) - 3C_{44}}{\zeta - 1}. \tag{B.19}$$

Bibliography

[1] C. J. Humphreys, "Solid-state lighting," MRS Bulletin **33**, 459 (2008).

[2] E. F. Schubert and J. K. Kim, "Solid-state light sources getting smart," Science **308**, 1274 (2005).

[3] F. A. Ponce and D. Bour, "Nitride-based semiconductors for blue and green light emitting devices.," Nature **386**, 351 (1997).

[4] J. Wu, "When group-III nitrides go infrared: New properties and perspectives," Journal of Applied Physics **106**, 011101 (2009).

[5] H. Amano, M. Kito, K. Hiramatsu, and I. Akasaki, "P-type conduction in Mg-doped GaN treated with low-energy electron beam irradiation (LEEBI)," Japanese Journal of Applied Physics **28**, L2112 (1989).

[6] I. Akasaki and H. Amano, "Breakthroughs in improving crystal quality of GaN and invention of the p-n junction blue-light-emitting diode," Japanese Journal of Applied Physics **45**, 9001 (2006).

[7] S. Nakamura, T. Mukai, M. Senoh, S. Nagahama, and N. Iwasa, "$In_xGa_{1-x}N/In_yGa_{1-y}N$ superlattices grown on GaN films," Journal of Applied Physics **74**, 3911 (1993).

[8] T. Asano, M. Takeya, T. Mizuno, S. Ikeda, Y. Ohfuji, T. Fujimoto, K. Oikawa, S. Goto, T. Hashizu, K. Aga, et al., in "Novel In-Plane Semiconductor Lasers III", edited by C. F. Gmachl and D. P. Bour (2004), vol. 5365 of "Proc. SPIE", pp. 297–305.

[9] R. Dahal, B. Pantha, J. Li, J. Y. Lin, and H. X. Jiang, "InGaN/GaN multiple quantum well solar cells with long operating wavelengths," Applied Physics Letters **94**, 063505 (2009).

[10] H. K. Cho, J. Y. Lee, G. M. Yang, and C. S. Kim, "Formation mechanism of V defects in the InGaN/GaN multiple quantum wells grown on GaN layers with low threading dislocation density," Applied Physics Letters **79**, 215 (2001).

[11] C. J. Humphreys, in "Turning Points in Solid-State, Materials and Surface Science: A Book in Celebration of the Life and Work of Sir John Meurig Thomas" (The Royal Society of Chemistry, 2008), pp. 698–710.

[12] M. R. Krames, O. B. Shchekin, R. Mueller-Mach, G. O. Mueller, L. Zhou, G. Harbers, and M. G. Craford, "Status and future of high-power light-emitting diodes for solid-state lighting," Journal of Display Technology **3**, 160 (2007).

[13] S. Chichibu, K. Wada, and S. Nakamura, "Spatially resolved cathodoluminescence spectra of InGaN quantum wells," Applied Physics Letters **71**, 2346 (1997).

[14] S. Chichibu, T. Azuhata, T. Sota, and S. Nakamura, "Spontaneous emission of localized excitons in InGaN single and multiquantum well structures," Applied Physics Letters **69**, 4188 (1996).

[15] K. P. O'Donnell, R. W. Martin, and P. G. Middleton, "Origin of luminescence from InGaN diodes," Physical Review Letters **82**, 237 (1999).

[16] Y.-H. Cho, G. H. Gainer, A. J. Fischer, J. J. Song, S. Keller, U. K. Mishra, and S. P. DenBaars, "S-shaped temperature-dependent emission shift and carrier dynamics in InGaN/GaN multiple quantum wells," Applied Physics Letters **73**, 1370 (1998).

[17] P. G. Eliseev, P. Perlin, J. Lee, and M. Osiński, "blue temperature-induced shift and band-tail emission in InGaN-based light sources," Applied Physics Letters **71**, 569 (1997).

[18] S. Hammersley, D. Watson-Parris, P. Dawson, M. J. Godfrey, T. J. Badcock, M. J. Kappers, C. McAleese, R. A. Oliver, and C. J. Humphreys, "The consequences of high injected carrier densities on carrier localization and efficiency droop in InGaN/GaN quantum well structures," Journal of Applied Physics **111**, 083512 (2012).

[19] J. A. Davidson, P. Dawson, T. Wang, T. Sugahara, J. W. Orton, and S. Sakai, "Photoluminescence studies of InGaN/GaN multi-quantum wells," Semiconductor Science and Technology **15**, 497 (2000).

[20] A. Dunn, B. F. Spencer, S. J. O. Hardman, D. M. Graham, S. Hammersley, M. J. Davies, P. Dawson, M. J. Kappers, R. A. Oliver, and C. J. Humphreys, "Investigating efficiency droop in InGaN/GaN quantum well structures using ultrafast time-resolved terahertz and photoluminescence spectroscopy," Physica Status Solidi (c) **13**, 252 (2016).

[21] N. I. Bochkareva, V. V. Voronenkov, R. I. Gorbunov, A. S. Zubrilov, P. E. Latyshev, Y. S. Lelikov, Y. T. Rebane, A. I. Tsyuk, and Y. G. Shreter, "Effect of localized tail states in InGaN on the efficiency droop in GaN light-emitting diodes with increasing current density," Semiconductors **46**, 1032 (2012).

[22] C. J. Humphreys, "Does In form In-rich clusters in InGaN quantum wells?," Philosophical Magazine **87**, 1971 (2007).

[23] T. M. Smeeton, M. J. Kappers, J. S. Barnard, M. E. Vickers, and C. J. Humphreys, "Electron-beam-induced strain within InGaN quantum wells: False indium cluster detection in the transmission electron microscope," Applied Physics Letters **83**, 5419 (2003).

[24] M. J. Galtrey, R. A. Oliver, M. J. Kappers, and C. J. Humphreys, "Three-dimensional atom probe studies of an $In_xGa_{1-x}N$/GaN multiple quantum well structure: Assessment of possible indium clustering," Applied Physics Letters **90**, 061903 (2007).

[25] F. Tang, T. Zhu, F. Oehler, W. Y. Fu, J. T. Griffiths, F. C.-P. Massabuau, M. J. Kappers, T. L. Martin, P. A. J. Bagot, M. P. Moody, et al., "Indium clustering in *a*-plane InGaN quantum wells as evidenced by atom probe tomography," Applied Physics Letters **106**, 072104 (2015).

[26] D. M. Graham, A. Soltani-Vala, P. Dawson, M. J. Godfrey, T. M. Smeeton, J. S. Barnard, M. J. Kappers, C. J. Humphreys, and E. J. Thrush, "Optical and microstructural studies of InGaNGaN single-quantum-well structures," Journal of Applied Physics **97**, 103508 (2002).

[27] G. Sarau, M. Heilmann, M. Latzel, and S. Christiansen, "Disentangling the effects of nanoscale structural variations on the light emission wavelength of single nano-emitters: InGaN/GaN multiquantum well nano-leds for a case study," Nanoscale **6**, 11953 (2014).

[28] R. W. Martin, P. G. Middleton, K. P. O'Donnell, and W. Van der Stricht, "Exciton localization and the stokes shift in InGaN epilayers," Applied Physics Letters **74**, 263 (1999).

[29] P. R. C. Kent and A. Zunger, "Carrier localization and the origin of luminescence in cubic InGaN alloys," Applied Physics Letters **79**, 1977 (2015).

[30] V. Fiorentini, F. Bernardini, F. D. Sala, A. D. Carlo, and P. Lugli, "Effects of macroscopic polarization in III-V nitride multiple quantum wells," Physical Review B. **60**, 8849 (1999).

[31] M. Auf der Maur, A. Pecchia, G. Penazzi, W. Rodrigues, and A. Di Carlo, "Efficiency drop in green InGaN/GaN light emitting diodes: The role of random alloy fluctuations," Physical Review Letters **116**, 027401 (2016).

[32] E. Taylor, P. R. Edwards, and R. W. Martin, "Colorimetry and efficiency of white LEDs: Spectral width dependence," Physica Status Solidi (a) **209**, 461 (2012).

[33] P. Waltereit, O. Brandt, A. Trampert, H. T. Grahn, J. Menniger, M. Ramsteiner, M. Reiche, and K. H. Ploog, "Nitride semiconductors free of electrostatic fields for efficient white light emitting diodes," Nature **406**, 865 (2000).

[34] P. Dawson, S. Schulz, R. A. Oliver, M. J. Kappers, and C. J. Humphreys, "The nature of carrier localisation in polar and nonpolar InGaN/GaN quantum wells," Journal of Applied Physics **119**, 181505 (2016).

[35] H. Masui, H. Yamada, K. Iso, S. Nakamura, and S. P. DenBaars, "Optical polarization characteristics of m-oriented InGaN/GaN light-emitting diodes with various indium compositions in single-quantum-well structure," Journal of Physics D: Applied Physics **41**, 225104 (2008).

[36] T. Paskova, "Development and prospects of nitride materials and devices with nonpolar surfaces," Physica Status Solidi B **245**, 1011 (2008).

[37] C. Bayram and R. Liu, in "III-Nitride Semiconductor Optoelectronics", edited by Z. Mi and C. Jagadish (Elsevier, 2017), vol. 96 of "Semiconductors and Semimetals", pp. 411 – 435.

[38] Y. Zhao, Q. Yan, C.-Y. Huang, S.-C. Huang, P. S. Hsu, S. Tanaka, C.-C. Pan, Y. Kawaguchi, K. Fujito, C. G. V. de Walle, et al., "Indium incorporation and emission properties of nonpolar and semipolar InGaN quantum wells," Applied Physics Letters **100**, 201108 (2012).

[39] T. Kitamura, Y. Suzuki, Y. Ishida, X. Shen, H. Nakanishi, S. Chichibu, M. Shimizu, and H. Okumura, "Optical properties of cubic InGaN/GaN multiple quantum wells on 3C-SiC substrates by radio-frequency plasma-assisted molecular beam epitaxy," Physica Status Solidi (a) **188**, 705 (2001).

[40] S. F. Chichibu, M. Sugiyama, T. Onuma, T. Kitamura, H. Nakanishi, T. Kuroda, A. Tackeuchi, T. Sota, Y. Ishida, and H. Okumura, "Localized exciton dynamics in strained cubic $In_{0.1}Ga_{0.9}N$/GaN multiple quantum wells," Applied Physics Letters **79**, 4319 (2001).

[41] J. Piprek, "Efficiency droop in nitride-based light-emitting diodes," Physica Status Solidi (a) **207**, 2217 (2010).

[42] E. Kioupakis, P. Rinke, K. T. Delaney, and C. G. V. de Walle, "Indirect auger recombination as a cause of efficiency droop in nitride light-emitting diodes," Applied Physics Letters **98**, 161107 (2011).

[43] L.-W. Wang, "Calculations of carrier localization in $In_xGa_{1-x}N$," Physical Review B **63**, 245107 (2001).

[44] S. Schulz, M. A. Caro, C. Coughlan, and E. P. O'Reilly, "Atomistic analysis of the impact of alloy and well-width fluctuations on the electronic and optical properties of InGaN/GaN quantum wells," Physical Review B **91**, 035439 (2015).

[45] Q. Liu, J. Lu, Z. Gao, L. Lai, R. Qin, H. Li, J. Zhou, and G. Li, "Electron localization and emission mechanism in wurtzite (Al,In,Ga)N alloys," Physica Status Solidi B **247**, 109 (2010).

[46] O. Marquardt, T. Hickel, J. Neugebauer, and C. G. V. de Walle, "Polarization effects due to thickness fluctuations in nonpolar InGaN/GaN quantum wells," Applied Physics Letters **103**, 073115 (2013).

[47] C.-H. Kim and B.-H. Han, "Valence subbands and optical gain in wurtzite and zinc-blende strained GaN/AlGaN quantum wells," Solid State Communications **106**, 127 (1998).

[48] D. Watson-Parris, M. J. Godfrey, and P. Dawson, "Carrier localization mechanisms in $In_xGa_{1-x}N$/GaN quantum wells," Physical Review B **83**, 115321 (2011).

[49] S. Schulz, M. A. Caro, L.-T. Tan, P. J. Parbrook, R. W. Martin, and E. P. O'Reilly, "Composition-Dependent Band Gap and Band-Edge Bowing in AlInN: A Combined Theoretical and Experimental Study," Applied Physics Express **6**, 121001 (2013).

[50] J. F. Nye, "Physical Properties of Crystals: Their Representation by Tensors and Matrices (2^{nd} ed.)" (Oxford University Press, 1985).

[51] H. Anton and C. Rorres, "Elementary Linear Algebra: Applications Version" (Wiley, 2014), eleventh ed.

[52] F. D. Murnaghan, "Finite Deformation Of An Elastic Solid" (John Wiley & Sons, Inc, 1951).

[53] L. Landau and E. Lifshitz, "Theory of Elasticity (Third Edition)" (Butterworth-Heinemann, 1986).

[54] K. Brugger, "Thermodynamic definition of higher order elastic coefficients," Physical Review **133**, A1611 (1964).

[55] F. Birch, "Finite elastic strain of cubic crystals," Physical Review **71**, 809 (1947).

[56] A. E. H. Love, "Mathematical Theory of Elasticity (4^{nd} ed.)" (Cambridge University Press, 1927).

[57] R. S. E. Ellad B. Tadmor, Ronald E. Miller, "Continuum Mechanics and Thermodynamics" (Cambridge University Press, 2012).

[58] M. Born and K. Huang, "Dynamical theory of crystal lattices", Oxford classic texts in the physical sciences (Clarendon Press, Oxford, 1954).

[59] L. Kleinman, "Deformation potentials in silicon. I. uniaxial strain," Physical Review **128**, 2614 (1962).

[60] A. Segmüller, "Observation of bond-bending in strained germanium," Physics Letters **4**, 277 (1963).

[61] P. N. Keating, "Effect of invariance requirements on the elastic strain energy of crystals with application to the diamond structure," Physical Review **145**, 637 (1966).

[62] M. A. Caro, S. Schulz, and E. P. O'Reilly, "Hybrid functional study of the elastic and structural properties of wurtzite and zinc-blende group-III nitrides," Physical Review B **86**, 014117 (2012).

[63] C. S. G. Cousins, "Inner elasticity," Journal of Physics C: Solid State Physics **11**, 4867 (1978).

[64] C. S. G. Cousins, "The symmetry of inner elastic constants," Journal of Physics C: Solid State Physics **11**, 4881 (1978).

[65] J. L. Birman, "Theory of the piezoelectric effect in the zincblende structure," Physical Review **111**, 1510 (1958).

[66] M. A. Caro, S. Schulz, and E. P. O'Reilly, "Theory of local electric polarization and its relation to internal strain: Impact on polarization potential and electronic properties of group-III nitrides," Physical Review B **88**, 214103 (2013).

[67] R. M. Martin, "Piezoelectricity," Physical Review B **5**, 1607 (1972).

[68] F. Bernardini, V. Fiorentini, and D. Vanderbilt, "Spontaneous polarization and piezoelectric constants of III-V nitrides," Physical Review B **56**, R10024 (1997).

[69] P. Y. Yu and M. Cardona, "Optical Properties I" (Springer Berlin Heidelberg, Berlin, Heidelberg, 2010), pp. 243–344.

[70] P. Löwdin, "On the nonorthogonality problem connected with the use of atomic wave functions in the theory of molecules and crystals," The Journal of Chemical Physics **18**, 365 (1950).

[71] J. C. Slater and G. F. Koster, "Simplified LCAO method for the periodic potential problem," Physical Review **94**, 1498 (1954).

[72] C. T. Coughlan, Ph.D. thesis, University College Cork (2016).

[73] J. Heyd, G. E. Scuseria, and M. Ernzerhof, "Hybrid functionals based on a screened coulomb potential," The Journal of Chemical Physics **118**, 8207 (2003).

[74] A. Zakutayev, "Design of nitride semiconductors for solar energy conversion," J. Mater. Chem. A **4**, 6742 (2016).

[75] S. Nakamura and S. Chichibu, "Introduction to Nitride Semiconductor Blue Lasers and Light Emitting Diodes" (Taylor & Francis, London, 2000).

[76] T. Liu, S. Jiao, H. Liang, T. Yang, D. Wang, and L. Zhao, "Enhanced carrier localization in near-ultraviolet multiple quantum wells using quaternary AlInGaN as the well layers," RSC Adv. **5**, 33892 (2015).

[77] S. F. Chichibu, A. Uedono, T. Onuma, B. A. Haskell, A. Chakraborty, T. Koyama, P. T. Fini, S. Keller, S. P. Denbaars, J. S. Speck, et al., "Origin of defect-insensitive emission probability in In-containing (Al,In,Ga)N alloy semiconductors," Nature Materials **5**, 810 (2006).

[78] P. Perlin, M. Osiński, and P. G. Eliseev, "Optical and electrical characteristics of single-quantum-well InGaN light-emitting diodes," MRS Proceedings **449**, 1173 (1996).

[79] Q. Li, S. J. Xu, W. C. Cheng, M. H. Xie, S. Y. Tong, C. M. Che, and H. Yang, "Thermal redistribution of localized excitons and its effect on the luminescence band in InGaN ternary alloys," Applied Physics Letters **79**, 1810 (2001).

[80] A. Morel, P. Lefebvre, S. Kalliakos, T. Taliercio, T. Bretagnon, and B. Gil, "Donor-acceptor-like behavior of electron-hole pair recombinations in low-dimensional (Ga,In)N/GaN systems," Physical Review B **68**, 045331 (2002).

[81] T.-J. Yang, R. Shivaraman, J. S. Speck, and Y.-R. Wu, "The influence of random indium alloy fluctuations in indium gallium nitride quantum wells on the device behavior," Journal of Applied Physics **116**, 113104 (2014).

[82] F. Urbach, "The long-wavelength edge of photographic sensitivity and of the electronic absorption of solids," Physical Review **92**, 1324 (1953).

[83] Y.-S. Wang, N.-C. Chen, C.-Y. Lu, and J.-F. Chen, "Optical joint density of states in InGaN/GaN-based multiple-quantum-well light-emitting diodes," Physica B: Condensed Matter **406**, 4300 (2011).

[84] R. M. Martin, "Elastic properties of ZnS structure semiconductors," Physical Review B **1**, 4005 (1970).

[85] S. J. Plimpton, "Fast parallel algorithms for short-range molecular dynamics," Journal of Computational Physics **117**, 1 (1995).

[86] E. P. O'Reilly, A. Lindsay, S. Tomić, and M. Kamal-Saadi, "Tight-binding and kp models for the electronic structure of Ga(In)NAs and related alloys," Semicond. Sci. Technol. **17**, 870 (2002).

[87] T. B. Boykin, N. Kharche, G. Klimeck, and M. Korkusinski, "Approximate band-structures of semiconductor alloys from tight-binding supercell calculations," Journal of Physics: Condensed Matter **19**, 036203 (2007).

[88] M. Zieliński, "Valence band offset, strain and shape effects on confined states in self-assembled InAs/InP and InAs/GaAs quantum dots," Journal of Physics: Condensed Matter **25**, 465301 (2013).

[89] P. G. Moses, M. Miao, Q. Yan, and C. G. Van de Walle, "Hybrid functional investigations of band gaps and band alignments for AlN, GaN, InN, and InGaN," The Journal of Chemical Physics **134**, 084703 (2011).

[90] L.-W. Wang and A. Zunger, "Solving shrödinger's equation around a desired energy: Application to silicon quantum dots," Journal of Chemical Physics **100**, 2394 (1994).

[91] S. Schulz, M. A. Caro, L.-T. Tan, P. J. Parbrook, R. W. Martin, and E. P. O'Reilly, "Composition-dependent band gap and band-edge bowing in AlInN: A combined theoretical and experimental study," Applied Physics Express **6**, 121001 (2013).

[92] C. Coughlan, S. Schulz, M. A. Caro, and E. P. O'Reilly, "Band gap bowing and optical polarization switching in $Al_{1-x}Ga_xN$ alloys," Physica Status Solidi (b) **252**, 879 (2015).

[93] M. Usman and E. P. O'Reilly, "Atomistic tight-binding study of electronic structure and interband optical transitions in $GaBi_xAs_{1-x}$/GaAs quantum wells," Applied Physics Letters **104**, 071103 (2014).

[94] B. Monemar, P. Paskov, J. P. Bergman, G. Pozina, V. Darakchieva, M. Iwaya, S. Kamiyama, H. Amano, and I. Akasaki, "Photoluminescence in n-doped $In_{0.1}Ga_{0.9}N/In_{0.01}Ga_{0.99}N$ multiple quantum wells," MRS Internet Journal of Nitride Semiconductor Research **7**, 1092 (2002).

[95] M. J. Galtrey, R. A. Oliver, M. J. Kappers, C. J. Humpreys, P. H. Clifton, D. Larson, D. W. Saxey, and A. Cerezo, "Three-dimensional atom probe analysis of green- and blue-emitting In_xGa_{1-x}NGaN multiple quantum well structures," Journal of Applied Physics **104**, 013524 (2008).

[96] S. F. Chichibu, A. C. Abare, M. S. Minsky, S. Keller, S. B. Fleischer, J. E. Bowers, E. Hu, U. K. Mishra, L. A. Coldren, S. P. DenBaars, et al., "Effective band gap inhomogeneity and piezoelectric field in InGaN/GaN multiquantum well structures," Applied Physics Letters **73**, 2006 (1998).

[97] O. Brandt, P. Waltereit, U. Jahn, S. Dhar, and K. Ploog, "Impact of In bulk and surface segregation on the optical properties of (In,Ga)N/GaN multiple quantum wells," Physica Status Solidi (a) **192**, 5 (2002).

[98] S. Schulz, T. J. Badcock, M. A. Moram, P. Dawson, M. J. Kappers, C. J. Humphreys, and E. P. O'Reilly, "Electronic and optical properties of nonpolar a-plane GaN quantum wells," Physical Review B **82**, 125318 (2010).

[99] P. Rinke, M. Winkelnkemper, A. Qteish, D. Bimberg, J. Neugebauer, and M. Scheffler, "Consistent set of band parameters for the group-III nitrides AlN, GaN, and InN," Physical Review B **77**, 075202 (2008).

[100] B. Lee and L. W. Wang, "Band gap bowing and electron localization of Ga_x,In_{1-x},N," Journal of Applied Physics **100**, 093717 (2006).

[101] D. Watson-Parris, Ph.D. thesis, University of Manchester (2011).

[102] D. Thouless, "Electrons in disordered systems and the theory of localization," Physics Reports **13**, 93 (1974).

[103] R. J. Bell, J. P. Dean, and D. C. Hibbens-Butler, "Localization of normal modes in vitreous silica, germania and beryllium fluoride," J. Phys. C: Solid St. Phys **3**, 2111 (1970).

[104] Y. Meir, A. Aharony, and A. B. Harris, "Quantum percolation in magnetic fields," Physical Review Letters **56**, 976 (1986).

[105] F. B. Naranjo, M. A. Sanchez-Garcia, F. Calle, E. Calleja, B. Jenichen, and K. H. Ploog, "Strong localization in InGaN layers with high In content grown by molecular-beam epitaxy," Applied Physics Letters **80**, 231 (2002).

[106] K. O'Donnell, R. Martin, C. Trager-Cowan, M. White, K. Esona, C. Deatcher, P. Middleton, K. Jacobs, W. V. der Stricht, C. Merlet, et al., "The dependence of the optical energies on InGaN composition," Materials Science and Engineering: B **82**, 194 (2001).

[107] W. Sritrakool, V. Sa-yakanit, and H. R. Glyde, "Band tails in disordered systems," Physical Review B **33**, 1199 (1986).

[108] T. Mukai, M. Yamada, and S. Nakamura, "Characteristics of InGaN-based uv/blue/-green/amber/red light-emitting diodes," Japanese Journal of Applied Physics **38**, 3976 (1999).

[109] T. Deguchi, K. Sekiguchi, A. Nakamura, T. Sota, R. Matsuo, S. Chichibu, and S. Nakamura, "Quantum-confined stark effect in an AlGaN/GaN/AlGaN single quantum well structure," Jpn. Journal of Applied Physics **38**, L914 (1999).

[110] S. Schulz, T. J. Badcock, M. A. Moram, P. Dawson, M. J. Kappers, C. J. Humphreys, and E. P. O'Reilly, "Electronic and optical properties of nonpolar a-plane GaN quantum wells," Physical Review B **82**, 125318 (2010).

[111] K. Okamoto, J. Kashiwagi, T. Tanaka, and M. Kubota, "Nonpolar m-plane InGaN multiple quantum well laser diodes with a lasing wavelength of 499.8 nm," Applied Physics Letters **94**, 071105 (2009).

[112] P. Waltereit, O. Brandt, A. Trampert, H. T. Grahn, J. Menniger, M. Ramsteiner, M. Reiche, and K. H. Ploog, "Nitride semiconductors free of electrostatic fields for efficient white light-emitting diodes," Nature **406**, 865 (2000).

[113] N. F. Gardner, J. C. Kim, J. J. Wierer, Y. C. Shen, and M. R. Krames, "Polarization anisotropy in the electroluminescence of m-plane InGaN/GaN multiple-quantum-well light-emitting diodes," Applied Physics Letters **86**, 111101 (2005).

[114] S. Schulz, O. Marquardt, C. Coughlan, M. A. Caro, O. Brandt, and E. P. O'Reilly, "Atomistic description of wave function localization effects in $In_xGa_{1-x}N$ alloys and quantum wells," Proc. SPIE **9357**, 93570C (2015).

[115] S. Schulz, S. Schumacher, and G. Czycholl, "Tight-binding model for semiconductor quantum dots with a wurtzite crystal structure: From one-particle properties to coulomb correlations and optical spectra," Physical Review B **73**, 245327 (2006).

[116] S. Schulz, D. P. Tanner, E. P. O'Reilly, M. A. Caro, T. L. Martin, P. A. J. Bagot, M. P. Moody, F. Tang, J. T. Griffiths, F. Oehler, et al., "Structural, electronic, and optical properties of m-plane InGaN/GaN quantum wells: Insights from experiment and atomistic theory," Physical Review B **92**, 235419 (2015).

[117] D. P. Tanner, M. A. Caro, E. P. O'Reilly, and S. Schulz, "Atomistic analysis of the electronic structure of m-plane InGaN/GaN quantum wells: Carrier localization effects in ground and excited states due to random alloy fluctuations," Physica Status Solidi (b) **253**, 853 (2016).

[118] D. Sutherland, T. Zhu, J. T. Griffiths, F. Tang, P. Dawson, D. Kundys, F. Oehler, M. J. Kappers, C. J. Humphreys, and R. A. Oliver, "Optical studies of non-polar m-plane (1100) InGaN/GaN multi-quantum wells grown on freestanding bulk GaN," Physica Status Solidi B **252**, 965 (2015).

[119] Y. J. Sun, O. Brandt, M. Ramsteiner, H. T. Grahn, and K. H. Ploog, "Polarization anisotropy of the photoluminescence of m-plane (In,Ga)N/GaN multiple quantum wells," Applied Physics Letters **82**, 3850 (2003).

[120] L. Y. Lee, "Cubic zincblende gallium nitride for green-wavelength light-emitting diodes," Materials Science and Technology **0**, 1 (0).

[121] D. J. As, "Recent developments on non-polar cubic group III nitrides for optoelectronic applications," Proc. SPIE **7608**, 76080G (2010).

[122] D. J. As, T. Frey, D. Schikora, K. Lischka, V. Cimalla, J. Pezoldt, R. Goldhahn, S. Kaiser, and W. Gebhardt, "Cubic GaN epilayers grown by molecular beam epitaxy on thin - SiC/Si (001) substrates," Applied Physics Letters **76**, 1686 (2000).

[123] S. A. Church, S. Hammersley, P. W. Mitchell, M. J. Kappers, S. L. Sahonta, M. Frentrup, D. Nilsson, P. J. Ward, L. J. Shaw, D. J. Wallis, et al., "Photoluminescence studies of cubic GaN epilayers," Physica Status Solidi (b) pp. 1600733–n/a (2017), 1600733.

[124] F. Wu, Y.-D. Lin, A. Chakraborty, H. Ohta, S. P. DenBaars, S. Nakamura, and J. S. Speck, "Stacking fault formation in the long wavelength InGaN/GaN multiple quantum wells grown on m-plane GaN," Applied Physics Letters **96**, 231912 (2010).

[125] J. A. Chan, J. Z. Liu, and A. Zunger, "Bridging the gap between atomic microstructure and electronic properties of alloys: The case of (In,Ga)N," Physical Review B **82**, 045112 (2010).

[126] K. Kim, W. R. L. Lambrecht, and B. Segall, "Elastic constants and related properties of tetrahedrally bonded BN, AlN, GaN, and InN," Physical Review B **53**, 16310 (1996).

[127] P. Han and G. Bester, "Interatomic potentials for the vibrational properties of III-V semiconductor nanostructures," Physical Review B **83**, 174304 (2011).

[128] F. Grosse and J. Neugebauer, "Limits and accuracy of valence force field models for $In_xGa_{1-x}N$ alloys," Physical Review B **63**, 085207 (2001).

[129] J. E. Bernard and A. Zunger, "Strain energy and stability of Si-Ge compounds, alloys, and superlattices," Physical Review B **44**, 1663 (1991).

[130] D. Powell, M. A. Migliorato, and A. G. Cullis, "Optimized tersoff potential parameters for tetrahedrally bonded III-V semiconductors," Physical Review B **75**, 115202 (2007).

[131] S. Steiger, M. Salmani-Jelodar, D. Areshkin, A. Paul, T. Kubis, M. Povolotskyi, H.-H. Park, and G. Klimeck, "Enhanced valence force field model for the lattice properties of gallium arsenide," Physical Review B **84**, 155204 (2011).

[132] T. Mattila and A. Zunger, "Predicted bond length variation in wurtzite and zinc-blende InGaN and AlGaN alloys," Journal of Applied Physics **85**, 160 (1999).

[133] C. Pryor, J. Kim, L. W. Wang, A. J. Williamson, and A. Zunger, "Comparison of two methods for describing the strain profiles in quantum dots," Journal of Applied Physics **83**, 2548 (1998).

[134] M. J. P. Musgrave and J. A. Pople, "A general valence force field for diamond," Proceedings of the Royal Society of London A: Mathematical, Physical and Engineering Sciences **268**, 474 (1962).

[135] M. A. Caro, S. Schulz, and E. P. O'Reilly, "Origin of nonlinear piezoelectricity in III-V semiconductors: Internal strain and bond ionicity from hybrid-functional density functional theory," Physical Review B **91**, 075203 (2015).

[136] A. Polian, M. Grimsditch, and I. Grzegory, "Elastic constants of gallium nitride," Journal of Applied Physics **79**, 3343 (1996).

[137] C. S. G. Cousins, Ph.D. thesis, University of Exeter (2001).

[138] C. S. G. Cousins, "Internal strain in diamond structure elements: a survey of theoretical approaches," Journal of Physics C: Solid State Physics **15**, 1857 (1982).

[139] S. P. Łepkowski and I. Gorczyca, "Ab initio study of elastic constants in $In_xGa_{1-x}N$ and $In_xAl_{1-x}N$ wurtzite alloys," Physical Review B **83**, 203201 (2011).

[140] O. H. Nielsen and R. M. Martin, "Stresses in semiconductors: ab initio calculations on Si, Ge, and GaAs," Physical Review B **32**, 3792 (1985).

[141] M. A. Caro, S. Schulz, and E. P. OReilly, "Comparison of stress and total energy methods for calculation of elastic properties of semiconductors," Journal of Physics: Condensed Matter **25**, 025803 (2013).

[142] T. M. Henderson, J. Paier, and G. E. Scuseria, "Accurate treatment of solids with the HSE screened hybrid," Physica Status Solidi (b) **248**, 767 (2011).

[143] J. Paier, M. Marsman, K. Hummer, G. Kresse, I. C. Gerber, and J. G. ngyn, "Screened hybrid density functionals applied to solids," The Journal of Chemical Physics **124**, 154709 (2006).

[144] A. J. C. B. de Saint-Venant, "Memoire sur la Torsion des Prismes" (1855).

[145] M. Z. Bazant, Ph.D. thesis, Harvard University (1997).

[146] M. BORN, in "Lattice Dynamics", edited by R. WALLIS (Pergamon, 1965), pp. 1 – 7.

[147] M. Born, "Zur raumgittertheorie des diamanten," Annalen der Physik **349**, 605 (1914).

[148] J. L. Martins and A. Zunger, "Bond lengths around isovalent impurities and in semiconductor solid solutions," Physical Review B **30**, 6217 (1984).

[149] R. Benchamekh, S. Schulz, and E. O'Reilly, "Theoretical analysis of influence of random alloy fluctuations on the optoelectronic properties of site-controlled (111)-oriented InGaAs/GaAs quantum dots," Physical Review B **94**, 125308 (2016).

[150] A. Paul, M. Luisier, and G. Klimeck, "Modified valence force field approach for phonon dispersion: fromzinc-blende bulk to nanowires," Journal of Computational Electronics **9**, 160 (2010).

[151] T. Ameen, H. Ilatikhameneh, J. Charles, Y. Hsueh, S. Chen, J. Fonseca, M. Povolotskyi, R. Rahman, and G. Klimeck, in "14th IEEE International Conference on Nanotechnology" (2014), pp. 921–924.

[152] M. A. Nusimovici and J. L. Birman, "Lattice dynamics of wurtzite: CdS," Physical Review **156**, 925 (1967).

[153] C. Kittel, "Introduction to Solid State Physics, (2^{nd} ed.)" (Wiley, New York, 1956).

[154] S. Beer, J. Jackovitz, D. Feldman, and J. Parker, "Raman and infrared active modes of aluminium phosphide," Physics Letters A **26**, 331 (1968).

[155] T. Azuhata, T. Sota, and K. Suzuki, "Second-order raman spectra and lattice dynamics in AlAs," Journal of Physics: Condensed Matter **7**, 1949 (1995).

[156] P. N. Keating, "Theory of the third-order elastic constants of diamond-like crystals," Physical Review **149**, 674 (1966).

[157] A. Mooradian and G. Wright, "First order raman effect in III-V compounds," Solid State Communications **4**, 431 (1966).

[158] S. W. Ellaway and D. A. Faux, "Effective elastic stiffnesses of InAs under uniform strain," Journal of Applied Physics **92**, 3027 (2002).

[159] O. L. Lazarenkova, P. von Allmen, F. Oyafuso, S. Lee, and G. Klimeck, "Effect of anharmonicity of the strain energy on band offsets in semiconductor nanostructures," Applied Physics Letters **85**, 4193 (2004).

[160] C. S. G. Cousins, "Elasticity of carbon allotropes. I. optimization, and subsequent modification, of an anharmonic keating model for cubic diamond," Physical Review B **67**, 024107 (2003).

[161] M. Łopuszyński and J. A. Majewski, "Ab initio calculations of third-order elastic constants and related properties for selected semiconductors," Physical Review B **76**, 045202 (2007).

[162] H. Wang and M. Li, "Ab initio calculations of second-, third-, and fourth-order elastic constants for single crystals," Physical Review B **79**, 224102 (2009).

[163] O. H. Nielsen, "Optical phonons and elasticity of diamond at megabar stresses," Physical Review B **34**, 5808 (1986).

[164] J. R. Drabble and A. J. Brammer, "The third-order elastic constants of indium antimonide," Proceedings of the Physical Society **91**, 959 (1967).

[165] H. J. McSkimin and P. A. Jr., "Thirdorder elastic moduli of gallium arsenide," Journal of Applied Physics **38**, 2610 (1967).

[166] Y. Abe and K. Imai, "Anharmonic properties of ultrasounds in diamond-type crystals and quartz plate under an intense exicitation," Japanese Journal of Applied Physics **25**, 67 (1986).

[167] J. Sörgel and U. Scherz, "Ab initio calculation of elastic constants and electronic properties of ZnSe and ZnTe under uniaxial strain," The European Physical Journal B-Condensed Matter and Complex Systems **5**, 45 (1998).

[168] O. L. Lazarenkova, P. von Allmen, F. Oyafuso, S. Lee, and G. Klimeck, "An atomistic model for the simulation of acoustic phonons, strain distribution, and Grüneisen coefficients in zinc-blende semiconductors," Superlattices and Microstructures **34**, 553 (2003), proceedings of the joint 6th International Conference on New Phenomena in Mesoscopic Structures and 4th International Conference on Surfaces and Interfaces of Mesoscopic Devices.

[169] F. Cerdeira, C. J. Buchenauer, F. H. Pollak, and M. Cardona, "Stress-induced shifts of first-order raman frequencies of diamond- and zinc-blende-type semiconductors," Physical Review B **5**, 580 (1972).

[170] D. Gerlich, "Fourth order elastic moduli of diamond structure materials," Journal of Applied Physics **77**, 4373 (1995).

[171] F. H. Stillinger and T. A. Weber, "Computer simulation of local order in condensed phases of silicon," Physical Review B **31**, 5262 (1985).

[172] D. Kundys, D. Sutherland, M. J. Davies, F. Oehler, J. Griffiths, P. Dawson, M. J. Kappers, C. J. Humphreys, S. Schulz, F. Tang, et al., "A study of the optical and polarisation properties of InGaN/GaN multiple quantum wells grown on a-plane and m-plane GaN substrates," Science and Technology of Advanced Materials **17**, 736 (2016), pMID: 27933113.

[173] "Matlab optimization toolbox," (2016), the MathWorks, Natick, MA, USA.

[174] W. R. Inc., "Mathematica, Version 11.2,", champaign, IL, 2017.

[175] D. Vanderbilt, S. H. Taole, and S. Narasimhan, "Anharmonic elastic and phonon properties of Si," Physical Review B **40**, 5657 (1989).